Aspects in the Design of Spaceborne and Terrestrial Gravitational Wave Detectors.

Alison Cameron McLaren[1]

Department of Physics and Astronomy
The University of Glasgow
Glasgow, Scotland.

Thesis submitted for the degree of
Doctor of Philosophy

30th September 1996

[1] Supported by a Research Studentship from the Particle Physics and Astronomy Research Council.

To my family.

Acknowledgements

There are many people whom I would like to thank for their contribution to this work. Some by way of practical help, and others for the support and friendship which I have been lucky enough to receive when it was most needed.

Firstly, I would like to thank all of my colleagues in the gravitational waves research group at Glasgow for their interest, and for many useful hints and discussions. I would like to acknowledge my two supervisors, Professor Jim Hough and Dr Norna Robertson, for their practical advice and encouragement during the course of my work and the writing of this thesis. In addition, I would like to thank Ken Strain and Dave Robertson for their long-term interest and involvement in much of my work - this was especially appreciated during the long period of seismic isolation work, which would otherwise have been a fairly solitary experience!

I am indebted to Sharon Twyford Ray Hutchins and Alastair Grant with whom I have shared an invaluable friendship, support and sense of humour, which will not be forgotten. Excellent technical assistance has been provided by Allan Latta, Colin Craig and Angus McKellar. I also gratefully acknowledge several enjoyable discussions with Mr. Roger Bennet (Rutherford Appleton Laboratory).

I have dedicated this thesis to my family, for their continued support and interest. In particular I owe a very special thank-you to my grandfather Robert Mitchell, and to my parents John and Moira for their invaluable encouragement and good influence, especially during the course of my Ph.D. I would also like to thank Fiona, and my flat-mates Katerina, Sue and Louise for their support, friendship, and some welcome good times. And finally, to my husband Jonathan, who will never know how important and appreciated his unbelievable patience, love and support has been to me in the last three years - I could not have asked for more.

Abstract

The aim behind much of the work outlined in this thesis has been mainly towards the development of test mass pendulum suspension systems suitable for laser gravitational wave detectors. These suspension systems have a dual purpose, namely providing seismic isolation and thermal noise reduction at the test mass. The techniques utilised throughout this work are comprised of a passive seismic isolation unit constructed from alternate layers of heavy metal and rubber (or spring) units, followed by the suspension of the test mass as a pendulum hung by fused silica fibres from the top of the isolation stage. Reviews of the theoretical work underpinning these systems have also been given, where the importance of low resonant mode frequencies of the isolation system, and high quality factors of the pendulum suspension fibres are highlighted .

In chapter 2, details of the design, testing and current performance of a passive test mass seismic isolation system, constructed from layers of heavy metal and RTV-615 silicone rubber, are presented. The results of an experimental study of the anomalous compression characteristics of RTV (which lead to vertical stack resonant modes which are higher in frequency than one would normally expect) are also reported. Further to this it is shown that the compression modulus is subject to considerable stiffening when such units are placed under load.

The construction and testing of a suspension system for the measurement of high pendulum and material quality factors are described, focusing on reducing recoil damping of the test pendulum. Results to date are reported for both measurement of pendulum and material quality factor of fused silica fibres.

A theoretical analysis of the level of cross-coupling of seismic noise expected in the GEO 600 suspension system is presented, where the main mechanisms considered are cross-coupling due to the radius of curvature of the Earth, and stiffness inequality of the test mass suspension wires.

A theoretical study of attitude stability and phase-front distortion is carried out for LISA, a space-borne laser interferometric system. By considering the Fraunhofer phase variation in the far field resulting from distortions on a wavefront transmitted between two craft, the tolerable limit to the level of distortion on transmission is established.

Preface

A basic review of the nature, sources and detection of gravitational waves is covered in Chapter 1 of this thesis. This chapter will also include a short section on noise sources affecting the sensitivity of detectors.

Following this, a report on work carried out towards the reduction of seismic noise effects in both the GEO 600 system, and the Glasgow 10 m prototype detectors, is contained in Chapter 2. Work on the MATLAB modelling program used in this chapter was carried out in conjunction with Dr. Kenneth Strain in the Department of Physics and Astronomy at Glasgow.

Chapters 3, 4 and 5 are based on aspects of thermal noise reduction in the pendulum systems currently being considered for GEO 600. This work was a continuation of the progress made by J. E. Logan and colleagues in the area of thermal noise, where relevant references have been included throughout the text. The author was involved primarily in the construction and testing of a suitable test-system which was sufficiently free of recoil effects for the measurement of high pendulum and material quality factors of fused silica fibres. Silica suspension fibres were pulled using an RF oven, built by Mr. Raymond Hutchins (Department of Electrical & Electronic Engineering, Glasgow University). Electronics used to provide a TTL reference signal for recoil phase measurements carried out on the improved system (Fig.(4.16(b)), section 4.2.6) were designed and built by Prof. J. Hough (Department of Physics and Astronomy at Glasgow). Chapter 5 and Appendix B contain listings of code written by the author for use in data acquisition. The author gratefully acknowledges the use of sections of in-house configuration code, prefixed by '*am*' in the listing, with the kind permission of Dr. Alastair MacLeod (Department of Physics and Astronomy at Glasgow). Section 5.4.2 contains a brief review of the most recent results measured by Miss S.M Twyford, Dr. S. Rowan and Professor J. Hough using the equipment and data acquisition program set up by the author.

Chapter 6 contains the results of a short theoretical project carried out for the proposed spaceborne interferometric detector 'LISA', where the noise induced by the combined effects of laser phase front distortion and attitude stability of the space craft were investigated. The resulting analysis of this work, carried out in collaboration with Professor J. Hough and Dr. David Robertson, University of Glasgow, has led to the establishment of the tolerable limit to the combined surface quality of the spacecraft optical system for likely values of the attitude (pointing) requirements of the 'LISA' telescope.

Contents

List of Figures

Fig(4.9(a)): Experimental arrangement for measurement of phase lag between measurement port, P, *and signal from feedback output to coil.*

Fig(4.9(b)): Section of experimental trace for evaluation of $\phi_{o/p}$, *indicating measurement of measured phase shift,* ϕ_{meas} *and electronic phase shift* ϕ_{elec}.

Fig(4.10): Circuit diagram of phase lead filter in accelerometer circuitry.

Fig(4.11): Experimental set-up for measurement of pendulum accelerometer resonant frequency (ω_f *) with feedback lop switched on.*

Fig(4.12): Experimental arrangement for measurement of pendulum accelerometer characteristics without feedback. Feedback loop switched off. Signal induced in (unused) feedback coil plotted on chart recorder, showing accelerometer ring-down.

Fig(4.13): Experimental arrangement for evaluation of tank recoil phase lag in original condition.

Fig(4.14): Data points measured during evaluation of recoil phase lag of tank in original condition. Note levels of ground line ('GR'), electronic phase shift reference line (ϕ_{elec} *) and measured phase line (* ϕ_{ave} *).*

Fig(4.15): Improved tank arrangement.

Fig(4.16(a)): Experimental arrangement for initial measurement of phase lag between accelerometer signal and laser TTL reference.

Fig(4.16(b)): Circuit diagram of electronic arrangement required to convert 2 Hz pulse signal from the laser and slit set-up, to a 1 Hz square wave suitable for a low frequency input to the digital lock-in.

Chapter 1
The nature, sources and detection of gravitational waves.

1.1
Introduction.

The existence of gravitational waves was first predicted by Einstein in his General Theory of Relativity (Einstein,1916). Almost all of the fundamental postulates of this theory have by now been proved experimentally, with the direct observation of these waves remaining as one of the most challenging scientific projects in experimental physics this century. A great deal of progress has been made world-wide in this field over the last few decades both in the design and implementation of terrestrial detectors, and in design proposals for those in space. The successful detection of gravitational radiation will have great significance, both for the astronomical community (through the opening of the 'gravitational window' on the universe) and also for fundamental physics where aspects of relativity theory may be verified.

Associated with predictions from relativity, there is indirect evidence of the emission of gravitational waves by the binary pulsar PSR1913+16. Here the observed rate of orbital decay is in agreement with that predicted due to gravitational radiation reaction (Taylor and Weisberg, 1982). As the production of gravitational waves of a detectable amplitude relies on large accelerations of very heavy masses, it is expected that when gravitational waves are directly observed they will have often originated from an astrophysical source of high activity.

This chapter gives a brief review of the nature, sources and detection of gravitational waves. A more thorough review of these topics can be found in, e.g., Press and Thorne (Press and Thorne, 1972), Blair (Blair, 1991) and Schutz (Schutz 1996).

1.2
The Nature of Gravitational Waves.

Gravity is the weakest of the four fundamental forces of nature. However, as it is always of one sign and of long range it is this force which tends to dominate over large distance scales in the universe. The description of the effect of gravity on a body as being due to the curvature of space, rather than a force depending on the mass of the body, was postulated by Einstein in his General Theory of Relativity. Gravitational waves are ripples in the curvature of spacetime, whose effect is to induce a time-varying strain in the local spacetime curvature. Just as electromagnetic waves are produced through the acceleration of charge, the acceleration of mass will result in the emission of gravitational waves which are transverse and propagate at the speed of light. One significant difference between gravitational and electromagnetic waves is that as mass has only one sign it is necessary for the acceleration of matter to result in a change in the quadrupole moment of the system for emission to take place. Thus, only asymmetric accelerations of matter will produce gravitational radiation. In addition to this, the gravitational force is very weak compared to the electromagnetic force; thus we can expect that the interaction of a test body with gravitational waves will result in a very small effect. However, the highly penetrative nature of gravitational waves will enable them to carry a great deal of information about the astrophysical process producing them, without suffering from the interaction with surrounding matter common in the emission and propagation of electromagnetic waves.

In order to understand the principles behind the detection of gravitational waves, we must consider their effect on a test body or detector. The interaction of gravitational radiation with a ring of free test particles is illustrated in Fig(1.1).

Gravitational waves give rise to tidal forces which can be described in terms of a dimensionless amplitude, h, representing the strain induced in space as the wave propagates. There are two independent polarisation states; the 'plus' polarisation (illustrated here) is denoted h_+ and the 'cross' polarisation (where the strain pattern of the test particles is rotated by 45°) denoted by $h_\times$.

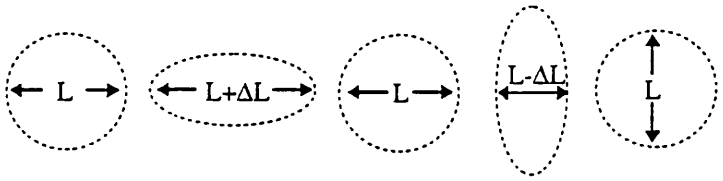

Fig (1.1): ***Effect of passage of a single cycle of a gravitational wave on ring of free test particles, of diameter L.*** *Quadrupole nature of radiation gives rise to perpendicular dimension changes* $\pm \Delta L$.

The amplitude of the gravitational wave is defined as $h = 2\Delta L/L$ which, for typical signals, is extremely small - generally of order 10^{-22} or so over the characteristic bandwidth of the signal. Any mechanism devised for their detection must be able to match this sensitivity.

The range of astrophysical sources which are thought most likely to produce gravitational radiation in the frequency regimes observed by terrestrial detectors (from a few tens of Hertz to a few kilohertz) is discussed in the following section. There will also be a discussion of possible low frequency sources (where f lies in the range 10^{-4} - 10^{-1} Hz), which should be observable by detectors placed in the quiet environment of space.

1.3
Sources of Gravitational Waves.

Astrophysical sources can in general be divided into two main categories, according to the expected form of emission of the gravitational radiation. One such category includes burst sources of radiation, where the emitted wave will last for only a few cycles. The second category contains the periodic sources, which give rise to continuous emission of gravitational radiation. In addition to the waveforms above, it is expected that there will also be a stochastic background of gravitational radiation. This section will provide a brief overview of these sources, including some of those expected at low frequencies. A

more comprehensive discussion can be found in Bonazzola and Marck (Bonazzola and Marck, 1994), Blair (Blair, 1991), and Schutz (Schutz, 1996).

1.3.1
Burst sources.

Bursts of gravitational radiation tend to be produced as a result of some cataclysmic acceleration of matter in the universe. Such an event may occur during a supernova explosion, where the core of a massive star collapses suddenly, or during the final few seconds of binary system coalescence. Let us now consider these sources further.

- Supernovae

The classification of supernovae as type I or type II, is based on the composition of the original stellar core. Type I supernovae (where the stellar core of the progenitor is composed mainly of carbon) are less well understood than type II, however there are two main mechanisms from which type I supernovae are believed to be formed. The first scenario is the nuclear detonation of a white dwarf in a binary system following accretion of matter from a companion star. The second possibility is formation as a result of the merger of a white dwarf binary system, where matter from the smaller, destroyed companion star forms a thick accretion disc round the survivor. The remaining white dwarf then accretes mass and angular momentum, until the Chandrasekhar limit is reached, whereupon the star will collapse under its own gravity.

The second form (type II) is very different, and results from the sudden collapse of a massive star whose core is composed mainly of iron, and can therefore no longer generate enough thermal radiation to support itself from self-gravity. Following this exhaustion of its nuclear fuel a type II supernova will result when the stellar core suddenly collapses to form a neutron star or black hole, with the resulting shock wave blasting out the surrounding shell of material.

If the original star was rotating with a high level of angular momentum, the collapsing core may become unstable, resulting in a non-spherical collapse. As the production of gravitational radiation requires a high level of acceleration of matter in an asymmetric

system, the strength of the resulting radiation will depend on the degree of sphericity and the rate of collapse of the stellar core.

In addition to the emission of gravitational radiation expected by type II supernovae, it is thought that type I supernovae (of the latter type described) will emit gravitational waves where the accretion disc is very thick and the angular momentum of the progenitor star is high.

It is not easy to predict the magnitudes of either the rate of collapse or the degree of asymmetry, but an approximation to the amplitude h that one may expect from this source is given by equation (1.1) below (Schutz, 1996). Here a gravitational wave with frequency f and energy ΔE is emitted in a time τ. The distance to the source is denoted by r, where this evaluation has been based on the distance to the Virgo cluster (~15 MPc). At such a distance, obtainable by first generation of interferometric detectors such as LIGO and GEO 600, one might expect an event rate of around one per year (Schutz, 1996). It is hoped that second generation detectors will be able to conduct searches at distances of many tens of MPc, where it is thought that the event rate will rise to around one per day.

$$h = 5\times 10^{-22}\left(\frac{\Delta E/M_{\odot}c^{2}}{10^{-3}}\right)^{1/2}\left(\frac{15\,\mathrm{MPc}}{r}\right)\left(\frac{1\,\mathrm{kHz}}{f}\right)\left(\frac{1\,\mathrm{msec}}{\tau}\right)^{1/2} \qquad (1.1)$$

where $M_{\odot}$ denotes one solar mass. Note that values of ΔE, f and τ will depend on the type of collapse scenario envisaged.

- Compact binary coalescence.

Binary systems, consisting of two compact objects (such as neutron stars or black holes) orbiting each other due to their mutual gravitational attraction, provide another asymmetric source which will emit gravitational waves. The strength of the gravitational wave emission increases with the orbital eccentricity of the system, with the strongest signals being produced at periastron (where the accelerations are highest). The resulting loss of energy and momentum leads to orbital decay, and eventually to coalescence of the two stars, which will provide a source of burst radiation in the observable frequency

range for terrestrial detectors. Orbital decay consistent with that expected as a result of this gravitational radiation reaction has already been observed in the binary pulsar PSR1913+16, where details of the orbital period have been obtained through examination of the doppler shifted pulsar arrival times.

During the final few seconds prior to coalescence, this form of signal will be characterised by a 'chirp' of gravitational radiation due to the rapid increase in both amplitude and frequency of the waveform. For example, the orbital frequency of a binary system may increase from ~ 100 Hz to ~ 1 kHz in just a few seconds, changing on a timescale given by(Schutz, 1986):

$$\tau = \frac{f}{\dot{f}} = 7.8\left(\frac{m_T}{M_\odot}\right)^{-2/3}\left(\frac{\mu}{M_\odot}\right)^{-1}\left(\frac{f}{100}\right)^{-8/3} \text{ seconds} \qquad (1.2)$$

where $M_\odot$ has the value of one solar mass, $m_T M_\odot$ is the total mass and $\mu M_\odot$ the reduced mass of the binary system. The average strain amplitude induced by the wave is given by (Schutz, 1986):

$$h_{rms} = 10^{-23}\left(\frac{m_T}{M_\odot}\right)^{2/3}\left(\frac{\mu}{M_\odot}\right)\left(\frac{f}{100\text{ Hz}}\right)^{2/3}\left(\frac{100\ MPc}{r}\right) \qquad (1.3)$$

where the distance to the source is denoted by r.

In general, a global network of at least three gravitational wave detectors will be able to determine information such as the distance to the source, the source strength (h), and the frequency and polarisation of the wave, from observation of such systems. It has been noted by Schutz (Schutz, 1986) that the product $h_{rms}\tau$ will be independent of both the total mass and reduced mass of the binary system, thus allowing the extraction of the value of r (the distance to the source) without making any assumptions about the mass values of the source. This may be carried out in conjunction with optical redshift observations or statistical methods where the recession velocity of the source may be evaluated (Schutz in (Bender et al, 1996)). As the value of 'r' will have been made to a high accuracy ($\approx$ 0.1%, (Schutz, 1996)) the gravitational wave information obtained will allow the evaluation of Hubble's constant and the cosmological deceleration parameter to high accuracy.

An area of uncertainty at present is the likely rate of detection of such coalescence events. Recent evidence from large area pulsar surveys ((Curran & Lorimer, 1995), and references therein) has indicated that the number of neutron star-neutron star binary systems is much less than previous models, which were based on much sparser pulsar search data, had predicted. Curran and Lorimer have set the event rate to a level of approximately 1 event every 8 years for distances out to around 100 MPc. It is expected that second generation detectors will be able to search to distances of around 600 MPc, whereupon they predict an event rate of around 3 per year. However, they believe that these results may be pessimistic; the existence of a much larger population of binary systems with very short orbital periods, which would not have been picked up during the pulsar searches, has been theoretically postulated by Tutukov & Yungelson (Tutukov & Yungelson, 1993).

In addition, the contribution of [1]black-hole binary systems to the event rate should not be ignored. It is believed that a reasonable fraction of binary systems should contain a black hole, which would provide a signal amplitude that is around four times larger, thus an event rate that is higher, than that from neutron star binary systems. Recent work carried out by Wilson and Mathews (Wilson & Mathews, 1995) has suggested that general relativistic effects may cause otherwise stable binary stars to individually collapse to black holes prior to merging which, if so, would increase the likelihood of this source. Wilson and Mathews have also found that the binary orbit becomes unstable at much greater separation distances than previously thought, thus decreasing the frequency of the coalescence and bringing it closer to the maximum sensitivity region of first generation detectors.

The detection of gravitational radiation from coalescing compact binary systems may also shed some light on the source of γ-ray bursts, thought to be due to, e.g., coalescence of neutron star-neutron star or neutron star-black hole binary systems (Bonazzola and

Marck, 1994, and references therein) at cosmological distances. Satellite experiments, e.g. the Burst and Transient Source Experiment (BATSE), have observed around one γ-

[1] The frequency range of ground based experiments will restrict the observation of black hole binaries to those of fairly low mass (M~10^2 solar masses). Measurements made in space in the very low frequency range ($10^{-1} - 10^{-4}$ Hz) will allow access to much more massive black holes (M~$10^5 - 10^7$ solar masses) which are expected to provide even higher signal amplitudes.

ray burst per day. Curran and Lorimer's results on the merger rate of such systems suggest that the bursts must originate from distances beyond 1 GPc for this event rate to be possible.

1.3.2
Periodic sources.

Periodic emission of gravitational waves may result from an asymmetric, stably rotating system, such as a rotating neutron star. There are various mechanisms which may result in some degree of asymmetry in such a star. For instance, should the rotating neutron star have high angular momentum after formation, normal modes may be induced which propagate in the opposite sense to the rotation of the star (Schutz, 1996). The star will eventually stabilise following loss of angular momentum due to the emission of gravitational radiation. Following this, rotating neutron stars may be left with some degree of ellipticity due to the residue of these irregularities, frozen in as the star cooled, which will give rise to the emission of gravitational waves at twice the rotation frequency of the system. Asymmetry may also arise if a rotating neutron star in a binary system accretes matter from its companion star (Wagoner, 1984). The accreting star may be spun up during this process, again exciting normal modes in the star, with the eventual emission of gravitational waves until sufficient angular momentum has been lost to allow the star to re-stabilise. Accretion that is not aligned with the rotation axis of the star may also cause the star to precess, again giving rise to gravitational radiation (Schutz, 1996). There will be an increase in the strength of emission for higher rotation rates and greater deviations from spherical symmetry.

1.3.3
Stochastic background.

It is expected that there will also be a stochastic background of gravitational radiation, resulting from the superposition of many sources that are randomly situated in time and space, including binary systems and cosmological sources.

For binaries outwith our galaxy, the combined radiation will have no intrinsic directionality thus giving rise to a random background. It is also believed that the

stochastic background may include remnants of primordial radiation, emitted following any inflationary period in the early stages of the universe((Schutz, 1996) and references therein).

Another, potentially stronger, possible source may be due to the vibration of closed loop cosmic strings (Allen & Shellard, 1992). Recent work carried out by Brustein et al (Brustein et al, 1995) has suggested that the background spectrum of gravitational radiation produced by cosmic strings may lie within the observation band of the advanced LIGO detector. As it is believed that cosmic strings may in fact act as seeds for the formation of new galaxies, observation of the radiation emitted from these objects may provide valuable information on the process of galaxy formation.

1.3.4
Low frequency sources

In addition to the detection of gravitational waves using terrestrial detectors, which mainly operate at frequencies between a few tens of hertz and a kilohertz, there is also the possibility of detection using spaceborne systems. An example of such a proposed detector, 'LISA', will be discussed further in Chapter 6, and will operate over a frequency range . 10^{-4} - 10^{-1} Hz . Thus, although many of the sources outlined in previous sections will lie above the detection range of 'LISA', there will be a wide variety of sources whose expected emission at low frequencies will enable their detection by such a system. Many of these low-frequency sources are perhaps among the most interesting for both astronomy and fundamental physics alike. We shall now briefly discuss some of these sources, although a more thorough review can be found in Schutz (Schutz, 1996), Bender et al (Bender et al, 1996) and references therein.

The orbital motion of binaries whose orbital period is less than around 3 hours will give rise to the emission of periodic gravitational radiation within the LISA detection threshold. It is expected that LISA will undertake observation of several forms of galactic binary systems, of which neutron star binaries, and the X-ray and common envelope binaries are examples. The orbital period of the neutron star-neutron star binary PSR1916+13 (7.68 hours) will place it outwith the detection range. However it is

expected that there will be many other neutron star binary candidates for observation, from which 'LISA' will provide information on the population statistics of binary neutron star systems.

X-ray and common envelope binaries exist where one star in a binary system becomes compact and accretes matter from its companion. This will result in the emission of X-rays during the accretion process. Eventually the companion star will become so close that it will disappear from optical view. However, there will still be a significant emission of gravitational waves. It is believed that there will be a number of such systems whose orbital periods are short enough to allow detection by LISA. In general, the detection of such periodic systems will allow information to be gathered on such issues as distance, spatial distribution, and population of the various types of binary system in our galaxy. However, there may also be a significant background below around 3 mHz, arising due to a large number of white dwarf binary systems within the LISA detection range, which may mask signals from some galactic binaries, compact object binaries at cosmological distances, and the lower frequency region of the stochastic background.

Perhaps one of the more unusual sources within the LISA threshold will be solar *g*-modes. Observation by conventional means have provided evidence of the solar *p*-modes[**], which take place outwith the convection zone where the mass density is lowest. However, the solar *g*-modes have not yet been detected as the largest amplitude of motion occurs deep in the solar interior where there is a high mass density. This mode may produce detectable perturbations in the local (Newtonian) gravitational field which may be observed by LISA. An instrument dedicated to the observation of these modes, SOHO, was launched last year; as the sensitivity of LISA is expected to match that of SOHO, it is hoped that LISA will also be able to observe this source.

The most important likely source to be observed by LISA will be massive black holes or massive black hole binary systems at the heart of distant galaxies. These binaries will provide very strong signals, allowing LISA to determine their position to better than 1 minute of arc. Optical redshift information, combined with LISA distance information (1.3.1) would allow the determination of the Hubble constant and deceleration parameter to much greater accuracy than achieved by conventional means (Schutz (1986)).

[**] Solar p-modes are the acoustic modes of oscillation of the Sun. The g-modes are also normal modes, but can be thought of as giving rise to 'global' rather than superficial disturbances.

Observations made of black hole mergers, and of the orbital path followed by neutron stars during capture by black holes, will also provide critically important strong-field tests of General Relativity.

1.4
Detectors.

Direct observation of gravitational radiation will require the development of detectors that are sensitive to the extremely small strains in space induced by the waves. There are two main detector types under consideration world-wide, namely resonant bar antennas and laser interferometers. This section will provide a basic overview of these terrestrial detector types with more thorough discussions being found by various authors throughout Blair (Blair, 1991), and also in Hough, Danzmann, Schutz et al, (Hough, Danzmann, Schutz et al, 1994). Additional information regarding the function of spaceborne laser interferometric antennae is included in the introductory section Chapter 6.

1.4.1
Resonant bar detectors.

Resonant bar antennae were originally proposed by Weber (Weber, 1960) as a means of detecting the passage of gravitational waves as they impinge on the Earth. This method has been further developed by researchers in the USA, Australia, Europe and the Far East.

As its name suggests, this type of antenna essentially consists of a massive, right circular cylindrical bar of some highly resonant material (e.g. aluminium or niobium). The fundamental longitudinal resonant frequency of such a bar, generally with a mass of a few tonnes, is typically in the region of 1 kHz which is a reasonable frequency for gravitational wave detection. The passage of a gravitational wave of around this frequency, with suitable polarisation and orientation will cause a change in the amplitude and phase of the signal at the fundamental resonant frequency of the bar. The resonant motion of the ends of the bar are monitored by some form of sensitive transducer, and changes looked for. The resonant bar antenna is by nature a narrowband device, where

the system as a whole must be able to detect changes in the motion of the ends of the bar of less than around 10^{-18}m . The sensitivity of these detectors will be limited by the presence of thermal noise associated with the resonant mode of the antenna, and the noise level of the transducer and amplifiers. To reduce the effect of thermal noise, bars are constructed from materials with low levels of intrinsic losses (high quality factor) which are then cooled to temperatures below that of liquid-helium (4.2 K). Losses to the external surroundings are also minimised by suspending the bar in vacuum. The additional effect of spurious vibrational noise from the external environment can be reduced using a series of mechanical filters in the bar suspension system.

The final limit to the sensitivity achieved will ultimately be determined by the Heisenberg Uncertainty Principle, even in a system where the level of thermal noise is negligible. It has been noted, however, that this limit may be circumvented through a change in the measurement technique employed (e.g. Caves, 1982). For example, let us consider a mass, m, whose amplitude of motion can be described by the magnitude of the vector X, say. This vector consists of two quadrature components, X_1 and X_2, corresponding to the amplitude of motion associated with the displacement of the oscillator and its momentum respectively. Thus we can state that $X = X_1 + jX_2$. The detection methods currently used to measure the motion of the mass are phase-insensitive, and thus measure both X_1 and the quadrature component X_2 together and with the same level of noise. Thus, the quantum-limit to the accuracy with which one can measure the position of the mass can be written:

$$\Delta X_1 \, \Delta X_2 = \left(\frac{\hbar}{m \, \omega_a} \right)$$

$$\Delta X_1 = \Delta X_2 = \sqrt{\left(\frac{\hbar}{m \, \omega_a} \right)} \qquad (1.4)$$

If a phase-*sensitive* measurement were made, information could be obtained about a single quadrature component (e.g. displacement, X_1) only and to arbitrarily high accuracy, with the bulk of the measurement error being incurred in the other quadrature component, the associated momentum X_2. This increased error in X_2 will not affect the overall measurement error, provided no information on X_2 is sensed. This technique,

known as 'back action evasion', requires considerably more experimental development before such a process may be used but, if implemented, it is believed that such a scheme would circumvent the systematic quantum limit level imposed by the current measurement method.

There presently exists a network of detectors, developed by researchers at the Universities of Rome, Western Australia and Louisiana State, where a narrowband sensitivity of $h_{rms} \approx 6 \times 10^{-19}$ (LSU) has been achieved. One interesting future development is the planned construction of spherical solid-mass antennae (Abramovici et al, 1995). These have two main advantages over traditional bar detectors in that they are much greater in mass than a bar of the same frequency (without greatly increasing the overall size of the antenna), and that they have five quadrupole modes as compared with the single fundamental mode of a bar (thus acting like a 'multiple antenna').

1.4.2
Laser interferometric detectors.

Laser interferometric detectors were originally developed by Weiss (Weiss, 1972) and Forward (Forward, 1978). There are in fact two forms of terrestrial laser interferometer used for gravitational wave detection, both of which are based in principle on the simple Michelson interferometer (Fig.(1.2)). Unlike the resonant bar antenna, which measures strain in one direction only, the orthogonal configuration of the Michelson interferometer lends itself to measurement of differential changes in armlength and is therefore well suited to measurement of quadrupole distortions in space such as those produced by gravitational waves.

As can be seen from Fig.(1.2), light from a common source is divided into two beams of approximately equal intensity through partial reflection at a beam splitter. Following reflection from a mirror at each end the return beams are then recombined at a photodiode, where an interference pattern will be observed. A differential change in the lengths of the arms (e.g. through interaction with gravitational waves) will give rise to a corresponding change in the phase difference between the returning beams, indicated by a change in the intensity of the observed light.

The test masses must be 'free' in order for the effect of interaction with the incoming gravitational waves to be fully realised. The masses are suspended as pendulums in vacuum, with compliant mountings between ground and the suspension point.

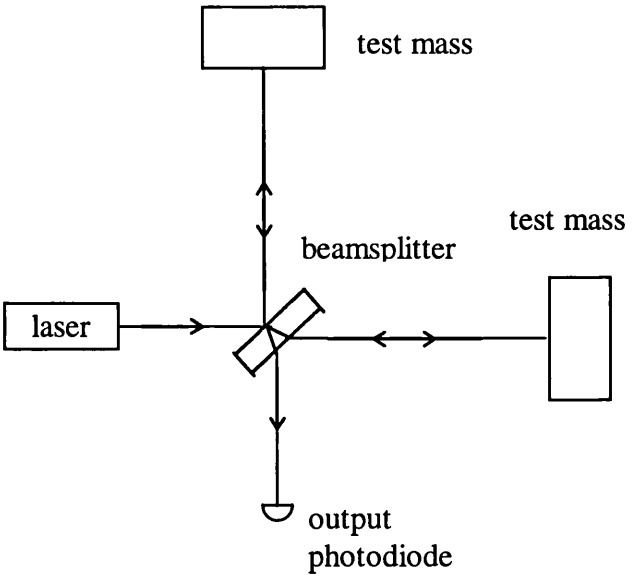

Fig(1.2): ***Schematic diagram of a simple Michelson Interferometer.***

In this way the masses are essentially free in the frequency region between the upper resonant modes of the mounting and suspension units and the internal modes of the test masses themselves (typically around a few tens of hertz to a few kilohertz say). Thus an interferometric detector is broadband in nature, with the sensitivity being highest in broad regions where the external noise sources have been sufficiently reduced, rather than at a single resonant mode of the mass.

The length of each arm is defined by the distance out to a test mass, whose mirrored surface reflects the beam. Recalling the expression for strain amplitude (section 1.2), $h = 2\Delta L/L$, one can increase the sensitivity by increasing the armlength (L) of the detector, until L is ~ $\lambda_{GW}/4$ (i.e. the maximum signal will obtained when the light is stored inside the arm for a time equivalent to half the period of the gravitational wave). For typical signal wavelengths however, this would imply that armlengths of order 75 km (for a signal of frequency 1 kHz) or longer would be required - a length which is clearly unfeasible. The armlength can be brought down to more manageable proportions,

typically around 3 km for a full size detector, through the use of multiple reflections of the light inside the cavity. Originally there were two forms of multi-pass scheme under development, namely the delay-line and the Fabry-Perot (resonant cavity) detectors.

- Delay-Line Detectors.

This detector configuration was first proposed by Weiss (Weiss, 1972) and was, until recently, under development by researchers at the Max Plank Institute for Quantum Optics (MPQ, Germany), and is presently being used by a group at the Institute of Space and Astronautical Science (Japan). A simple schematic diagram of a delay line interferometer is shown in Fig.(1.3(a)).

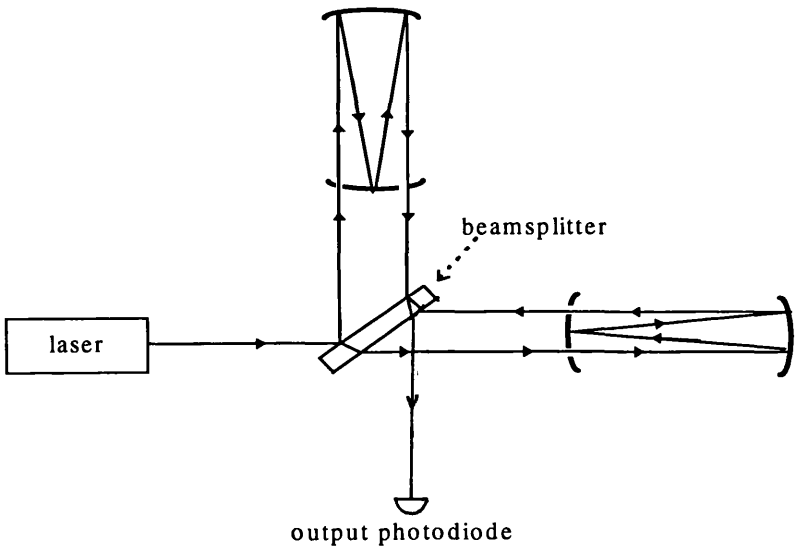

Fig(1.3(a)): ***Schematic diagram illustrating a simple interferometer with a delay line in each arm.*** *Only four passes of light in the arms are shown for clarity.*

Each delay line is formed using a pair of spherical mirrors. The input beam is injected into the delay line through a small hole in the input mirror. The mirror geometry is arranged such that the beam is eventually transmitted through an output hole after the required number of traverses has taken place inside. The beams do not overlap during this process. Recombination takes place at a photodiode where the output signal is maintained at a dark fringe using feedback techniques where, e.g., Pockels cells are used in each arm to sense any deviation from the dark fringe operating point using modulation techniques, and feed back an appropriate signal to correct this (Winkler in Blair (Blair,

1991)). The feedback voltage signal required to do this is a measure of the phase (hence armlength) change and is used as the interferometer output.

As the beam spots are spatially separated round the mirror edge, the mirror must be correspondingly large for many traverses. This is one disadvantage of the delay line design. Also, interferometers of this type may be susceptible to additional phase noise due to the presence of scattered light within the delay lines. Although the interferometer should be insensitive to fluctuations in the frequency of the laser light source (as this is common to both arms), scattered light may have travelled a significantly different path than the main beam before exiting the beamsplitter and recombining with the main interferometer output at the photodiode. It is for these reasons that delay line detectors are generally out of favour now (Winkler, 1993), with the resonant cavity method being preferred. For the intermediate scale GEO 600 system, however, a variation of the delay-line has been chosen as the detector configuration. In this instance, the mirrors in each arm do not directly face each other, and are laterally displaced (Fig.(1.3(b)). In this way, on injection into the arm the beam bypasses the first mirror, rather than being injected through a hole, which it is hoped will help reduce the initial scattering of the beam. Any scattered light which is present will not be able to become trapped in the arm and will be less likely to recombine with the main beam. The GEO 600 delay line will involve four passes of the beam.

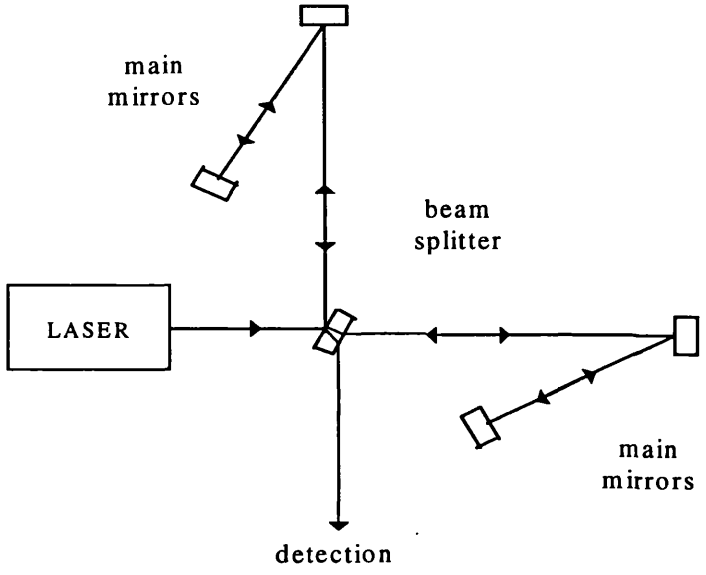

Fig(1.3(b)): Schematic diagram of the GEO 600 4-beam delay line detector configuration. *(Angles are exaggerated).*

To date a maximum strain amplitude sensitivity of $1.1\times10^{-19}/\sqrt{\text{Hz}}$ above 1.5 kHz has been achieved by the MPQ 30m armlength prototype delay line detector (Shoemaker et al, 1988).

Resonant cavity interferometers, which use resonant cavities in each arm to store the laser light, were pioneered on a 10m prototype at Glasgow University (Drever et al, 1980), and are now also being developed on the 40m prototype detector at the California Institute of Technology and on a 20 m prototype detector in Japan (ISAS). The initial motivation for this design was to reduce the problem of internal scattered light by making the beams travel identical paths.

- Resonant cavity interferometers

As can be seen in Fig.(1.4), the beams are stored in resonant Fabry-Perot cavities placed in each arm, and are not spatially separated. The laser light is passed through a 50% beam-splitter, with half of the original beam being sent to each cavity. One cavity, known as the 'primary cavity', is held on resonance by adjusting the laser frequency to match a resonant mode of this cavity. Should the length of this cavity change, the laser wavelength will be altered accordingly. The passage of a gravitational wave through the system would induce a differential change in armlength, resulting in a change in the laser wavelength as it follows the primary cavity length.

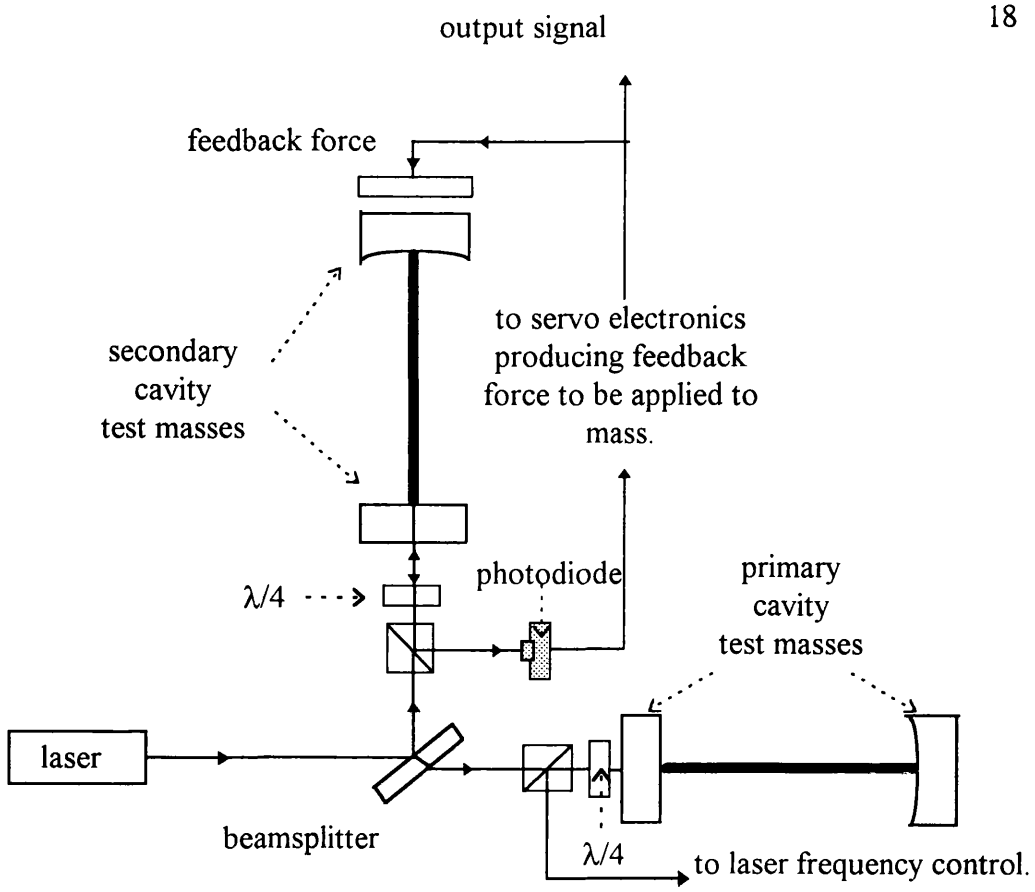

Fig.(1.4): ***Greatly simplified schematic diagram of an interferometric detector with Fabry-Perot cavities in the arms.***

The stabilised laser light is also sent directly to the secondary cavity whose length is adjusted using a feedback loop attached to the cavity mirrors keeping the secondary cavity on resonance with the incoming light. The resulting feedback signal required to keep the secondary cavity on resonance with the laser light would provide the gravitational wave signal

In principle this system should suffer less from the problems associated with scattered light than the delay-line interferometer, and would also allow the use of smaller cavity mirrors as the beams are not required to be spatially separated. However, as both cavities must be held on resonance with the laser light the resonant cavity configuration requires more sophisticated control systems to allow precise orientation of the test masses and high levels of frequency stabilisation of the laser light. The gravitational wave sensitivity of the Glasgow 10m resonant cavity prototype has reached $6\times10^{-20}/\sqrt{\text{Hz}}$ above 600 Hz (Robertson et al, 1995). Recently the American 40m prototype, run jointly by MIT and Caltech, has reached a strain sensitivity of $10^{-20}/\sqrt{\text{Hz}}$ (Bender et al, 1996). A great deal of current effort is being concentrated

on the development of long baseline detectors which, it is hoped, will be operational by the turn of the century. Researchers in the USA are presently constructing a pair of detectors with 3 km armlength which will form the LIGO detector system. It is planned that this will operate in conjunction with a planned 3 km instrument (forming the long baseline VIRGO detector) to be built in Cascina, Italy. In addition, the German/British collaborative effort has been stepped up with the construction of an intermediate length, 600 m baseline detector, [2]GEO 600. Construction has already begun at a site near Hanover, with first operation planned to take place in a similar timescale to that of LIGO and VIRGO. The operation of a network of such detectors is necessary to allow the detection, measurement and source location of gravitational wave signals.

1.5
Sources of noise in interferometric gravitational wave detectors.

The detection of gravitational radiation requires that high levels of interferometer sensitivity be achieved. For example, in the proposed GEO 600 system, a target sensitivity equivalent to order $h \approx 10^{-22}/\sqrt{\text{Hz}}$ at 100 Hz will be required. To achieve this requires that the total displacement noise in one arm is $\delta x \leq 3\times10^{-20}\,\text{m}/\sqrt{\text{Hz}}$. There are several sources of noise present in interferometric detectors that are likely to contribute to the sensitivity limit, the most significant of which will be discussed in this section and evaluated for GEO 600. A more comprehensive review of possible noise sources for several interferometric detector systems can be found in, e.g., Blair (Blair et al, 1991), Abramovici (Abramovici et al, 1992), and Hough, Danzmann, Schutz et al (Hough, Danzmann, Schutz et al, 1994).

[2] It should be noted that much of the work reported in the remainder of this thesis has been directed primarily towards the development of the GEO 600 detector.

1.5.1
Heisenberg Uncertainty Principle.

The accuracy with which the position of a mass suspended as a pendulum can be determined will be limited by the Heisenberg Uncertainty Principle. The minimum detectable differential change in separation of two end masses, each of mass m, measured at the frequency of interest f (over a bandwidth Δf) will be limited to (Edelstein et al, 1978):

$$x_{up} = \left[\frac{\hbar}{(\pi^2 f^2 m)}\right]^{1/2} \mathrm{m}/\sqrt{\mathrm{Hz}} \qquad (1.5)$$

In the case of the GEO 600 detector, the varying contributions from the optical components in the system (due, for example, to different mass values and numbers of bounces) must be taken into account. It has been found that the limit placed by the uncertainty principle on the maximum gravitational wave amplitude sensitivity of the GEO 600 detectors expected to be of order $< h > \approx 2.5 \times 10^{-23} / \sqrt{\mathrm{Hz}}$ at 100 Hz (Rowan, 1995).

The effect of the uncertainty principle can be reduced by increasing the armlength of the detector. This noise source will, in general, have a less significant effect than other noise sources.

1.5.2
Photon counting statistics.

Corresponding to the differential change in position of the test masses due to interaction with gravitational radiation will be a change in the relative phase of the light from each arm. This in turn leads to a change in the intensity of the light at the output of the interferometer. The minimum detectable change in intensity is set by photon counting statistics (also known as photon shot noise). In a time τ the statistical uncertainty in counting n photons is $\sqrt{n}$. The signal to noise ratio resulting from this photon counting

error can be reduced by maintaining the output of the detector on a dark fringe. For an idealised detector with no loss of light at the mirrors, the limiting sensitivity set by this noise source can be expressed as equation (1.6) below (Hough et al, 1987):

$$h = \left(\frac{1}{\tau_s}\right)\left[\frac{\pi \hbar \lambda}{2\varepsilon I_0 c}\right]^{1/2} \quad /\sqrt{Hz} \tag{1.6}$$

where λ is the wavelength of the laser light, ε is the quantum efficiency of the photodiode, c is the speed of light in vacuum, $\hbar = h/2\pi$ and I_0 is the illuminating light power. The optimum value of τ_s, the storage time of light in the cavity, is half the period of the gravitational wave. It can be seen from equation (1.6) that this limit can be reduced through increasing the power of the illuminating laser light. The storage time in the cavity can be set through the choice of a suitable reflectivity of the input mirrors. One possible method of increasing the illuminating light power is to use a technique known as standard recycling. If the losses throughout the optical system can be kept low and the interferometer is operated on a dark fringe, there will be very little absorption of the stored light. By positioning a recycling mirror at the input to the interferometer (Fig.(1.5), position *M*) this light can be reflected back into the cavity, thus increasing the stored light power.

In this way for an interferometer of armlength L, with end mass reflectivity R, and input mass reflectivity chosen such that the storage time is equal to half the period of the gravitational wave, the effect of shot noise can be reduced (e.g. Drever in Blair, 1991) leading to a limiting sensitivity given by:

$$h \approx \left[\frac{\hbar \lambda f(1-R)}{\varepsilon I_0 L}\right]^{1/2} \Big/ \sqrt{Hz} \tag{1.7}$$

There are other possible methods of improving the detector sensitivity by reducing the effect of shot noise. One such scheme, known as dual recycling, has been proposed by Meers (Meers, 1988). Here an additional, partially transmitting mirror (the 'signal recycling mirror') is placed at the interferometer output in front of the photodiode. If

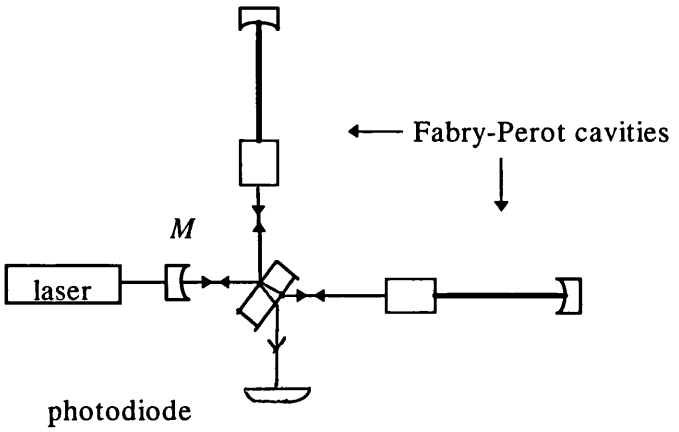

Fig(1.5): ***Schematic diagram of a Fabry-Perot interferometric gravitational wave detector using standard (broadband) recycling.***

the interferometer is operating perfectly, the light arriving at the interferometer output will consist solely of the signal sidebands, produced due to modulation of the original laser waveform by the passage of a gravitational wave through the system. Careful positioning of the signal recycling mirror will form a resonant cavity in the system which will support one of these sideband frequencies. In addition to the build up of power from the standard recycling mirror inside the system, there will also be an enhancement of the signal sidebands. One main difference between these two examples is that standard recycling gives rise to a broadband increase in the shot-noise limited sensitivity of the interferometer. As the dual recycling system resonates one of the signal sidebands this will also allow a tuned, narrowband increase in sensitivity, centred round the signal frequency to be obtained. A dual recycling scheme has been experimentally demonstrated to increase the sensitivity of an interferometer (Strain and Meers, 1991).

1.5.3 Seismic noise.

The level of ground motion at most urban sites due to seismic and other vibration noise generally increases during daytime, and is almost certainly dominated by that from man-made sources. For this reason, the construction of long baseline gravitational wave detectors is generally carried out on green-field sites, as far from sources of man-made ground disturbance as possible. Even so, there will remain a measurable level of ground noise in the horizontal, vertical, rotation and tilt directions whose effect must be

significantly reduced if the tiny path length changes induced by gravitational waves are to be detected. This can be done by introducing suitable seismic isolation measures into the detector design.

A commonly used isolation system is the simple pendulum, where the intrinsically low mechanical losses have the additional advantage of reducing the internal mechanical motion (thermal noise) of the connection (refer to Chapter 3). In order to provide the level of seismic isolation required to reach the target sensitivity, the pendulum is generally suspended from some form of additional isolation system. This is typically comprised of a [3]passive seismic isolation stack, made from of layers of heavy masses separated by elastic spring units. With careful design, passive systems such as the stack and double pendulum combination investigated in this work, are believed to provide adequate performance in a frequency range from around 100 Hz.

Work is also being carried out on a passive isolation system for the VIRGO detector (Braccini et al, 1995) which is constructed from a seven layer cascaded series of pendulums hung from soft metal leaf-springs followed by the test mass suspension from a specially designed device known as a 'marionetta' (whose primary function is to provide an isolated platform to which the test mass orientation control forces can be applied). This superattenuator system is expected to provide sufficient isolation at relatively low frequencies (from below 10 Hz), but involves considerably more engineering input than the more commonly used stack and pendulum passive isolation system design. Another system utilising cantilever springs is currently being developed for use in the suspension of the niobium cryogenic bar detector at the University of Western Australia (Ju et al, 1993).

Measurements have been made at several locations (e g, (Hough et al, 1989), (Shoemaker et al, 1988)), suggesting that the typical amplitude spectral density, above approximately 1 Hz, for both horizontal and vertical [4]motion for a 'quiet-site' can be approximated by equation (1.9) below. This spectral density will be used throughout the work reported here.

---

[3] Active isolation systems, where unwanted motion is sensed and actively corrected, have also been investigated by various workers e.g. (Robertson et al, 1982), (Stebbins et al, 1994).

[4] The tilt motion amplitude spectral density has also been measured at a typical site (Cantley, 1991), showing a typical tilt noise amplitude of $2 \times 10^{-11}\ {}^{rad}/_{\sqrt{Hz}}$ at 100 Hz.

$$\delta x \approx \frac{10^{-7}}{f^2}\ \mathrm{m}/\sqrt{\mathrm{Hz}} \qquad (1.8)$$

Without isolation, vertical and horizontal seismic motion would contribute a displacement noise level of $10^{-11} m/\sqrt{Hz}$ at 100 Hz. As thermal noise alone at 100 Hz is expected to reach a level of $3\times10^{-20}\ \mathrm{m}/\sqrt{\mathrm{Hz}}$ it is necessary to ensure that seismic noise is significantly lower than this. To reach the horizontal displacement noise level required by GEO 600 it is therefore necessary to provide an isolation factor of around 10^{11} at 100 Hz. The design principles of the kind of passive seismic isolation system favoured for both the Glasgow detector and GEO 600 are discussed further in Chapter 2.

1.5.4
Thermal noise.

Another important limit to the sensitivity achieved will be set by thermal noise. As thermal noise drives the resonant modes of a mechanical system, there are two main routes through which it can affect suspended masses; namely through the modes of the suspension and the internal modes of the test masses. Suspension thermal noise is associated mainly[5] with the horizontal modes of the pendulum and the violin modes of the suspension wires, giving rise to real horizontal translation of the test mass. Internal mode thermal noise corresponds to the vibrational modes of the mass itself where apparent horizontal 'movement' is detected due to distortions of the mass surface, and not due to real translation of the centre of mass.

The thermal motion of a simple pendulum, of mass m and quality factor Q, has a peak value at the pendulum mode resonant frequency f_{pend}. This frequency typically has a value of 1 Hz. Far above this resonance the thermal motion background associated with this mode has a spectral density given by Saulson (Saulson, 1990 and references therein) as equation (1.9).

---

[5] There will also be noise corresponding to other modes of the pendulum, e.g. vertical, tilt, and rotation. However, although these have been included in the evaluation of the thermal noise level for GEO 600, (Logan, in Hough, Danzmann, Schutz et al, (1994)) has found that they are in fact negligible to thermal motion corresponding to the horizontal mode, providing that the beams are well centered.

$$< x_{pend}(f) >= \left[\frac{4 k_B T f_{pend}^2}{(2\pi)^3 m f^5 Q_{pend}} \right]^{1/2} \quad \mathrm{m}/\sqrt{\mathrm{Hz}} \qquad (1.9)$$

where k_B is Boltzmann's constant, T is the temperature and f is the frequency of interest. This equation assumes that the pendulum is essentially damped due to internal friction in the suspension material. These losses are characterised by the loss function $\phi(\omega)$, which is related to the quality factor on resonance by $\phi(\omega_0) = Q$. This loss function is nowadays assumed to be independent of frequency. The issue of the appropriate form of $\phi(\omega)$, and the implications for thermal noise is discussed in Chapter 3. It can be seen from equation (1.9) that the thermal motion background associated with the pendulum mode can be reduced through the use of low-loss suspensions where the pendulum quality factor is high(or $\phi(\omega)$ is small).

It is expected that for GEO 600 the corresponding level of thermal noise associated with the pendulum mode of the suspended mass will be (Logan, in Hough, Danzmann, Schutz et al (1994)):

$$x_{pend} \approx 6.5 \times 10^{-21} \left[\frac{f_{pend}}{1\,Hz} \right] \left[\frac{100\,Hz}{f} \right]^{5/2} \left[\frac{16\,kg}{m} \right]^{1/2} \left[\frac{10^7}{Q_{pend}} \right]^{1/2} \mathrm{m}/\sqrt{\mathrm{Hz}} \qquad (1.10)$$

In order to achieve low pendulum losses it is also important to ensure that the violin mode quality factors are also as high as possible. Violin modes typically appear from a few hundred hertz in the working frequency range. It has been shown by Gillespie and Raab (Gillespie and Raab, 1993), Gonzales and Saulson (Gonzales and Saulson, 1994) and Logan (Logan et al, 1993(b)) that where the rocking mode of the pendulum has been constrained the violin mode and pendulum mode quality factors (hence background noise level) are related by the following expression (where ϕ is assumed to be independent of frequency):

$$Q_{pend} = 2 Q_{violin} \qquad (1.11)$$

It is therefore important to ensure that the violin mode losses are as low as possible when trying to achieve high pendulum Q's. One way of reducing the violin losses is the provision of well-defined break-off points where the suspension wires leave the mass. In addition to this, high violin mode quality factors also allow these modes to be notched out of the detector frequency response without significant loss of bandwidth (although it is also wise to ensure that the violin mode harmonic series begins at as high a frequency as possible).

Thermal noise associated with the internal modes of the system will also peak at the associated system resonances, in this case the internal modes of the test mass. Just as the dimensions of seismic isolation stack elements is chosen according to the corresponding internal mode frequencies, the dimensions of the test mass will be chosen in such a way that the lowest internal mode has a frequency much higher than the range of interest. However, there will still be a background level of thermal motion associated with this mode, generally becoming dominant with respect to pendulum mode thermal noise at around 100 Hz or so, which must be taken into account. Through the summation of the effects of many internal modes, at frequencies far below that of the fundamental internal mode, the thermal motion background will have a spectral density described by:

$$< x_{mass}(f) >= \left[\sum_n \left(\frac{4k_B T}{\alpha_n m \omega_n^2 Q_n(\omega) 2\pi f} \right) \right]^{1/2} \mathrm{m}/\sqrt{\mathrm{Hz}} \qquad (1.12)$$

where the mass of the oscillator is replaced by the effective mass, $\alpha_n m$, where α_n depends on the geometry of the optical mode of the illuminating beam, and also on the mass and resonant frequency of the oscillator (Gillespie, 1995).

Following the work by Gillespie and Raab (Gillespie, 1995), it has been stated by Logan in Hough, Danzmann, Schutz et al (Hough, Danzmann, Schutz et al, 1994) that the thermal noise at frequencies well below the internal modes of a test mass of diameter 25 cm and thickness 15 cm, subject to an incident laser beam of 2 cm diameter will be:

$$\langle x_{test\ mass} \rangle \approx 2.8 \times 10^{-20} \left[\frac{100\ Hz}{f} \right]^{1/2} \text{m}/\sqrt{\text{Hz}} \qquad (1.13)$$

where the quality factor of the internal modes, $Q_n(\omega)$, is a constant equal to 5×10^6 . Similarly, for a beamsplitter mass suitable for GEO 600, where the thickness is 7cm and all other parameters are as listed above, the thermal noise from the internal modes is predicted by Logan to be:

$$\langle x_{beamsplitter} \rangle \approx 5.3 \times 10^{-20} \left[\frac{100\ Hz}{f} \right]^{1/2} \text{m}/\sqrt{\text{Hz}} \qquad (1.14)$$

Thus, the limit expected to the sensitivity of GEO 600 (Fig.(1.3(b)) due to the total internal and pendulum mode thermal noise at 100 Hz may be expressed as

$$h_{th} = \frac{1}{L} \left[\frac{5}{2} \left(x^2_{mass} + x^2_{pend} \right)_{\substack{test \\ mass}} + \frac{1}{2} \left(x^2_{mass} + x^2_{pend} \right)_{\substack{beam \\ splitter}} \right]^{1/2} = 9.8 \times 10^{-23} \ / \sqrt{\text{Hz}} \qquad (1.15)$$

The numerical factors allow for the fact that the beam is in contact with the first mirror in each arm twice before leaving the system. From this expression (equation (1.15)) it can be seen that the reduction of the effect of thermal noise will rely on the use of low loss materials for the test masses. Much work has been carried out in this field recently by, e.g., Braginsky (Braginsky et al, 1992), Kovalik and Saulson (Kovalik and Saulson, 1993), and Logan (Logan, 1993(a)).

1.5.5
Other noise sources.

Discussion so far has provided a brief review of the principle sources of noise that are likely to limit the performance of an interferometric detector. However, there are other sources of noise which may also come into play. These include: fluctuations in pressure of the residual gas inside the detector which can give rise to a variation in the optical path length of the light beams; noise associated with the laser light, for instance due to frequency and intensity fluctuations, which require to be stabilised using some form of feedback system; noise resulting from some misalignment of the optical cavities which allows fluctuations in the geometry of the laser beam to couple in. Misalignment can be reduced by the use of auto-alignment systems; details of recent work in this area for the Glasgow 10m prototype can be found in Morrison (Morrison, 1993).

1.5.6
Summary of predicted noise levels for GEO 600.

Figure (1.6), taken from the GEO 600 proposal document (Hough, Danzmann, Schutz et al, 1994), shows a graphical summary of the main noise sources discussed in sections 1.5.1 to 1.5.4. These curves assume the use of a 4-pass delay line system with 5 W of illuminating laser light (1.06 μm) power. A dual recycling scheme, (with signal recycling set to wide bandwidth) is assumed to be in place. As can be seen, the region of best sensitivity lies approximately in the region of 80 - 600 Hz. At the lower frequency end the sensitivity is expected to be limited by residual seismic noise up to around 80 Hz, where the effect of thermal motion associated with the pendulum and internal modes of the test mass and suspension wires takes over. The seismic noise curve assumes the use of a four-layer seismic isolation stack followed by the suspension of the test mass as a double pendulum (Chapter 2). The thermal noise curve is based on a pendulum Q of 10^7, and internal mode Q values of 5×10^6. Towards higher frequencies the detector sensitivity is limited mainly by photon shot noise.

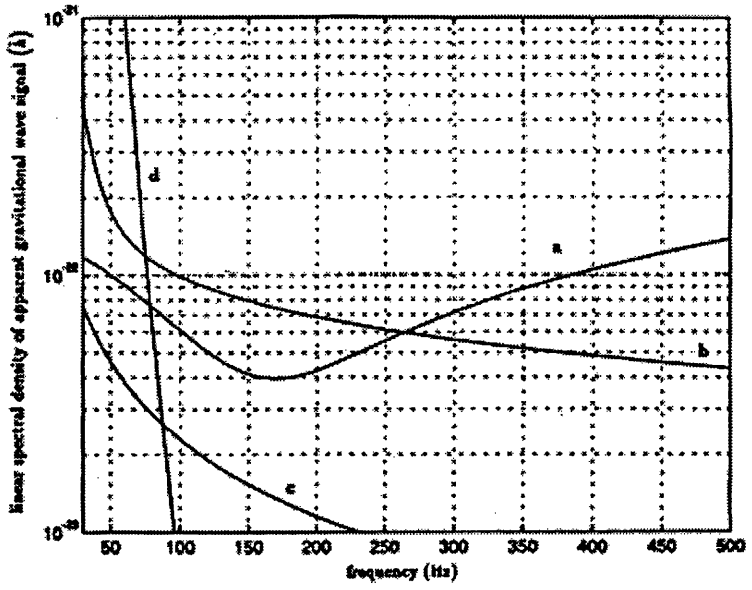

Fig(1.6): Summary of limits set on sensitivity linear spectral density by the principal noise sources in GEO 600. *Curve* a *represents the photoelectron shot noise,* b *the level of thermal noise in the system,* c *the limit set by the Heisenberg Uncertainty Principle, and* d *the level of seismic noise expected in the system.*

Chapter 2
Aspects of the seismic isolation for Glasgow and GEO600 detectors.

2.1
Introduction.

The topic of seismic noise as an important low-frequency noise source has been introduced in section 1.5.3. This chapter will now deal with several aspects of seismic isolation which are fundamental to the effective vibration control of the test mass and other suspended masses of the GEO 600 detector. An introduction to the principles of isolation for detectors employing passive stack and pendulum isolation systems, is contained in section 2.1.1. This is followed by the background to a simple method of modelling the performance of these stacks in section 2.1.2. As the ability to predict the stack performance depends on having knowledge of the stiffness of the rubber used, it is useful to consider the theory of standard rubber behaviour, which is reviewed in 2.1.3. This section also includes an introduction to work carried out previously to characterise the non standard load-stiffening behaviour of a class of rubber known as two-part cold cure silicone rubber (or RTV). Further investigation of this behaviour was carried out and reported in section 2.2, where the simple modelling method was also developed further in light of these findings. In sections 2.3 and 2.4 this model was then applied to the design of RTV and heavy metal isolation stacks for both the Glasgow 10m prototype and GEO 600 test masses. Another aspect of the spring units considered for GEO 600 is examined in section 2.4.2, where a method of out-gassing control of the RTV units was investigated.

2.1.1
An introduction to the principles behind a passive isolation system suitable for GEO 600.

Consider the single layer stack below (Fig.(2.1)), consisting of a single mass, m_1 mounted on a set of rubber units. The combined spring constant of these units in a certain

direction can be denoted by the complex spring constant $k(1+j\phi(f))$, where $\phi(f)$ is the phase lag (or loss-function) existing between the applied force and the resulting displacement of the mass.

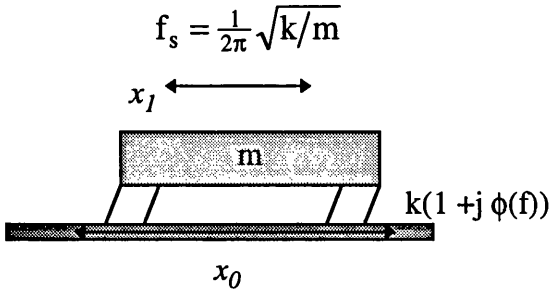

Fig.(2.1): ***Motion of a single layer stack.*** *Above the resonant mode frequency* f_0, $|x_1/x_0| < 1$, *i.e. attenuation of ground motion* x_0 *will be taking place.*

Where internal damping dominates that from other sources (e.g. viscous damping due to surrounding air), the equation of motion is given by:

$$m\ddot{x}_1 = -k(1+j\phi(f))(x_1 - x_0) \tag{2.1}$$

We can solve this equation for the transfer function (or 'transmissibility') $\frac{x_1}{x_0}(f)$, given by equation (2.2) below:

$$\frac{x_1}{x_0}(f) = \frac{f_s^2(1+j\phi(f))}{(f_s^2 - f^2) + j f_0^2 \phi(f)} \tag{2.2}$$

where the resonant frequency of the stack is defined to be $f_s = 1/2\pi\left(\sqrt{k/m}\right)$. A full discussion of the form of $\phi(f)$ can be found in Chapter 3, where it is seen that in general $\phi(f)$ can have one of two forms. For the case of viscous internal damping (which is dependent on the velocity of the oscillator), $\phi(f) = \xi f$ where ξ is a constant. Where the internal losses are due to anelasticity in the oscillator $\phi(f) = \eta$ where η is a

constant ((Kimball and Lovell, 1927), (Giaime et al, 1994)).

The exact form of the stack transfer function (equation (2.2)) with frequency will depend on that of $\phi(f)$. For both cases, equation (2.2) shows that at low frequencies (i.e. where $f << f_s$), the transmissibility of the stack tends to unity; that is to say there will be direct transmission of ground motion to the top of the stack. Beyond the resonant frequency ($f >> f_s$) the stack will begin to attenuate this motion, with the slope of the transmission roll-off being $(f_s/f)^2$, or 12 dB per octave (Fig.2.2). In the case of internal viscous damping, however, this rate of attenuation will not last indefinitely, as eventually the frequency-dependent damping term begins to have an effect. This change occurs at $f = f_s Q$ (where $Q = 1/\phi(f_s)$ is the quality factor of the system which defines the sharpness of the resonant response). Thereafter the slope tends toward $(f_s/Q f)$, or 6 dB per octave. An advantage may be found in the case of structural damping, where the slope will continue to fall as 12 dB per octave, unless some additional viscous loss mechanism is present in the system.

Extension of this to an *n*-layer stack of these layers, results in *n* resonant vibration modes of the stack, whose frequencies are not simply related to that of the single layer. In multi-layered stack systems, the attenuation of ground motion begins at frequencies higher than that of the last stack vibration mode. Although attenuation will begin at a higher frequency, the roll-off is given by the multiple of the attenuation levels provided by each individual layer. For this equal layer system, this will be of the form $(f_s/f)^{2n}$, continuing until a frequency $f_s Q$ where the rate of attenuation will halve for the case of viscous damping.

Assuming (as a worst case) that some form of viscous damping dominates, then the isolation provided by the stacks in the region of attenuation is given for the horizontal and vertical by:

$$I_{sh} = \left(\frac{f_{sh}}{Q_{sh} f}\right)^n \quad ; \quad I_{sv} = \left(\frac{f_{sv}}{Q_{sv} f}\right)^n \tag{2.3}$$

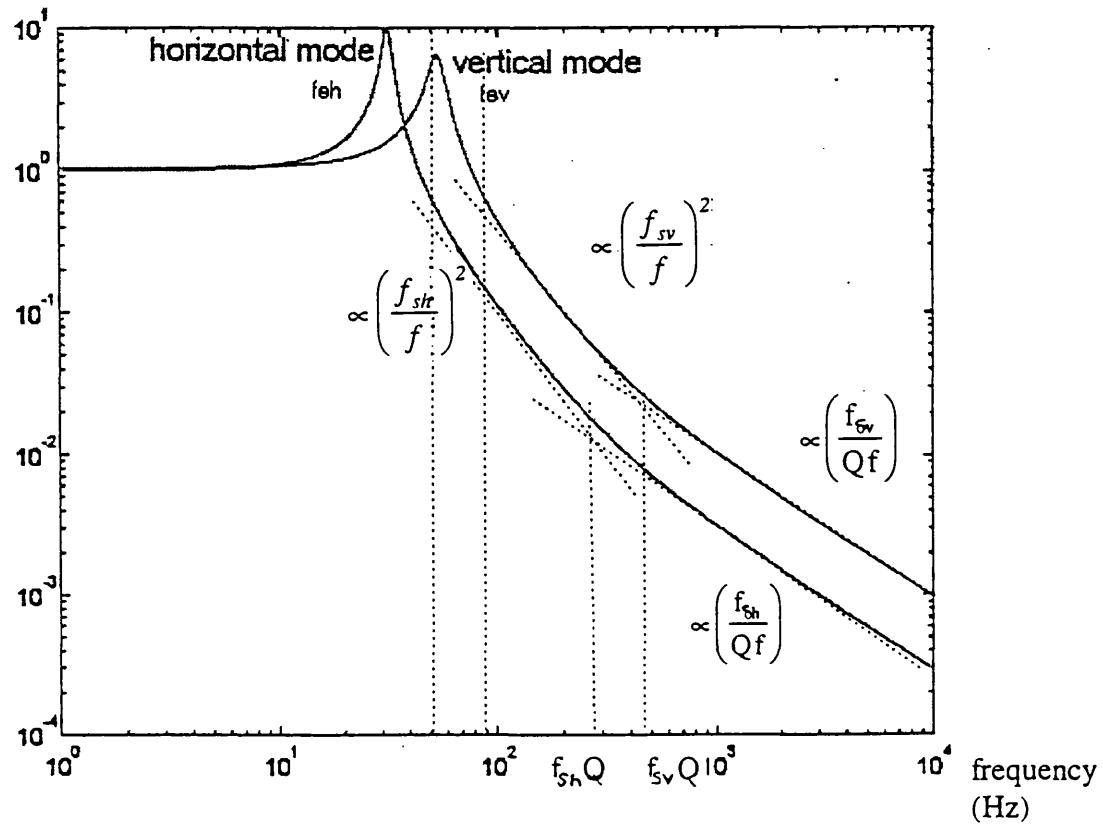

*Fig.(2.2): **Summary of the typical features found in the transmission spectra of a single layer stack system.** This is illustrated for both the vertical and horizontal directions as marked.*

It is important when designing such stack systems to have vibration mode frequencies that are as low as possible in order to provide a reasonable level of attenuation as soon as possible. Care should also be taken in the choice of metal element dimensions, as the presence of high frequency internal resonant modes within the working frequency range can seriously degrade the isolation level achieved.

- The double pendulum.

In addition to providing a greater degree of isolation from ground motion, the use of the pendulum suspension system for test masses, and other suspended optical components, will also reduce the levels of thermal motion at the mass (Chapter 3). The choice of a

double pendulum suspension, rather than a simple pendulum, allows additional seismic isolation from the extra stage. It is necessary to control the position and orientation of the test mass using a feedback system, with the force being applied to the mass via a local coil and magnet driver. In the double pendulum system this force is applied to the intermediate mass rather than to the test mass directly, allowing the effect of any electronic noise in the feedback system to be attenuated (at frequencies higher than that of the pendulum resonance) by the natural filtering action of the lower stage. At higher frequencies some feedback forces will also be applied directly to the test mass to control the cavity length.

Let us consider such a double pendulum (Fig.(2.3)), where the resonant frequencies of the upper and lower pendulum stages, of mass m_1 and m_2 respectively, in the horizontal and vertical are denoted by f_{ph1}, f_{ph2} and f_{pv1}, f_{pv2}.

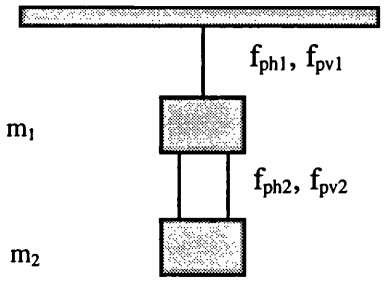

Fig.(2.3): Simple schematic diagram of a typical double pendulum suspension .

It is shown in (Cantley, 1991) that, at frequencies higher than the upper resonance of the coupled system and below the wire resonant frequencies, the isolation factors provided by a high Q double pendulum in the horizontal (equation (2.4)) and vertical (equation (2.5)) are given approximately by:

$$I_{ph} = \frac{\left(1+\frac{m_2}{m_1}\right) f_{ph1}^2 f_{ph2}^2}{f^4} \qquad (2.4)$$

and

$$I_{pv} = \left(\frac{f_{pv1}}{f}\right)^2 \left(\frac{f_{pv2}}{f}\right)^2 \tag{2.5}$$

Due to the stiffness anisotropy present in rubber units, and the difference in horizontal and vertical test mass restoring forces, the attenuation of vertical seismic noise by both the stacks and the suspension system is less efficient than in the horizontal (Fig.(2.2)). Although it is horizontal motion of the test mass which we are trying to prevent, this strong residue of vertical motion cannot be ignored if any mechanism exists where it can give rise to horizontal motion of the test-mass (known as cross-coupling). This can easily dominate direct horizontal noise. For the GEO 600 system, the level of cross-coupling one would expect has been considered (Appendix A), resulting in a conservative upper estimate of 0.1%, although this value will vary with test mass design. Assuming that the noise contributions are uncorrelated, the total residual noise level, δx_{mass}, at the test mass is found from:

$$\delta x_{mass} = \sqrt{\delta x_h^2 + \delta x_{\substack{cross \\ coupled}}^2} \tag{2.6}$$

We can combine the stack and pendulum isolation factors to find δx_{mass} (at frequencies well away from the vibration modes of the stack and the internal modes of the stack masses themselves) for a given seismic input δx_{noise} ,δy_{noise} in the horizontal and vertical respectively. For an n-layer stack at frequencies $f > f_s Q_s$, followed by a double pendulum the residual noise can be can be expressed as:

$$\begin{aligned} \delta x_h &= \delta x_{noise} \left(\frac{f_{sh}}{Q_{sh} f}\right)^n \left(\frac{f_{ph}}{f}\right)^4 \left(1 + \frac{m_2}{m_1}\right) \\ \delta x_{\substack{cross \\ coupled}} &= \delta y_{\substack{noise \\ input}} \left(\frac{f_{sv}}{Q_{sv} f}\right)^n \left(\frac{f_{pv1}}{f}\right)^2 \left(\frac{f_{pv2}}{f}\right)^2 C \end{aligned} \tag{2.7}$$

Where the horizontal and vertical resonant frequencies of a single layer of the stack are denoted here by f_{sh} and f_{sv}, with corresponding quality factors Q_{sh} and Q_{sv}, and the cross coupling factor is denoted by C.

2.1.2
Modelling method used to predict stack performance for direct transmission of horizontal and vertical noise.

The correct design of a stack system, where target isolation levels are reached by the required frequency in the working range, relies very much on the ability to reasonably predict its resonant behaviour. Previous work has been carried out at Glasgow on the isolation performance of a passive system subject to seismic noise in the [6]vertical, horizontal and tilt directions (Cantley, 1992). Results from this work indicated that although tilt noise at the surface of the earth can be transmitted through to the mass, the overall effect will be significantly reduced if the rubber units are embedded into the metal stack elements. It will also be critically important to ensure that the test mass is suspended from the centre of mass of the top stage of the isolation system. As it is assumed that these steps will be taken to a sufficient level in the final GEO 600 design, the following work is concerned primarily with the effects of horizontal and vertical noise transmission through the system. Assuming this, the simple model illustrated below in Fig.(2.4) (for the case of a generalised [7]four layer stack) is sufficient to model the isolation performance of the stack.

The position co-ordinate of each stack element is denoted by ζ, and can be chosen to represent either the vertical or horizontal direction. The total stiffness per layer of the rubber units in this chosen direction is denoted by k, the value of which will be determined by the dynamic modulus, number and dimensions of the rubber units in each layer. This feature was important in the case of RTV units where it was found that the

[6] It is noted that the effects of rotational seismic noise have not yet been fully investigated (Cantley, 1991). It is recognised, however, that this may lead to additional horizontal noise at the point of suspension if this is offset from the vertical axis through the centre of the stack and may well be the subject of future investigations to ascertain whether this is a significant effect.

[7] This model can be extended to any number of layers or combinations of spring constants.

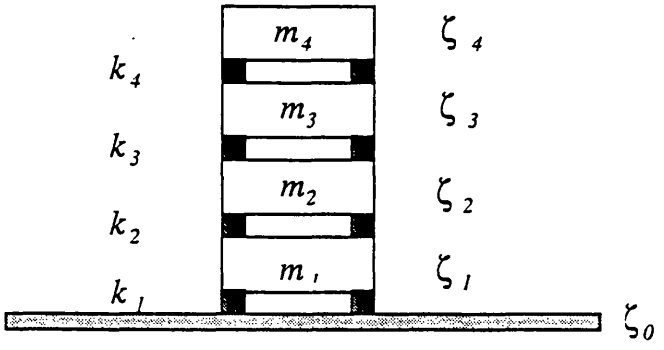

Fig.(2.4): Simple stack model forming basis of analytical technique. Horizontal or vertical position co-ordinates are denoted by ζ, and rubber stiffness per layer by k.

spring constant of identical units varied according to the static load above. This model therefore allowed the straightforward inclusion of this feature. In addition the masses may be unequal (although to simplify the model, they are usually expressed in terms of a multiple or a fraction of a common mass value, *m*). It is sufficient to model a single leg* to gain a reasonable picture of the full stack behaviour with the top mass being equivalent to the fraction of the top plate mass supported by that leg. The use of this model, in the light of experimental results reported later in this chapter, will be considered again in section 2.2. We can illustrate its use in the prediction of the transmission spectrum of a stack for a given seismic input, ζ_0. This allows the attenuation region and roll-off to be identified.

For this general case we can write the equations of motion (without damping) of each mass in the usual way as in equation (2.8). The fundamental resonant modes of each individual layer are given by $f_{0n} = 1/2\pi\sqrt{k_n/m_n}$

$$\begin{aligned} m_1\ddot{\zeta}_1 &= -k_1(\zeta_1 - \zeta_0) + k_2(\zeta_2 - \zeta_1) \\ m_2\ddot{\zeta}_2 &= -k_2(\zeta_2 - \zeta_1) + k_3(\zeta_3 - \zeta_2) \\ m_3\ddot{\zeta}_3 &= -k_3(\zeta_3 - \zeta_2) + k_4(\zeta_4 - \zeta_3) \\ m_4\ddot{\zeta}_4 &= -k_4(\zeta_4 - \zeta_3) \end{aligned} \qquad (2.8)$$

* Where the stack is comprised of several identical units, or 'legs', joined above by a rigid top plate. (This is commonly used in systems such as those considered here, where it is necessary to suspend a mass from the centre of the stack).

The transfer function of this system can be found by solving for ζ_4/ζ_0, which will be of the form $\frac{\zeta_4}{\zeta_0}(f)=\frac{f_{01}^2 f_{02}^2 f_{03}^2 f_{04}^2}{G(f)}$, where the denominator, $G(f)$, gives the characteristic equation of the system for given values of mass and stiffness. Solving for the poles of $\frac{\zeta_4}{\zeta_0}(f)$ gives the values of the coupled mode resonant frequencies, f_1 to f_4, for the system. A software package such as MATLAB will also plot the transmissibility as a function of frequency, allowing the form of the predicted stack performance to be examined. It should be noted that a suitable level and form of damping should be included in the model to allow the correct transmission roll-off to be presented. For model results presented in this chapter the damping is incorporated by means of a complex spring constant, $k = k(1 + j\phi)$, where the level of damping losses present in the system is represented by a suitable value ofϕ.

2.1.3
Review of dynamic characteristics of rubber.

Returning to consider the performance of vibration isolation stacks in the lower frequency regime (<100Hz), we must note that to achieve low frequency stack vibrational modes will require careful thought in the choice of the rubber spring elements used. There now follows an overview of aspects of conventionally accepted theory concerning the dynamic behaviour of [8]rubber units under compressive load. A very readable account of the wider field can be found in the works of PB Lindley and LR Mernagh, of which references (Lindley, 1969) and (Mernagh, 1969) are recommended.

[8] It should be noted that the standard theory outlined here, as is generally the case, has been based on observations made with mainly natural gum rubber, and other natural rubber compounds which have been subjected to various additional processes, e.g. vulcanisation and/or filling with such substances as carbon black.

- Horizontal behaviour of rubber units

Conventionally accepted theory on the dynamic behaviour of natural rubber compounds under compressive load (Lindley, 1969) assumes that the magnitude of the shear modulus, G, is a constant of the rubber, regardless of its dimensions. However, it is also important to realise that the observed value of shear modulus may well have been modified through bending of the units. As a useful rule of thumb, bending will occur if the ratio $\frac{height}{breadth} > 0.25$. The dynamic modulus setting the horizontal resonant frequency, f_{0h}, is therefore an *apparent* value of shear modulus, G', for that particular unit which is related to both the actual value (G) and the above ratio.

The modified shear modulus, G', due to bending is given by:

$$G' = \frac{G}{\left(1 + \frac{z^2}{36\,k_r^2}\right)} \tag{2.9}$$

where z is the height of the rubber unit, and k_r is the radius of gyration of the rubber unit cross-section about a neutral axis. (For rectangular units $k_r^2 = L^2/12$ where L is the longest horizontal cross-sectional dimension. Also, for cylindrical units $k_r^2 = D^2/16$, where D is the diameter of the cylinder (Lindley, 1969).)

For a rubber unit with top surface area to height ratio A/z, under a load m, standard theory predicts that the horizontal stiffness, k_h, and resonant frequency, f_h can be found using the following simple relations:

$$k_h = \frac{G'A}{z}$$

$$f_h = \frac{1}{2\pi}\sqrt{\frac{k_h}{m}} \tag{2.10}$$

- Vertical (compression) behaviour of rubber units.

The vertical behaviour of rubber under a compressive load is rather more complicated than in shear. For most other materials, vertical dynamic behaviour is governed by the Young's Modulus, E_0 of the material concerned. Where no volume change takes place in the material, Poisson's Ratio (ν), has the value 0.5, and E_0 is related to the shear modulus, G, by the following standard relationship (Snowdon, 1979):

$$E_0 = 2G(1+\nu) = 3G \tag{2.11}$$

Rubber behaviour on the other hand depends on a modified version of Young's Modulus, the value of which depends on the Shape Factor, S, of the unit concerned, where:

$$S = \frac{one\ loaded\ area}{total\ force\ free\ area} \tag{2.12}$$

For rectangular units of length L, breadth B, and thickness z, $S = \frac{LB}{2z(L+B)}$. Similarly, cylindrical units of rubber with diameter D and height z, have a Shape Factor given by $S = D/4z$. This modified Young's Modulus (known as the Compression Modulus, E_c), is given by standard theory in the form of equation (2.13)

$$E_c = E_0\left(1+2\Theta S^2\right) \tag{2.13}$$

(where Θ is a dimensionless constant related to the rubber hardness, and is approximately unity for soft rubbers). It is clear from equation (2.13) that considerable increase in E_c occurs where rubber units have a high shape factor (i.e. a relatively small amount of outer surface area with which the rubber can take up the compressive strain through

bulging). It is vitally important for rubber units to have enough freedom to bulge in order to maintain their compliant properties.

Most test units considered for our purposes have a very low shape factor ($S < 1$), therefore one would expect that $E_c \approx E_0$ for soft rubbers. For these low shape factors, it is generally accepted that rubber remains linear for strains up to at least 30% (Lindley,1969; Greenhalgh, 1993). Hence the following rules of thumb, concerning E_c and corresponding stiffness and resonant frequency, are commonly used to predict the vertical behaviour from known horizontal characteristics:

1) Where $S < 1$, we would expect from standard theory that the rubber would remain linear up to compressive strains of at least 30% i.e. G and E_c remain constant.
2) For soft rubber, with $S < 1$, we expect that the vertical behaviour be determined by the compression modulus, $E_c \approx 3G$.
3) Assuming this, we can predict the vertical behaviour from that in the horizontal from $k_v = \frac{E_c A}{z}$ and $f_v \approx \sqrt{3}\, f_h$.

- Application of standard theory results to simple stack model.

For these rules of thumb, where the dynamic moduli suffer no change as a result of compressive strains under around 30%, we can now define the 'standard theory' form of the simple stack model discussed in section 2.1.2.

As a consequence of rule 1) above we would expect that the dynamic moduli, hence the spring constants (k_h, k_v) of the rubber units be equal in each layer of the stack where there are an equal number of identical units per layer. A schematic diagram of the standard theory stack model appropriate for use in the horizontal is shown in Fig.(2.5). Solution of the equations of motion for such a stack, using MATLAB or other means, would allow standard theory predictions of the horizontal stack resonant frequencies to be made.

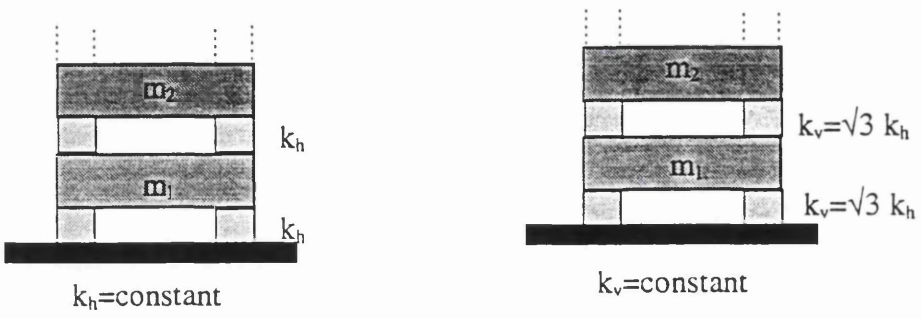

(2.5(a)) **(2.5(b))**

Fig.(2.5): Implications of standard rubber theory on simple stack model.

We would also expect, from rules 2) and 3), that the vertical spring constant used in the vertical stack model be found directly from the horizontal spring constant if known. Hence the solution of the equations of motion of the stack model shown in Fig.(2.5(b)) will give the standard theory predictions of the stack vertical behaviour

These rules of thumb have been commonly used in the past for the design of isolation stacks (e.g. Cantley, 1991; Greenhalgh, 1993.). However, we shall see later in section 2.2 that although these standard theory predictions of rubber behaviour are known to hold for natural rubber compounds, they have not been seen to hold for a two-part, cold-cure soft silicone rubber, RTV 615 (Lake (in Mernagh, 1969)). As the possible use for this particular silicone rubber is of great interest for this work, it is important that any deviations in its behaviour from standard theory predictions should be investigated. Preliminary investigations into the non-standard behaviour of silicone rubber have previously been carried out by Painter (1954), which serves as a useful introduction to the further examination of silicone rubber reported later in this chapter. This paper outlined results for the behaviour of both G and E_c under shear and compressive strain respectively, for units with a single shape factor of 0.32. His results for shear modulus show that G remains constant up to applied static shear strain values of around 50%. In the vertical, however, Painter has found that E_c exhibits a very rapid increase compared with natural rubber. He has found that the increase in E_c with applied strain is linear* up to strains of around 30%, thereafter showing strong non-linearity. This work did not however include any investigation of the possibility of variation in E_c with shape factor.

---

* It should be noted that where *Ec* is a constant, the corresponding *k* will also be constant. Thus any plot of applied stress versus resulting strain of the material will be linear, with the constant gradient giving the value of *Ec*. If, however, *Ec* is not a constant, but changes throughout the measurement, the resulting gradient will also vary, giving rise to a non-linearity in *k*.

However, in spite of its unusual mechanical behaviour, this material possesses many properties which make it desirable for use in such an application, and will very likely be the choice of rubber for the GEO 600 stacks. RTV has also been used in conjunction with Viton rubber in experiments for the LIGO passive seismic isolation system (Giaime et al, 1994). These workers have noted that the RTV out-gassing rate is very low - measured to be of order 7×10^{-13} Torr L / s cm^2 for out-gassing of Nitrogen. In addition to this, the long-term creep effects common to many rubbers were not significantly observed for the RTV stacks. Also, as RTV begins in liquid form it has the advantage that it can be easily moulded to any shape. However, it has also been noted by workers with LIGO and at Glasgow that the quality factor (Q) of the RTV is higher than normally desirable, and that the corresponding loss function, $\phi(\omega)$, is approximately constant with frequency.

2.2
Investigation of the compression characteristics of RTV 615 silicone rubber.

2.2.1
Experimental overview

The broad experimental aim of this work was to evaluate the shear and compression moduli for RTV, and to examine the behaviour of each with load. Once the relationship between dynamic modulus and load was known, it was then desirable to develop a more suitable model for predicting the stack performance, rather than the standard theory model outlined in 2.1.2.

The dynamic moduli, E_c and G were evaluated from the horizontal and vertical resonant frequencies of single layer RTV stacks under load, as in equation (2.10). The resonant frequencies were identified from the stack transmissibility spectra obtained using the following experimental set-up, Fig.(2.6(a)). The main change for vertical measurements was the use of a vertical drive table (Fig.(2.6b)) rather than the horizontally-driven base plate. The drive table was constructed from a large reinforced glass plate mounted on an equilateral triangle arrangement of identical electromagnetic drivers. This table could

accommodate loads up to around 9 kg. The balance of the plate and drive were carefully checked to ensure that the excitation provided by the vertical drive table was as close to vertical as possible, thus avoiding complicated cross-coupled modes in the stack. A swept-sine signal, provided by the DSA (Hewlett-Packard Dynamic Spectrum Analyser, model 35665A) via a power amplifier unit, was used to drive the stacks, with the transfer function being measured and plotted by the DSA. Care was taken during stack construction to prevent any misalignment of the stack as this could give rise to cross-coupled features, making analysis of results difficult. The settle time (time taken for the analyser to allow dissipation of transient effects) and integration time were generally chosen to be around 5 and 7 cycles at the resonant frequency respectively which gave an optimally good trace quality without unduly increasing the recording time.

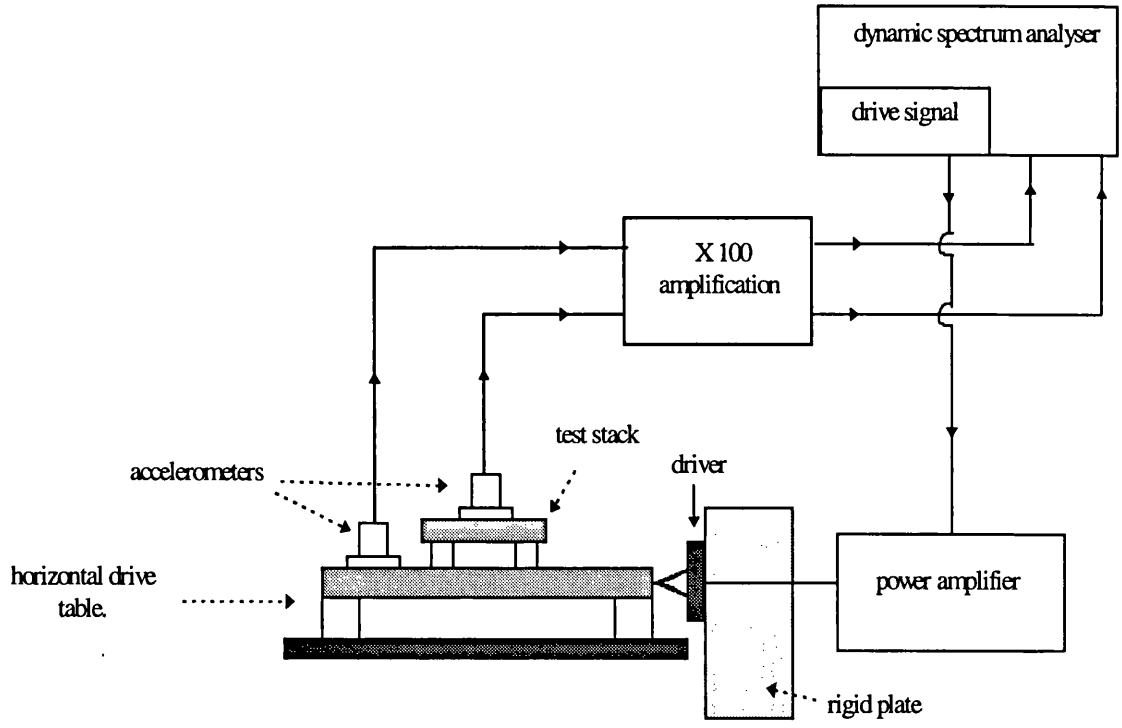

Fig.(2.6(a)): Experimental set-up for horizontal transmissibility measurements.
This was converted for vertical measurement by replacing the wooden base-plate and horizontal driver with the vertical drive table described in ***Fig.(2.6(b))*** *below.*

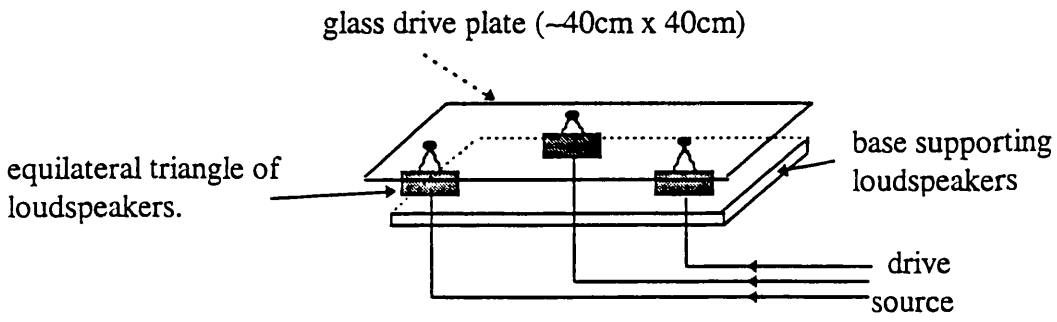

Fig.(2.6(b))

2.2.2
Investigation of horizontal characteristics of RTV units under compression, and comparison with standard model.

The horizontal transmissibility spectra of a single layer stack and a three layer equal mass test stack were measured. These were constructed from 1.7 kg masses with four rectangular rubber units per layer (S = 0.34, $A/z = 9.6\times10^{-3}$ m per unit) (Fig.(2.7)).

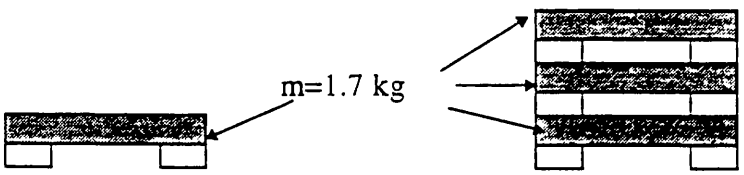

Fig.(2.7): Single and three -layer test stacks.

The horizontal resonant frequency of the single layer stack was found to be $f_0 = (11.3 \pm 0.1)$ Hz. The [9]apparent shear modulus G' was found to be $G'_{rect} = 2.23\times10^{5}\,\mathrm{Nm}^{-2}$ from f_0 and equation (2.10). The true shear modulus, G, was then evaluated using equation (2.9) which, for these rectangular units of length

[9] Bending must be taken into account for these rectangles as *height/breadth = 0.625*.

$L = 8\text{mm}$, gave a value of [10] $G = (2.52 \pm 0.05) \times 10^5 \text{Nm}^{-2}$ For the rectangular units used in these tests, the corresponding value of horizontal spring constant was $k_h = 8570\ \text{Nm}^{-1}$ [11] per layer in the standard theory stack model. By inserting this spring constant into each layer of the standard theory model, the performance of the three layer test stack could be examined for evidence of unusual stiffening.

- Prediction of horizontal behaviour of RTV stacks.

The results obtained from experimental tests of the three layer stack response were compared with standard theory model predictions of the horizontal vibration mode frequencies. This is based on the assumption that k_h is equal in each layer of the stack, with a constant value of $8570\ \text{Nm}^{-1}$ throughout the whole motion. These results are shown in Fig.(2.8). Examples of the predicted and experimental transmissibility spectra obtained are shown in Fig.(2.9), where the loss function value was taken to be $\phi = 0.056$ in accordance with the measured horizontal Q of this stack of 17.8.

STACK	MODE	STANDARD MODEL PREDICTION (Hz)	EXPERIMENTAL RESULT (Hz)
three layer	f_{HA}	5.03 Hz	5.04 ± 0.15 Hz
(Fig(2.7), (2.9))	f_{HB}	14.07 Hz	14.3 ± 0.5 Hz
	f_{HC}	20.37 Hz	23 ± 3 Hz

Fig.(2.8): ***Table of results comparing horizontal resonant frequencies of three layer RTV stack with standard theory predictions using the model described in 2.1.3.***

On the whole there seems to be good agreement between the standard theory predictions

[10] Later measurements of f_h using cylindrical units were found to agree with predictions based on this value of G, which was then used throughout this work.

[11] 'per layer' indicates that the value is the total for 4 RTV units under the mass of the single layer.

and experimentally found results. Later, in section 2.3, the standard theory horizontal predictions for a four layer, unequal mass stack considered for the 10m prototype, were also found to compare very well with experimentally found results. Experimental results would suggest that the shear RTV behaviour conforms to standard theory, does not stiffen horizontally under compression within the limits of load (strain $\leq 30\%$) and rubber unit dimensions tested here, and that generally accepted rules of thumb are reasonable.

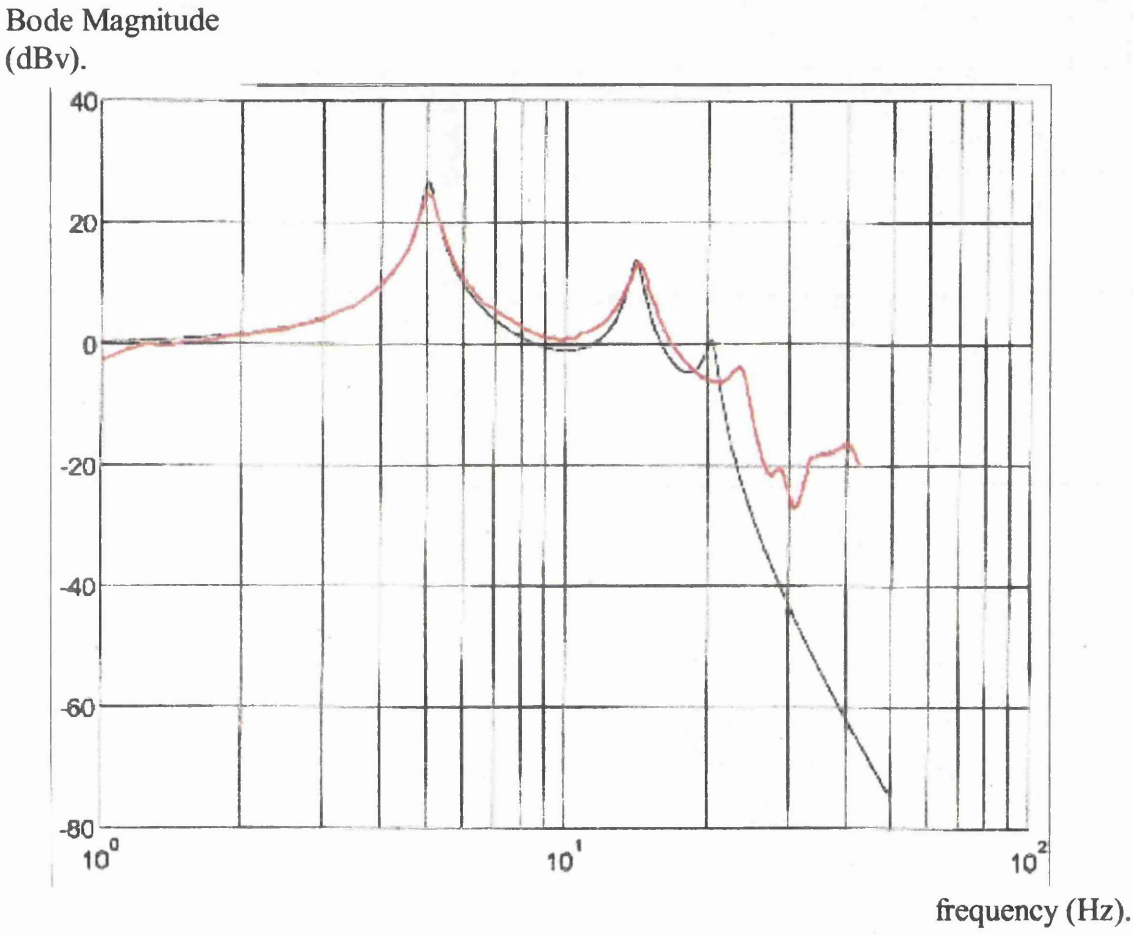

Fig.(2.9) Comparison of standard theory stack model prediction of three layer RTV stack performance (black line) and experimentally found transmissibility spectrum for this stack. *MATLAB plot based on a constant stiffness in each layer of* $k = 8570(1 + j(0.056))Nm^{-1}$.

2.2.3 Investigation of the vertical characteristics of loaded RTV units.

Vertical transmissibility spectra were taken for a single layer stack of four rectangular units under various loads, m. The vertical resonances were identified from the transmission spectra allowing the evaluation of k_v and E_c in each case. Any deviations from standard theory, which would imply that $E_c \approx 3G$ (thus constant), could therefore be identified and the relationship between E_c and applied static stress F/A examined. For these tests, masses of 1.7 kg and the rectangular rubber units were used once again. The results[12] are shown in Fig.(2.10.(a,b)) below along with the corresponding load. No significant variation was found in the vertical quality factor (similar in value to the horizontal quality factor) during these tests.

The value of E_{cEXP}, corresponding to each experimentally found frequency was calculated from equation (2.13). It is clear from the results in figures (2.10(a,b)) that there is a considerable amount of stiffening present, characterised by an unusual increase in E_{cEXP} (and thus also in k_v), even for these low stress values where the strain on the rubber units was very much less than 30%.

Fig.(2.10(b)) shows E_{cEXP} plotted against the stress applied by the load, F/A, and compared with the theoretical prediction, E_{cTHR}.

As was observed by Painter, there appears to exist a linear relationship between stiffening and the applied stress from the load. For these particular units, the best fit straight line to this data was found to be:

$$S = 0.34: \qquad E_{cEXP} = 7.6 \times 10^5 \left(1 + 2.3 \times 10^{-6} \left(F/A\right)\right) \text{ Nm}^{-1} \qquad (2.14)$$

The exact form of this result will be discussed later in this section, but it already clear that the stiffening feature observed will have implications on the simple model used to predict the vertical resonances of a stack made from these RTV rectangles.

---

[12] Theoretical predictions from standard theory are shown with the subscript *THR*.

mass, m(kg)	f_{vEXP} (Hz).	E_{cEXP} (Nm^{-2}) ($\times 10^6$)	f_{vTHR} (Hz).	E_{cTHR} (Nm^{-2}) ($\times 10^6$)	$\frac{E_{cEXP}}{E_{cTHR}}$
1.7	28.3±0.3	1.39±0.03	19.57	0.756±0.015	1.80±0.05
3.4	24.5±0.3	2.09±0.05	13.84	0.756±0.015	2.76±0.09
5.1	21.5±0.3	2.42±0.07	11.3	0.756±0.015	3.20±0.11
6.8	21.2±0.3	3.15±0.09	9.79	0.756±0.015	4.17±0.15
8.5	21.0±0.3	3.9±0.1	8.75	0.756±0.015	5.10±0.17

Fig.(2.10(a)): ***Table of results for experimental and theoretical vertical resonant frequencies of RTV units under various loads.*** *Corresponding values of compression modulus are included.*

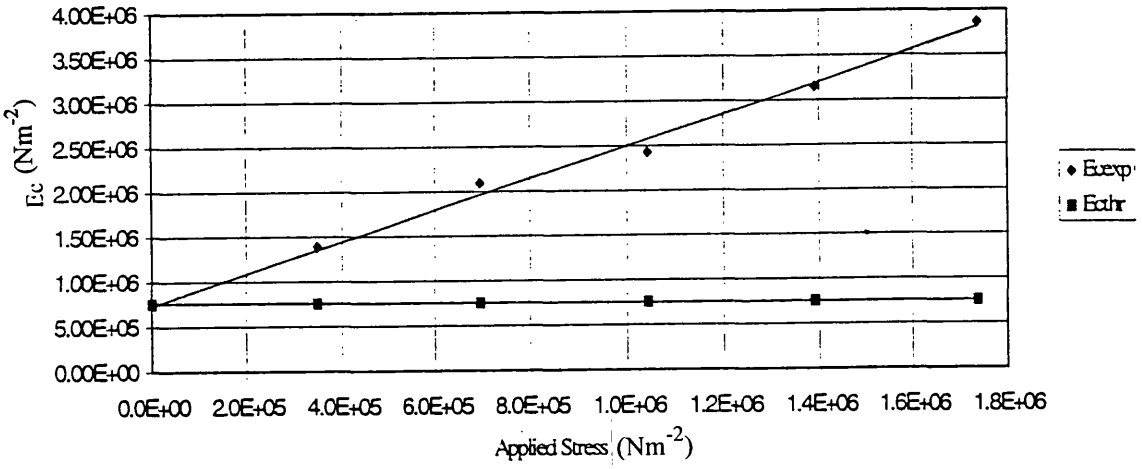

Fig.(2.10(b)): ***Plot of compression modulus vs pressure (SI units) for data in Fig.(2.10(a)).*** *Note the steady linear increase in* E_c *as opposed to the constant value expected.*

In the vertical, it is clearly now necessary to use a different value of k_v in each layer of the stack model, determined by the value of E_c corresponding to the static load m above. For masses in the range tested, equation (2.14) can be used to predict this value.

e.g. for the four layer stack shown in Fig.(2.11), we shall use MATLAB to model the vertical response of the stack taking this load-stiffening into account.

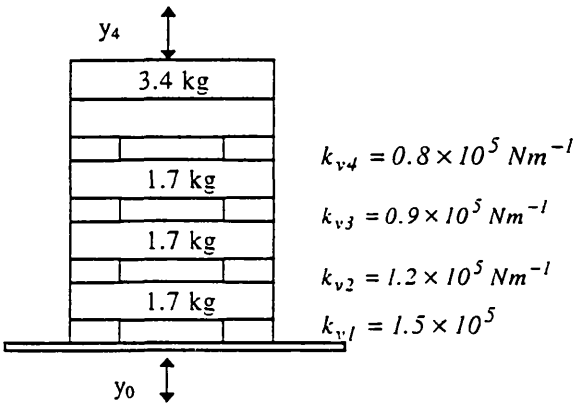

Fig.(2.11): Model used to predict non-standard vertical resonant frequencies of four layer RTV stack. *Stiffness values (per layer) found from* $k_v = m(2\pi f_{vEXP})^2$ *according to static load above. Matlab then used to find transmissibility,* $(y_4(f)/y_0(f))$ *as normal*

The predicted vertical transmissibility spectrum, where structural damping has been included with value $\phi(\omega) = 0.056$ (section 2.2.2) is shown in Fig.(2.12), with the experimentally found trace included for comparison. It is clear that there is extremely good agreement between the new model predictions and the actual behaviour of the stack, with stiffening due to load having been fully taken into account.

Again, several other stack configurations, constructed from the 1.7 kg masses and rectangular units used here, were tested; similar agreement was found between the experimental results and this extended form of the simple stack model. The model now appears to work very successfully in predicting the vertical resonances of RTV stacks, providing the static load-stiffened value of k_v is inserted into the model.

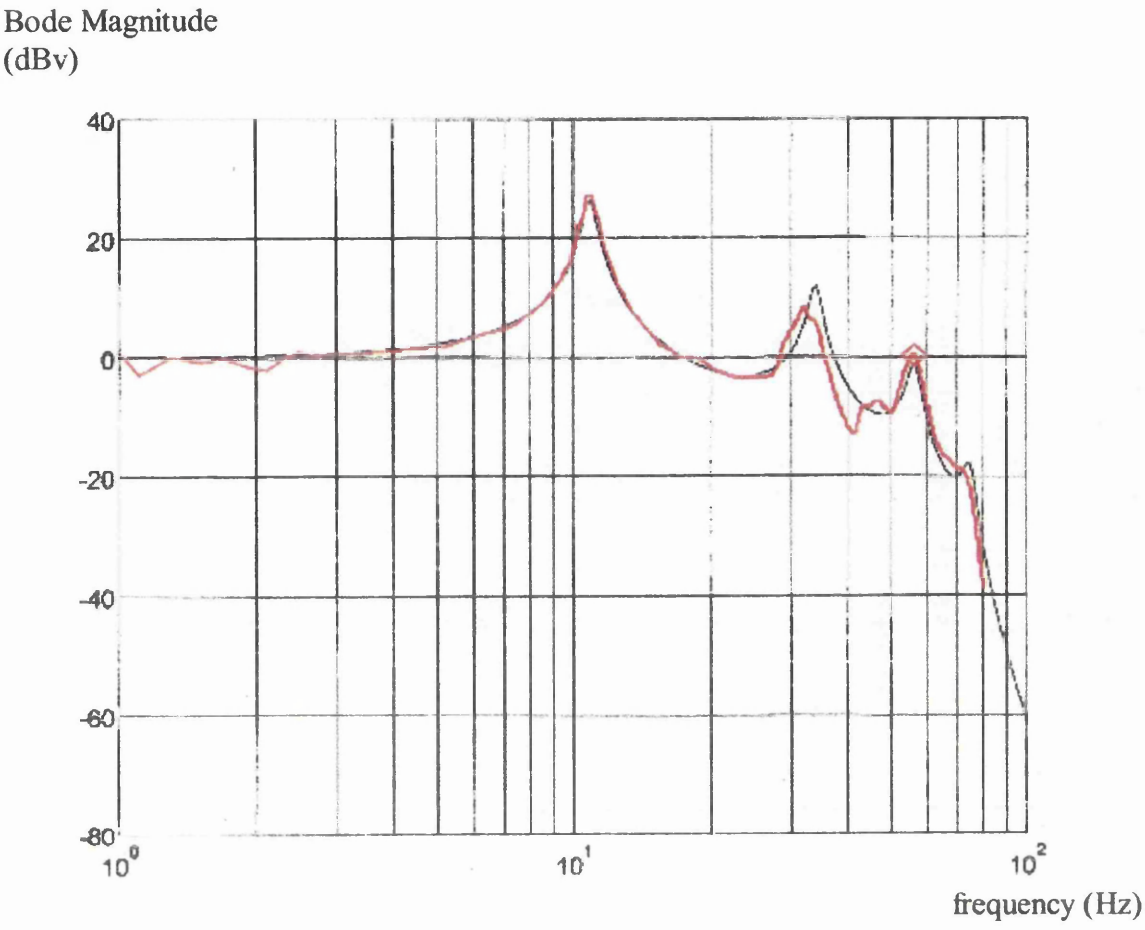

Fig.(2.12): Comparison of experimental and predicted results in the vertical for a four layer stack (Fig.(2.11)). *The predicted results (black line) were based on the model in Fig(2.11) with the inclusion of a structural damping coefficient, chosen to give predicted peaks with Q~18 (equal to that of the actual stack).*

As the probable dependence on the dimensions of the rubber unit was not explicit in equation (2.14), this formula was not expected to hold for other rubber pieces. It was therefore desirable to find empirical formulae to allow prediction of the behaviour of RTV units of a shape and dimensions more likely to be considered for in the GEO 600 system. As will be discussed later in section 2.4, cylindrical units were required to allow the encapsulation of the units in soft metal bellows.

A series of tests were carried out for a set of cylindrical units whose shape factor defined the likely range considered for GEO 600. In this way, information could also be

obtained as to the presence, or otherwise, of any variation in E_c with shape and dimensions as well as load. Knowledge of this aspect of RTV behaviour may well become important if future plans incorporate a shape of unit which differs from those used previously.

Three test units were chosen (Fig.(2.13)), with shape factors S=1, S=0.8 and S=0.16. The experimental results of E_c versus pressure are shown in Fig.(2.14) for each shape tested.

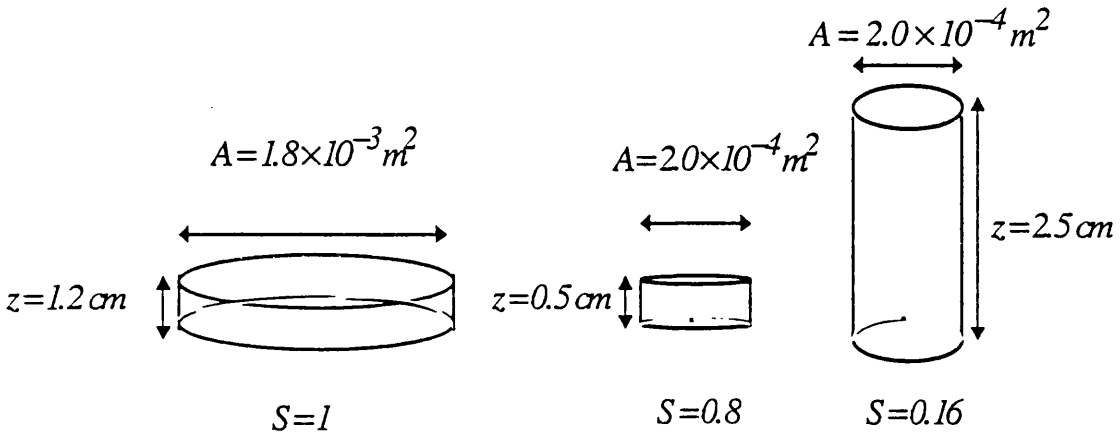

Fig.(2.13): Range of cylindrical shapes tested.

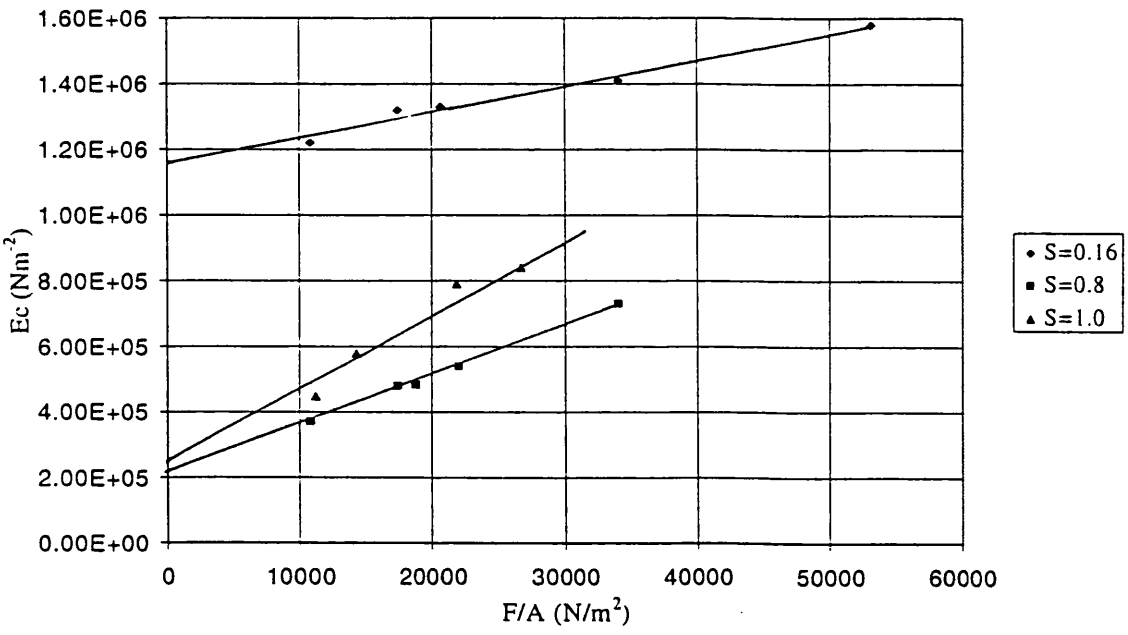

Fig.(2.14): Plot of compression modulus vs pressure for cylindrical units (Fig.(2.13)).

Again, the trend in each case was linear with visible increase in stiffness with applied stress, where the observed strain in the RTV units were less than 30%. However, from the variations in gradient and y-axis intercept value observed from this data, it is now also clear that E_c has some additional dependence on the shape factor of the cylinders - a feature which can be seen from the equations characterising the behaviour of each unit tested (equations (2.15)):

$$\begin{aligned} S = 0.16: &\quad E_c = 11.6\times10^5\left[1+7\times10^{-6}(F/A)\right] \\ S = 0.80: &\quad E_c = 2.03\times10^5\left[1+76\times10^{-6}(F/A)\right] \\ S = 1.0\ : &\quad E_c = 2.02\times10^5\left[1+124\times10^{-6}(F/A)\right] \end{aligned} \qquad (2.15)$$

(S.I. units).

From the data gathered it seems that the initial, unloaded compression modulus of the RTV units is larger for smaller shape factors - that is to say that unloaded tall, thin units will have an initially higher value of E_c than shorter, broader ones. However, for increasing load on the units, the rate of increase in the compression modulus is actually considerably *less* for these low shape factor units than for high shape factors.

It is not yet clear why the unloaded value of E_c should be larger for low shape factors. It is perhaps not surprising that the unloaded value of E_c has a dependence on shape, even from a standard theory viewpoint, but this observed trend for RTV will most likely require a greater understanding of the internal structure of RTV for its explanation.

The second observation can be understood by the fact that low shape factor units have a greater free surface area which allows the loaded unit to bulge more easily. One would therefore expect that, as the rubber can more easily accommodate the induced strain, the rate of stiffening will be less.

Another point to note on the rectangle results is that, relative to the observed trend for the cylinders, the rate of stiffening for the rectangular set is lower than expected according to the rectangle shape factor, S=0.34. Although the shape factor defines the relative amount of force-free area, this result may indicate that the exact form of this area may also be of significance (e.g. the rectangular units have a force-free area which is divided into discrete , flat 'panels' rather than a single curved surface). To further test

this hypothesis will of course require additional measurements on rectangular units but, although interesting, this was not necessary for the development of GEO 600 stacks.

2.2.4
Further notes on the behaviour of RTV units under compression.

The compression moduli of RTV cylinders with S=0.16 were measured under higher mass values (up to 50 kg) and have been seen to conform to the S=0.16 formula, contained in equation (2.15), within an error typically corresponding to ~ 2 Hz for single layer vertical frequencies of around 12 Hz, which was tolerable for this work.
An important point to note is the high quality factor (Q) observed experimentally during resonant frequency tests of the RTV. Throughout all tests, RTV was seen to have a fundamental mode Q of around 18 - a level which could result in undesirably large movements of the stack on resonance. It was also found that a model incorporating a structural damping term (where damping is independent of frequency), rather than viscous, more accurately predicted the shape of the resonant peaks of RTV stacks. The main consequence of this feature would be that at frequencies above $f_0 Q$, an RTV stack would continue to roll-off with a slope $\propto (1/f)^{2n}$ (as discussed in section 2.1.1). This will not be assumed however until further investigation has been carried out, thus the more pessimistic form (equation(2.7)) will be used throughout this work.

Although solid RTV test units have been shown to be unusually stiff and have high Q, the nature of RTV is amenable to the use of creative design solutions aimed at overcoming the practical problems associated with these points. Recent results (Plissi, 1996) have indicated that the stiffness of RTV units under a certain load can be reduced through the addition of vertical holes moulded into the RTV units as they cure. As will be discussed later (2.4), this feature may well have to be incorporated into the design anyway for additional reasons. Experimental investigation (Plissi, 1996) into the use of graphite filler in the RTV has also provided encouraging results in the reduction of the RTV quality factor to around 5 without contributing significantly to the stiffness. As

mentioned in previous sections, this will be of importance in the final stack design as the presence of high stack Q values on resonance is undesirable, although the effect of filling RTV in this way on, e.g., mechanical strength and long term creep should be fully investigated.

2.3
Redesign of the Glasgow seismic isolation system.

There now follows an account of the redesign of the seismic isolation system, used for several years prior to 1993 for the Glasgow 10 m prototype test masses.

2.3.1
Original system - description and problems.

Originally the lead stack elements in the Glasgow detector were horseshoe-shaped as this design gave very good mechanical stability and easy access to suspensions. Later experimental tests of this stack (Bongs, 1993) indicated the presence of a strong internal mode of these horseshoes at 450 Hz which coincided with a high frequency (violin) resonance of the suspension wires. Through this route vibration noise was transmitted directly to the test mass itself, providing a major contribution to a large noise peak measured at 450 Hz in the detector sensitivity spectrum (Morrison, 1993). Identification of this problem made the redesign of the Glasgow stack a high priority - the procedure for this is outlined in section 2.3.2. In addition to the necessary removal of the stack internal mode, it was also desirable to improve the vacuum properties of the stack. RTV was used in the stack, and the results obtained in the previous section 2.2 used to make the initial choice of stack design for the Glasgow system. The design chosen, with the reasons for this choice are now discussed.

2.3.2
Design solutions for Glasgow system.

Originally, the double pendulum for the Glasgow test mass suspension system was intended to have vertical frequencies of $f_{pv1} = 30\,\text{Hz}$ and $f_{pv2} = 20\,\text{Hz}$ for the upper and lower stages respectively. In addition, the fraction of residual vertical motion at the test mass giving rise to horizontal motion of the mass was estimated to be around 10^{-3} (0.1 %). This fraction is commonly referred to as the 'cross-coupling factor', C, and is discussed at greater length in Appendix A. It was also assumed that the lengths of the pendulum suspension wires would be approximately $l_1 = 10\,\text{cm}$ and $l_2 = 25\,\text{cm}$ for the upper and lower stages respectively, thus giving rise to individual horizontal mode frequencies $f_{ph1} = 1.6\,\text{Hz}$ and $f_{ph2} = 1\ \text{Hz}$. The masses of the two stages were taken to be $m_1 = 0.4\ \text{kg}$ for the intermediate mass and $m_2 = 2\ \text{kg}$ for the test mass. Thus the levels of isolation expected to be provided by the double pendulum system in the horizontal and vertical were:

$$I_{ph} = \left(\frac{f_{ph1}}{f}\right)^2 \left(\frac{f_{ph2}}{f}\right)^2 \left(1 + \frac{m_2}{m_1}\right) \approx 1.5 \times 10^{-7}$$

$$I_{pv} = \left(\frac{f_{pv1}}{f}\right)^2 \left(\frac{f_{pv2}}{f}\right)^2 \approx 3.6 \times 10^{-3} \qquad (2.16)$$

at frequencies greater than the coupled resonances of the system. As is commonly the case, it was expected that the level of horizontal displacement noise at the test mass would be due to the cross-coupling of residual vertical motion at the second pendulum stage.

For a quiet site, the level of seismic noise expected at 100 Hz is typically $\delta x_{noise} = 10^{-11}\ \text{m}/\sqrt{\text{Hz}}$ in the horizontal and vertical (Chapter 1), but for this detector site an estimated increase of a factor of 100 on the noise level was assumed, giving the value $\delta x_{noise} = 10^{-9}\ \text{m}/\sqrt{\text{Hz}}$. It was intended that this initial stack design provide a

level of isolation at 100 Hz such that the residual horizontal motion at the test mass be no greater than $\delta x_{mass} \approx 10^{-17}$ m/$\sqrt{\text{Hz}}$.

The mass and performance of the four layer stack, whose vertical transmissibility spectrum was investigated in section 2.2 (figures (2.11) and (2.12)), indicated that this would be a suitable basis for the design. Predictions made by the MATLAB model on the horizontal performance were also [13]encouraging, and are shown in Fig.(2.15).

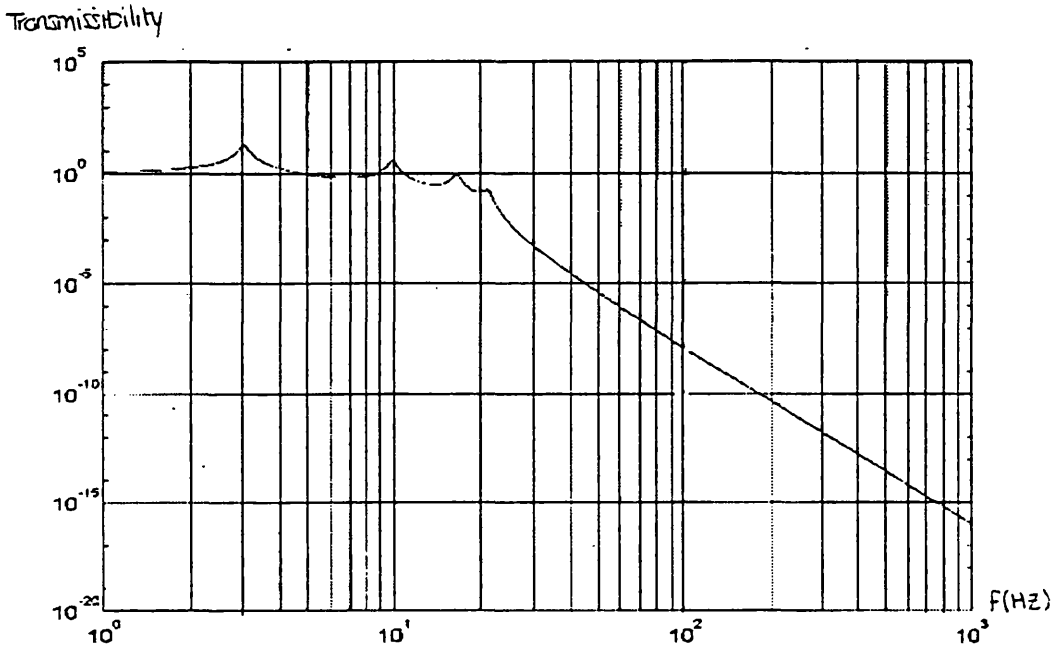

Fig.(2.15): predicted horizontal transmissibility of the four layer stack (Fig.(2.11)), using the procedure described in 2.2.2.

The dimensions of the lead bricks were such that the lowest internal resonances lay higher than 3 kHz (verified experimentally) which was safely outwith the working frequency range. In addition, mechanical stability and easy access were provided by using 4 such stacked 'legs', where the fourth layer was combined to form the top-plate (mass ~ 15 kg, giving rise to ~ 3.75 kg over each leg). The horizontal coupled modes were predicted to lie at: f_{HA}=3.03 Hz, f_{HB}=9.87 Hz, f_{HC}=16.44 Hz and f_{HD}=20.98 Hz. It can be seen from Fig.(2.12) (section 2.2.3) that those in the vertical were expected, by experiment and theory, to be approximately f_{VA}=11 Hz, f_{VB}=33.6 Hz,

[13] Note that these plots assume that the Q of the Glasgow stack will not have been reduced from the tested value of 20-30.

f_{VC} =56 Hz, f_{VD} =71 Hz. In this way, a broad band of attenuation was possible between 100 Hz and 1 kHz, with predicted isolation factors in the horizontal and vertical being 10^{-8} and 10^{-3} respectively. Figure (2.16) shows details of the new stack.

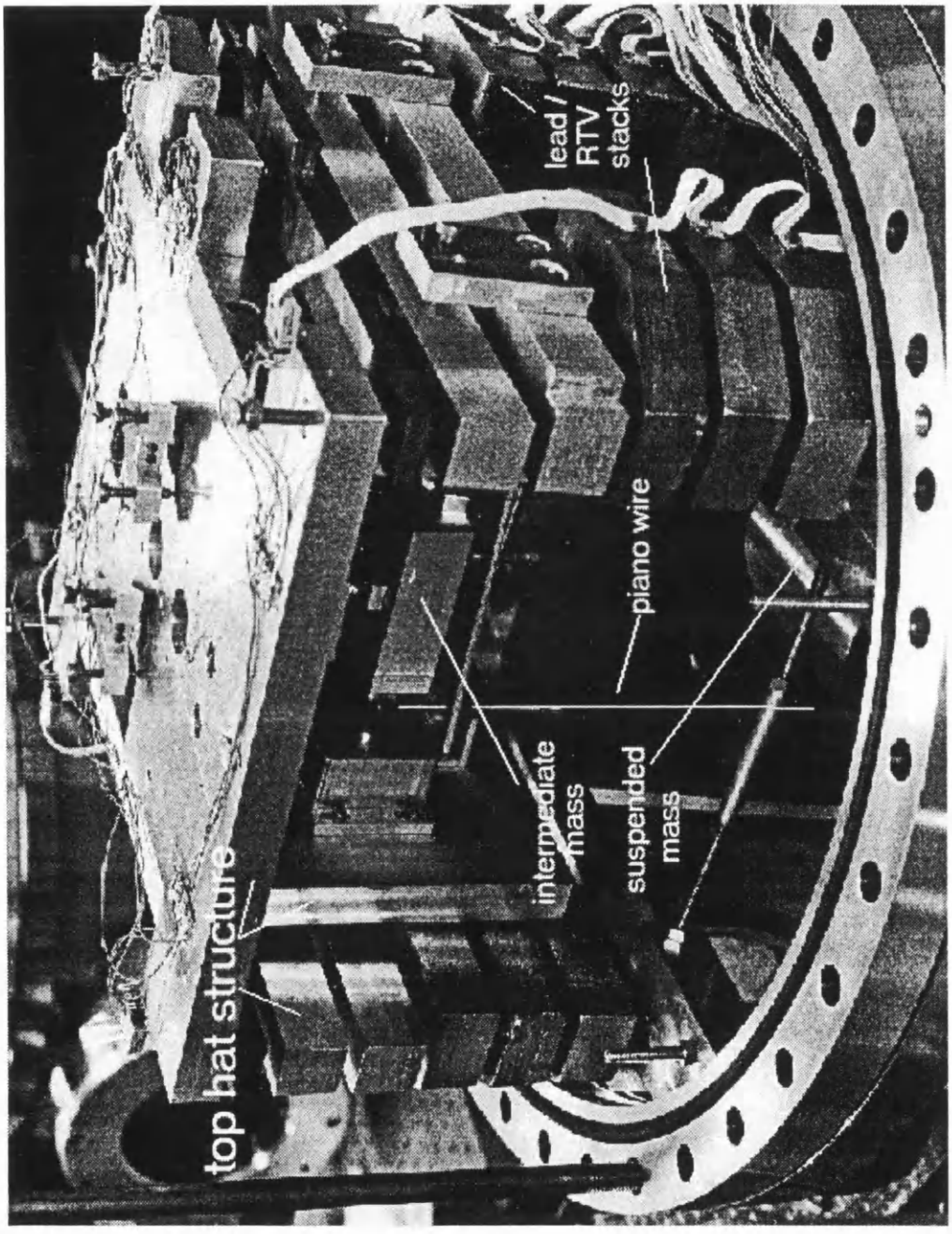

Fig.(2.16): In situ photograph of the redesigned seismic isolation[14] stacks for the Glasgow 10m prototype.

[14] The bricks were shaped slightly at the corners to allow their installation into the circular vacuum tanks, thus preventing their effect from being 'short-circuited' through contact with the tank walls.

2.3.3
Experimental tests and results.

The new stack was tested experimentally in vacuum to reduce the effect of acoustic noise. An electromagnetic driver, constructed from a 30 cm diameter loudspeaker with a central cone attachment (Fig.(2.17)) was used to apply a swept sine drive horizontally at the base of the stack.

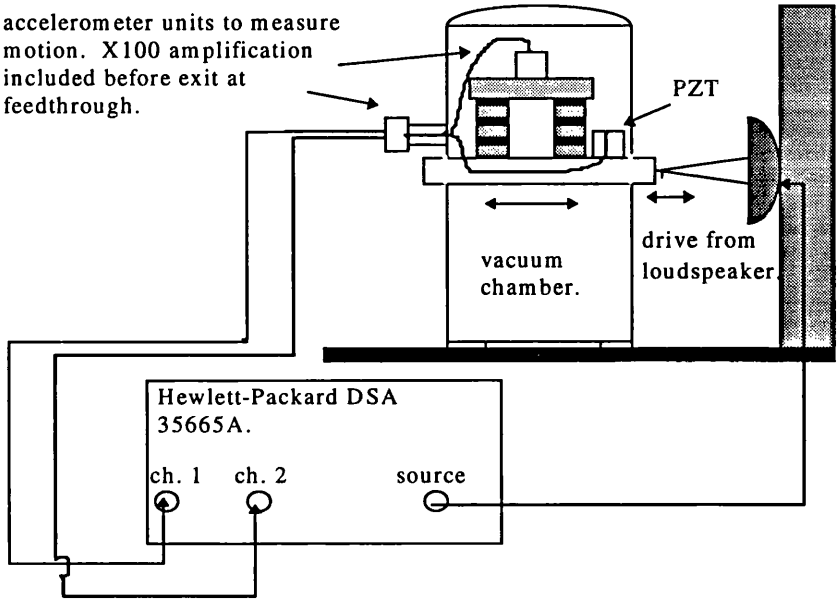

*Fig.(2.17): **Experimental arrangement for test of stack response to a horizontal drive.** The drive was provided by a 30 cm diameter loudspeaker connected to the drive source output of a Hewlett-Packard dynamic spectrum analyser.*

The corresponding horizontal transfer function was measured from 1 Hz to 1 kHz with two small accelerometers (Bruel & Kjaer, model numbers 4379 and 4378), with pre-amplification of both signals achieved using a simple non-inverting operational amplifier based circuit, with feedback resistance chosen to give a signal gain of 100.

- **Results**

As expected from the predictions of horizontal and vertical mode frequencies, the transfer function recorded between 1 Hz and 100 Hz showed considerable structure due to these modes. The experimentally found horizontal modes lay at the frequency positions marked in Fig.(2.18) below; $f_{HA} \approx 2.0 \pm 0.5$ Hz, $f_{HB} \approx 9.0 \pm 1.0$ Hz, and $f_{HD} \approx 20.5 \pm 0.5$ Hz, where f_{HC} was not visible on the trace. The vertical mode frequencies were also identified (as marked on the trace). All of the experimentally found mode frequencies agreed well with those predicted (Fig.(2.12) and Fig.(2.15)).

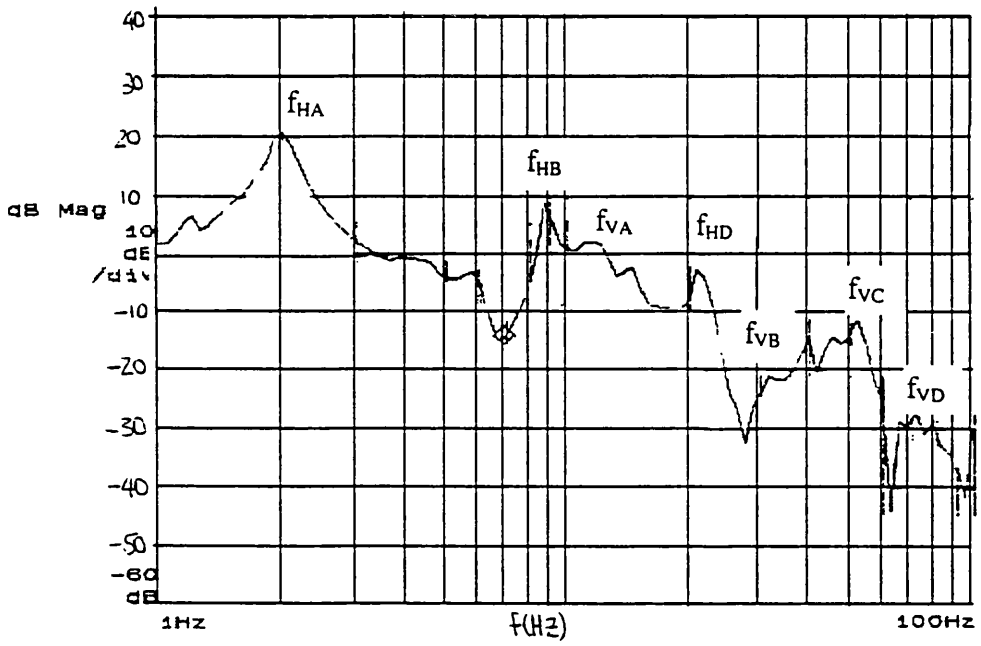

Fig.*(2.18): Transfer function result for Glasgow stack, taken between 1 Hz and 1 kHz, with horizontal and vertical modes identified ('H' and 'V' subscripts respectively). The remaining structure was thought most likely to be due to tilt modes in the stack.*

The results of transfer function measurements taken between 100 Hz and 1 kHz are shown in Fig.(2.19) which shows the upper limit to the horizontal stack performance along with the results from the original stack.

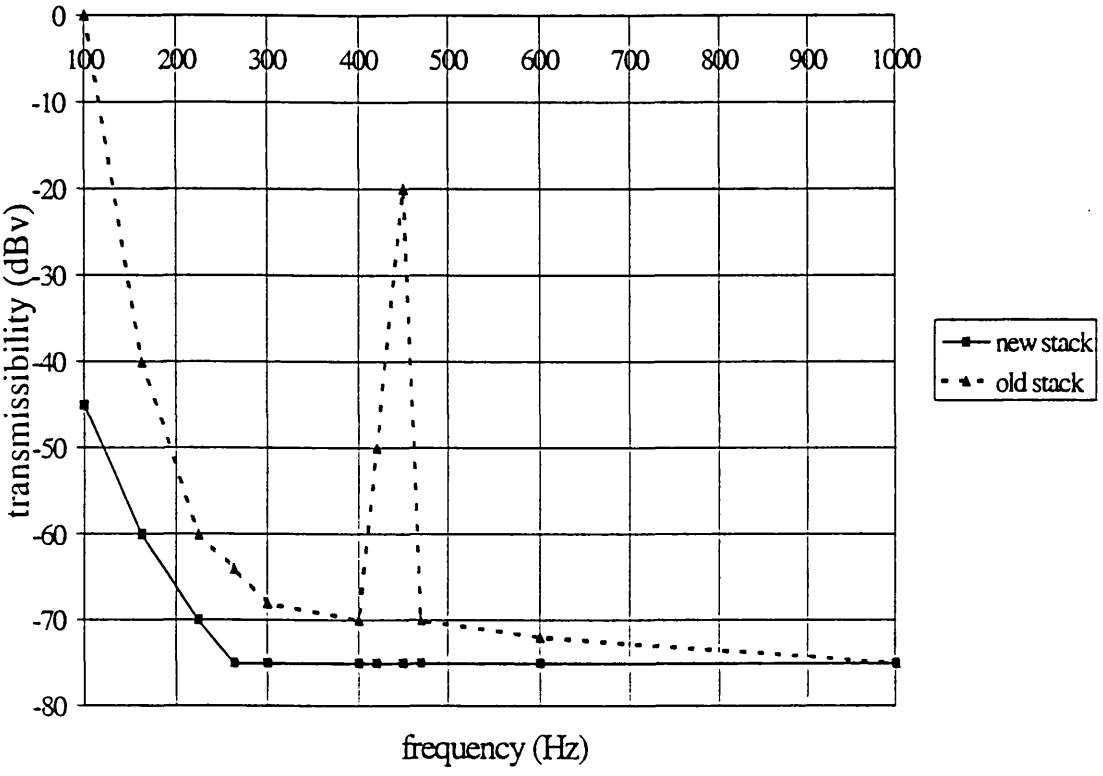

Fig.(2.19): Upper limit to the horizontal stack performance (full line) and results from the [15]original stack (dotted line). Above 100 Hz, trace shows only electronic noise at around 1.7×10^{-4}.

In addition to demonstrating very good stability, this design of stack provided a significant increase in attenuation of ground signals by a factor of around -45 dB_v (5.6×10^{-3}) at 100 Hz. (Attenuation also began at a much lower frequency, typically around 20 Hz, as opposed to 100 Hz in the original stack). Most important was the complete removal of the resonant feature at 450 Hz, with a resultant improvement in attenuation by a factor of at least -55 dB_v (1.7×10^{-3}) in this region.

Comparison with the predicted horizontal transmissibility (Fig.(2.15)) shows that the level of isolation reached by 100 Hz during this stack test is less than that predicted. However, it should be noted that it is unlikely, given the nature of the experimental set-

[15] Original stack results shown here recorded by E. Morrison and K Bongs (Bongs, 1993).

up, that the stack response recorded is due solely to directly transmitted horizontal noise. It is rather more likely that the resulting trace will show the combined effect of this and other noise, arising from, e.g., cross-coupled tilt modes being excited in the stack. Several vertical and tilt features could be seen on transmission spectra taken between 1 Hz and 100 Hz. The importance of this effect has been investigated by Cantley (Cantley, 1992), and seemed a reasonable explanation as this work indicated that tilt routes through the stack may actually dominate directly transmitted horizontal noise. In spite of this the resulting isolation level (which can be taken as a worst case) was of order 6×10^{-3} which, when combined with the horizontal pendulum isolation I_{ph} (equation (2.16)), more than meets the performance requirement of $\delta x_{mass} \approx 10^{-17}\,\mathrm{m}/\sqrt{\mathrm{Hz}}$ at 100 Hz.

In summary, the expected performance of the Glasgow 10 m prototype stack at 100 Hz in the horizontal and vertical is expected to be:

$$I_{sh} \leq 6\times10^{-3} \quad , \quad I_{sv} \approx 10^{-3} \tag{2.17}$$

thus, in combination with equations (2.6) and (2.7), and with a seismic input of order $10^{-9}\,\mathrm{m}/\sqrt{\mathrm{Hz}}$, this gives rise to an expected noise level at the test mass of:

$$\delta x_{mass}(100Hz) \approx 3.7\times10^{-18}\ \mathrm{m}/\sqrt{\mathrm{Hz}} \tag{2.18}$$

which is dominated by vertical noise which has been cross coupled ($C = 10^{-3}$) at the double pendulum. From equation (2.17) and the likely seismic noise input, it was expected that there would be approximately $10^{-12}\,\mathrm{m}$ vertical motion at the top of the stack.

- In situ performance update of stacks in the 10m prototype.

Following the installation of the isolation stack in 1993 (Robertson & Killbourn, 1993), several features of the double pendulum have changed. The parameters of the pendulum eventually suspended are summarised in Fig.(2.20) below:

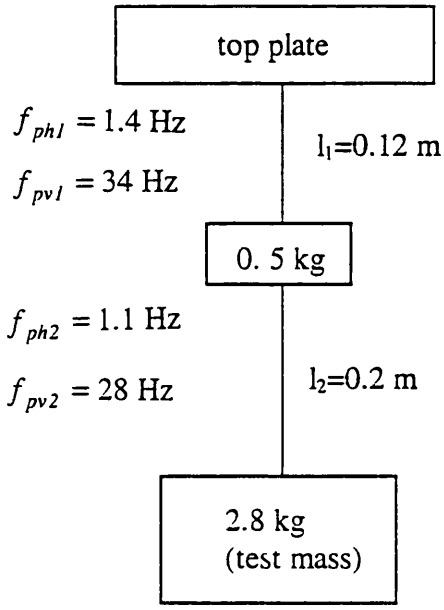

Fig.(2.20): Summary diagram of the Glasgow 10 m prototype double pendulum. Uncoupled frequencies of each stage of the pendulum are as marked.

There are two suspension wires, each of radius 175 μm, on the upper stage, with four suspension wires below, each of radius 87.5 μm, holding the test mass. The Young's modulus of the steel piano wire used was $1.8\times10^{11}\,\mathrm{Nm}^{-2}$. It should be noted that the wire radii used were greatly over the minimum value set by the breaking stress. For this pendulum, the cross-coupling factor for the lower pendulum stage (at frequencies $\geq 100\ Hz$) was calculated to be $C \approx 10^{-3}$. This evaluation used the cross-coupling equation (A.34) in Appendix A, where the wire separation is $2r = 5$cm, the test mass diameter and thickness are d = 12.5 cm and t = 10 cm respectively, the beam centering error is $\varepsilon \approx 0.3$ cm and a 5% difference in k_v has been assumed.

Although the vertical and horizontal frequencies of each stage are similar to those assumed during the design, the upper vertical *coupled* mode frequency of was found to be $f_{cv2} = 110$ Hz, thereafter providing an isolation level of $I_{pv} = 5.7\times10^{-4}$ by 200

Hz. This has led to seriously reduced vertical isolation at 100 Hz, as there is no isolation contribution (and perhaps even some amplification of noise) from the double pendulum. In fact the level of residual motion at the test mass has been measured (Killbourn, 1996) to be of order $10^{-15}\ \mathrm{m}/\sqrt{\mathrm{Hz}}$ at 100 Hz - a value that is a factor of approximately 100 greater than expected in the original design. However, the residual vertical motion of the stack has been measured (Killbourn, 1996) to be $10^{-12}\,\mathrm{m}$, as expected from the combination of the seismic input and stack isolation. Assuming no attenuation or amplification from the double pendulum (i.e. 0dB at 100Hz in pendulum transfer function) we can expect a horizontal displacement noise level at the test mass of

$$\begin{aligned}\delta x &= \left(\delta x_{top}\right)\left(I_{pv}\right)(C)\\ &= \left(10^{-12}\ m/\sqrt{Hz}\right)(1)\left(10^{-3}\right) = 10^{-15}\ \mathrm{m}/\sqrt{\mathrm{Hz}}\end{aligned}$$

It therefore seems likely that the poor isolation performance is due to the lack of isolation from the double pendulum, arising from the high upper coupled mode frequency at 110Hz. The residual noise level is dominated by vertical noise from the stacks, cross-coupled to the horizontal in the second pendulum stage. In the vertical the stacks have performed as expected during design.

- Future work for the 10 m prototype isolation system.

There are no plans to change the stacks at present, but it is intended that the pendulum be re-made using thinner wire and suspended as a whole from asoft leaf-spring rather than directly from the top plate (Killbourn, 1996). The spring constant of this leaf spring will be $740\ \mathrm{Nm}^{-1}$. The coupled modes of the pendulum in this systemhave been evaluated theoretically by Killbournto be 2 Hz and 60 Hz (rather than 28 Hz and 110 Hz as was the case previously), with a third mode due to the leaf-spring being damped. Experiments are currently underway in situ, where it is hoped that an improved level of isolation at 100Hz will be achieved.

2.4
Design aspects of a possible GEO 600 seismic isolation stack.

This section will outline a proposal for a possible simple stack design for GEO 600, as described in (Hough, Danzmann, Schutz *et al*, 1994), which consists of a 4-layer heavy-metal/RTV stack followed by a double pendulum test mass suspension. Recalling the discussion contained in section Chapter 1, the goal of [16]this seismic isolation system design was to provide an attenuation factor of at least 10^{11} at 100 Hz. For the design proposal discussed here the contribution from the stacks to the overall isolation factor at 100 Hz is required to be at least 10^{5} , assuming a value of vertical to horizontal cross coupling of 0.1% at the second pendulum stage.

2.4.1
Introduction

- Double Pendulum: design and isolation

Details of the design for the double pendulum suspension system proposed for GEO 600 are discussed in Chapter 3, where the choice of many aspects was based on the thermal noise aspects of this system. A more thorough discussion on the design choice can be found in Hough, Danzmann, Schutz et al (1994) and Hough et al (1996).

Suspension wires of length of 25 cm, giving rise to a (conservative) 1 Hz horizontal resonant frequency, are proposed for each stage of the double pendulum. It is proposed that the intermediate mass (3 kg) be suspended on a single loop (2 wires) of piano wire (breaking stress ~ 2700 MPa), giving rise to an upper stage vertical resonant frequency (f_{pvl}) of ~ 15 Hz. It is planned that suspension of the test mass (16 kg) be carried out using 2 or 4 fused silica fibres. Based on a breaking stress value of ~ 800 MPa, this

[16] It is possible that this goal will be revised to provide thermal noise-limited performance at 50 Hz, to allow the inclusion of several other sources of interest in the observation band. Recent references regarding this work are Strain et al, (1996) and Hough et al, (1996).

would result in a vertical resonant frequency of the lower stage (f_{pv2}) of ~20 Hz. In both cases the strain on the suspension wires/fibres is set to be a factor of 3 from the breaking stress.

Recall that an estimate of the attenuation one can achieve using this double pendulum suspension system can be found from equation (2.19) below:

$$\text{Horizontal:} \qquad I_{ph} = \left(\frac{f_{ph}}{f}\right)^4 \left(1 + \frac{m_2}{m_1}\right)$$

$$\text{Vertical:} \qquad I_{pv} = \left(\frac{f_{pv1}}{f}\right)^2 \left(\frac{f_{pv2}}{f}\right)^2 \tag{2.19}$$

For the typical GEO 600 parameter values discussed above, this will give an attenuation factor of approximately 6×10^{-8} in the horizontal, and 10^{-3} in the vertical at 100 Hz.

- Possible isolation stack design to meet required sensitivity at 100 Hz.

A simple schematic diagram of the typical style of seismic isolation system utilised in the Glasgow detector, and proposed for GEO 600, is shown in Fig.(2.21) (where only two legs have been shown for clarity).. Here the stack system is again composed of several identical stacked legs, joined above by a heavy top plate.

Although based on the principles employed in the new Glasgow stack, the seismic isolation stack design considered here would require some important alterations to the basic design. As this stack would be made to a much larger scale, it was proposed that the main GEO 600 stack design consist of three legs to provide adequate space and beam clearance for optical arrangements contained in the main 1 m diameter tanks. The total mass in each of the layers was chosen to be 24 kg over three legs, with a top plate of mass 50 kg connecting the legs at the top. The individual brick masses are 8 kg, with dimensions of around $6\,\text{cm} \times 2\,\text{cm} \times 10\,\text{cm}$, where the frequency of the first internal mode is 8 kHz.

The second double pendulum shown represents the reaction mass suspension system, included in the design to mount orientation control and electronic damping components which act on the main test mass suspension (Hough, Danzmann, Schutz et al, 1994).
The RTV units chosen for initial tests were cylindrical with diameter 16 mm and height 25 mm, corresponding to a shape factor of 0.16, as used in the RTV tests outlined in section 2.3.3. As the vertical behaviour of these units was known from the work discussed in there, they provided a reasonable starting point for the design.

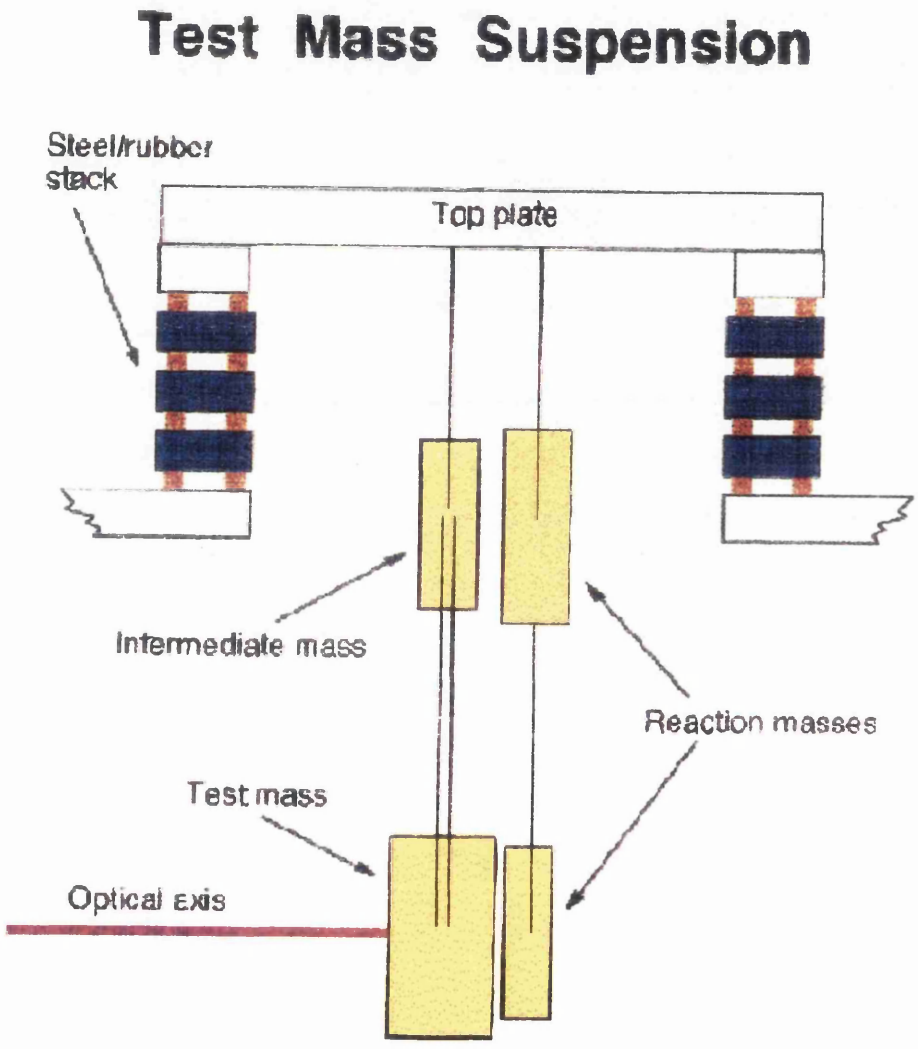

Fig.(2.21): ***Schematic diagram of the proposed GEO 600 passive isolation system.***

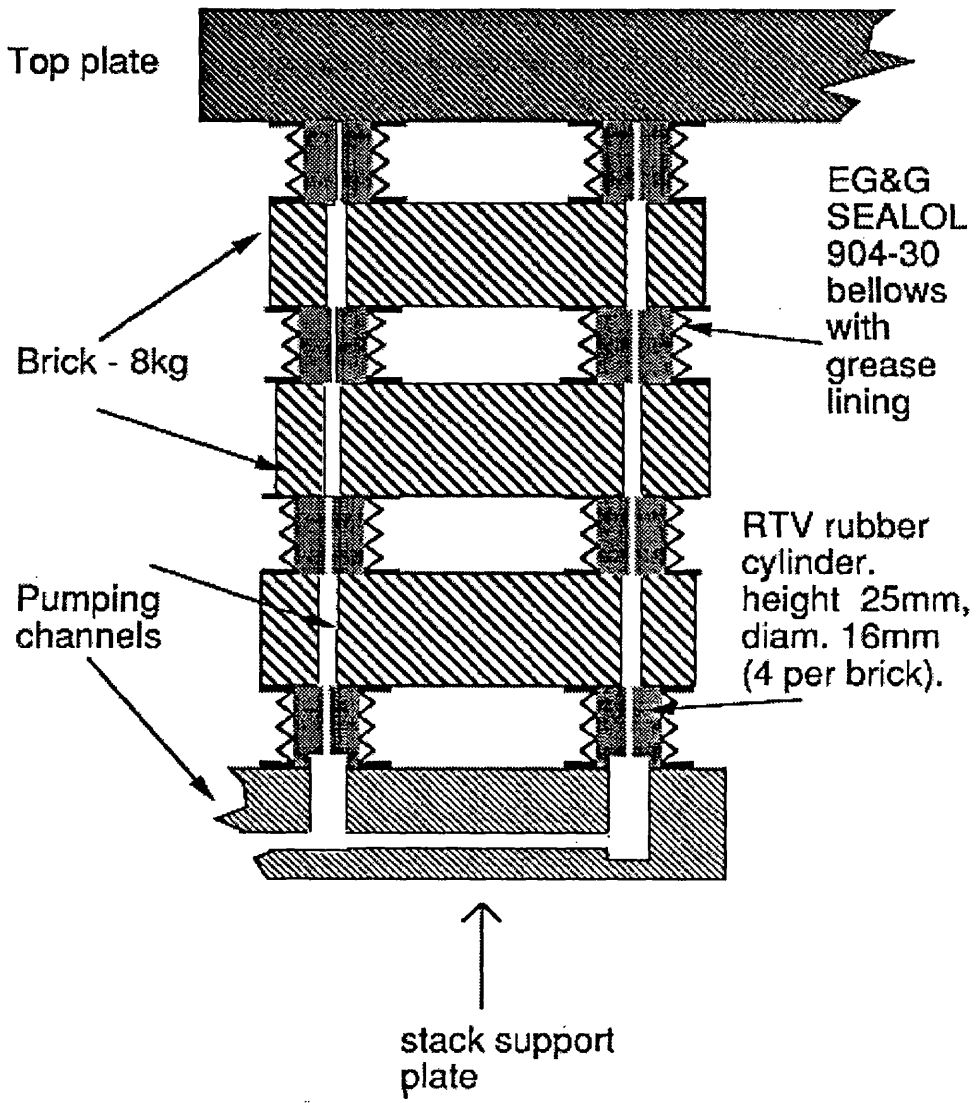

Fig.(2.22): ***Schematic diagram of a single leg of the proposed stack, where the cylindrical RTV units have been encapsulated by soft metal bellows.*** *Note the requirement for pump channels up the length of the stack.*

In addition to the basic stack design, there will also be the question of out-gassing control in the GEO 600 system. It will be extremely important to prevent out-gassing of hydrocarbons and sulphurous materials into the system, from any non-metallic elements present, as this could cause widespread damage to mirror coatings. This has led to stringent vacuum requirements throughout the detector (Hough, Danzmann, Schutz et al, 1994), where it will be required that the stack out-gassing rate be brought down to levels

of order $10^{-12}\left(\text{mbar l}/\text{cm}^2\text{s}\right)$. It is therefore proposed that a good vacuum rubber such as RTV be used, and that these RTV units be shielded from the system in thin-walled steel vacuum bellows, to be pumped separately from the main system. The use of a good UHV material, such as pre-cleaned stainless steel, will also be required to replace lead in the stacks. The main features of the vacuum aspects of the stack are shown in Fig.(2.22) above for a single leg.

The expected isolation performance of this stack will be dealt with in section 2.4.3, where consideration will be given to both the stiffness of the bellows and the non-standard load-stiffening of RTV. Experiments toward the use of bellows in such a system will be covered in the following section.

2.4.2
Out-gassing control of RTV rubber units.

Introduction to choice of metal bellows as a suitable capsule.

The choice of a suitable encapsulation method for the RTV units has proved to be extremely challenging due to the nature of the requirements that it must meet before it can be considered for use in the system. For example, great care must be taken when introducing metal elements of any kind into seismic isolation systems due to internal resonances. There are other strict conditions to which any proposed method must conform in order to be considered for use, thus introducing a challenging technical aspect to the design.

In the first instance, as a single defective capsule could have serious consequences for the mirrors it must allow ample room for the rubber to bulge, without tearing or creasing, a feature which is particularly important during initial loading of the stack when the largest deformations of the rubber occur. In addition to this the capsule must be capable of withstanding the difference in pressure between the capsule interior and the rest of the system. Most importantly of all, however, was the need for a solution which would not unreasonably impede the performance of the rubber as an isolator, either by physical restriction or by the presence of high order modes in the capsule itself.

The best solution appears to be the use of vacuum bellows, generally used as flexible vacuum-tight couplings. These have several advantages, including their widespread availability and that they are generally manufactured to ultra high vacuum specifications. They also benefit from a structure which allows a large range of linear movement in the [17]vertical and horizontal without buckling or tearing.

The choice of bellows for the system depends critically on the correct combination of stiffness and dimensions. Thin walled edge-welded bellows can be suitably soft, while being relatively cost-effective for small scale tests. The welding method employed during their manufacture should, however, be taken into account for these bellows units in situ as certain techniques (e.g. 'soft-soldering') will not provide joints which remain leak-tight after bake-out in the detector system.

A suitable test-bellows was found for use with the RTV cylinders chosen for use (section 2.3), namely the edge-welded 904-30 bellows made by EG&G SEALOL (Fig.(2.23)). These bellows would fit closely round these rubber units while still allowing room for rubber movement (Fig.(2.24)). Thirty convolutions in length, they also had a low enough spring rate to allow the spring constant of the RTV units to dominate in the vertical. It should be noted that the horizontal and vertical spring rates of the bellows were very similar. However, this was not considered to be a problem as it was generally the vertical performance of this vibration isolation system which was of greatest concern.

Quantity	E.G.&G 904-30 bellows	RTV cylinder (S=0.16)
Outer diameter	30.48 mm	16 mm
Inner diameter	17.78 mm	not applicable
Free Height, z	28.2 mm	25 mm
$^{18}k_{h\ (per\ unit)}$	1688 Nm^{-1}	^{19}2500 Nm^{-1} (constant up stack)
$k_{v\ (per\ unit)}$	1575 Nm^{-1}	$^{20}5\times10^{4}$ Nm^{-1} (average up stack)

Fig(2.23): data table for E.G.&G SEALOL 904-30 bellows.

[17] It is expected that bellows will be considerably stiffer than the encapsulated rubber units in rotation. The consequences of this feature should be taken into account when considering the effect of rotational seismic noise on such a stack.

[18] Horizontal and vertical bellows spring constant data values were calculated from formulae supplied by manufacturer. Horizontal formula known to have a high error value (at least 30%).

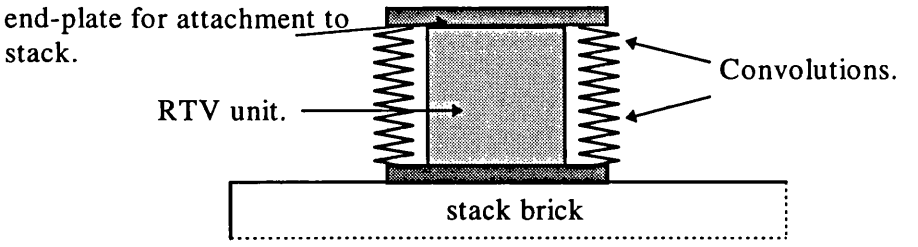

Fig.(2.24): ***Single bellows containing an RTV rubber unit.*** *Stainless steel endplates are attached to allow welding of bellows/RTV unit to stack brick.*

As this was a specialised application of these bellows, it was necessary to test their frequency response. This was carried out for the vertical and horizontal directions, with both individual bellows, and bellows filled with an RTV cylinder (as proposed for the final stack system). In particular the resonant frequencies, and the presence of higher order internal modes were investigated.

2.4.2.1
Vertical frequency response tests of E.G.&G SEALOL 904-30 bellows.

The vertical drive arrangement used in the vertical testing of the EG&G SEALOL 904-30 bellows was similar to that shown schematically in Fig.(2.6(a)) (section 2.2), where the vertical drive was provided using the arrangement shown in Fig.(2.25) below. When testing bellows in this way it is important to ensure that trapped air can freely escape as the bellows compress, and for this reason a split ring mounting was placed between the top of the bellows and accelerometer 2. In addition, acoustic coupling is always a hazard when carrying out this kind of experiment in air. The level of acoustic coupling in the experiment was measured by suspending the top accelerometer a distance of around

---

[19] Predicted for a cylindrical unit (assuming no bending) of the chosen dimensions from shear modulus data for RTV, as reported in section 2.3.2. This is stiffer than would actually be the case in practice as bending will most likely take place to some extent, but is used as a worst case value.

[20] This value corresponds to the average load-stiffened vertical spring constant of RTV units with S=0.16 under the static loads considered in this stack design. Individual values were obtained using equation (2.15), the process for which is discussed further in section 2.4.3.

1mm from the top of the bellows and running the transfer function measurement as usual. As can be seen from Fig.(2.26), acoustic noise was taken to be negligible in this set up.

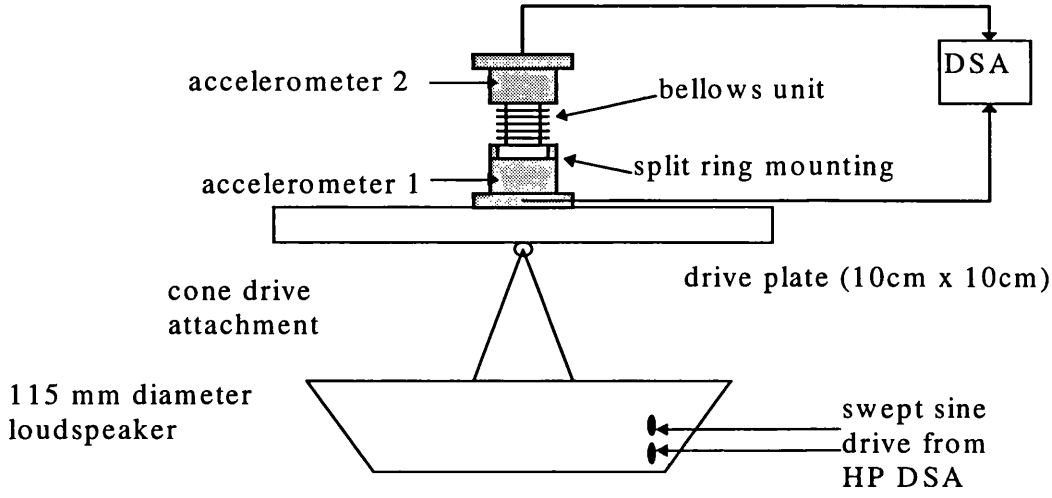

Fig.(2.25): ***Vertical drive arrangement for bellows test.*** *Loudspeaker connected to drive source in Hewlett-Packard spectrum analyser.*

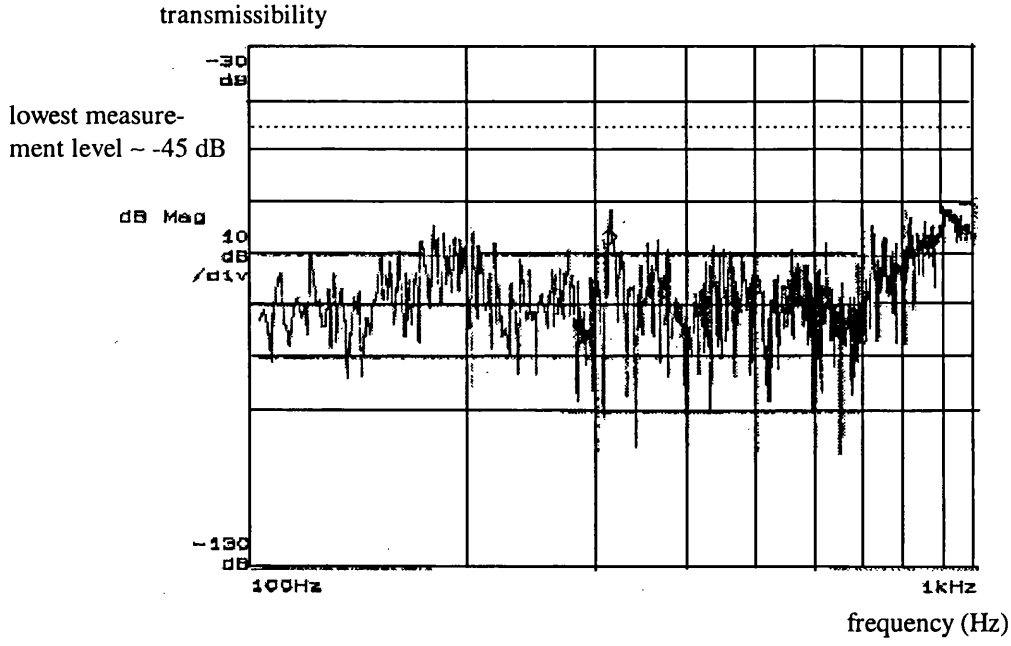

Fig.(2.26): ***Acoustic noise trace, recorded between 100Hz and 1kHz.*** *Measurement level at least ~ 15 dB above acoustic noise level.*

The vertical frequency response of a single, empty bellows and of a single damped bellows, under the mass of the accelerometer (0.175 kg), were tested in the range 5 Hz

to 1 kHz.

- Vertical test results of 904-30 bellows

Single bellows

The Bode magnitude and phase plots for the empty bellows were measured by the spectrum analyser for a swept sine drive and are shown in Fig.(2.27).

The fundamental bellows resonance can be seen at $f_0 = 13.7\ \text{Hz}$. From the value of vertical bellows spring constant supplied by the manufacturer of $1575\,\text{Nm}^{-1}$, we would have expected this to be 15 Hz. However, as the frequency resolution of the analyser during this measurement was around 1.6 Hz, the supplied value of $k_v)_b = 1575\,\text{Nm}^{-1}$ per bellows was assumed throughout the rest of this work.

Until 80-100 Hz the spectrum behaves as one would expect from a second order system such as this, with an initial slope of ~ 12 dB/octave. However, as can be seen from the traces a large family of higher order modes (f_1 to f_6) are present in the bellows spectrum from 100 Hz to 1 kHz. As these resonances would undoubtedly compromise the vibration isolation of the detector at these frequencies, their removal was necessary if the bellows were to be considered any further.

All bellows resonances require that a certain number of convolutions be able to expand and contract. Damping was achieved by filling the convolutions with a coating of grease, which would work by dissipating the bellows energy on resonance. The same experimental set up was used to test the vertical transfer function of a single, *greased* bellows. The resulting Bode magnitude and phase plots are shown in Fig.(2.28), where the addition of grease can be seen to have the following encouraging results:

1) The complete removal of higher order bellows resonances f_2 to f_6.
2) The reduction in amplitude of resonance f_1 to almost negligible proportions.
3) Significant reduction of fundamental vertical bellows resonance, f_0, by approximately 20dB, with a corresponding reduction in the bellows quality factor from 30 to ~ 4.

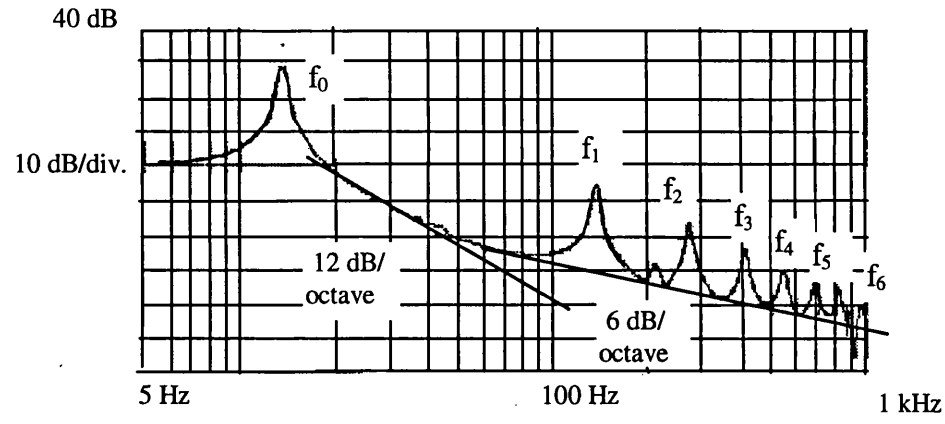

Fig.(2.27): Bode magnitude and phase plots for the frequency response of a single 904-30 bellows under 0.175 kg. *Note the family of internal resonances above 100 Hz.*

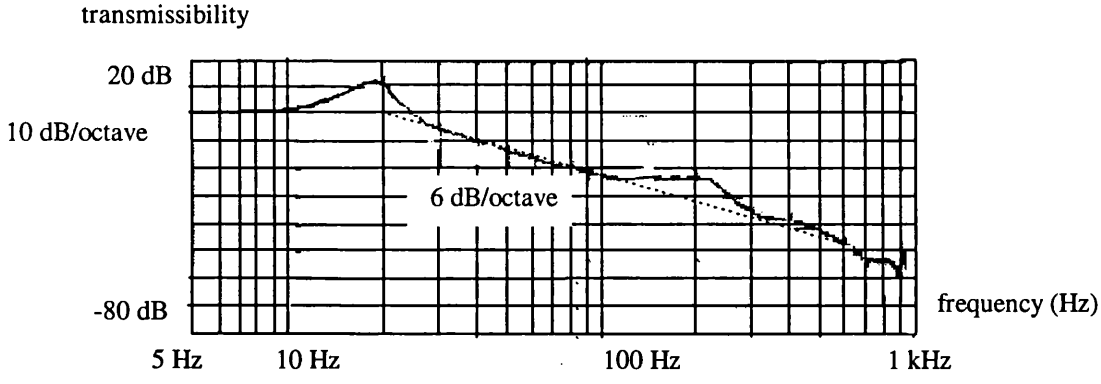

Fig.(2.28): Bode magnitude and phase plots for the frequency response of a single 904-30 bellows, damped internally with grease.

2.4.2.2
Horizontal test results of 904-30 bellows

Using the apparatus described in section 2.3.2, tests of the bellows horizontal response (without grease) were also carried out, with the following measurements being taken:

1) 4 × 904-30 bellows under 1.86 kg brick.

2) 4 × RTV cylinders alone under 1.86 kg. Each RTV cylinder has S=0.16, A/Z = 0. 008

3) 4 × 904-30 bellows, each containing an RTV cylinder, under 1.86 kg.

Although the vertical response of this type of bellows can be predicted from manufacturer's data with a reasonable degree of confidence, in the horizontal this is not the case as the bellows motion is not straightforward. However, an empirical formula (equation (2.20)), supplied by the manufacturer can be used, albeit with a high error (~30% or so), to get an approximate value of horizontal spring constant. The terms K^* and L_f are the size correction factor and bellows free length whose respective values for the 904-30 bellows are: K=873 mm^2 and L_f = 28.2 mm.

$$k_h)_b \approx \frac{k_v)_b \, K}{L_f^2} \tag{2.20}$$

where $k_v)_b = 1575\,\mathrm{Nm}^{-1}$ is the bellows vertical spring constant as before. Thus $k_h)_b$ is predicted to be: $k_h)_b \approx 1688\,\mathrm{Nm}^{-1}$ per bellows unit, which corresponds to a horizontal resonant frequency of 9.6 Hz for 4 such units under the 1.86 kg test load used here.

On their own, the cylinders will almost certainly bend, thus the bending-modified value of shear modulus, $G' = 1.2 \times 10^5\,\mathrm{Nm}^{-2}$ (equation (2.9)) should be used. Thus $k_h)_{rtv}$ can be found using the equation $k_h)_{rtv} = \frac{G'A}{Z}$ as described in section 2.1.3. Note that where bellows are also present, bending will be restricted to some extent. Hence the standard value of shear modulus, $G = 2.52 \times 10^5\,\mathrm{Nm}^{-2}$ should be used as a conservative estimate. Thus, where bending takes place we can expect that: $k_h)_{rtv} = 968\mathrm{Nm}^{-1}$ per unit, and that where bending does not take place: $k_h)_{rtv} = 2016\,\mathrm{Nm}^{-1}$ per unit. These correspond

---

* Size correction factor defined by manufacturer as $K = 1.5\left(\frac{OD+ID}{2}\right)^2$, where OD and ID are respectively the outer and inner diameters of the bellows.

to horizontal resonant frequencies of 7.2 Hz and 10.5 Hz respectively for 4 such cylinders under 1.86 kg.

Finally, as the concentric combination of RTV and bellows units behave as a parallel spring system, we can find the combined horizontal spring constant from the results obtained for the bellows and RTV on their own using:

$$k_h = k_h)_b + k_h)_{rtv} \tag{2.21}$$

The maximum value expected for the parallel combination of the bellows and RTV springs is: $k_h = 3704\,\mathrm{Nm}^{-1}$ per unit, corresponding to a maximum resonant frequency of 14.2 Hz for 4 such units under the 1.86 kg test load.

The following table (Fig.(2.29)) shows the experimental results from the above list of tests, which can be compared with the results predicted above.
Results from these tests indicated that there were no high order modes visible above the fundamental horizontal bellows resonance of $f_{hb} = 6.1$ Hz:, within the acoustic noise [21]limitations of this larger experimental set-up. This horizontal resonant frequency was much lower than that expected from the empirical formula supplied by the manufacturer, although this overestimated value predicted will be used as a worst case value when modelling the GEO 600 system.
The horizontal resonant frequency of the RTV cylinders alone under 1.86 kg was found to be 7.4 Hz, which compared well to the predicted value of 7.2 Hz when bending was taken into account. (This result again indicates the standard nature of the behaviour of RTV in the horizontal).

[21] The transmissibility spectrum for a single layer stack such as this was expected to be affected by acoustic noise at approximately 400 Hz, as observed in other measurements using this apparatus.

Horizontal test units under load	load (kg)	$f_h)$	[1] k_h	Predicted k_h
4× 904-30 bellows	1.86	$f_h)_b = 6.0 \pm 0.5$ Hz	$k_h)_b = 680 \pm 40$ Nm^{-1}	$k_h)_b = 1690 \pm 510$ Nm^{-1}
4 × RTV cylinders	1.86	$f_h)_r = 7.5 \pm 0.5$ Hz	$k_h)_{rtv} = 1005 \pm 45$ Nm^{-1}	$k_h)_{rtv} = 970 \pm 50$ Nm^{-1}
4 × 904-30 bellows, containing RTV cylinders	1.86	$f_h)_{r+b} = 10.5 \pm 0.5$ Hz	$k_h)_{r+b} = 2040 \pm 70$ Nm^{-1}	$k_h)_{r+b} = 3700 \pm 60$ Nm^{-1}

Fig(2.29): table of results for horizontal frequency and spring constant evaluations of various RTV/bellows units.

The horizontal spring frequency expected from the RTV and bellows combination under 1.86 kg was 9.6 Hz - an evaluation based on the experimentally found values of $f_h)_b$ and $f_h)_r$ above. Experimental results indicated, however, that the combined frequency was actually $f_h)_{r+b} = 10.54$ Hz . This discrepancy was almost certainly due to restriction of the RTV bending by the bellows.

From these results, it was concluded that the horizontal performance of the RTV/bellows combination was satisfactory for use in the GEO 600 system. A list of the resulting spring constants used in the GEO 600 stack performance model is now described in section 2.4.2.3.

2.4.2.3
Summary of bellows results, and application to GEO 600.

From experimental tests carried out on the horizontal and vertical frequency response of the E.G.&G 904-30 edge welded vacuum bellows, the following pieces of information were found for use in the GEO 600 system design:

[22] Values quoted per spring unit.

1) Horizontal spring constant: The manufacturer's estimate of $k_h)_b \approx 1688\,\mathrm{Nm}^{-1}$ per bellows was found to be more severe than was actually the case. However, as a worst case limit this value will be used where appropriate as the bellows contribution to horizontal stiffness in performance modelling of GEO 600.

2) Vertical spring constant: The manufacturer's estimate of $k_v)_b = 1575\,\mathrm{Nm}^{-1}$ per bellows was found to be correct within the experimental error of the test. This value was used as the bellows contribution to the vertical stiffness of the GEO 600 seismic isolation stacks.

3) Combined horizontal spring constants of the RTV cylinders and bellows: It was found that in the horizontal the bellows units restricted bending of the RTV cylinders, thus increasing the contribution of the RTV to the overall horizontal stiffness. The value of RTV horizontal stiffness was found to lie in the region between the value expected where bending of the units was present $(968\ \mathrm{Nm}^{-1})$, and that where the units were undergoing shear only $(2016\,\mathrm{Nm}^{-1})$. As a worst case however, the latter case was used which, in combination with $k_h)_b \approx 1688\,\mathrm{Nm}^{-1}$ gave a value of: $k_h = 3704\,\mathrm{Nm}^{-1}$ per bellows/rubber unit. When using the MATLAB simple stack model, as discussed in the following section 2.4.3, this value will be used to define the total horizontal stiffness per unit per layer.

4) Combined vertical spring constants of the RTV cylinders and bellows: As the vertical motion of this combination was more straightforward than in the horizontal, the combined spring constant will be taken to be:

$$k_v)_n = k_v)_b + k_{vn})_{rtv} = 1577 + k_{vn})_{rtv}$$

per unit for layer n of the stack. Recalling section 2.3.3, it will be necessary to evaluate the vertical stiffness of the RTV units in each layer according to the static

load above, giving rise to a value of $k_{vn})_{rtv}$ which can be substituted in the equation above. Note that the bellows vertical spring constant is expected to remain constant.

5) Removal of high order bellows modes: As a result of experimental work outlined in section 2.4.2.1, the removal of bellows high order modes will most likely be carried out using some form of viscous damping compound in the convolutions. Tests carried out here used ordinary grease for convenience but eventually some form of silicone vacuum grease will be used, as this must be eventually suitable for a high vacuum environment. Damping of this sort has been observed to be extremely effective in removing these modes, thus making the bellows suitable for use as a shielding capsule in the GEO 600 isolation system.

The application of these points and observations to the prediction of the performance of the GEO 600 stack, as proposed here, is discussed in the following section.

2.4.3
Predicted performance of this seismic isolation system design.

So far we have discussed several technical issues surrounding the simple proposal for seismic isolation stacks for the GEO 600 detector. It is now necessary to consider the expected performance of such a stack in the horizontal and vertical directions and any additional practical problems, both of which may well highlight a required change to the basic design.

The question of performing a simple modelling technique on stacks such as these, where only direct transmission of noise in the horizontal and vertical is being considered, has been outlined throughout this chapter. A similar procedure will be followed here for a leg of the proposed design. There now follows an account of the method used for each direction, with the results obtained in each case.

- Horizontal prediction of stack performance at100 Hz.

The horizontal equations of motion of the proposed stack (shown schematically in Fig.(2.30)) are:

$$\begin{aligned} 8\ddot{x}_1 &= -k_h(1+j0.25)(x_1-x_0)+k_h(1+j0.25)(x_2-x_1) \\ 8\ddot{x}_2 &= -k_h(1+j0.25)(x_2-x_1)+k_h(1+j0.25)(x_3-x_2) \\ 8\ddot{x}_3 &= -k_h(1+j0.25)(x_3-x_2)+k_h(1+j0.25)(x_4-x_3) \\ 17\ddot{x}_4 &= -k_h(1+j0.25)(x_4-x_3) \end{aligned} \tag{2.22}$$

where k_h (for the bellows and RTV units per layer) has approximately the value:

$$k_h = (3704\times 4) = 1.5\times 10^4\,\mathrm{Nm}^{-1} \tag{2.23}$$

By solving (2.22) for the transfer function x_4/x_0, for this value of k_h per layer, gave the following prediction of the horizontal stack performance (Fig.(2.31)). This prediction is based on the assumption that the RTV quality factor has been reduced to $Q_{sh}=4$.

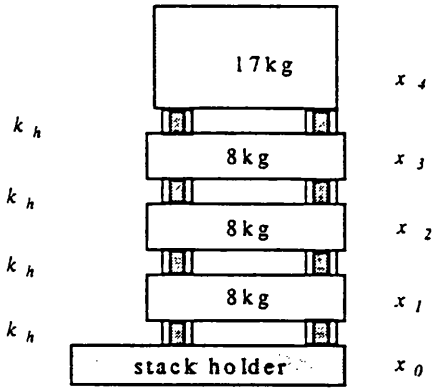

Fig(2.30): ***Schematic diagram of a single leg of the GEO 600 stack where the horizontal spring constant per layer of each leg is constant and given by*** $k_h = 1.5\times 10^4 Nm^{-1}$.

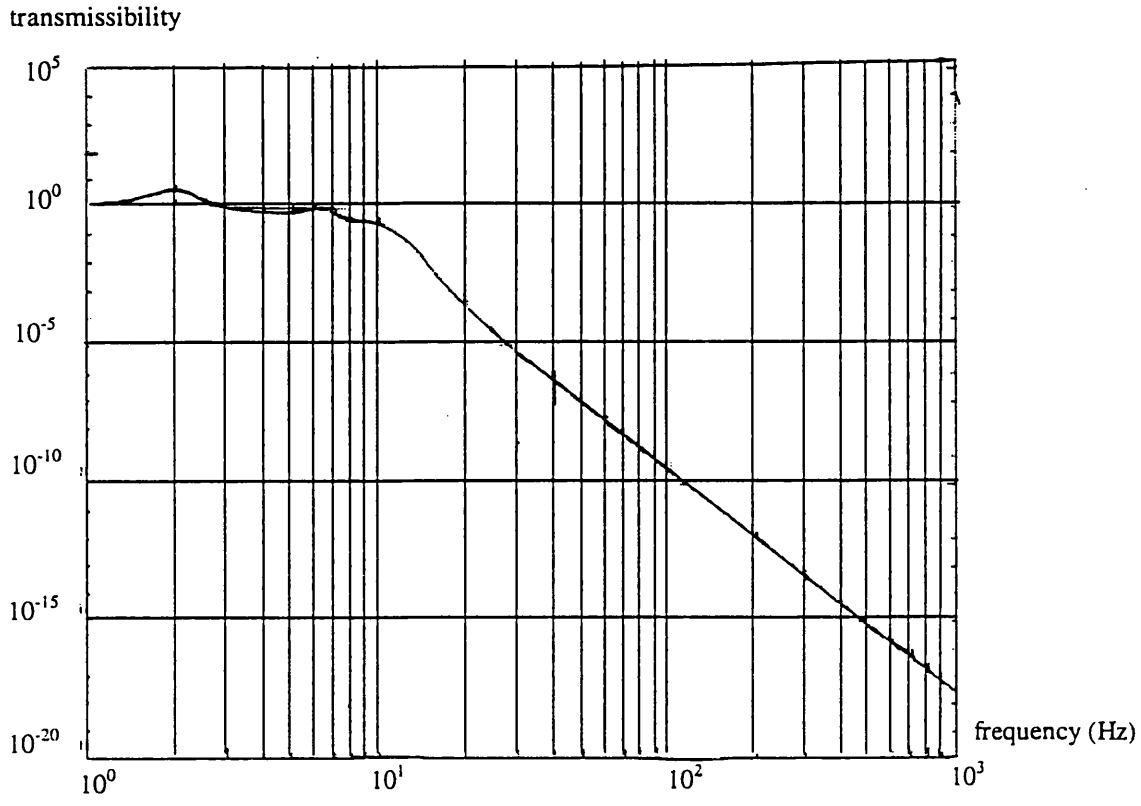

Fig(2.31): ***MATLAB prediction of the horizontal performance of the GEO 600 stack for direct transmission of horizontal seismic noise.***

- Vertical prediction of 100 Hz stack performance

Consider the stack shown in Fig.(2.32) below, corresponding to a single leg of this GEO 600 stack.

It has already been observed that the correct evaluation of the vertical spring constant of RTV requires that the total static load above the layer of rubber concerned be fully taken into account according to the RTV load-stiffening equation (2.15), (recall this equation

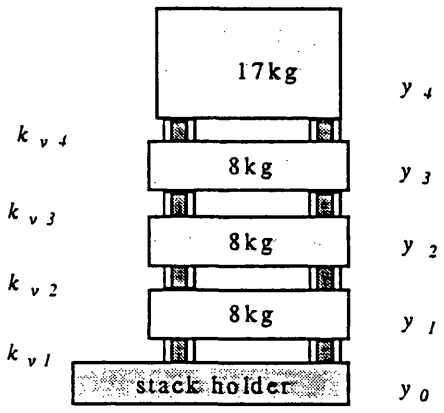

Fig(2.32): ***Schematic diagram of a single leg of the GEO 600 stack as used in model.*** *Note the inclusion of 1/3 the total suspended mass on the static load of the fourth layer. Spring constants vary from layer to layer according to the static load above.*

was found for units of shape factor S=0.16, as used in this design). In this instance the total static load also includes that due to one third of the suspended mass, which is represented by an addition to the mass of the top plate carried by one leg. The table in Fig.(2.33) below lists the parameter values for this stack, resulting in the vertical equations of motion (2.24):

$$\begin{aligned} 54\ddot{y}_1 &= -k_{v1}(y_1 - y_0) + k_{v2}(y_2 - y_1) \\ 46\ddot{y}_2 &= -k_{v2}(y_2 - y_1) + k_{v3}(y_3 - y_2) \\ 38\ddot{y}_3 &= -k_{v3}(y_3 - y_2) + k_{v4}(y_4 - y_3) \\ 30\ddot{y}_4 &= -k_{v4}(y_4 - y_3) \end{aligned} \qquad (2.24)$$

layer (n)	mass (kg)	total static load on layer (kg)	combined k_{vn} per layer (Nm^{-1})
1	8	54	2.14×10^5
2	8	46	1.88×10^5
3	8	38	1.56×10^5
4	(50/3 + 38/3)=30	30	1.31×10^5

Fig(2.33): ***Summary table of static loads and vertical spring constants per layer of the stack leg.***

The equations of motion (2.24) were solved for y_4/y_0 using MATLAB, which allowed the prediction of the vertical stack performance, the result of which can be seen in Fig.(2.34) below:

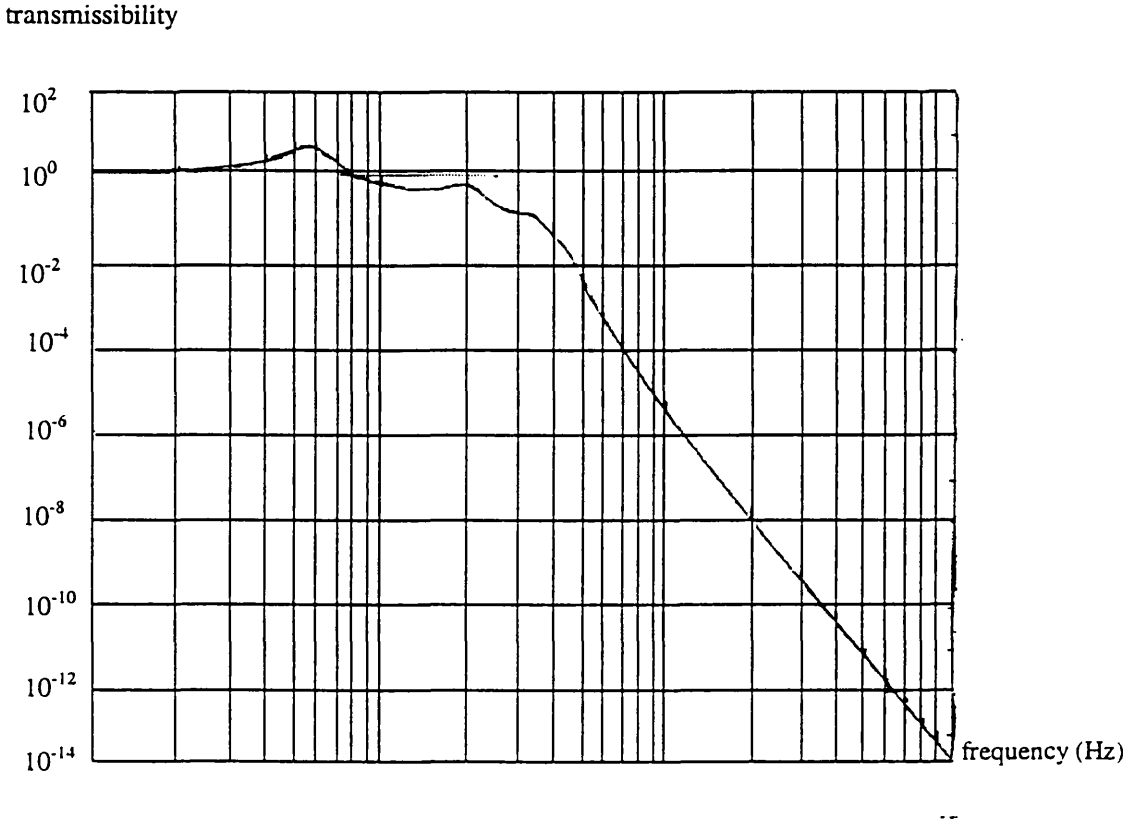

Fig(2.34): ***Vertical performance prediction for GEO 600 stack design, for direct transmission of vertical noise.***

- Discussion of predicted results

The approximate levels of isolation expected from this preliminary stack design are reasonably encouraging - particularly in the horizontal where the isolation factor has been predicted to lie in the region of 10^9 at 100 Hz. We may also conclude from these plots (Fig.(2.34)) that there is a clear dominance of vertical noise in the system, even

where the cross-coupling level is as low as 0.1%. As can be seen from Fig.(2.34) the predicted isolation factor in the vertical is slightly better than the level required, although it would be hoped that the value of around 10^5 may be improved through some minor modifications of the system.

These modifications may result from additional engineering work which would be essential to the future development of such a system, should it be pursued. A particular case for future attention would be the final shape of the RTV units (remember here we have assumed the very simple case of a solid cylinder). Internal pumping of the bellows units will be necessary to prevent an undesirable pressure gradient between the bellows interior and the ultra high vacuum environment outside. As one of the great advantages of using RTV is that it is cured from a liquid state, this will most likely be carried out by moulding one or more pump channels into the RTV units during cure. In general one can expect a reduction in the dynamic vertical stiffness (hence an improvement in isolation properties) of rubber units under compression for any relative increase in the free surface area - a belief which has been borne out during recent tests in this area at Glasgow (Plissi, 1996).

Work is also currently underway to develop an alternative stack design, based on several of the principles employed in the simple system investigated above. This revised system (Hough et al, 1996) is designed to allow GEO 600 to achieve a sensitivity level of approximately $2\times10^{-22}/\sqrt{\text{Hz}}$ at 50 Hz. Again, this design will incorporate the use of a four stage, three leg stack, this time with three RTV rubber units per stack brick being used in the first two stages only. The upper two stages will be formed using soft vertical springs. It is likely that a single large bellows will be used to encapsulate all three rubber components under each brick and will be damped using some form of grease as outlined during this work.

Chapter 3
A brief review of the main aspects of thermal noise associated with the pendulum mode of test mass suspensions.

3.1
Introduction

The subject of thermal noise has already been briefly raised in Chapter 1, where the importance of this noise source with respect to the GEO 600 detector has been outlined. To achieve the reduction of thermal noise to levels acceptable for GEO 600 will require that the suspension system satisfies certain design criteria, which will be discussed in this chapter.

Thermal noise tends to be peaked at the resonances of a system, and in general the operating range of a detector is chosen to lie as far away from these resonances as possible. As mentioned previously in Chapter 1 (and references therein) , there are several types of system resonance to be considered in a test mass suspension system of the kind generally considered for interferometric detectors. These are subject to both external and internal losses. For the desired strain sensitivity of GEO 600 to be achieved, it is believed that quality factors of 10^7 and 5×10^6 for the pendulum and internal modes respectively will be required (Hough, Danzmann, Schutz et al, 1994).

Although still at a conceptual stage, the main design criteria are well defined by experimental and theoretical work carried out by several workers in this field. However, for a particular material choice and production method many assumptions (e.g. the functional form of losses) may still require to be tested. The work reported in Chapters 4 and 5 is primarily aimed at beginning to investigate these assumptions for thermal noise related to the pendulum mode of suspensions made with materials produced at Glasgow. This is done by measuring losses associated with the pendulum mode of small-scale suspensions under light load, and material quality factor of unloaded fibres. It is hoped , however, that the continuation of this work will lead in the near future to full scale tests of a suspension system of similar scale and design to the GEO 600 test mass once the basic design principles have been tested.

In light of this, it is intended that this chapter provide an insight into the aspects of thermal noise associated with the pendulum mode of test masses for laser interferometric detectors. It is not intended to give an exhaustive account of the wider field of thermal noise, including internal and violin modes associated with these suspension systems, which are described in, e.g., Saulson (Saulson, 1990), Logan (Logan 1991, 1992, 1993(a),(b)), and Gillespie and Raab (Gillespie and Raab ,1993), (Gonzáles and Saulson, 1994), and (Gillespie, 1995).

3.1.1
Chapter contents

A brief introduction to the Fluctuation-Dissipation theorem is contained in section 3.1.2. This fundamental theorem demonstrates the importance of high quality factors, where external and internal sources of dissipation are minimised, for the systematic reduction of thermal noise. This section also includes an overview of the method used for the experimental evaluation of pendulum and material quality factors. A more thorough review may be found in Saulson (Saulson, 1990).

An introduction to external and internal damping, and of the frequency dependence of the losses associated with each, is contained in section 3.2. Section 3.3 discusses other pendulum system parameters which are of critical importance if high pendulum quality factors are to be achieved.

The production of a suspended test mass system with high pendulum quality factor will also rely on how suspension fibres are produced. The production methods employed to produce fibres suitable for the experimental work carried out in Chapter 4 and Chapter 5 is covered in section 3.4.

3.1.2
The fluctuation-dissipation theorem and thermal motion power spectrum associated with test mass suspensions

The manifestation of thermal noise as a fluctuation phenomenon was first observed as Brownian motion - the random displacement of small grains suspended in a liquid. This

was believed to result from statistical fluctuations in impacts exerted by liquid molecules which Einstein later showed to be closely linked to the dissipation mechanism present - in this case the viscosity of the liquid. The study of thermal motion in linear, dissipative systems was embodied by the Fluctuation-Dissipation theorem, produced by Callan and Greene (Callan and Greene, 1952). This theorem predicts that the power spectral density of the thermal motion of a system with damping is of the form:

$$x^2_{therm}(\omega) = \frac{4k_B T}{\omega^2} \Re(Y(\omega)) \tag{3.1}$$

where $\Re(Y(\omega))$ is the real (dissipative) part of the admittance of the system, and the other symbols have their usual meaning. The relationship between $\Re(Y(\omega))$ and the dissipation present in the system can be illustrated using the common example of a mass m on a spring of stiffness k, with natural frequency $\omega_0 = \sqrt{k/m}$, undergoing simple harmonic oscillation driven by the fluctuating thermal driving force F_{therm}. Assume the system is subject to external viscous damping, the level of which is described by the constant b. The equation of motion of the system can be described in the usual way by:

$$F_{therm} = m\ddot{x} + b\dot{x} + kx \tag{3.2}$$

In terms of the velocity of the mass, $\dot{x}$, this becomes:

$$F_{therm}(\omega) = \left(b + j\left(m\omega - \frac{k}{\omega} \right) \right) \dot{x} \tag{3.3}$$

The admittance of a mechanical system is defined to be $Y(\omega) = \dot{x}/F(\omega)$ which, in this case, has the form:

$$Y(\omega) = \frac{b - j(m\omega - k/\omega)}{b^2 + (m\omega - k/\omega)^2} \tag{3.4}$$

Substitution of the real part of equation (3.4) into equation (3.1), yields the following form of the thermal motion power spectral density of such an oscillatory system:

$$x_{therm}^2(\omega) = \frac{4k_B Tb}{\omega^2\left(b^2 + (m\omega - k/\omega)^2\right)} \tag{3.5}$$

At angular frequencies well below the resonance ($\omega << \omega_0$),

$$x_{therm}^2(\omega) = \frac{4k_B Tb}{k^2} \tag{3.6}$$

while the thermal motion power spectral density*on* resonance can be expressed as:

$$x_{therm}^2(\omega_0) = \frac{4k_B T}{\omega_0{}^2 b} \tag{3.7}$$

The final frequency region of interest is where$\omega >> \omega_0$:

$$x_{therm}^2(\omega) = \frac{4k_B Tb}{m^2\omega^4} \tag{3.8}$$

As can be seen from equations (3.6) and (3.8), the shape and level of the background noise floor will be determined by the magnitude and angular frequency dependence of *b* (e.g. in the example here *b* is a constant with frequency, but this may not always be the case). This feature indicates that reduction in the level of the thermal motion background (away from system resonances) would necessitate a corresponding reduction in the losses present in the system. We can characterise the level of losses in the system in terms of its quality factor, Q, where this is defined by:

$$Q = 2\pi\left[\frac{Energy\ stored\ by\ oscillator}{Energy\ lost\ per\ cycle}\right] \tag{3.9}$$

Where viscous damping is present in the system, the quality factor can also be described by:

$$Q = \frac{m\omega_0}{b} \tag{3.10}$$

A reduction in system dissipation should therefore should therefore lead to an increase in the quality factors associated with system resonances. We can therefore define a quality factor required for each resonance which will result in a thermal motion background of the desired level.

Associated with the dissipation is the loss angle, $\phi(\omega)$, whose functional form will depend solely on that assumed for $\Re(Y(\omega))$. Equation (3.1) is more usefully expressed in terms of the loss angle, $\phi(\omega)$, and this will be shown more fully in the following section 3.2 . The sensitivity of interferometric detectors is often evaluated at some frequency in the working range, typically 100 Hz, thus providing a useful benchmark in judging the overall performance. Direct measurement of the thermal motion background at 100 Hz is extremely difficult, and is best approached by extrapolation from the measured losses at the resonant frequencies of the system, provided the correct frequency dependence is known. Section 3.2 will also discuss the various forms of dissipation affecting pendulum suspensions, and the likely consequence on the shape of the thermal motion background.

3.2
Forms of dissipation affecting pendulum and material quality factors.

In a carefully constructed system, there are three main forms of dissipation affecting pendulum suspensions or unloaded fibres (the additional question of recoil damping being addressed in Chapter 4). Two of these sources of damping, due to surrounding gas and external magnetic fields, are proportional to the velocity of the oscillator and are therefore viscous in nature. The third dissipation mechanism is internal friction in the suspension material itself. There is some evidence (Kimball & Lovell, 1927; Quinn et al, 1992; Kovalik & Saulson, 1993) that for many solids losses due to internal friction are

not viscous in nature. This form of dissipation is known as structural damping. Although the effects of external viscous damping due to surrounding air and magnetic fields can be made negligible, that of internal friction cannot and will set the fundamental upper limit to the material Q.

3.2.1
External viscous damping of the pendulum and fibres.

As material and pendulum quality factor experiments are generally carried out in vacuum conditions, the effect of external velocity damping of both pendulums and freely oscillating fibres due to surrounding gas can be greatly reduced. This is also true for test masses in gravitational wave detectors themselves.

Magnetic damping due to eddy currents in the test mass and suspensions, induced by nearby feedback coils, can also be reduced. This is done through the use of suspension materials with very low electrical conductivity and magnetic susceptibility. For laboratory tests of pendulum quality factor (such as described in Chapter 4), where external feedback coils are not present in the experimental arrangement, the effect of external viscous damping due to surrounding gas tends to be the dominant effect[23].

There are two ways of looking at the functional form of viscous losses, $\phi(\omega)$, depending on whether the loss is defined on, or away from, system resonances. To illustrate this point, consider the gas-damped pendulum shown in Fig.(3.1) below. The equation of motion of a pendulum of mass, m and resonant angular frequency, $\omega_0 = \sqrt{g/l}$, subject to external gas damping is given by:

$$F = -mg\sin\theta - b\dot{x} \tag{3.11}$$

[23] The magnetic damping due eddy currents induced inside a light glass mass (used throughout the work outlined in Chapter 4) by movement in the Earth's magnetic field (Hough, 1996), was found to limit the pendulum quality factor to around 10^{12}. This effect was less serious than gas damping of the same mass by at least a factor of 10^3.

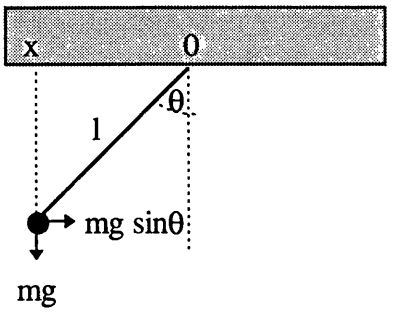

Fig.(3.1): Schematic diagram of simple pendulum of length l subject to viscous losses.

Where θ is small this can be rewritten as:

$$\begin{aligned} F(x) &= -m\omega_0^2 x - jb\omega x \\ &= -m\omega_0^2\left(1 + j\frac{b\omega}{m\omega_0^2}\right)x \end{aligned} \tag{3.12}$$

From this it can be seen that the phase angle, $\phi(\omega)$, existing between the applied force, $F(x)$ and the resulting displacement, x due to external viscous damping, is given by equation (3.13) below:

$$\phi(\omega) = \frac{b\omega}{m\omega_0^2} \tag{3.13}$$

As one might expect for external viscous damping, the loss function behaves as $\phi(\omega) \propto \omega$ in a system with resonant frequency ω_0. However, we are mainly interested in measurements made actually on the resonant frequency of the pendulum, or other oscillator. It is clear from equation (3.13) that the losses predicted at the resonant frequency of the oscillator behave as $\phi(\omega_0) \propto \frac{1}{\omega_0}$. Also, recalling equation (3.10), one can see that the resulting quality factor of an oscillator subject to damping of this form, and defined at the resonant frequency ($\omega = \omega_0$), is given by:

$$Q(\omega_0) = \frac{m\omega_0}{b} = \frac{1}{\phi(\omega_0)} \tag{3.14}$$

Thus, for an oscillator subject to external viscous damping, $Q(\omega_0) \propto \omega_0$.

Equation (3.14) really defines the upper limit to the measurable Q for a given system, subject to damping losses described by b. By redefining b in terms of parameters related to the surrounding gas it is possible to calculate the level of vacuum required for the measurement of high pendulum quality factors (in the absence of other damping sources). The results obtained from this work are used here mainly in the small-scale laboratory measurement of quality factors (Chapter 4 and Chapter 5), but can be equally applied to full scale detector test masses in situ.

For a typical system under vacuum, this problem can be addressed on a statistical level, assuming that the mean free path of the surrounding gas molecules is large compared to any dimension of the body.

Consider the pendulum in Fig.(3.2) below, swinging in a residual gas containing n molecules, of molecular mass m, per unit volume.

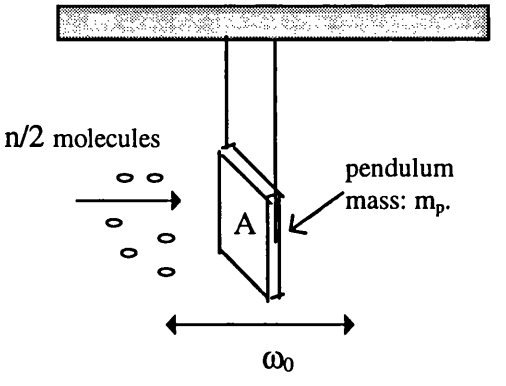

Fig(3.2): Pendulum, of mass m_p, and resonant angular frequency ω_0, subject to viscous damping through interaction with surrounding dilute gas. *As it swings, each side of the pendulum plate will be struck by n/2 gas molecules per unit volume swept out.*

Each side of the pendulum mass, (with cross sectional area 'A'), will be struck by $n/2$ molecules per unit volume swept out by the plate, each travelling with rms velocity $c/\sqrt{3}$ normal to the surface. The fluctuation in the total number of molecules striking the pendulum mass in a time t, in the direction of motion of the pendulum, will be:

$$\sqrt{\frac{ncAt}{\sqrt{3}}} \tag{3.15}$$

We shall now establish an expression for the fluctuation in the force exerted by these molecules on the pendulum mass. Using this, an expression relating the pressure of the residual gas to the pendulum Q can be found.

Consider the momentum, $mc/\sqrt{3}$, of a single gas molecule. Assuming this molecule collides elastically with the pendulum mass there will be a transfer of momentum, equivalent to twice this amount, from the molecule to the mass. In a time interval, t, this will result in a force being applied to the mass which can be expressed as $\frac{2mc}{t\sqrt{3}}$.

Recalling our expression in equation (3.15), the fluctuation in the force, ΔF, experienced by the pendulum mass due to all the molecules in the surrounding gas is:

$$\Delta F = \sqrt{\frac{ncAt}{\sqrt{3}}}\left(\frac{2mc}{t\sqrt{3}}\right) \tag{3.16}$$

Now, the density of the gas is $\rho = nm$, and the kinetic energy of the gas molecule can be expressed as $mc^2 = 3k_B T$, where k_B is Boltzmann's constant. By also considering the pressure of the gas, $P = \rho c^2/3$, the equation describing the square of this fluctuating force can be written as;

$$\Delta F^2 = 4\rho\sqrt{\frac{P}{\rho}}\frac{Ak_B T}{t} \tag{3.17}$$

The following substitutions, where $\Re$ is the ideal gas constant, can now be made to allow the expression of our equation in a more suitable form;

$$PM = \rho \Re T \Rightarrow \rho = \frac{PM}{\Re T} \text{ and}$$
$$\frac{1}{t} = 2\Delta f \tag{3.18}$$

where the first expression in equation (3.18) is the ideal gas law with mass of one mole of gas represented by M. By writing the time, t, taken for the momentum transfer from the colliding molecule to the plate in terms of frequency, equation (3.17) becomes;

$$\Delta F^2 = 8P\sqrt{\frac{M}{\Re T}} A k T \Delta f = 4\left(2PA\sqrt{\frac{M}{\Re T}}\right) k T \Delta f \tag{3.19}$$

This is similar in form to the more familiar Johnson noise for the voltage fluctuations across a resistor. Through comparison, one can then see that there is a resistive term $\left(2PA\sqrt{M/\Re T}\right)$ which is the mechanical analogue of electrical resistance. It is this term which will control the level of dissipation in the system. This term is defined to be related to the quality factor in the following way (French, 1965);

$$Q = \frac{m_p \omega_0}{b} = \frac{m_p \omega_0}{2PA}\sqrt{\frac{\Re T}{M}} \tag{3.20}$$

where m_p and M are the masses of the pendulum bob and of one mole of the residual gas respectively. This expression is used to calculate the vacuum levels required for the measurement of pendulum and material quality factors.

3.2.2
Internal damping

Internal friction is thought to arise due to the finite response time required by a material to fully respond to an applied strain. Thus the effect of internal friction can be simply modelled as the departure of a material from perfect elasticity by the introduction of the response phase lag $\phi(\omega)$. As such, it can then be expressed as a generalised form of Hooke's Law below;

$$F = -k(1 + j\phi(\omega))x \tag{3.21}$$

A material whose stress-strain behaviour conforms to equation (3.21) is said to be anelastic.

The phase lag $\phi(\omega)$, exists between an applied sinusoidal force, F, and the displacement response, x, of the material. It is thought to arise from the finite relaxation time taken by certain internal degrees of freedom of the material to reach an equilibrium state as the force is applied. A full discussion of this can be found in (Saulson, 1990), based on the publications of C. Zener, and Nowick et al. Internal friction in a material can result from the superposition of many sources of internal relaxation in a material, although possible mechanisms for this are not yet fully understood for fused silica.

One source of internal friction in fused silica which is known to be of great importance is the thermoelastic effect, associated with heat conduction in the material (Zener, 1937). This effect occurs when a material with non-zero coefficient of thermal expansion flexes. Due to the compression and stretching of the opposing fibre surfaces as it bends, a fluctuating thermal gradient is set up leading to a fluctuating heat flow. Internal friction processes, such as thermoelastic damping have losses defined by a characteristic relaxation time, τ, the phase lag being of the form;

$$\phi(\omega) = \Delta \frac{\omega\tau}{1 + (\omega\tau)^2} \tag{3.22}$$

* A.S Nowick and B.S Berry. *Anelastic Relaxation in Crystalline Solids* (Academic, New York, 1972).

For thermoelastic losses the strength of the damping is given by Zener (Zener, 1937) as $\Delta = \frac{E\alpha^2 T}{\rho c}$, where E is the elastic modulus, c is the specific heat at constant volume, α is the coefficient of thermal expansion of the material, and ρ, its density.

For the case of freely oscillating fibres the predominance of a single relaxation mechanism, such as thermoelastic damping, is characterised by a broad damping maximum. The frequency position of this maxima, associated with the thermoelastic effect, is dependent on the thickness, d, and thermal properties of the fibre. Zener derived the following expression for the characteristic frequency of ribbon fibres;

$$f_{char} = \frac{1}{2\pi\tau} = \frac{\pi}{2}\frac{K}{\rho c d^2} \tag{3.23}$$

where K is the thermal conductivity of the material.

For several solids, the losses due to internal friction have been observed to be independent of frequency (Kimball & Lovell, 1927) over a large frequency range - a result which is perhaps not immediately apparent from the form of equation (3.22). However, a tentative explanation of the observed effects may be found when one considers the presence of many such loss curves, each with a characteristic damping maximum. The net effect of these may be such that $\phi(\omega)$ appears constant.

It is worth noting at this stage the relationship between Q and $\phi(\omega_0)$ for internal damping. Rewriting equation (3.21) as;

$$F = \left(\frac{jk}{\omega} - \frac{k\phi(\omega)}{\omega}\right)\dot{x} \tag{3.24}$$

we can see that the general form of the damping coefficient for internal friction, given by the real part of the impedance is of the form:

$$b(\omega) = \Re\left(\frac{F}{\dot{x}}\right) = \frac{k\phi(\omega)}{\omega} \tag{3.25}$$

Consider now equation (3.20). Substitution of $b(\omega)$, for the case of $\omega = \omega_0$, gives the following expression for $Q(\omega)$;

$$Q(\omega_0) = \frac{m\omega_0^2}{k\phi(\omega_0)} = \frac{1}{\phi(\omega_0)} \tag{3.26}$$

Hence it can be seen that the functional form of $Q(\omega_0)$ for an oscillator subject to internal friction is also determined by the frequency dependence of the loss angle $\phi(\omega_0)$. For the case of internal structural damping in the system, $\phi(\omega_0) = \eta$ (where η is a constant), giving $Q(\omega_0) = 1/\eta$ which is independent of frequency. For internal viscous damping, we have $\phi(\omega_0) = \xi\omega_0$ (where ξ is also a constant) and $Q(\omega_0) \propto 1/\omega_0$ which is of course inversely proportional to frequency.

As the magnitude of $\phi(\omega)$ is dependant on the internal stresses of the material, it is obviously important to try to reduce their effect. For instance, it is known that localised heating of a material can set up internal thermal stresses, leading to mechanical weakness and possibly greater losses. Contamination by impurity atoms is also thought to increase internal friction, as are surface contaminants and micro-cracking. A suitable production method will address these issues, to ensure that losses are as low as possible and obey the assumed functional form.

3.2.3
Implication of functional form of internal losses on thermal motion.

It can be seen in (Saulson, 1990) that the functional form of losses due to internal friction has considerable consequence on the form of $x^2_{therm}(\omega)$. For internal damping this has the general form shown in equation (3.27);

$$x^2_{therm}(\omega) = \frac{4k_B T\omega_0^2 \phi(\omega)}{\omega m\left(\left(\omega_0^2 - \omega^2\right)^2 + \omega_0^4 \phi(\omega)^2\right)} \tag{3.27}$$

where $\phi(\omega)$ is a generic function of frequency. Typical thermal displacement power spectra are shown in Fig (3.3). Whether the background noise spectrum behaves as the upper or lower plotted line depends solely on the form of $\phi(\omega)$ in equation (3.27).

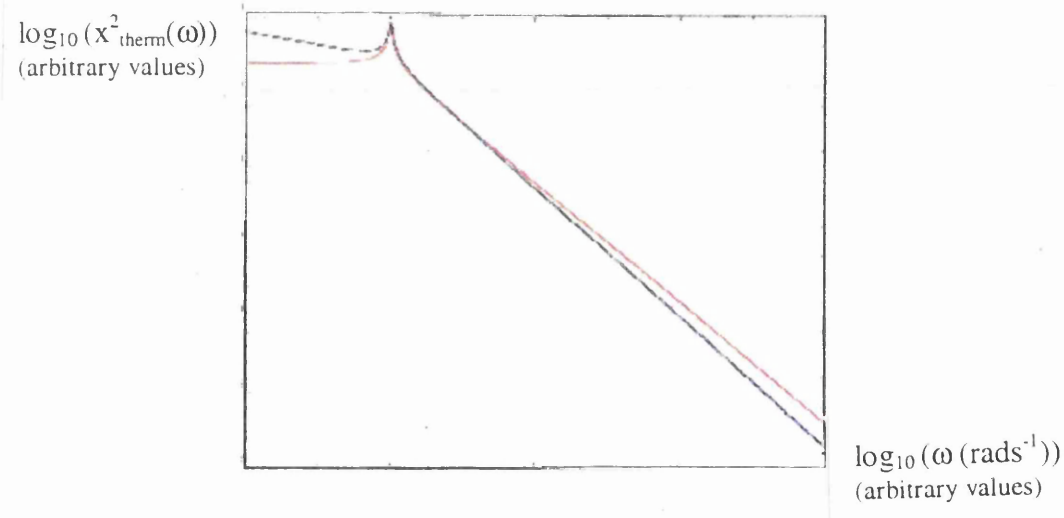

Fig(3.3): Comparison of thermal noise displacement power spectra for viscous and structural internal damping.. *Prior to the resonant mode the black curve (structural damping) falls as* $x^2_{therm} \propto 1/\omega$ *and the red curve is constant with* ω. *Following resonance, the black curve (structural damping) falls as* $x^2_{therm} \propto 1/\omega^5$ *and the red curve as* $x^2_{therm} \propto 1/\omega^4$.

The red plotted line corresponds to the predominance of viscous internal damping in the system, where $\phi(\omega) \propto \omega$. Where $\phi(\omega) \approx constant$ we have the black line indicating the predicted thermal motion power spectrum for structural damping. It is

sufficient here to note the difference in behaviour of the predicted thermal noise background determined by whichever dissipation mechanism is dominant in the system. In particular the region between the pendulum mode and the first internal mode of the test mass is of greatest concern for frequencies of interest in gravitational wave detection; it can be seen that a model which assumes the dominance of structural damping would suggest an increase in the level of background thermal motion in the frequency band directly preceding the first internal mode of the mass

Resolution of the form of $\phi(\omega)$ must be achieved to allow the correct prediction of the fundamental limit set by thermal motion in gravitational wave detection. It is extremely difficult to measure $\phi(\omega)$ directly, although it is possible to gain this information by examining the frequency dependence of quality factors associated with system resonances.

3.3
The suspension of test masses.

Discussion so far has centred on sources of dissipation affecting quality factors, and the need to reduce these damping levels for effective production and measurement of low loss oscillators. Closely linked to this will be the choice of material, the suspension method itself and the geometry of the suspension fibres. An overview of these issues will now be given.

3.3.1
Material choice.

In addition to possessing a high level of intrinsic quality factor, a suitable choice of material for detector test masses and suspensions will be required to have additional important properties (Logan, 1992, 1994(a)). For instance, for beam-splitter masses the material is required to have low absorption (to reduce heating effects) and have low birefringence to reduce distortion in the beam. To prevent distortion of the test mass due to the high incident laser light power, a high thermal conductivity and low coefficient of thermal expansion will be required. In addition, a suitable material for mirror masses for

the GEO 600 detector should be able to be polished to a surface finish of better than 4 nm (Winkler et al, 1994) over distance scales of around $\pi \times$ beam diameter (~a few cm). The material choice must also take account of the probable future requirement for some form of monolithic test mass and suspension unit, hence the chosen test mass material must also make a suitable choice for the fibres. There are several materials which could potentially be considered for the purpose of test mass suspension including fused silica, sapphire and silicon. These materials have been found to have low losses ((Logan, 1993(a)); (Kovalik and Saulson, 1993)), with measurements of the intrinsic losses of fused silica, indicating the possibility of achieving pendulum Q values for of order 10^7 ((Martin, 1978), (Braginsky et al,1992)).

The material chosen for the preliminary fibre studies reported in this thesis was fused silica, as it was considered both economical and viable in terms of its physical qualities.. However, it is by no means guaranteed that one can easily produce fibres with consistently low losses, and also the strength and durability required. It is intended that current and future work at Glasgow include the measurement of quality factor, and eventually of long-term fatigue behaviour, of fused silica fibres produced at Glasgow. It is hoped that this will eventually lead to the successful production of fibres with the low levels of intrinsic loss required for preliminary GEO 600 measurements.

3.3.2
Suspension method.

The need for an appropriate method of suspension becomes apparent when one considers the effect of both the seismic noise and thermal noise levels associated with the suspended mass. The choice in this case is suspension in the form of a pendulum, with the test mass being supported from suspension fibres made from fused silica. As the main horizontal restoring force is provided by the gravitational field which is essentially loss-free, a suspension of this form can have losses, ϕ_p, which are very much lower than the intrinsic material losses, ϕ_w. A discussion of this can be found in Martin (1978), and also in Saulson (1990) where it is shown that in a system where rocking of the mass is

not constrained we have the following relationship between losses in the pendulum mode and the bending wire, as given in equation (3.28).

$$\phi_p = \phi_w \left(\frac{E_w}{E_w + E_g} \right) \approx \phi_w \left(\frac{E_w}{E_g} \right) \tag{3.28}$$

where E_w and E_g are the energy stored in the wire and the gravitational field respectively. Furthermore, (Saulson, 1990) also shows that the [24] relationship between material and pendulum Q values for a mass suspended on n suspension fibres each of length l, (provided that coupling between pendulum and rocking modes is low) can be expressed by the following equation (3.29).

$$Q_{pend} = \frac{2mgl}{n\sqrt{TEI}} Q_{mat} \tag{3.29}$$

For typical values of tension, T, Young's modulus, E, and bending moment, I, it is possible to achieve pendulum quality factors of around 100-1000 timeshigher than the measured material quality factor. Even with the pendulum suspension however, care must be taken in the case of light suspended masses. When conducting laboratory experiments to test the pendulum quality factor of fibres, it is desirable to use masses that are reasonably heavy with fibres that are as thin as possible to ensure the gravitational restoring force on the pendulum mass remains as large as possible compared with the fibre restoring force.

For the actual detector test masses however, the value of the suspended mass is chosen for a variety of reasons, e.g. according to the size of mirror required, the frequencies of the internal modes (set by the aspect ratio of the mass) and the uncertainty principle. The fibre cross sectional area is then fixed such that the stress on the fibre due to the choice of mass is at least a factor of 3 lower that the breaking stress of the material.

---

[24] Note that this equation assumes that the mass is free to rotate, therefore bending takes place at one end of the wire only. Where four suspension wires are used, rotation is constrained (Gonzáles and Saulson, 1994), thus leading to twice the level of losses in the wire. In this instance, equation (3.29) becomes $$Q_{pend} = \frac{2mgl}{4\sqrt{TEI}} \frac{Q_{mat}}{2} = \frac{mgl}{4\sqrt{TEI}} Q_{mat}.$$ (3.29(a)).

It is intended that experiments be carried out to make direct comparisons between experimentally measured values of Q_{mat} and Q_{pend}, although this can be difficult to do directly where $Q_{mat} > 10^6$ or so.

3.3.3
Choice of cross-sectional shape and area of fibres.

From equation (3.29) it can be seen that the values of two parameters of the suspension fibres, i.e. the bending moment, I, and mass, m, are of great importance to the enhanced value of Q achieved. Although the minimum area, A, of the fibres is fixed for a given mass, there remains some flexibility in the choice of cross-sectional shape. Two options currently under consideration are fibres of circular and rectangular cross sectional shape (also referred to as 'cylindrical' and 'ribbon' fibres), whose bending moments of inertia are defined as in Fig.(3.4).

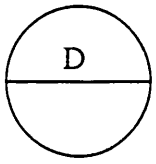

$$I_{circ} = \frac{\pi D^4}{64}.$$

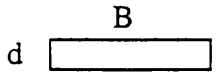

$$I_{rect} = \frac{Bd^3}{12}$$

Fig.(3.4): Fibre cross-sections defining the parameters involved in the expressions for bending moment of inertia of fibres with cylindrical and rectangular cross section.

Consider the cylindrical fibre shown in Fig.(3.4). If one considers the use of a ribbon fibre (with rectangular cross-section), it can be see that the bending moment can be greatly reduced through use of a fibre that is suitably thin (but of greater width), without reducing the cross-sectional area. This decrease in I_{rect} should result in a higher pendulum quality factor than obtained using a cylindrical fibre of the same area. It is this potential for an increase in Q_{pend} through I which has inspired the investigation of ribbons as a potential fibre shape. There are, however, practical points to consider. In the first instance is the question of production of these ribbons. Perhaps more limiting,

however, is the kinematic behaviour of a ribbon suspension; flexing is only likely to take place in one direction, leading to the need for 'cross-hinges' for attachment to the test mass and to the structure above. Work is currently continuing in this area (Logan et al, 1996).

3.4
Methods of fibre production employed in Glasgow.

In this section the two main methods used here in the production of fused silica fibres for testing both the pendulum quality factor in Chapter 4 and the material quality factor of fused silica ribbon fibres in Chapter 5 will be discussed.

Fused silica fibres are routinely drawn for optical communication applications. However, commercial sources would be unable to produce ribbon fibres at a reasonable cost and would not allow the production of fibres whose ends 'swell' to a larger diameter. This has been shown to be an advantage due to important findings on the effect of clamping of fibres on the pendulum mode losses, carried out by (Quinn et al, 1994) and also by (Martin, 1978). They have found that for high pendulum quality factors to be obtained the fibre must swell to a larger diameter at the fixed end, to avoid the problem of 'stick-slip' of the vibrating fibre at the clamped end. This tends to be a problem mainly for large amplitudes of fibre motion. In addition to this it is thought that damping may also occur if the fibre end has been mechanically damaged in the clamp. For these reasons, fibres are generally pulled from rods which are then left attached to the fibre ends, providing larger end-pieces for clamping. This end rod lends itself easily to both optically contacting or gluing, which would be of advantage when considering monolithic or quasi-monolithic suspensions. When considering the question of production of these fibres from a rod of fused silica, there were therefore two main options; namely hand-pulling using an oxy-hydrogen blow-torch to melt a section of the rod, or pulling fibres from the rod using an RF oven built for this purpose[25].

The first option is generally the most commonly used outside the commercial field and has the advantage of being relatively quick and easy to do. However, it was observed

[25] R. F. oven constructed by Mr. R Hutchins, Dept. of Electrical and Electronic Engineering, University of Glasgow.

that hand-pulling in this way generally led to a non-uniform variation in diameter along the fibre length (Twyford, 1994), and also a difficulty in producing a 'matched pair' of fibres for construction of a pendulum. Another aspect of this kind of pulling method was that only small sections of material at a time were heated with the blow-torch; this gave rise to the concern that thermal gradients may be set up in the fibre, ultimately leading to a form of internal stress and a lowering of the quality factor, or even mechanical weakness. In addition to the points listed, the blow-torch method would also be less suitable for use as a production method for precise ribbon fibres, which have a rectangular cross-section. The alternative to this method was to use an RF oven, photographs of which can be seen in figures (3.5) and (3.6).

The rod was passed through the centre of a carbon core and fastened top and bottom to geared motors. The oven typically operated at a frequency of around 400 kHz with a maximum power output to the coil of order 25 kW. The carbon core could be expected to heat to the required temperature within 2 minutes. High quality, reactor-grade carbon was the preferred core material as it withstood the high temperature required to melt the silica rod (~1800°C) without disintegrating or reacting with the silica. It was imperative throughout the use of the oven to maintain a flow of argon gas through the heating chamber. This measure ensured that the level of air in the chamber never reached the levels required for combustion of material inside the oven. The pulling itself was done using the geared motors above and below the rod, feeding the material into the 'hot spot' in the core from above, and pulling from below. This method also ensured that the fibre diameter was reasonably uniform and that, by keeping the motor settings the same, reasonably matched pairs of fibres could be produced. It was also thought that future development of an annealing technique using the oven could reduce the possibility of thermal stresses being present in the fibres. The oven method required to be tested however, and comparison tests made with quality factor results from hand pulled fibres to assess its suitability.

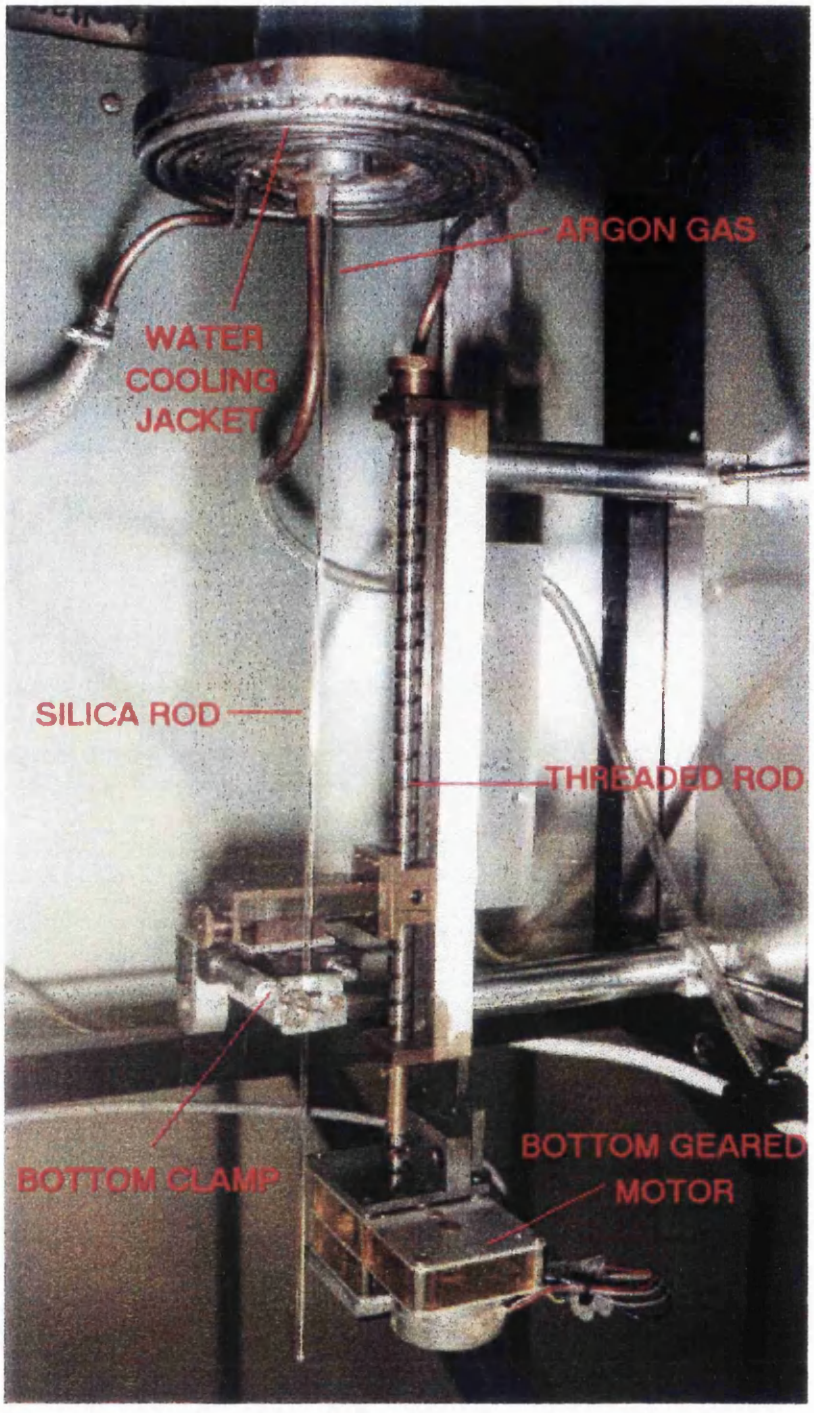

Fig(3.5): RF oven used for fibre pulling. *Glass shield, carbon furnace and RF coils removed, showing clamped rod down centre. Bottom clamp and geared motor, used for controlling fibre pulling rate, marked on diagram.*

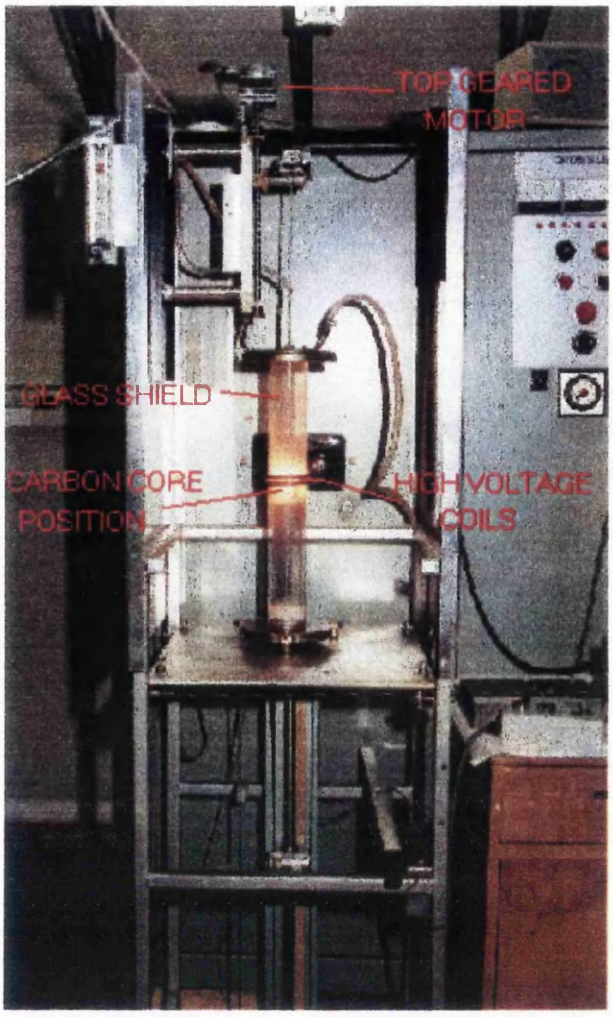

Fig(3.6): Entire RF oven, in use. *Glass shield, carbon furnace and RF coils now replaced as marked. Rod held above oven in the pre-pull position, with pull commencing when section of rod held inside the carbon core reaches the required temperature.*

3.5
Measurement of $Q(\omega_0)$.

One can define and measure the quality factor of an oscillator by considering the transient solutions of the simple harmonic motion equation with damping (this subject is fully discussed in French (French,1965)). Here the quality factor can be defined in terms

of the time taken for the stored energy of an oscillator to exponentially decay to $1/e$ of its initial value or, alternately, the decay time of the amplitude of free vibration.

Consider a weakly damped harmonic oscillator, with angular resonant frequency ω_0, undergoing free decay. The displacement,x, of the oscillator at a time t is expressed as:

$$x = A_0 \cos(\omega t + \alpha) e^{-\gamma t/2} \tag{3.30}$$

where A_0 is the maximum value of x, and α is a constant representing the initial phase of the motion. Information about the damping present in the system is contained in γ, which is given by $\gamma = \omega_0/Q$. Equation (3.30) indicates that the oscillation will undergo exponential decay with the value of subsequent maxima being determined by the exponential decay 'envelope'. This decay term allows the prediction of the amplitude value some time into the decay:

$$A(t) = A_0 e^{-\gamma t/2} \tag{3.31}$$

We can define $t = 2/\gamma$ to be the time taken for the amplitude to decay to $1/e$ of its initial value, and is also known as the amplitude 'ring-down' time (τ_A). By substitution for γ into this expression, we can define the quality factor in terms of this amplitude decay time in the following way:

$$Q = \frac{\omega_0 \tau_A}{2} \tag{3.32}$$

For the case of the oscillator energy ring down time, we have $\tau_E = 1/\gamma$ (as energy is proportional to the square of the amplitude), leading to Q defined by;

$$Q = \omega_0 \tau_E \tag{3.33}$$

In the simple harmonic system of the pendulum or freely oscillating fibre used in the following work, the quality factor is obtained by plotting the natural logarithm of

amplitude values against time. For amplitude values described by equation (3.32), this leads to a linear data plot of the form:

$$\ln A(t) = a_0 - (\gamma t/2) \tag{3.34}$$

with y- axis intercept $a_0 = \ln(A_0)$, and gradient $\gamma/2$. Evaluation of the gradient of the best fit straight line to data plotted in this way yields τ_A for the oscillator under test, yielding the value of Q.

This method was used to evaluate the pendulum quality factors of fused silica suspension fibres in Chapter 4, and the material quality factor of freely oscillating fibres which are firmly clamped at one end (Chapter 5) In the case of the freely oscillating fibre, where sensitivity to surrounding mechanical vibrations is greater than for a swinging pendulum, examination of the endpoint level of the decay curve itself allows the determination of the level of background drive present. Where present, this background level must be subtracted from the measured amplitudes before the exponential fit is attempted. Examples of these plots can be found in results sections 4.3.3 and 4.3.4, with the background removal procedure discussed in 5.3.

3.6
Initial measurements of pendulum and material quality factors of fused silica fibres.

It was intended that fused silica fibres, produced as described in the previous section, be used to suspend light glass masses. In this way, measurement could be made of the pendulum quality factor for the various fibres produced. It was also intended that tests be made to find the material quality factor of these fused silica fibres, by measuring the free decay of the fibre on its own (unloaded). This would allow the validity of equation (3.29) to be checked for fibres produced by the methods outlined in section 3.4.

Initial Q_{pend} experiments carried out in Glasgow by J.E. Logan and colleagues (Logan et al, 1995) used pairs of hand-pulled cylindrical fused silica fibres, whose ends were glued to the sides of light glass plates. Results from these initial tests gave pendulum quality

factors of around 5×10^6 and 6×10^6 for suspended masses of 70 g and 210 g respectively. The same pair of fibres were used in each test, with the mass being increased through the addition of extra plates on either side of the original. As the fibre diameter was not therefore scaled with the increase in mass, one would have expected (from equation (3.29)) that the quality factor would increase according to $Q_{pend} \propto \sqrt{m}$. It was observed that the Q_{pend} measured for the 210 g mass fell short of its predicted value of 8×10^6, believed to be due to recoil damping of the pendulum caused by insufficient rigidity of the suspension structure. This result provided the starting point for much of the work reported in Chapter 4, where the question of recoil damping and the minimisation of its limit to measurable Q_{pend} were fully addressed. Preliminary measurements were then carried out for both hand-pulled and oven-pulled fibres as a first step toward continuing the measurement of pendulum quality factor of fused silica fibres produced in Glasgow.

Measurement of material quality factor, in this case using a fused silica ribbon fibre, was also carried out by J.E. Logan (Logan, 1994(b)). This measurement gave a value of around 5×10^5 which was suspected to be recoil damped.
Again, with a system where the effect of recoil has been sufficiently reduced, it was intended to continue these material quality factor measurements for fibres produced in Glasgow. In this way, several fundamental aspects of the GEO 600 test mass suspension design could be validated before, in the future, progressing to investigation of more practical areas such as, e.g., the jointing technique to be used.

3.7
Proposed GEO600 suspension design.

The test mass suspension design for GEO600, presently in the initial stages of development, is based on the need for using materials with low intrinsic losses to achieve simultaneously high quality factors for the pendulum mode, internal modes and violin modes of the system. This process is fairly complex, owing to the fact that great care

must be taken to ensure the maintenance of these high quality factors, which are in general easily degraded through the use of construction techniques which have been typically employed in the past. The proposed GEO600 suspension system is described in Chapter 2 and is shown in Fig.(2.21).

A form of monolithic suspension has been proposed, where the fibres and mass are of the same material (Logan, 1996). Where all fused silica suspensions are used, it will also be possible to avoid the use of mechanical clamps, with optical contacting or perhaps good glue joints being preferred. Fusing the fibres directly to the mass, or welding fibres on, is not a favoured option at present due to the thermal stresses that this process would set up in a large test mass. It is generally believed that the less direct work done on the mass the better.

The use of four suspension wires[26] on the test mass allows tilt and rotation orientation control by the upper mass, which is attached to the top plate via a single loop of steel wire. Steel wire has a much poorer thermal noise performance than fused silica, but is suitable for use on the upper stage of the suspension as any excess thermal motion will be filtered through the normal mechanical action of the lower stage. Many of these design features must be tested before implementation of such a design - a requirement which will form the basis of much of the future work in this area at Glasgow.

[26] Glued or optically contacted.

Chapter 4
Experimental investigation of the pendulum quality factor of fused silica fibres.

4.1
Introduction

This chapter deals with work carried out to establish a suitable test system for measurement of the pendulum quality factor of a light, non-conducting mass suspended by fused silica fibres. The construction of a system in which the measurement of high pendulum quality would be possible was non-trivial, and presented several problems. Sections 4.1.1, and 4.2 contain discussions on the most serious problem present which tends to limit the measurement of Q_{pend}; that of recoil damping of the pendulum as it swings due to lack of rigidity in the suspension structure. It was necessary to test the level of recoil damping present prior to the suspension of the test pendulum. Section 4.2.1 contains the theoretical background on the measurement of the limit to the measurable Q set by recoil damping. The remaining sections in 4.2 are entirely devoted to these recoil measurements for both the original and final system designs.
Section 4.3 contains experimental results on the preliminary pendulum quality factor measurements carried out in this system for both hand-pulled and oven-pulled fibres. Conclusions and discussion drawn from the work covered in this chapter are outlined in section 4.4.

4.1.1
An introduction to recoil damping

Consider the restoring force of a pendulum as it swings. This will give rise to a recoil (reaction) force at the clamp point of the structure from which it is suspended. If the recoil motion of the system is large enough, and damped by some frictional effect, much of the pendulum's energy can be absorbed with a corresponding reduction in measured

Q. Consideration of the effect of recoil damping in experimental systems can be found in Martin (Martin, 1978), Quinn et al (Quinn et al, 1994) and Winterflood (Winterflood, 1994). An additional discussion on the nature this problem can be found in Saulson (Saulson, 1990). This work approximated the problem of recoil damping by considering a two stage system representing a low-loss oscillator (stage 2) suspended from a structure with low-Q resonances (stage 1), as illustrated in Fig.(4.1) below. The spring constants (denoted by k) of the connections between masses, and from the upper mass to ground, are shown in parallel with viscous damping dash-pots, represented by b'.

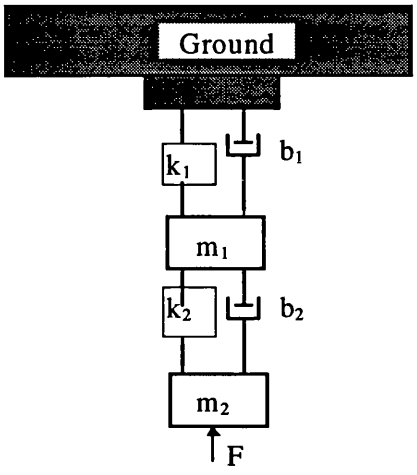

Fig(4.1): Schematic diagram of a double oscillator, where a driving force F is applied to the lower mass m_2.

The resulting expression for the limit to the measurable Q due to recoil damping was found by Saulson to be as in equation (4.1) below, where $\omega_1^2 = k_1/m_1$ and $\omega_2^2 = k_2/m_2$;

$$\frac{1}{Q_{2.recoil}} = \frac{1}{Q_{2.actual}} + \frac{1}{Q_1}\frac{m_2}{m_1}\left[\frac{\omega_1\omega_2^3}{\left(\omega_1^2 - \omega_2^2\right)^2}\right] \qquad (4.1)$$

From this equation it is clear that there are two possible methods of approach to solving the problem of recoil losses. Where the suspension structure can be modelled as a simple harmonic oscillator of known frequency and Q, it is possible to obtain the actual quality factor of the low loss oscillator using the above equation. Where the system cannot be simply modelled, another approach would be to construct the suspension structure in

such a way that the second term in this equation is minimised at the pendulum frequency which, if successful, would lead to $Q_{2.recoil} \approx Q_{2.actual}$. Looking again at equation (4.1), we can re-write the second term as below, assuming the normal working frequency of the pendulum is low compared with structural resonances.

$$\frac{1}{Q_1}\frac{m_2}{m_1}\left[\frac{\omega_1\omega_2^3}{\left(\omega_1^2-\omega_2^2\right)^2}\right]\rightarrow\phi_1\left(\frac{k_2\omega_2}{k_1\omega_1}\right) \qquad (4.2)$$

At low frequencies this term can be made negligible by a sufficiently low stiffness ratio of the pendulum and the support structure, and also by a small value of loss angle associated with the system, ϕ_1.

This method was appropriate for the system used in this work. In general the quantities k and ϕ describe the magnitude and phase of the stiffness of a system, with damping, in the form of a complex spring constant $k_{complex} = k(1 + j\phi)$. Following construction of the test system, a direct approach was taken to estimate the level of damping in the system by measuring the complex spring constant of the structure at the point of suspension at the normal pendulum frequency. These quantities were then used in the evaluation of the limit placed by recoil damping on the measurable Q for future fused silica pendulum tests This topic is examined inthe following section.

4.1.2
Initial set up to minimise recoil damping.

As has been discussed in section 4.1, it was possible to ensure that recoil motion of the experimental system was reduced by maximising k, the magnitude of the complex spring constant of the suspension structure, provided the loss angle, ϕ, remained sufficiently small. Such a system was originally attempted by Logan and colleagues where, to provide mechanically stable surroundings, consideration was given to the mountings of the vacuum tank containing the pendulum suspension. The vacuum tank was initially mounted on three phosphor-bronze hemispheres (diameter ~ 15 mm), bedded down on a

stainless steel base plate covering a large concrete block. This mounting provided a reasonable starting point for measurements, but was eventually found by Logan to lack the level of rigidity required for measurements of fused silica fibres with high pendulum Q (section 3.6).

Special attention was given to the design of the internal clamp structure and clamping device used to hold the pendulum when suspended. The pendulum was suspended from a robust 'top-hat' like structure (Fig.(4.2(a))), constructed from thick aluminium plates. This in turn was mounted on four vertical aluminium posts (diameter 5 cm) wedged inside the tank (not shown), forming a stable platform through the centre of which the pendulum was suspended. To increase rigidity all joints were bonded together using [27]Torr-Seal and also bolted. Small 'jaws' in a piece of aluminium plate, firmly held the end rod sections of the suspension fibres in tightly fitting cleared holes (Fig. (4.2(b)).

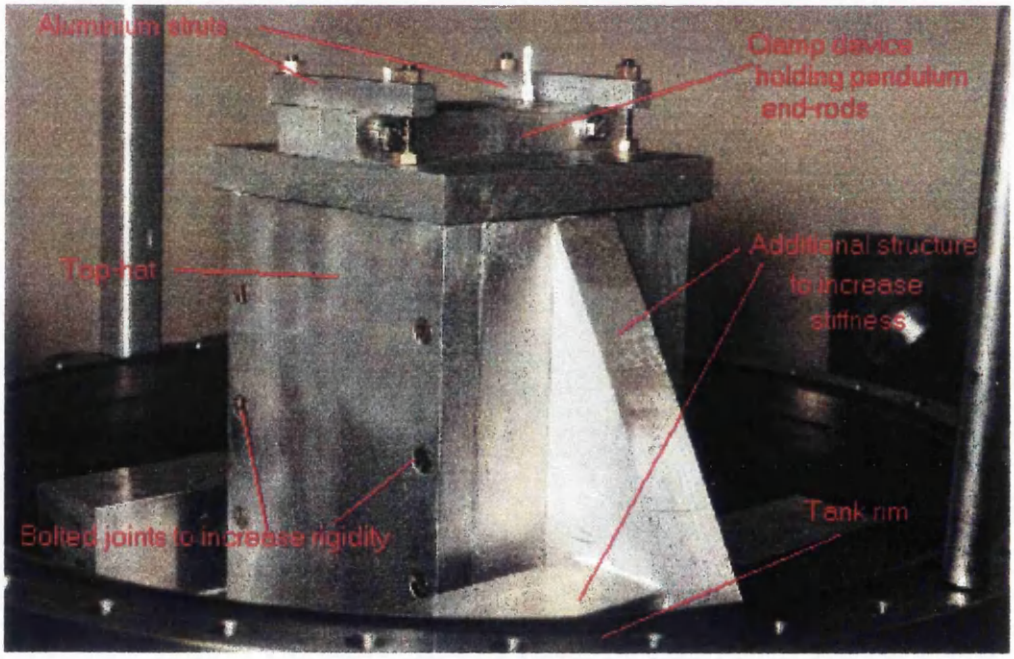

Fig.(4.2(a)): Photograph of 'top-hat' clamp structure, used for the suspension of light glass masses. *Pendulum under test is suspended from top clamp device (Fig.(4.2(b)), and hangs down through centre of top-hat.*

[27] Torr-Seal is a low pressure resin, produced by Varian for use as a bonding agent in high vacuum systems.

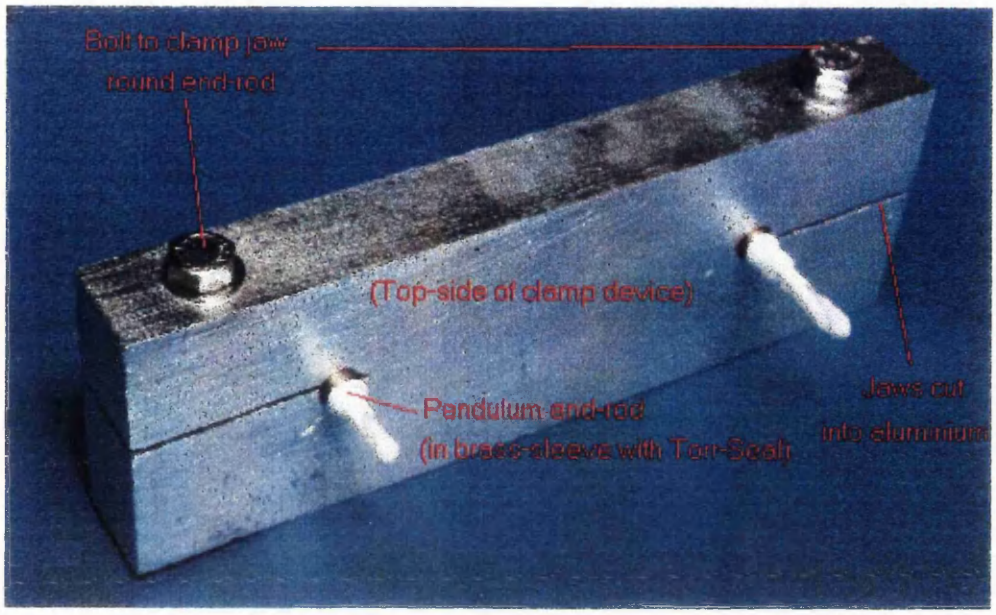

Fig(4.2(b)): Photograph of clamp-structure for pendulum suspension. *Top side facing. Fused-silica fibres exit clamp from other side.*

This was further tightened by bolting shut the small 'jaws' cut from the holes to the edges of the plate. Once in position above the top-hat this clamp was then strapped firmly down by aluminium struts bolted firmly down on the top hat.

As it was believed that measurements of Q_{pend} (3.7), carried out on this system, were possibly being limited by recoil, it was necessary to test the recoil characteristics of this system, as will now be discussed.

4.2
The Measurement of the Recoil Limit to Pendulum Q

4.2.1
A theoretical discussion.

In this section an expression will be developed to define the limit to the measurable pendulum Q in terms of the stiffness characteristics of the test system at the point of

suspension. Recall the definition of quality factor, Q, given in Chapter 2 and stated below;

$$Q_{limit} = 2\pi \left[\frac{Energy\ stored\ by\ pendulum}{Energy\ lost\ per\ cycle\ into\ support\ structure} \right] \qquad (4.3)$$

It is our intention to derive suitable expressions for both the energy lost per cycle and the stored energy by considering the power dissipated into the suspension point and the maximum kinetic energy of the pendulum mass,m, respectively (Fig.(4.3)).

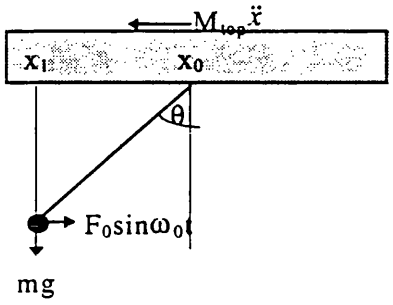

Fig(4.3): Simple diagram describing the simple pendulum system.

The support structure is modelled as a simple harmonic oscillator, characterised by stiffness, k, mass, M_{top}, and mechanical resistance, b. This oscillator is driven by the restoring force, $F = F_0 \sin\omega_0 t$, of the pendulum swinging below. This force can be represented by the projection on the imaginary axis of a rotating vector $F = \left(F_0 e^{j\omega t}\right)$, the general complex form of a sinusoidal driving force. Hence, the equation of motion of the structure can be written as;

$$F_0 e^{j\omega t} = M_{top}\ddot{x} + b\dot{x} + kx = -M_{top}\omega^2 x + jb\omega x + kx \qquad (4.4)$$

Solving for recoil displacement, x, gives;

$$x = \frac{F_0 e^{j\omega t}}{\left(-M_{top}\omega^2 + j\omega b + k\right)} = \frac{F_0 e^{j(\omega t - \phi)}}{\left[\left(k - M_{top}\omega^2\right)^2 + \omega^2 b^2\right]^{1/2}} \tag{4.5}$$

where ϕ, which can be determined experimentally, represents the difference in phase between the recoil displacement and the drive force due to the damping term 'b.' Differentiation of this yields the recoil velocity, 'v':

$$v = \frac{j\omega F_0 e^{j(\omega t - \phi)}}{\left[\left(k - M_{top}\omega^2\right)^2 + \omega^2 b^2\right]^{1/2}} = \frac{j\omega F_0\left[cos(\omega t - \phi) + j\,sin(\omega t - \phi)\right]}{\left[\left(k - M_{top}\omega^2\right)^2 + \omega^2 b^2\right]^{1/2}} \tag{4.6}$$

Recalling that the drive force was in fact a sine wave, only the imaginary part of this expression is of interest to us i.e.:

$$v = \frac{\omega F_0\left(cos(\omega t - \phi)\right)}{\sqrt{\left(k - M_{top}\omega^2\right)^2 + \omega^2 b^2}} \tag{4.7}$$

A typical test pendulum has an angular frequency $\omega_0 = 2\pi\,(1Hz)$. Therefore, by considering the low frequency behaviour of equation (4.7) (i.e. where $\omega \rightarrow \omega_0$ is much smaller than $\sqrt{k/M_{top}}$), the expression for recoil velocity can be simplified to equation (4.8) below, provided the mechanical resistance, b, is small;

$$v = \frac{\omega_0 F_0\left(cos(\omega t - \phi)\right)}{k} \tag{4.8}$$

We shall now use equation (4.8) to find the average dissipated power, given by $P_{ave} = \overline{(F.v)}$, giving;

$$P_{ave} = \frac{\overline{F_0^2 \omega_0\ [\,sin(\omega_0 t\ ).cos(\omega_0 t - \phi\ )]}}{k} \tag{4.9}$$

Whereupon further reduction yields the result that (for small ϕ);

$$P_{ave} = \frac{F_0^2 \omega_0 \phi}{2k} \tag{4.10}$$

Using the equation $E_{lost/cycle} = P_{ave}\left(\frac{2\pi}{\omega_0}\right)$, this expression can be used to obtain the following result (where $F_0 \approx mg\theta_{max}$);

$$E_{lost/cycle} = \frac{F_0^2 \pi \phi}{k} = \frac{m^2 g^2 \theta_{max}^2 \pi \phi}{k}. \tag{4.11}$$

Keeping this result in mind, we shall now look at the stored energy, E_{stored}, of the pendulum. This can be obtained by considering the maximum kinetic energy displayed by the pendulum mass during its motion. This will occur at the lowest point of the pendulum swing, at $\theta = 0\ rads$, where the velocity is a maximum. The stored energy is therefore expressed as;

$$\begin{aligned} E_{stored} &= \frac{1}{2} m\omega_0^2 x_{max}^2 \\ &= \frac{1}{2} m\omega_0^2 l^2 \theta_{max}^2 \end{aligned} \tag{4.12}$$

The limit to the measurable pendulum quality factor, as set by recoil damping in the system, can be found using equations (4.3), (4.11) and (4.12) to be:

$$Q_{limit} = \frac{1}{m\omega_0^2} \frac{k}{\phi}. \tag{4.13}$$

a result which is in agreement with equation (4.2). Examination of equation (4.13) shows that, for a given pendulum mass m and resonant frequency ω_0, the damping effect of recoil motion in the system can be reduced by maximising the stiffness, k, while ensuring the phase angle ϕ remains small.

An interesting point to note is the form of the complex spring constant of such a system. From equation (4.4) one can see that, by Hooke's Law;

$$k_{complex} = \frac{F}{x} = \left(k - m\omega^2\right) + j\omega b = \mathrm{K}e^{j\phi} \qquad (4.14)$$

Where $tan\phi \approx \frac{\omega b}{k}$ at low frequencies. The magnitude of the spring constant is $\mathrm{K} = \sqrt{\left(k - m\omega^2\right)^2 + \left(\omega b\right)^2}$ which, at low frequencies, tends to the value of k itself. Thus a low-frequency measurement of the stiffness magnitude, K, can be used directly for k in equation (4.13).

4.2.2
Overview of experimental principles behind measurement of recoil limit to Q.

As shown in section 4.2.1 evaluation of the recoil-limit to the measurable Q will require the evaluation of the stiffness of the suspension structure, k (Nm^{-1}), and the recoil phase lag between the applied force and the recoil displacement, ϕ (rads). To do this, a known sinusoidal force was applied at the point of suspension giving rise to a sinusoidal recoil displacement, and associated acceleration.

The magnitude of the stiffness of the structure was found from the ratio of this force to the resulting recoil displacement (as deduced from the measured magnitude of the recoil acceleration, using the relation $\ddot{X} = -\omega^2 X$), with the phase being measured directly.

One of the most important pieces of equipment used for these measurements was a lock-in analyser. This instrument can measure both the magnitude and phase of a small signal in the presence of a high level of background noise by comparing the phase of the signal being measured to that of a reference wave-form. For the purpose of our measurements, the 'signal' input was the recoil acceleration at the point of suspension, measured using an inverted pendulum accelerometer. This was compared in phase to a 'reference' input representing the applied force. The resulting Bode magnitude and phase outputs from the lock-in corresponded to the magnitude of the recoil acceleration, $\ddot{X}$, and the relative phase between this and the applied force. As acceleration and displacement are $180°$

out of phase, this phase measurement gave the magnitude of ϕ. The magnitude of the stiffness of the structure, at angular frequency ω, was found using Hooke's Law, where;

$$K = \frac{F}{X} = \frac{F\omega^2}{\ddot{X}}. \tag{4.15}$$

Note that the use of capitals here denotes the magnitude of the quantity. In this way, the quantities k and ϕ were found.

A diagram of the inverted pendulum feedback accelerometer can be seen in Fig.(4.4). Constructed from a small steel mass held vertically by two steel strips (approximately 10 cm $\times$ 5 cm), it was a reasonably compact instrument for measurement on the structure. It was also sensitive to low frequency signals (below around 10 Hz) and, due to the feedback nature of the instrument, was not expected to add a significant phase shift of its own to the measurements.

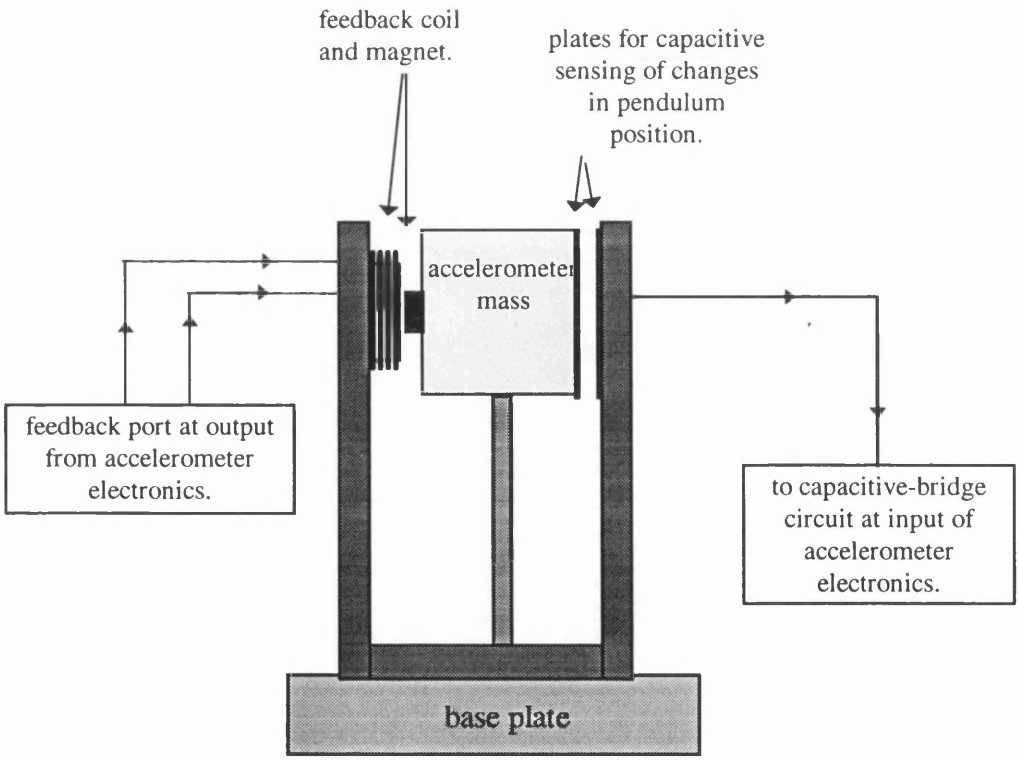

Fig(4.4) Main features of the inverted pendulum accelerometer.

The principles of operation of the pendulum accelerometer are as follows. A mass, mounted as some kind of pendulum whose point of suspension is rigidly attached to

earth, is used to monitor ground movement by measuring the relative displacement (x_r) of the mass and ground. The magnitude of this relative displacement is proportional to the ground acceleration ($\ddot{x}_g$) at frequencies up to the resonant angular frequency (ω_0) of the accelerometer. For the simple pendulum accelerometer the transfer function (open loop gain) of x_r to $\ddot{x}_g$ is of the form;

$$G = \frac{x_r}{\ddot{x}_g} = \frac{1}{s^2 + \frac{\omega_0}{Q_0} s + \omega_0^2} \tag{4.16}$$

where $s = j\omega$, and the natural quality factor measured on resonance is Q_0.

If a feedback circuit is included, the relative displacement signal is amplified, filtered, and sent back as a feedback force to the mass. A simple block diagram of such a system is shown in Fig.(4.5(a)), with the feedback route shown in bold. This diagram can be compared with that corresponding to the inverted pendulum accelerometer used in the experiment (Fig.(4.5(b)).

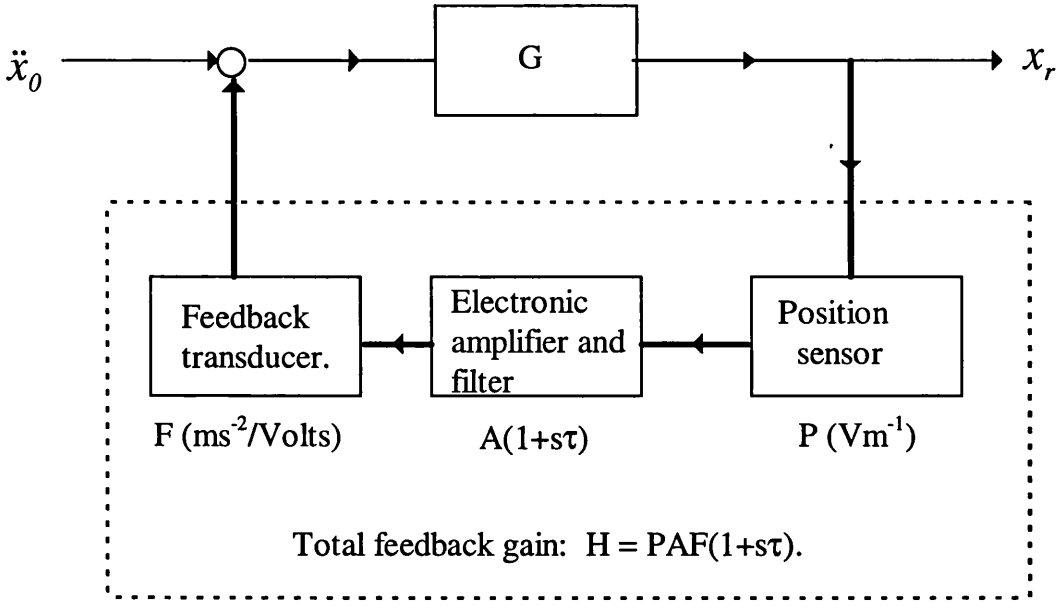

Fig.(4.5)(a): Block diagram outlining principle elements in a feedback system suitable for a pendulum accelerometer.

The gain of the accelerometer with feedback is $H = PAF(1+s\tau) = H_0(1+s\tau)$, where H is large and positive. The transfer function (closed loop) of the complete system with feedback is given by equation (4.17) below, where the subscript f indicates that the feedback loop is in operation.

$$\left.\frac{x_r}{\ddot{x}_g}\right|_f = \frac{G}{1+GH} = \frac{1}{s^2 + \frac{\omega_0}{Q_0}s + \omega_0^2 + H_0(1+s\tau)} \tag{4.17}$$

Rearranging this expression, and comparing with equation (4.16) yields equation (4.18) below:

$$\left.\frac{x_r}{\ddot{x}_g}\right|_f = \frac{1}{s^2 + s\left[\frac{\omega_0}{Q_0} + H_0\tau\right] + \left(\omega_0^2 + H_0\right)}$$

$$= \frac{1}{s^2 + s\left[\frac{\omega_f}{Q_f}\right] + \omega_f^2} \tag{4.18}$$

The inclusion of negative feedback to the system has two primary advantages. The resonant angular frequency of the pendulum is raised to a value, ω_f, given by $\omega_f^2 = \omega_0^2 + H_0$, thus increasing the bandwidth in which relative displacement is proportional to ground acceleration. Use of suitable filtering in the feedback electronics can damp the mechanical resonance of the pendulum, thus improving the dynamic range of the instrument.

It is useful to note also that the transfer function of feedback acceleration ($\ddot{x}_f$) to ground acceleration is $\frac{\ddot{x}_f}{\ddot{x}_g} = \frac{GH}{1+GH} \rightarrow 1$ where $GH >> 1$. Hence a direct measurement of ground acceleration can be made from the feedback acceleration signal over a frequency range $0 < \omega < \omega_f$.

For this experiment, recoil acceleration of the structure ($\ddot{x}$) took the place of ground acceleration ($\ddot{x}_g$) in the discussion above. It was intended that the feedback acceleration signal be used as the signal input for the lock-in. However, this signal could not be taken directly from the feedback point, as this output port had a floating earth. Instead, the signal was taken from a port directly before this, which was separated from the feedback output only by a unity gain buffer amplifier (Fig.(4.5(b))).

The possibility of unwanted phase shifts from this and other features of the experimental arrangement were investigated. These preliminary experiments are discussed in the following section 4.2.3.

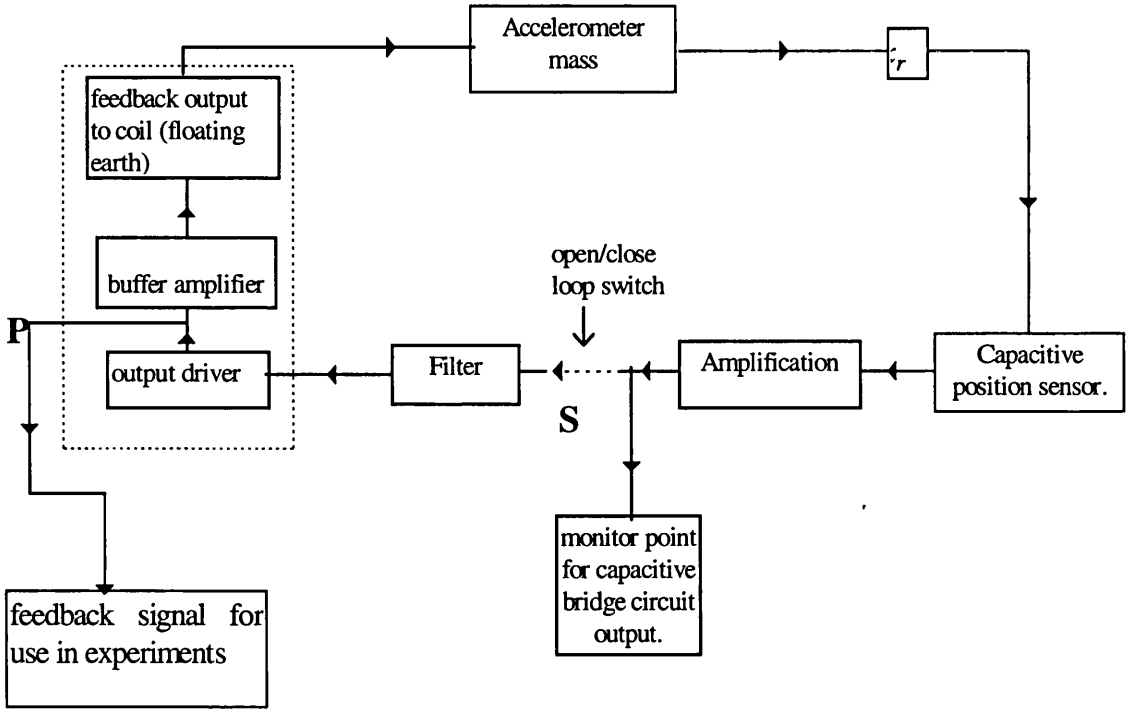

Fig.(4.5(b)): Simple block diagram of inverted pendulum accelerometer feedback system. *Of particular importance to note are the positions of the filter circuit (discussed in section 4.2.3) and the position of the feedback monitor point (marked 'P' on the above diagram) used to send the feedback acceleration signal to the lock-in analyser.*

4.2.3
Initial experiments prior to recoil damping evaluation

Calibration of the feedback accelerometer and assessment of sources of systematic phase shift in the experiment were carried out prior to the evaluation of system recoil characteristics. Evaluation of these phase shifts were carried out at the working angular frequency of the pendulum ($\omega_0 = 2\pi(1\text{Hz})$ rads^{-1}).

- Calibration of the feedback accelerometer

This was determined by measuring the output voltage of the accelerometer as a function of angular tilt about the vertical. As it was important to check that the calibration of the accelerometer was linear over a reasonable range of angles and independent of its gain, the measurement was performed for a range of small angular changes for a variety of gain settings. The calibration value was found to be 68 V / ms^{-2}

- Sources of additional systematic phase shift and their evaluation.

The identification of sources of systematic phase shift in the experiment was of great consequence to the accuracy with which any measurement of recoil phase could be carried out, as the phase lag angle was expected to be very small (perhaps only of the order of 0.5°). Ground termination of the chart recorder inputs, preceding any phase measurements, gave a ground line plot (in volts) corresponding to a phase difference of 0°. All phase measurements from the lock-in were made by plotting the voltage representing the phase output on the chart recorder with respect to this zero phase. Included in this plotted phase output were contributions from various sources of additional phase shift. These came in through either the reference or the signal route alone to the lock-in, thus preventing cancellation during the measurement. Evaluation of these additional shifts in phase was an important area of work, allowing eventual subtraction of these values from the overall phase measurement.

The following sources of phase shift were identified and are illustrated in Fig.(4.6) below.

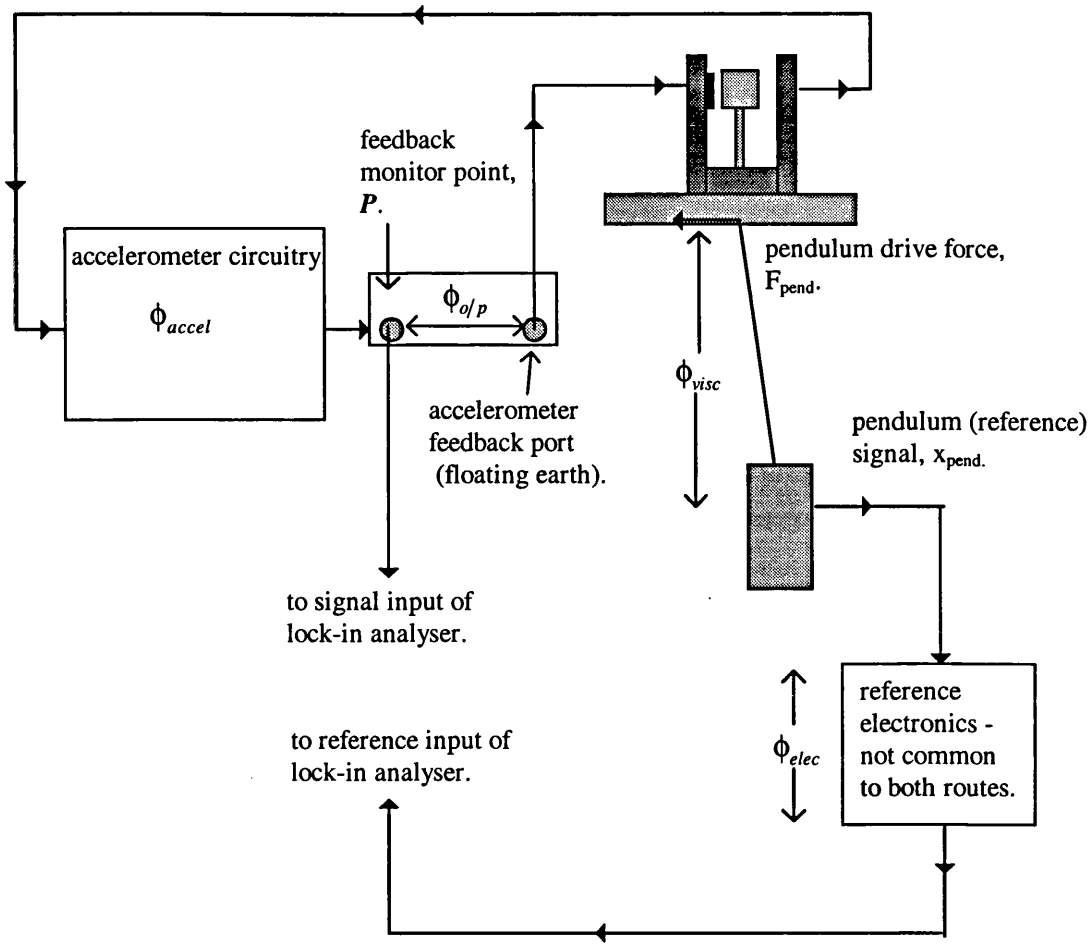

Fig.(4.6): Sources of additional phase shift likely to affect measurement of recoil phase lag.

1) Phase shift, ϕ_{elec}, due to the presence of peripheral electronic circuitry not present in both input routes to the lock-in.
2) Measurement of recoil phase lag, carried out in air, assumed that the shadow sensed displacement of the pendulum mass (used as the lock-in reference input) was in phase with the drive force, provided by the horizontal component of tension in the wire. However, an additional phase shift, ϕ_{visc} would exist between these two quantities due to viscous damping of the pendulum mass(and possibly the suspension fibres).
3) Phase shift existing between the floating earth output to the accelerometer feedback coil and the actual measurement output port immediately before it. This phase shift is referred to as $\phi_{o/p}$.

4) Additional phase shift ϕ_{accel}, due to a phase lead filter (Fig(4.5(b)) included in the accelerometer electronics.

Evaluation procedures:

1) Most sources of ϕ_{elec} can be taken into account during the course of the phase measurement. Once recordings of the zero phase line and lock-in phase output are completed, the additional contribution from electronic phase lag (only) can be found. This is achieved by disconnecting the accelerometer and sending the reference signal through both the reference and signal channels to the lock-in. As the two wave-forms are identical (and therefore in phase) the resulting plot should lie along the zero phase (ground) line. Any deviation from this line indicates that the lock-in is measuring the phase shift introduced by peripheral electronics; this value of ϕ_{elec} can then be measured with respect to the zero phase line and taken into account by subtraction from the measured phase. Note that all chart recordings (plotted in mV) representing the output of the lock-in analyser were calibrated by the manufacturer such that 10mV corresponded to 1°. Fig.(4.7(a,b)) below shows the arrangements for both (a) the actual phase measurement and (b) the electronic phase lag evaluation outlined here. This technique was vital to the accuracy of any phase measurement made with the lock-in and indeed formed a standard part of all measurements.

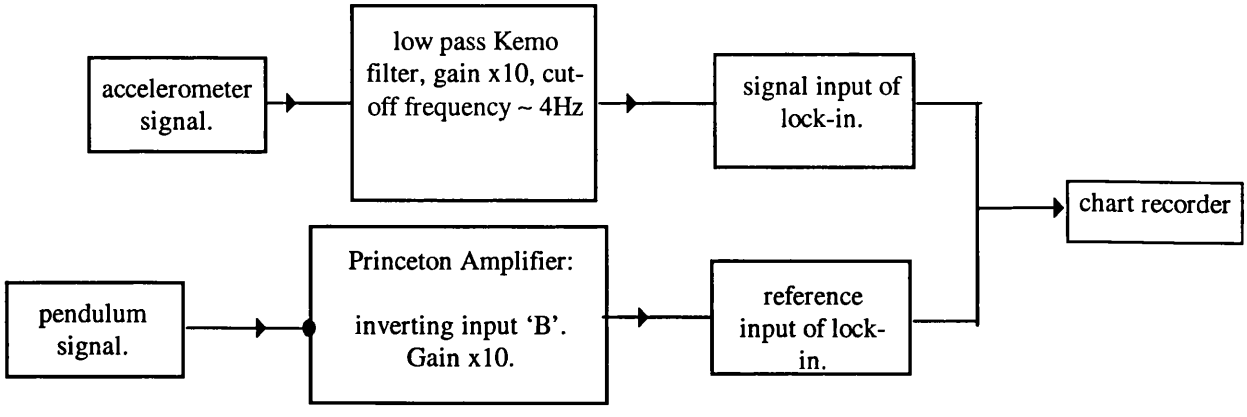

Fig.(4.7a): Block diagram of a typical measurement of the phase lag between the accelerometer signal and the pendulum reference signal.

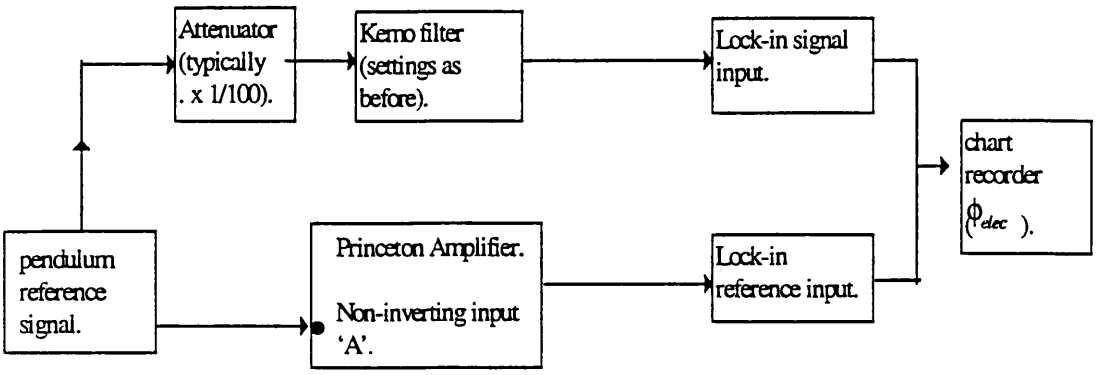

Fig.(4.7b): Block diagram showing corresponding set-up for measurement of ϕ_{elec}, *i.e. the phase lag between the reference and signal routes to lock-in due to non-identical electronic arrangements.*

However, this method only included those electronics present after the point where the reference was split for input to the reference and signal lock-in inputs. It was necessary to evaluate the additional phase shifts present due to the output resistance of electronic equipment not included in the above measurement (e.g. accelerometer and photodiode) with the stray capacity of BNC cables leading to the lock-in. This phase shift, resulting from the RC time constant of electronic equipment and cabling, is denoted by ϕ_{rc}. The phase lag incurred by the accelerometer output resistance in this way, calculated to be of order -10^{-5°, was in fact negligible. For initial measurements the phase shift due to the photodiode circuitry had a value of -0.395°, and was later modified, by reducing the photodiode output resistance, to give a phase shift of -10^{-5°.

2) It can be shown that the additional phase lag incurred between the horizontal component of tension in the wire, T_h, and the displacement of the mass, x_1, can be defined by;

$$tan\phi_{visc} = -\frac{1}{Q}. \qquad (4.19)$$

where Q is the quality factor of the pendulum.

This expression can be found by considering the motion of the damped pendulum, of length l, as it swings in air with angular frequency ω as shown below;

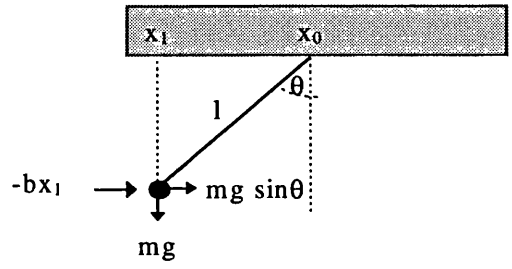

Fig.(4.8): Simple pendulum subject to viscous damping.

Ignoring wire restoring forces, the equation of motion of the pendulum is;

$$m\ddot{x}_1 \approx -mg\left(\frac{x_1 - x_0}{l}\right) - b\dot{x}_1 \tag{4.20}$$

whereupon division by m, and use of the standard notation $\omega_0^2 = \frac{g}{l}$ and $\gamma = \frac{b}{m} = \frac{\omega_0}{Q}$, gives the expression:

$$\ddot{x}_1 = -\omega_0^2(x_1 - x_0) - \gamma\,\dot{x}_1 \tag{4.21}$$

We wish to isolate the terms $(x_1 - x_0)$ and x_1 which contain phase information on the horizontal restoring force and the displacement of the mass respectively. Solution of (4.21) to obtain the transfer function $\frac{x_1 - x_0}{x_0}$ yields the result that;

$$\frac{x_1 - x_0}{x_1} = \frac{\omega_0^2 - j\omega_0\gamma}{\omega_0^2} \tag{4.22}$$

Hence the phase angle ϕ_{visc}, existing between $(x_1 - x_0)$ and x_1, can be expressed as $tan\phi = -\frac{\gamma}{\omega_0} = -\frac{1}{Q}$. Values of this quantity varied between measurements as different

recoil test pendulums were used each time the structure was stiffened. Therefore, individual results are attached to the relevant experiment throughout the remainder of this chapter. It should be noted that the values obtained were very small in both cases.

3) A bench-top experiment was set up to evaluate $\phi_{o/p}$, the phase lag between the measurement output port (**P**) and the feedback output, as shown in figures (4.5(b)) and (4.9(a)).

The feedback voltage signal at the accelerometer feedback coil was sent to the signal input of the lock-in analyser (using the floating earth facility on this input). It was not possible to utilise this facility during actual phase measurements as mains-earthed equipment (such as oscilloscopes) were connected in parallel with the lock-in input. With the feedback loop and the capacitive sensor circuitry disconnected, a 1Hz signal was injected into point **P** in Fig.(4.9(a)). The lock-in measured the difference in phase between the signal at the feedback port and the reference signal from the measurement port. Inversion of the reference signal, using the inverting input of a Princeton 113 amplifier, corrected for the effect of the buffer amplifier between the two ports. This assumed that the Princeton had no additional phase shift of its own, other than the 180° inversion, a reasonable assumption as Princeton amplifiers are designed with such a characteristic. The phase difference between the two outputs was plotted.

The electronic phase shift associated with this measurement was measured and subtracted from this plot; the resulting recordings are shown in Fig.(4.9(b)). Recall that resulting measurements made in mV may be converted to a phase shift (°) through use of the calibration 10 mV to 1°.

The final evaluation of phase shift between the measurement and feedback outputs was:

$$\phi_{o/p} = +0.2° \pm 0.05° \qquad (4.23)$$

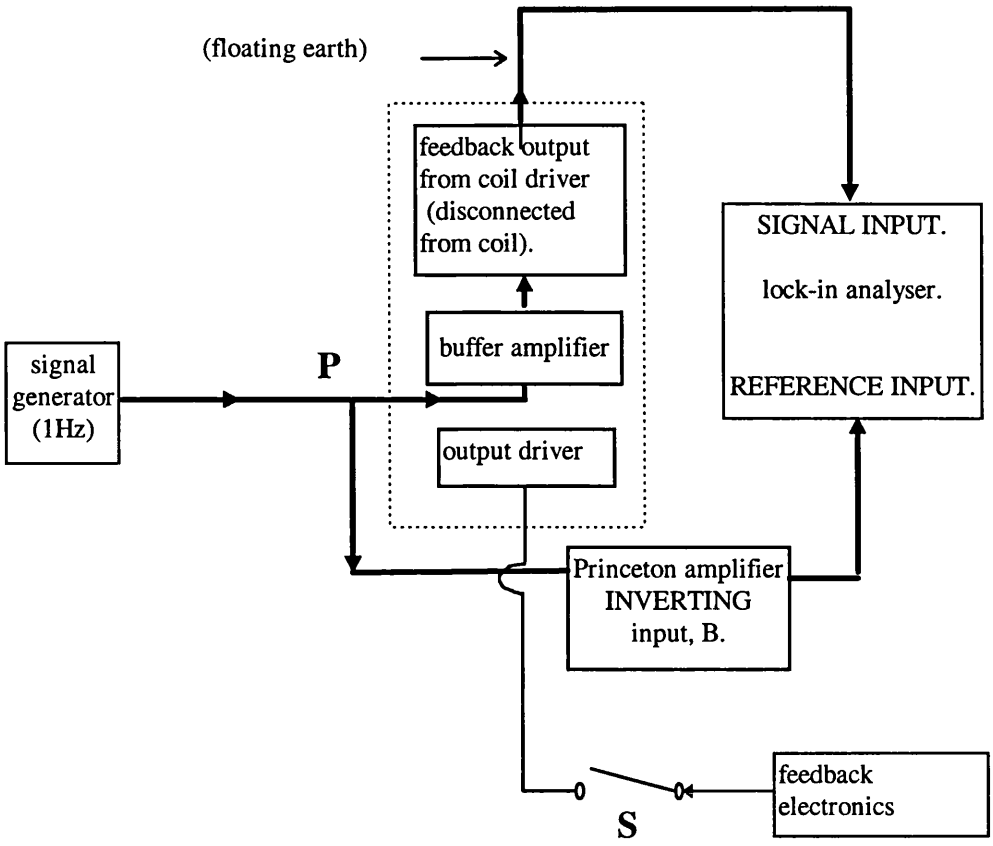

*Fig.(4.9(a)): **Experimental arrangement for measurement of phase lag between measurement port, P, and signal from feedback output to coil.** Bold lines indicate route used during measurement.*

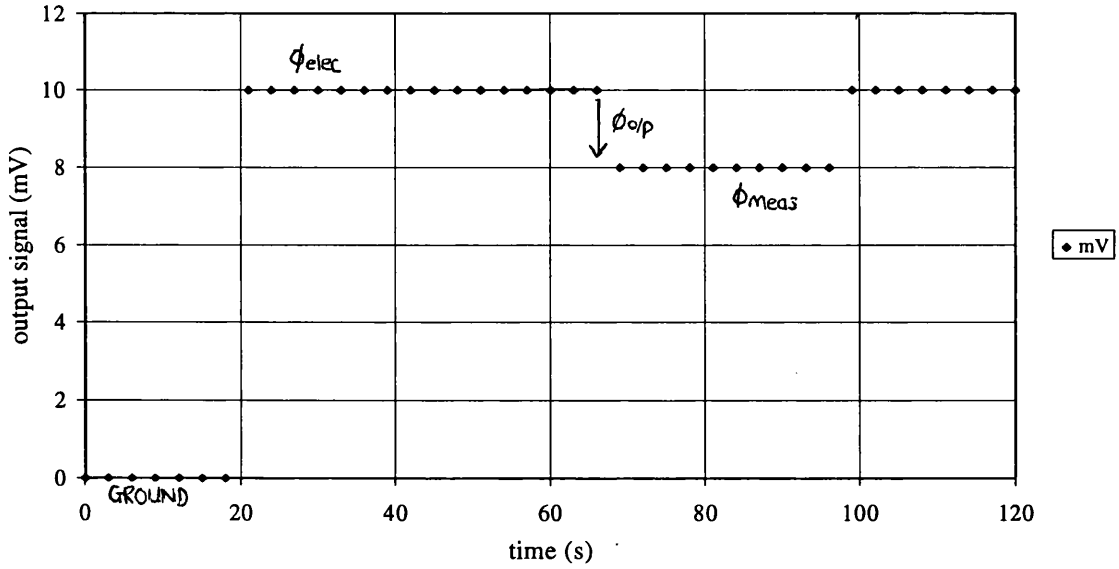

*Fig(4.9(b)): **Section of experimental trace for evaluation of $\phi_{o/p}$, indicating measurement of measured phase shift, ϕ_{meas} and electronic phase shift ϕ_{elec}.***

4) The final additional phase shift common to all measurements was ϕ_{accel}, expected to arise due to the electronic damping discussed earlier. The phase shift at 1 Hz due to this source was evaluated from the Bode phase plot associated with the overall transfer function of the accelerometer. The damping was provided by a high pass filter, the circuitry of which is shown in Fig.(4.10) below.

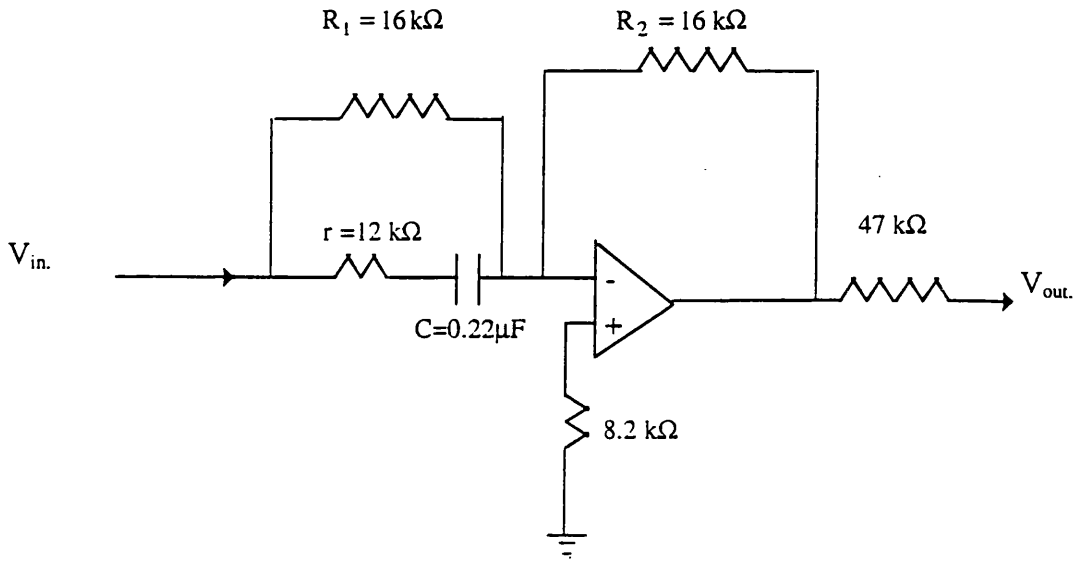

Fig.(4.10): Circuit diagram of phase lead filter in accelerometer circuitry.

The transfer function of this high pass filter was $\frac{V_0}{V_i} = -\frac{R_2}{R_1}\left(\frac{1+s\tau}{1+scr}\right)$, where $\tau = (R_1 + r)c$. This gives an expression for overall gain of the accelerometer of the form $H = H_0 \frac{R_2}{R_1}\left(\frac{1+s\tau}{1+scr}\right)$. Recalling the discussion in 4.2.2, the transfer function of feedback to recoil acceleration is of the form $\left.\frac{\ddot{x}_f}{\ddot{x}}\right|_f = \frac{GH}{1+GH}$. After substitution for G (equation (4.17)) and our expression for H above, this can be written:

$$\left.\frac{\ddot{x}_F}{\ddot{x}_0}\right|_f = \left(\frac{H_0\left(\frac{R_2}{R_1}\left[\frac{s\tau+1}{scr+1}\right]\right)}{s^2+\frac{\omega_0}{Q_0}s+\omega_0^2+H_0\left(\frac{R_2}{R_1}\left[\frac{s\tau+1}{scr+1}\right]\right)} \right)$$

$$= \frac{s\left(H_0\tau\, R_2/R_1\right)+\left(H_0\, R_2/R_1\right)}{s^3(rc)+s^2\left(1+\frac{\omega_0}{Q_0}\,rc\right)+s\left(\frac{\omega_0}{Q_0}+\omega_0^2 rc+H_0\tau\, R_2/R_1\right)+\left(\omega_0^2+H_0\, R_2/R_1\right)} \qquad (4.24)$$

Evaluation of the Bode phase associated with this transfer function was carried out using the BODE function in the Matlab 'Control Systems Toolbox'. Prior to this the coefficients of s, involving the parameters ω_f, ω_0, H_0 and Q_0 were evaluated experimentally. Values of circuit components were known (Fig.(4.10)). The accelerometer had a variable gain potentiometer ranging from 0 to 9 turns, with recoil measurements being made at an intermediate setting (~4 turns). Lower gain settings would decrease ω_f, thus increasing the phase shift at 1 Hz. In addition to the evaluation of ϕ_{accel} at 4 turns, these measurements were also made for the 'worst case' of ¾ turn.

- Evaluation of ω_f

Reference should be made to the diagram in Fig.(4.11) below showing the experimental set-up. The accelerometer was placed above a shaker table, driven by the internal white noise signal source of a Hewlett Packard dynamic spectrum analyser.

With the feedback loop switched on, the power spectrum of the accelerometer response (¾ turn) was recorded while in the frequency range 1 Hz to 100 Hz, clearly showing two peaks. The first peak (at 2.3 Hz) was found to be the resonant frequency of the shaker table under the accelerometer load. The second peak, corresponding to the resonance with feedback, lay at a value of $\omega_F = 2\pi(1059)$ rads^{-1} . (It was also found that the quality factor with feedback was Q_F = 5.06).

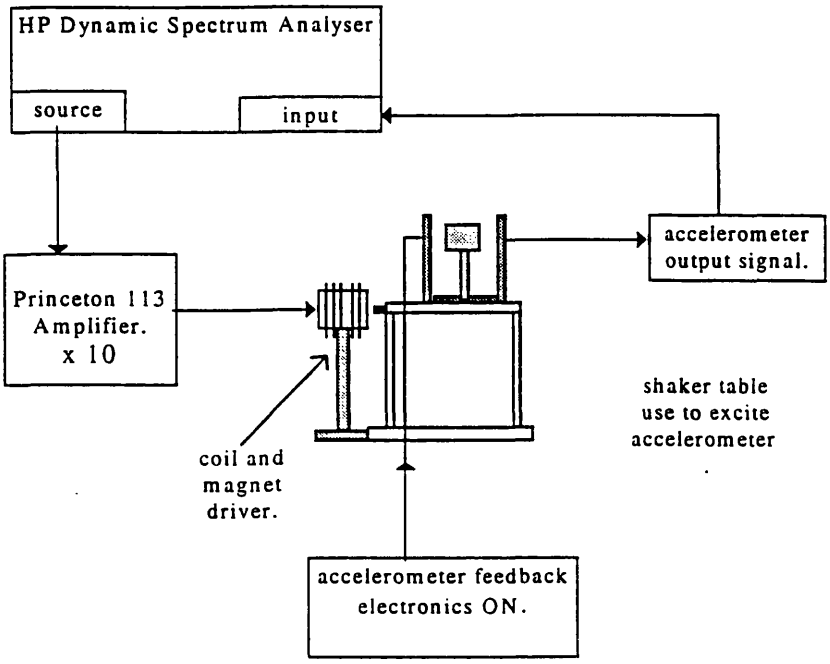

Fig.(4.11): Experimental set-up for measurement of pendulum accelerometer resonant frequency (ω_f) with feedback loop switched on. *Accelerometer mounted on a table supported by steel flexure strips, allowing a white noise drive to be applied at the base of the accelerometer. This originated from the spectrum analyser, and was applied to the table via a coil and magnet drive mechanism.*

- Evaluation of ω_0 and Q_0

The experimental set-up for these measurements is shown in Fig.(4.12). The feedback loop was switched off throughout the experiment to allow the natural frequency and Q to be measured. The accelerometer was lightly tapped and allowed to ring down naturally. The motion of the mass gave rise to a decaying sinusoidal signal induced in the feedback coil and magnet, which was plotted on the chart recorder. Wavelength and ring-down time information evaluated from this chart showed that $\omega_0 = 2\pi(2.5)\ \text{rads}^{-1}$, and $Q_0 = 52$.

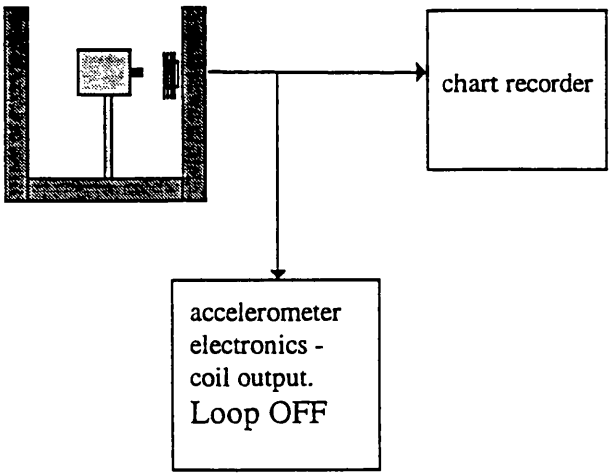

*Fig.(4.12): **Experimental arrangement for measurement of pendulum accelerometer characteristics without feedback.** Feedback loop switched off. Signal induced in (unused) feedback coil plotted on chart recorder, showing accelerometer ring-down.*

- Evaluation of H_0.

Using the relation $\omega_f^2 = \omega_0^2 + H_0$, the values of ω_0 and ω_F gave the value $H_0 = 4190\ \text{rad}^2\text{s}^{-2}$. Inspection of the MATLAB Bode phase plots of the accelerometer (¾ turn) in the region around 1 Hz showed the additional phase lag at this frequency to be very small, with a value of +0.12°, even in this worst case. The coefficients were re-evaluated again for a gain setting of 4 turns

Final results of additional phaseshift incurred by accelerometer phase lead filter:

$$\begin{aligned} \text{¾ turn: } & \phi_{accel} = +0.12^\circ \\ \text{4 turns: } & \phi_{accel} = +0.025^\circ \end{aligned} \qquad (4.25)$$

4.2.4
Measurement of recoil limited Q for original system design.

The experimental set-up for the evaluation of the recoil limited pendulum Q for the original system is shown in Fig.(4.13). The main intention behind the work recounted in this section was to establish, as a starting point, the degree of rigidity against recoil

motion afforded by the system in its original condition, and further to determine the value of the limit this would place on the highest pendulum Q measurable in the system.

- Evaluation of the stiffness, k, of the system.

The measurement technique employed for these initial tests used a loaded spring balance to provide the applied sinusoidal force. Using this method, the following experimental studies provided a valuable preliminary insight into the recoil behaviour of the original system.

1) investigation of internal recoil motion, existing through flexing of the joint between the tank shell and the internal clamp structure.
2) qualitative investigation of the recoil motion of the whole system.
3) evaluation of the stiffness, k, of the system.

In the first case the force was applied between the tank wall and the clamp structure, with motion being measured using two small piezo-electric accelerometers. These were mounted on the rim of the tank and the clamp, measuring the horizontal components of the acceleration of the tank and the clamp structure respectively. Any flexing of the joint would result in a difference between the signals read by the accelerometers. The signals were compared using a Hewlett-Packard spectrum analyser (HP-DSA 35665A) in transfer function mode. No significant relative motion was recorded, thus indicating internal motion in the structure was at a negligible level.

In the case of the actual stiffness of the structure, the inverted pendulum accelerometer was placed directly above the internal clamp structure to measure the magnitude of the recoil acceleration due to the applied force. This measurement was made using the analogue lock-in analyser (E.G.&G Princeton, model 5204), with the phase output sent directly to an oscilloscope. It was found that for an applied force of $2.8\,\mathrm{N_{rms}}$ the structure moved with a recoil acceleration of $1.1\times10^{-3}\,\mathrm{ms^{-2}}$. From this (section 4.2.2), the magnitude of the stiffness of the recoil structure was found to be

- $$k=(4.0\pm0.5)\times10^{5}\,\mathrm{Nm^{-1}} \qquad (4.26)$$

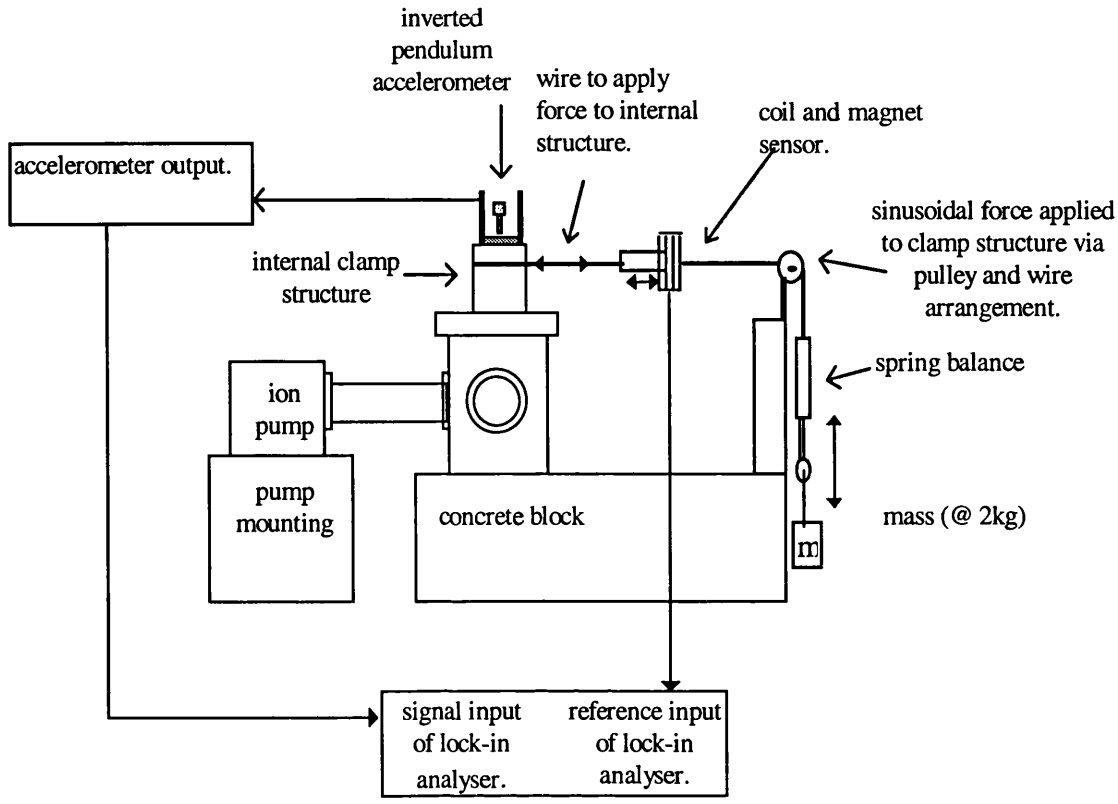

Fig.(4.13): Experimental arrangement for evaluation of original tank stiffness.

- Evaluation of recoil phase lag, ϕ.

Due to the poor quality factor and resulting phase shift between the movement of the mass on the spring-balance and the force applied to the structure, the pulley method was not suitable to provide the force for measurement of phase. Instead, a small lead pendulum of mass 1.2 kg, and dimensions 10 cm × 5 cm × 2.5 cm, was suspended in the tank in an identical way to that intended for the actual silica fibre Q measurements described later. A reasonable mass was required for these measurement as the light glass test mass would not have provided enough force to give a recoil signal of high enough signal to noise ratio at the top of the clamp. By keeping the pendulum length equal to

that of a typical test pendulum, the recoil behaviour of the system could be characterised at the normal working frequency of around 1Hz.

The reference input for the lock-in was obtained by shadow-sensing the motion of the pendulum. Shadow sensing was done using a white light source, focused on the side of the pendulum mass (as the pendulum mass itself was fairly thin). The resulting white light spot with shadow was focused down on a photodiode. The signal from this photodiode, a sine-wave showing the phase of the pendulum's motion, contained a d.c. offset of 0.15 V corresponding to the residual light level when the pendulum was stationary. It was necessary to remove this offset before use as the lock-in reference. The photodiode signal was passed into the non-inverting input 'A' of a Princeton amplifier, and the offset removed using a variable dc (battery) source attached to the inverting input 'B'. This left only the desired ac signal of 0.5 V (after amplification of × 10 from the Princeton).

The accelerometer was then carefully positioned above the point of suspension in the direction of swing of the pendulum. The output from the accelerometer, taken from the monitor point shown in Fig. (4.5(b)) as usual, was sent through a Kemo filter to reduce the effect of background seismic and mechanical disturbance. The Kemo was set as a low pass filter with corner frequency of 4 Hz and a gain of 10. The accelerometer output, filtered and amplified by the Kemo, was then sent to the signal input of the lock-in analyser to give the recoil motion of the system. The phase output of the analogue lock-in, calibrated as 10 mV per degree, was connected to a chart recorder.

With the experimental system thus set up, the zero phase ground line was plotted. Following this, the actual measurement of the recoil phase relative to the phase of applied force was taken. Measurement of the average phase recorded was taken by evaluation of the recorded phase at several points along the trace (see Fig.(4.14)). These phase values were then summed and averaged over the complete trace. This gave a value of average phase as $\phi_{ave} = -4.75^{\circ} \pm 0.34^{\circ}$.

Finally the additional phase lag, ϕ_{elec} (section 4.2.3 part 1), due to peripheral electronics was also plotted. A schematic diagram of the set-up used to take this measurement is shown in Fig.(4.7(b)). An attenuator was in place for this measurement only as the pendulum signal would have been too large for the lock-in signal channel. The lock-in

gave a very stable output showing the additional electronic phase lag to be $\phi_{elec} = -4.2^{\circ} \pm 0.05^{\circ}$.

The value of the additional phase lag due to viscous damping of the pendulum was then ascertained. Using the white light and photodiode set-up described, but with the signal going directly to the chart recorder, the pendulum was set swinging and its amplitude decay plotted. The pendulum Q was found to be of order 10^4 (corresponding to a ring-down time of 1hour in equation (3.32)). Hence the additional phase lag due to viscous damping was evaluated to be $\phi_{visc} = -\tan^{-1}\left(\frac{1}{10^4}\right)\text{rads} = -\left(5.7 \times 10^{-3}\right)^{\circ}$.

Hence the recoil phase lag, ϕ was evaluated as

$$\begin{aligned}\phi &= \phi_{ave} - \phi_{elec} - \phi_{visc} - \phi_{accel} - \phi_{o/p} - \phi_{rc} \\ &= -4.75^{\circ} - \left(-4.2^{\circ}\right) - \left(-5.7 \times 10^{-3^{\circ}}\right) - 0.025^{\circ} - 0.2^{\circ} - \left(-0.395^{\circ}\right) \\ &= -0.37^{\circ} \pm 0.34^{\circ}\end{aligned} \tag{4.27}$$

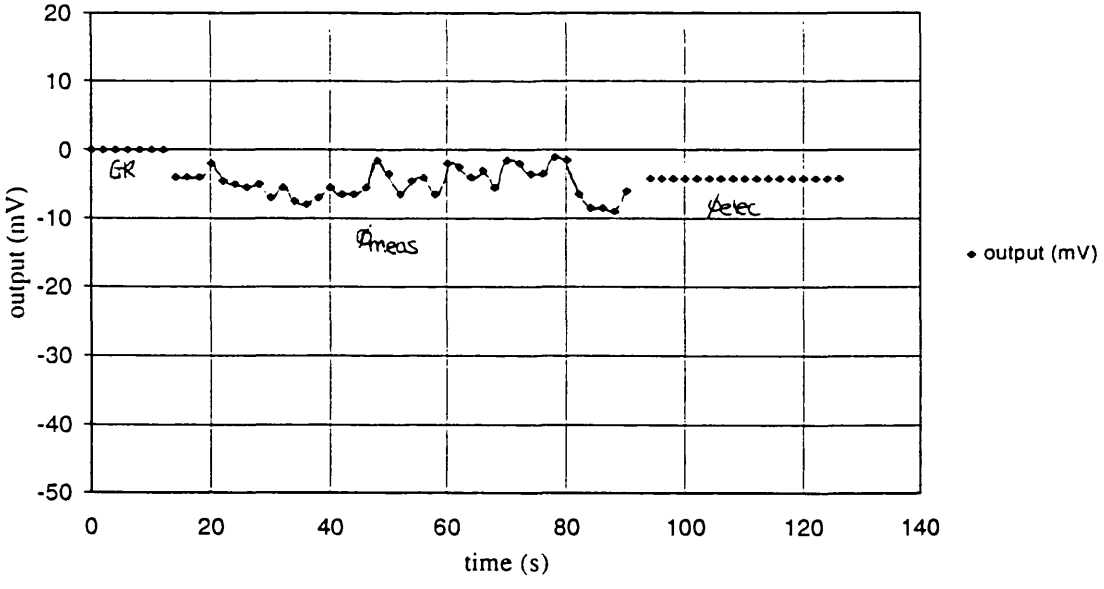

Fig.(4.14): Data points measured during evaluation of recoil phase lag of tank in original condition. *Note levels of ground line ('GR'), electronic phase shift reference line (ϕ_{elec}), and measured phase line.*

It was instructive to then use this stiffness and phase information in the evaluation of the limit placed on the measurable Q by recoil damping for a mass of 210g. By following the discussion outlined in section 4.2.1, this was found to be;

$$\bullet \quad Q_{limit} = (7.5 \pm 6.9) \times 10^6 \tag{4.28}$$

This result indicated that the level of recoil damping in the system was not only the most likely limiting factor to the initial measurements by JE Logan et al (recall maximum Q recorded was 6.3×10^6), but would also place a serious limitation on any future measurement involving high Q pendulums. Before any such Q measurements were attempted the system was re-built and the new limit measured, as described in the following section. Difficulty in maintaining measurement stability against background variation in temperature was observed during this measurement with the analogue lock-in amplifier. The effect of this can be observed in the analogue lock-in phase measurement error of order 0.34°. This analogue lock-in was replaced by a digital lock-in analyser (Stanford Research Systems, model SR830) whose specifications suggested a higher degree of stability, therefore making it a more suitable instrument for measurement in the stiffened system.

4.2.5
Steps taken to stiffen system.

Following the experiments outlined in the previous section, it was believed that the lack of rigidity of the structure may have been due to a rocking of the system as a whole. Arising from this was the concern that flexing of the pipe connecting the vacuum tank to the ion pump contributed to this motion due to instability in the pump mounting. As a counter-measure the ion pump was remounted on a concrete block, similar to that under the tank. The tank itself was remounted on two milled steel discs, replacing the three phosphor-bronze hemispherical ball-bearings, to provide a three point mounting for the tank (in conjunction with the ion pump mounting). To prevent movement of the tank on

the discs, a thin layer of Torr-Seal was applied round the joints between the discs and the tank above and base-plate below. See Fig.(4.15). Following these measures, the re-evaluation of recoil phase lag and the magnitude of the system stiffness was carried out, as outlined in the following text.

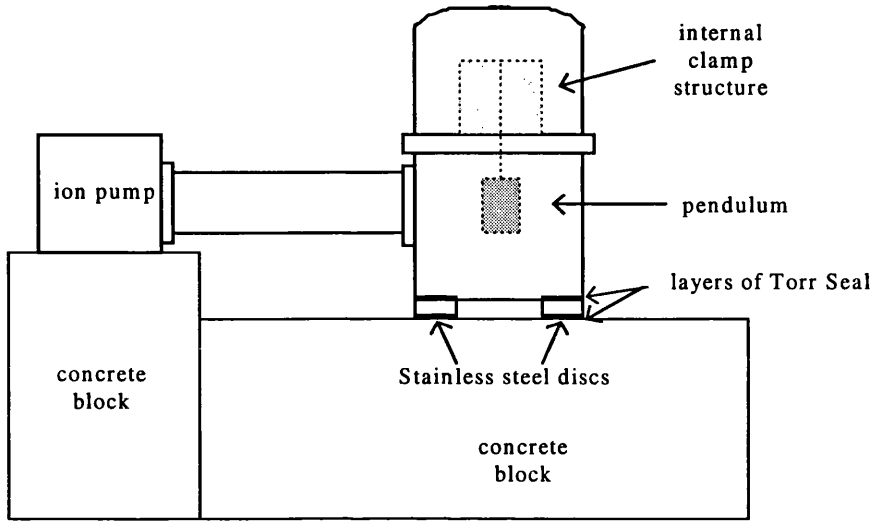

*Fig(4.15): **Improved tank arrangement.** Tank now mounted on 2 steel discs, with ion pump now stabilised due to improved mounting.*

4.2.6
Measurement of new recoil limited Q for stiffened system design.

As a consequence of the increased stiffness of the system the magnitude of the recoil signal for a given applied force was much lower than in the original measurement. This necessitated several large-scale alterations in the experimental method used for measurement of k and ϕ. Although broadly similar in principle to the method used previously, these changes are fully documented below.

- Main changes to experimental method for recoil-damping measurements in stiff systems.

The 1.2 kg lead pendulum used in previous measurements was found to be unsuitable for measurement in the re-stiffened system as it did not provide a recoil signal of high enough signal to noise ratio (against background vibrational noise). To provide a higher signal to noise ratio, a 10 kg lead mass suspended on piano wire from the clamp structure was used to provide the applied force to the system.

In addition to improving the recoil signal quality it was also necessary to provide a TTL reference input for the digital lock-in. The optical and electronic arrangements required to produce a reliable TTL signal are shown below in figures 4.16(a) and (b).

Here it can be seen that the flag and white light source used in the previous optical arrangement was replaced by a 10 mW HeNe laser, focused (using a +5 D lens fixed on the tank porthole window) down onto a fine slit (~200 μm) etched in a black flag. The slit was mounted in a central position above the pendulum mass to reduce sensitivity to rotational modes. As the resulting pulse signal, produced as the pendulum moved, was required to show the centre point of the pendulum swing, the laser and slit were aligned with the pendulum hanging at rest. It should be noted that with this arrangement pulses of twice the pendulum frequency were obtained; this was not immediately suitable for use as a reference with the 1Hz recoil signal. To provide the reference it was necessary to pass the signal through a JK flip flop divide by two circuit. The electronics themselves consisted of a photodiode with amplification (sensing the 2 Hz pulse from the laser and flag) followed by a comparator and flip-flop, producing a 1 Hz TTL square wave output which was then sent directly to the reference input of the lock-in.

This arrangement worked very well in producing a stable reference; however there were several practical considerations associated with the method of sensing the pendulum motion at the centre of its cycle. In the first instance, inclusion of this circuitry raised the question of a suitable approach to the usual measurement of ϕ_{elec}. Usually, the same reference signal would be sent through both the reference and signal routes to the lock-in, taking into account most electronic components involved during the measurement. This simple approach was not possible here, however, due to the frequency difference between the input and output of the TTL electronics. By shadow-sensing the pendulum motion using the white light source, an alternative 1 Hz reference signal, representing essentially the same information as contained in the TTL output, was created for use in the signal route to the lock-in. Using this arrangement (Fig.(4.17)), this signal was

compared with the reference input of the 1 Hz TTL from the reference electronics, thus giving a measure of ϕ_{elec} which included most sources of phase shift due to measurement electronics.

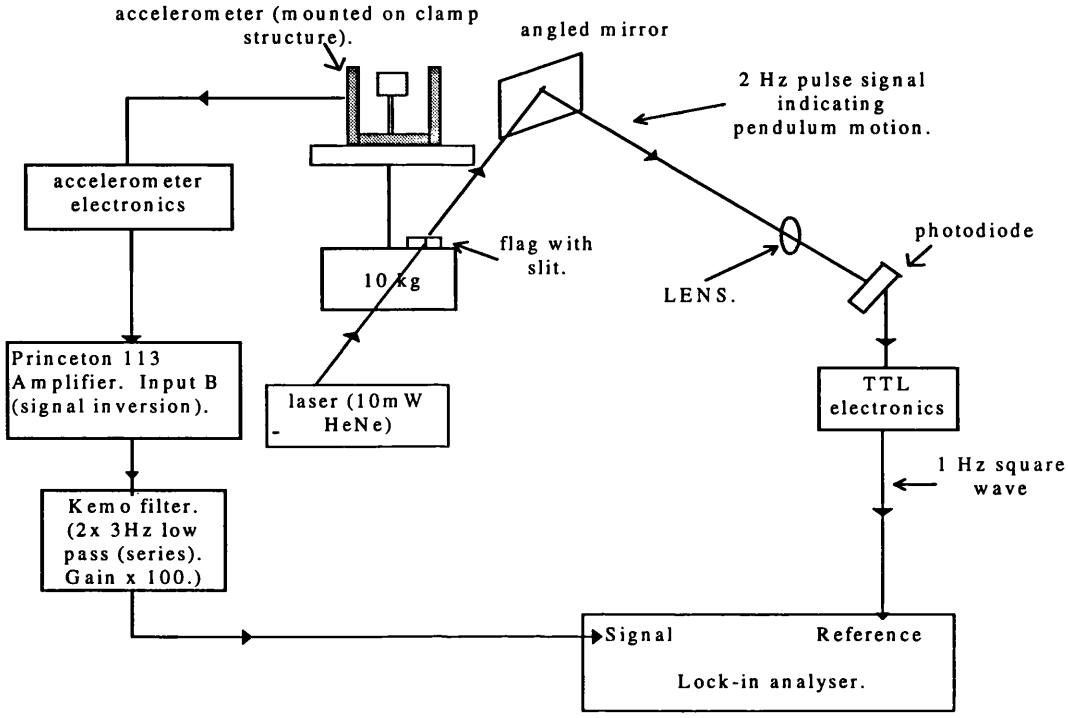

Fig(4.16(a)): Experimental arrangement for initial measurement of phase lag between accelerometer signal and laser TTL reference.

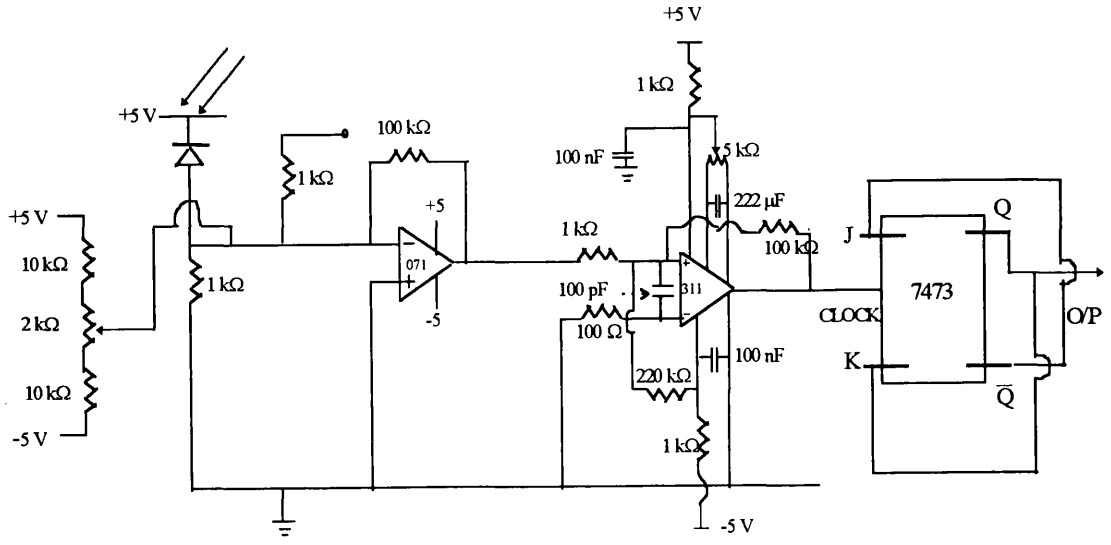

Fig(4.16(b)): Circuit diagram of electronic arrangement required to convert 2 Hz pulse signal from the laser and slit set-up, to a 1 Hz square wave suitable for a low frequency input to the digital lock-in.

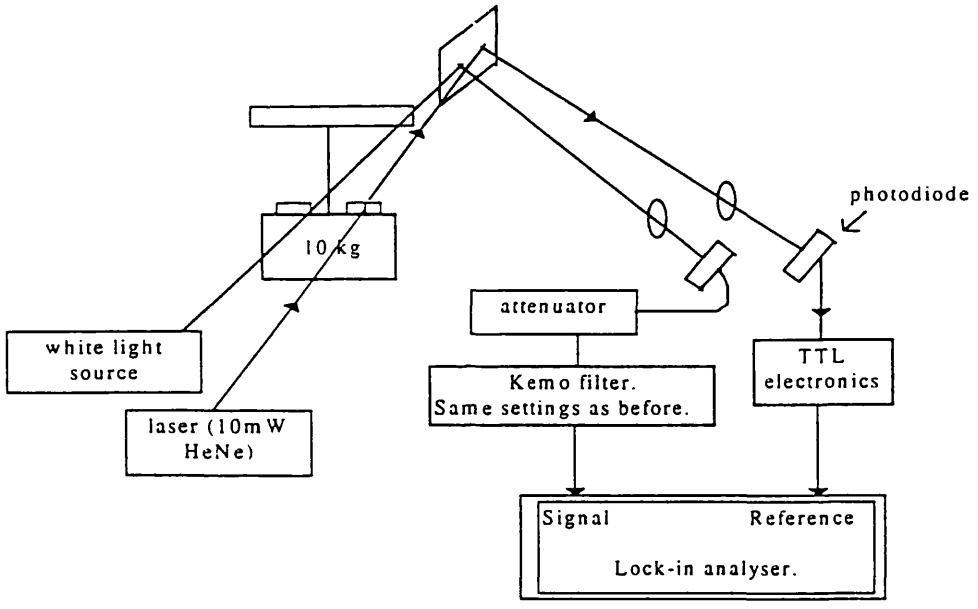

Fig.(4.17): Experimental arrangement for measurement of additional phase error ϕ_{elec}. *Attenuator included to bring white light signal size down to match that of the laser TTL before input to the lock-in.*

An additional problem was the noticeable sensitivity to the decreasing amplitude of the pendulum as its swing died down, which is now discussed.

- Measurement of recoil phase lag of the system

Following the set-up shown in Fig.(4.16(a)), the pendulum was set swinging and three recordings were made of the total phase lag between the laser TTL reference signal and the accelerometer recoil signal. Between each of these measurements, the electronic phase lag was measured by comparing the laser TTL signal with the white light pendulum reference signal (through the post accelerometer electronics) as shown in Fig.(4.17). The zero-phase line was also plotted in the usual way.

Results from these measurements are shown in Fig.(4.18). The most striking feature of the plotted data is the downward trend of both the total phase lag and electronic phase lag lines; this indicated a negative drift in the values of the total phase lag in the system (ϕ_{tot}, between the accelerometer signal and the reference) and the electronic phase contribution (ϕ_{elec})..

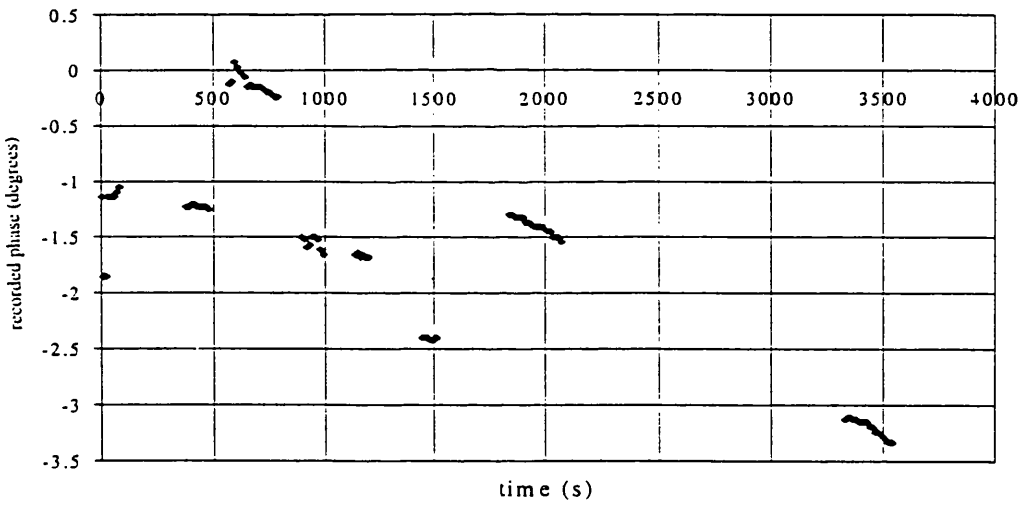

Fig(4.18): Phase measurement showing sensitivity to decay of pendulum swing amplitude. *Upper plot:* ϕ_{elec}*; lower plot:* ϕ_{tot}.

Recall that a pulse would be created as the slit edge cut the laser beam. This would happen at a point in the pendulum swing slightly away from the centre of the motion due to the finite width of the slit. It was thought that although this shift is not noticeable for large swing amplitudes, it would become more important as the pendulum motion died down, resulting in the drift observed.

To reduce this effect a feedback arrangement (Fig.(4.19)) was used to keep the swing at constant amplitude. A fraction of the TTL signal was used to trigger a Thandar signal generator to produce a sine-wave of the same frequency as the pendulum. This was then sent to a solenoid, of resistance 6.6 Ω, mounted in line with the centre of the face of the pendulum mass, which could then drive the pendulum by means of a small magnet mounted on the face. Using this arrangement the pendulum swing amplitude could be maintained provided the signal in the solenoid was in phase with the 1 Hz laser pulses from the reference electronics; in this way a force could be applied to the pendulum in the lowest point of its swing, where the velocity was a maximum. By comparing the phase of these two signals in practice it was found that the signal going to the solenoid lagged the laser pulse phase by around 45°. To correct this a high pass RC filter, which provided a phase correction of 45°, was included before the solenoid as can be seen in Fig.(4.19). In addition to this, a gain pot was included to allow adjustment of the level of the magnetic drive, thus allowing adjustment of the level at which the swing amplitude could be kept constant.

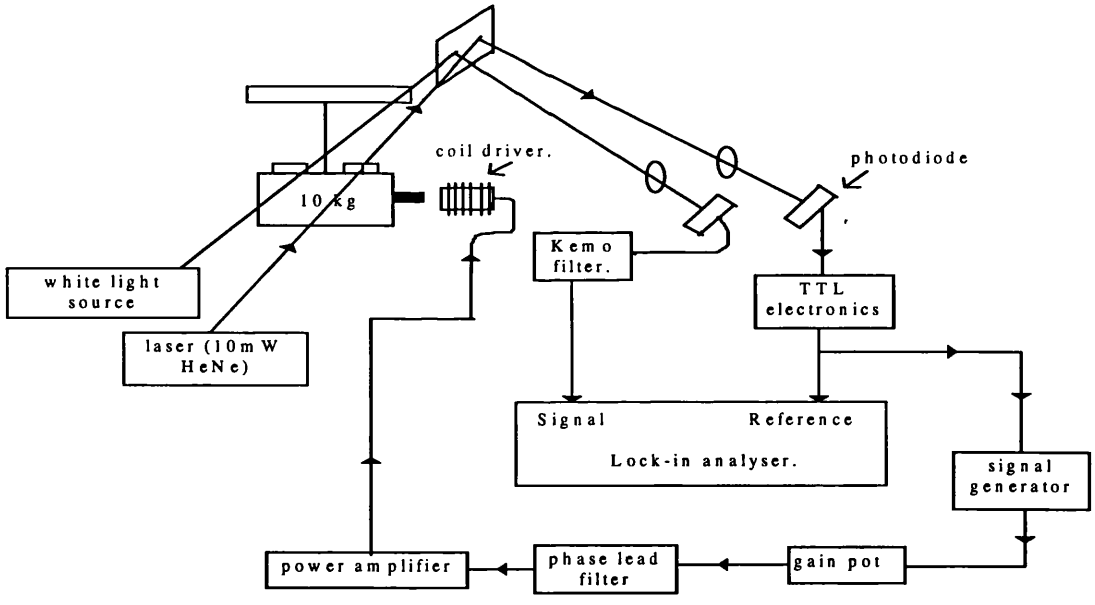

Fig.(4.19): Inclusion of coil drive feedback arrangement to prevent decay of pendulum swing amplitude.

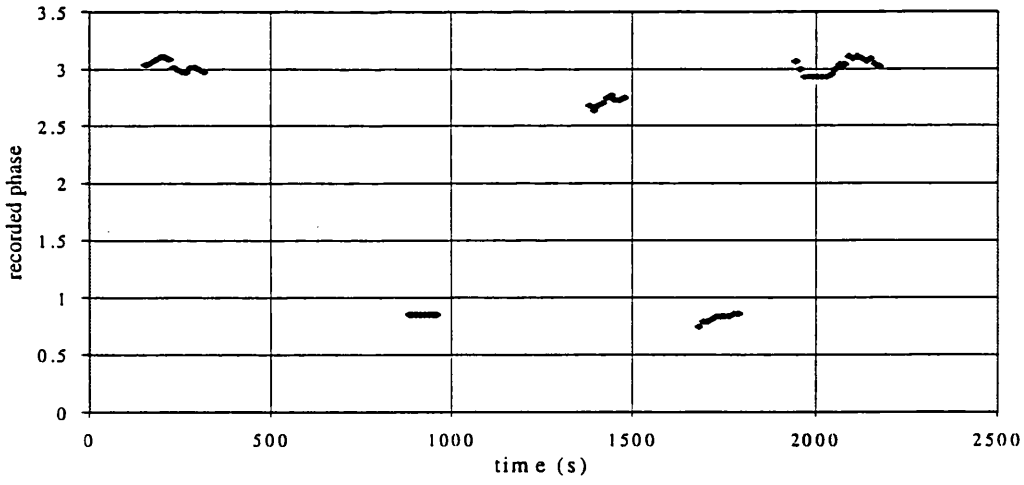

Fig.(4.20): Plot of phase data taken following introduction of coil and magnet feedback driver. *Note that the downward trend is no longer evident. Upper curve represents measurement of* ϕ_{tot} *(between accelerometer and laser TTL), and lower curve* ϕ_{elec} *(between white light signal and laser TTL). Values indicate a phase* lead, *caused by electromagnetic pickup by accelerometer.*

The phase experiment was then performed again as before. Results from these measurements are shown in Fig.(4.20). It was clear from this data that the magnetic drive had prevented the phase drift from re-occurring; however it was also clear that an additional complication was present, indicated by the fact that the two phase traces gave rise to a positive value of phase difference, rather than the negative value expected.
This was found to be due to magnetic pick-up by the accelerometer while the magnetic drive was running. The phase measurement was carried out for a final time by running the magnetic drive as normal during measurement ofϕ_{elec} (yielding an average phase of $-0.520^{\circ} \pm 0.001^{\circ}$), then switching it off temporarily during the course of the measurement of ϕ_{tot}. In this way, after allowing the phase to settle (typically to around $-1.91^{\circ} \pm 0.01^{\circ}$), traces of up to 100s length for ϕ_{tot} could be taken that were free from pick-up. Re-plotted data from this last measurement of phase lag can be seen in Fig.(4.21).

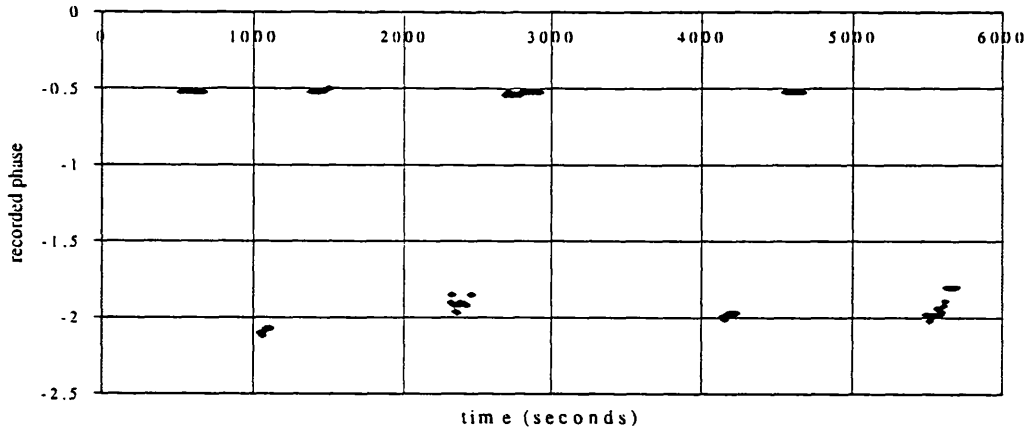

Fig(4.21): Plot of final phase data with time. Upper plot shows $\phi_{elec} = -0.520^\circ \pm 0.001^\circ$ *measured with respect to ground). Lower line represents* $\phi_{tot} = -1.91^\circ \pm 0.01^\circ$, *(accelerometer recoil signal to pendulum signal).*

The following additional phase shifts were also taken into account, as described in section 4.2.3.

$$\phi_{visc} = -0.01^\circ;\ \phi_{o/p} = +0.2^\circ \pm 0.05^\circ;\ \phi_{accel} = +0.025^\circ \qquad (4.29)$$

From this the following result for recoil phase lag was calculated:

$$\phi_{ave} = \left(-1.39 - 0.2 - 0.025 + 0.01\right)^\circ = -1.61^\circ \pm 0.05^\circ \qquad (4.30)$$

- Evaluation of magnitude of stiffness, k

Values of recoil acceleration magnitude leading to the calculation of k were taken in the usual way (see section 2.2.2) throughout the phase experiment documented above. The force applied by the pendulum was evaluated through measurement of the maximum pendulum swing angle (recall θ_{max} in section 2.2.1). This angular measurement was generally carried out by determination of the pendulum length and the maximum horizontal component of the pendulum motion.

Values of k were calculated as described, giving an average value of stiffness of the system of:

$$k = (5.49 \pm 0.67) \times 10^6 \text{ Nm}^{-1} \tag{4.31}$$

Hence the upper limit to the measurable Q set by recoil damping for a mass of 210 g was found to be:

$$\bullet \quad Q_{limit} = (2.36 \pm 0.29) \times 10^7 \tag{4.32}$$

4.3
Measurement of the Pendulum Q of a Light Glass Mass.

4.3.1
Construction of test pendulum.

A typical test pendulum for pendulum quality factor measurements of fibres produced by both the methods outlined in section 3.4 is shown below in Fig.(4.22). As can be seen from the diagram, two fibres (of length 22 cm) were used to suspend a light glass plate (of mass 210 g). The light mass was chosen to reduce recoil losses and also for relative ease of handling. A minimum fibre cross-sectional area of [28] $6.86 \times 10^{-9} \text{ m}^2$ was required for the 210 g mass. The plate had surface area $4.85 \times 10^{-3} \text{ m}^2$ perpendicular to the direction of swing.

There are several methods of joining fibres to the suspended mass. For steel wires, this has traditionally been done using a looped 'sling' of wire round the mass, with the break-off position on each side defined by a small 'lug'. Although this clear definition of break-off point can improve violin and pendulum mode quality factors, the use of lugs has been

---

[28] Based on a breaking stress value of $8 \times 10^8 \text{ Nm}^{-2}$ for fused silica.

seen to degrade the internal mode quality factors of suspended masses through friction effects (Logan et al, 1992). Although not important for measurement only of pendulum quality factor, a more suitable technique had to be found to allow the future measurement of all system quality factors in a monolithic system.

For these simple tests, the fibres were attached to either side of the glass mass by applying a thin layer of Torr Seal vacuum glue to the end rods of the fibres and attaching them in this way to the plate. To stabilise the plate and help prevent tilts of the mass as the pendulum swung the bottom break-off points of the fibres were glued level with the centre of mass of the glass plate. The tops of the fibres also had end-rods, which were critically important (Quinn et al, 1994) for the top attachment of the pendulum to the suspension structure during the experiment. These end-rods were an automatic advantage of both methods of fibre-pulling from fused silica rods and did not require welded joints.

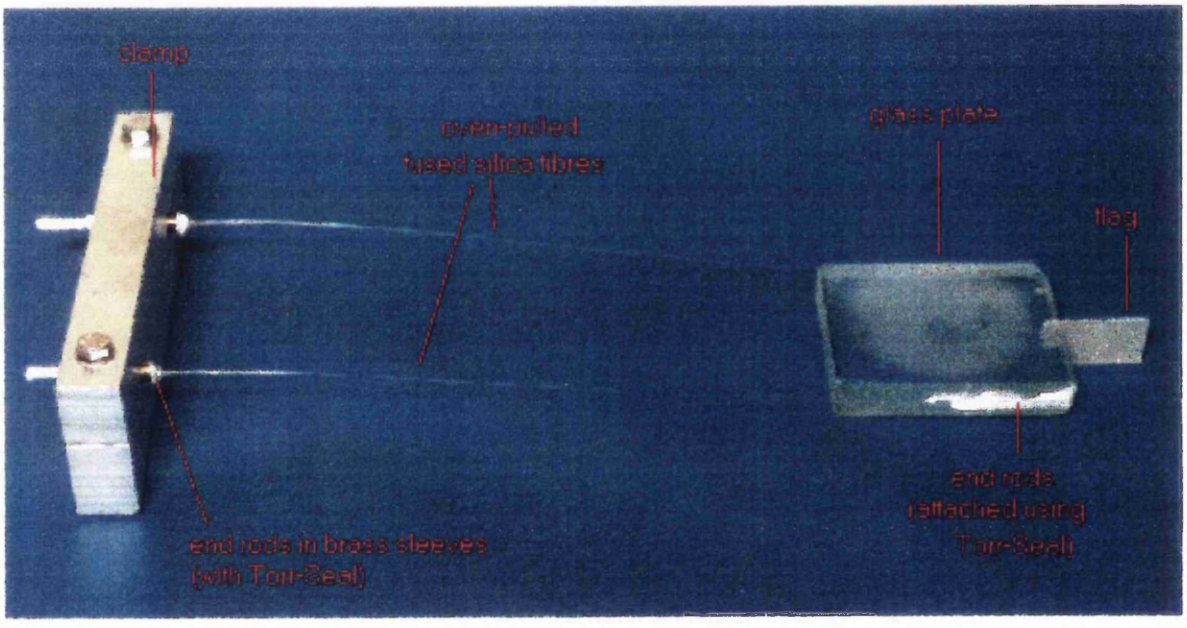

Fig.(4.22): Photograph of pendulum used for Q_{pend} measurement of glass test mass suspended by two oven-pulled fused silica fibres

---

* Note that the direction of the pendulum motion was perpendicular to the plane of the greater surface area.

4.3.2
The optical set-up for pendulum Q measurements.

Following the improvements made to the rigidity of the tank the experimental arrangement to measure the pendulum quality factor of fused silica suspension fibres was set up as shown in Fig.(4.23) below.

A shadow sensing technique was employed to detect the decay in amplitude of the pendulum motion with time, thus allowing the evaluation of the ring-down time. A small coil and magnet-driven lever (mounted on an adjustable clamp stand inside the tank) was used to initially excite the pendulum by striking the front face of the pendulum mass in the direction of swing. As the pendulum motion in a single longitudinal direction was being measured, it was desirable to align the lever as carefully as possible with the centre of this face in an attempt reduce the relative amplitude of other pendulum motions, e.g. sideways, rocking and tilt modes. As is usual with quality factor measurements of this nature, the effect of viscous damping due to air molecules striking the pendulum mass was reduced and made negligible by carrying out the measurement of amplitude decay

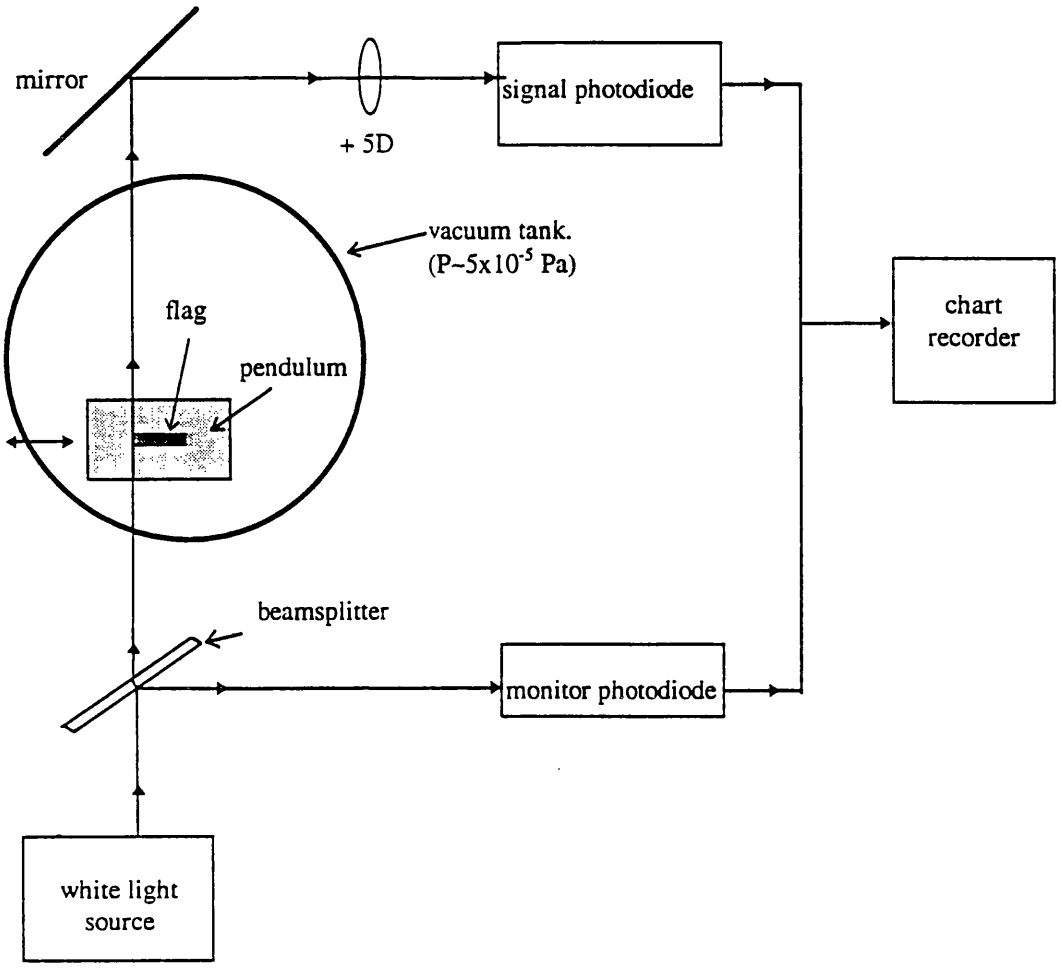

Fig(4.23): experimental arrangement for measurement of Q_{pend} .

under vacuum. Assuming a 'safe' limit to the pendulum Q of around 10^8 set by gas damping (based on a mass of 210 g, and resonant frequency of 1 Hz), equation (3.20) implies that a pressure of 4×10^{-1} Pa at room temperature would be sufficiently low to achieve this. It should be noted that these calculations are performed under the assumption that the main residual gas present is Nitrogen. Similar calculations based on the presence of material with molecular weight 500 (e.g. epoxy adhesive residue) also indicate that there would be no serious limit placed on the Q values measured under normal working pressures.

Typically a vacuum level of 5.3×10^{-5} Pa was maintained throughout the experiment. An additional importance of the use of vacuum conditions was the prevention of contamination of the fibres during the experiment, either from grease and dirt or through water uptake from the atmosphere, both of which are believed to lower the Q.

A collimated beam from a bright white light source was used to illuminate a small fibre-glass flag mounted under the centre of the pendulum mass. By mounting the flag centrally, the sensitivity of the measurement to rotational motion of the pendulum was reduced. After passing the pendulum flag, the beam with flag shadow was focused on to a photodiode with the resulting sinusoidal signal (corresponding to the amplitude of the pendulum motion) being sampled in bursts on a chart recorder. Typically, bursts for these measurements were taken every 6 hours for 20 minutes over the period of at least one week.

Although extrapolations from the data could have been made by sampling over a shorter period it was considered wise to collect data for longer in order to assess the behaviour of the pendulum over time.

It was extremely important that the intensity of the white light source remained as constant as possible as any variation in this would give the appearance of a change in the pendulum amplitude. As intensity changes were found to be caused by fluctuations in mains voltage, greater stability was achieved by running the white light source from a power supply, at a lower voltage than usual to increase the lifetime of the bulb. As shown in Fig.(4.23), the light intensity was monitored on a separate photodiode, but was found to remain constant during the course of the measurements.

4.3.3
Pendulum Q results for hand-pulled fibres.

Results for a pair of hand-pulled fibres suspending a glass plate of mass 0.21kg are shown in figure (4.24), which shows the plot of the natural logarithm of this amplitude data. This pendulum was set swinging and its amplitude decay recorded over a period of 234 hours. Q_{pend} was therefore found to have a value of:

- $Q = (1.90 \pm 0.57) \times 10^6$

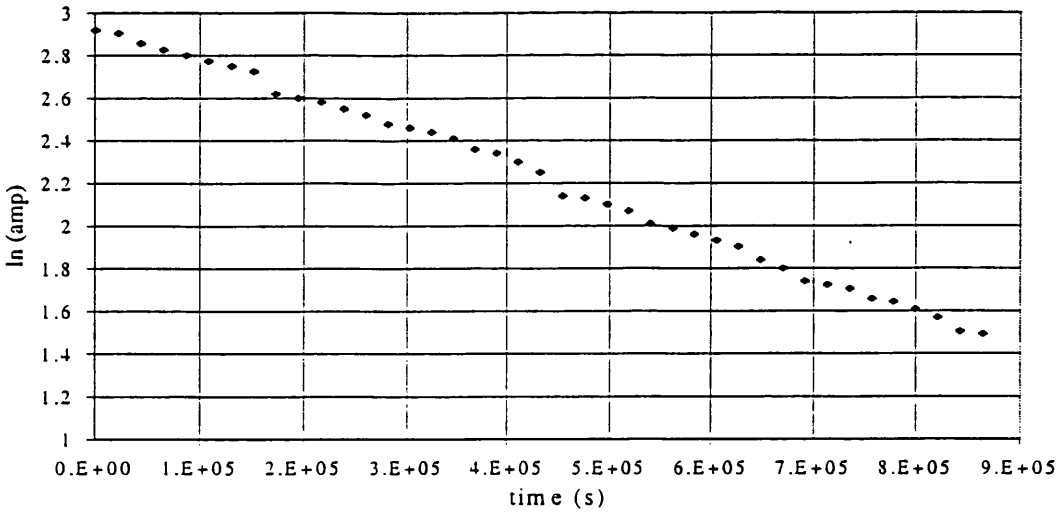

Fig(4.24): Plot of natural logarithm of pendulum amplitude with time (hand pulled fibres).

However, this fell short of the pendulum Q value previously measured for similar fibres (section 3.6). This was thought to be due to the innate inconsistencies involved in the blow-torch fibre production method, e.g. non-uniform heating of fibres possibly giving rise to thermal stresses in the fibres, or irregular variation in the diameter of the fibres along their length. In addition to these there was also concern about possible contamination of the fibres with carbon from the flame.

4.3.4
Pendulum Q results for oven-pulled fibres.

Using the RF oven a pair of fused silica fibres, matched in length (225 mm), were pulled and a test pendulum constructed as described in section 4.3.1. Once constructed it was hung in the usual way in the newly stiffened vacuum system and the optical arrangement outlined in section 4.3.2 used to detect the amplitude of the pendulum motion. The mechanical driver was again used to initially excite the pendulum, with great care being taken in the alignment to excite the pendulum as cleanly in the longitudinal mode as

possible. The initial vacuum level of the system was 6.6×10^{-5} Pa at the time of excitation, this value being observed throughout the duration of the experiment.

Analysis of the amplitude decay recorded after one week clearly showed that although the initial Q value ($Q_1 = (3.07\pm0.11)\times10^6$) was maintained for the first four days this was followed by an abrupt downturn which lowered the Q value substantially. Again, this new Q ($Q_2 = (8.13\pm0.29)\times10^5$) was sustained for around 2½ days before a similar catastrophic change took place. As the swing amplitude was becoming rather small at this point the pendulum was re-excited while the recording was continued. After a similar period it was apparent that this third Q value was in the region of $Q_3 = (1.91\pm0.097)\times10^5$. As this Q was now rather low the pendulum amplitude had died away in this time to a level which again necessitated the re-excitation of the pendulum. For the remaining 4 ½ days after this re-swing data was continued to be taken, yielding a final, slightly higher, Q value of $Q_4 = (3.77\pm0.11)\times10^5$. These results are shown in Fig.(4.25) below:

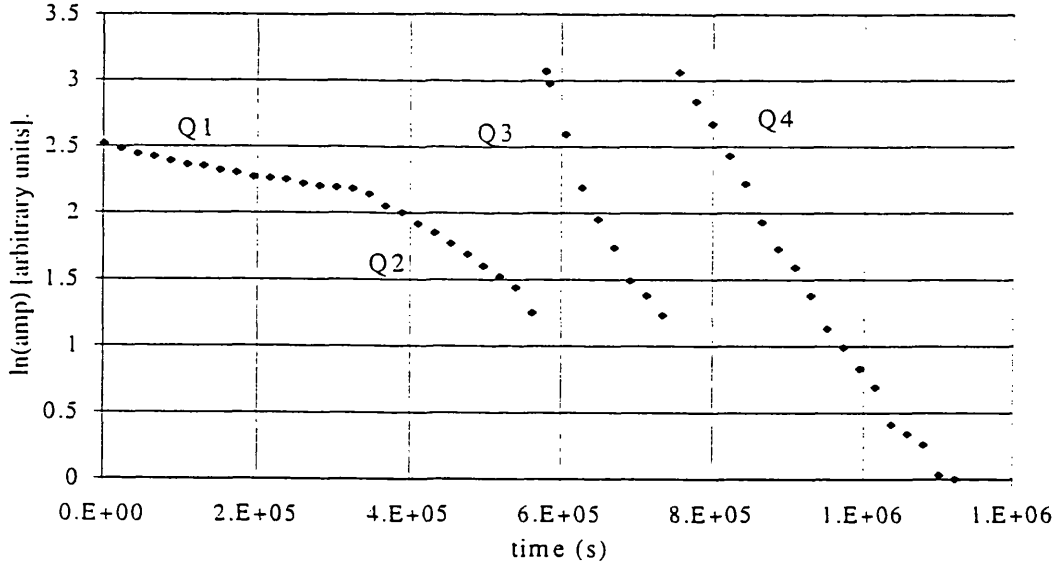

Fig(4.25): Plot of natural logarithm of pendulum amplitude with time for Q_{pend} measurement of pendulum suspended by 2 oven-pulled fibres.

4.4
Discussion of Q_{pend} Results.

The results reported in section 4.3 reflect the fact that although one would reasonably have expected the pendulum Q results from these oven-pulled fibres to far exceed those from their hand-pulled counterparts, it was clearly not the case in this instance. It certainly appeared on first inspection that some excess loss mechanism had developed during the test. Such a feature had been visible in the hand-pulled fibre results, but was not nearly so serious.

There were several aspects of the test-system which could have possibly been held accountable for the results observed; however, by either design or experiment, these had largely been anticipated and ruled out. For instance, shifts of the vacuum system on its mountings, leading to sudden large increases in the level of recoil damping from that initially measured, were extremely unlikely in this system. Another possibility could have been that of failure of the high vacuum e.g. due to small pockets of outgassing material in the vacuum system bursting out during the measurement. An event such as this could possibly lead to a sudden coating or damping of the fibres, with a corresponding degradation in Q. This was thought unlikely, but it may be wise in future tests to monitor tank pressure throughout the experiment. Another possibility was that there had perhaps been some loosening of the clamp used to suspend the pendulum which could give rise to a sudden mechanical loss. Again, however, great care had been taken while clamping the pendulum before measurement, and examination of the clamp structure as a whole afterwards revealed nothing untoward. It therefore seemed likely that the reason for the behaviour observed lay in the fibres.

Returning to consider the discussion contained in section 3.4, there are many processes present in both the production of fused silica fibres, and in the construction of the pendulum itself, which can result in a degeneration of the quality factor one may have reason to expect. For instance the production method chosen, with its associated conditions of pulling temperature and in-built mechanical and thermal stresses, may well have a bearing on the result. In addition, there is the question of micro-cracks on the fibre surface, or indeed internal flaws through the fibre. Also, from the construction point of view, although a great deal of care was taken while making up the pendulum,

the possibility of surface contamination of the fibres (albeit on a microscopic level) cannot be ignored.

A similar, sudden change in Q was also observed in the measurement conducted by Logan using hand-pulled fibres. It was thought that there may have been some aspect of the pulling methods which could have led to the results observed. For the most recent results, one conjecture was that the oven may have been pulling at too low a temperature. This had always been considered due to the fact that in order to reduce the length of the fibre 'neck' it was necessary for pulling to commence as soon as the rod began to drop under its own weight. At this point the rod was obviously molten, but it was thought that internal stresses could perhaps be set up in the fibre if the molten material had not reached a temperature where it was soft enough to pull. It was also considered that a similar result may have occurred if the fibre twisted slightly as it was pulled. These stresses could lead to cracks appearing after a finite time thus increasing the potential for damping. To investigate these points a dark-field microscope with cross-polarisers was used to examine the fibre for stresses; any such features would show up as a bright area on an otherwise dark region of unstressed material; in this case, as in all other fibres examined in this way, no such features were evident.

By using the dark-field set-up alone it was possible to determine if there were any surface contaminants or superficial micro- cracks present on the fibre. The main feature observed by this method was a tiny film of Torr-Seal on the surface, very close to the approximate bottom break-off position of one of the fibres (Fig.(4.26)). The fibres were also examined in this way for internal flaws and also for the presence of any material, e.g. carbon, which could have perhaps been deposited internally during the pull; no flaws or internal contaminants were found in this investigation however. The microscopic evidence suggested that the low starting Q and the reason for the subsequent abrupt degradation observed may have been due to the Torr Seal contamination in close proximity to a break-off point, leading to excess friction.

These measures were directed primarily toward explaining the sudden downturns in the quality factor; equally serious however was the low starting Q that the fibres exhibited prior to the first change. This could have been a natural by-product of the loss mechanism causing the changes observed, but is still under investigation and subject to further tests. There has, however, been some recent evidence to suggest that the break

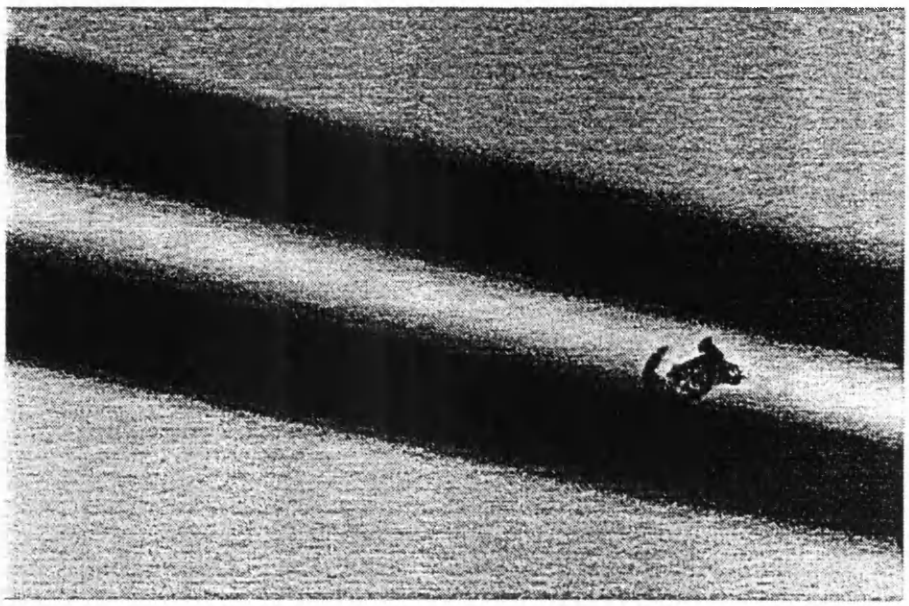

Fig.(4.26): Dark field microscope photograph of fibre, at bottom break-off position. Note small patch which may be a surface contaminant, possibly Torr-Seal.

in slope may alternatively have been due to the electrical charging and discharging of the pendulum system during the measurement. Breaks in slope are still evident in the most recent results (Hough et al, 1996), although the starting Q_{pend} is much higher with a value around 4.8×10^6. It is believed (Rowan et al, 1996) that the pendulum plate and fibres could have become charged due to liberation of electrons from the tank walls by ultra violet radiation emitted from the ion pump used to evacuate the system. Any subsequent discharge of the pendulum may have resulted in the sudden losses observed in the results.

From recent results reported in section 5.4 on the material quality factor of oven-pulled fibres, it would seem likely that pendulum quality factors of 10^7 should be possible, and current work is being directed toward achieving this.

Chapter 5
Measurement of the Material Quality Factor of Fused Silica Ribbon Fibres.

5.1
Introduction

Section 4.4 has outlined the preliminary results from Q_{pend} measurements using fused silica fibres. It was hoped that measurement of Q_{mat} would provide additional information on the quality factor of oven-pulled fibres, and at some later stage also on the relationship between Q_{pend} and Q_{mat}. Initial results of the measurement of Q_{mat} for a fused silica ribbon fibre indicated values of $Q_{mat} \geq 5 \times 10^5$ (Logan et al, 1994(b)). It was believed that this preliminary test system could be improved, however - a task which was undertaken for the measurements reported in this chapter.

5.2
Experimental set-up for measurement of material quality factor of fused silica ribbon fibres.

The main aspects of the experimental system used here were similar to those required for measurement of pendulum quality factor. Although ribbon fibres would be the main test shape for initial measurements, it was desirable to produce an experimental system which would allow tests on both ribbon and cylindrical fibres without the need for large-scale alterations. Measurement on cylindrical fibres is rather more complicated due to the elaborate motion that they undergo during decay; this has led to several extra design considerations, outlined here, which will be used in future tests of these fibres.

Recoil damping of fibres tends to be less of a problem than for suspended masses (due to the much smaller mass involved). However, this can only be considered to be the case

where a reasonably rigid clamp and vacuum structure has been provided for the fibres. This was carried out using methods analogous to those outlined in Chapter 4, which had been seen to be successful. As can be seen in Fig.(5.1), the clamp contained two different mechanisms for holding the fibre under test.

On one side a small piece of aluminium was bolted firmly down on a ribbon fibre, while on the other there was a 'jaw' providing a suitable clamp for cylindrical fibres. In this way, the same set-up could be used for cylindrical fibres, without requiring the removal of the internal structure. The work of Quinn and colleagues (Quinn et al, 1994) has stressed the importance of the use of fibres which 'swell' to a larger thickness at the end to be clamped. This effect has also been noted by Kovalik & Saulson (Kovalik & Saulson, 1993) in the measurement of the material quality factor of various materials. To prevent the swollen end of the ribbon fibre from being crushed by the clamp, it was sandwiched with Torr Seal between two very thin pieces of steel. It was intended that for cylindrical fibre tests the end-rods would be fitted with brass sleeves and clamped in the same way as fibres used in the pendulum measurements (section 4.1.2).

Following the discussion on external gas damping contained in section 3.2.1, care was taken to ensure that adequate vacuum levels were maintained at all times during the measurement. The vacuum system consisted of a rotary pump for providing a rough initial vacuum and to back up a turbo pump, which was used to continue the pumping to the required level. Calculation of the required vacuum level indicated that the pressure of residual gas inside the tank should be of order 3.12×10^{-4} Pa to prevent viscous damping of the fibre. For these preliminary measurements, the vacuum level during measurement was typically an order of magnitude better.

As a mechanical drive method, such as used in pendulum quality factor measurements, would be unable to selectively excite the various modes of the fibre, a capacitive drive mechanism was installed (Fig.(5.1)). This could be tuned in frequency to both the fundamental mode and enharmonic overtones of the fibre. This drive consisted of a pair of coplanar conductive plates, separated by a very fine slit, placed directly under the fibre around 1 cm from the tip. The plates were connected to a high voltage amplifier (maximum output ± 750 V about 750 V) which in turn was driven by a very stable

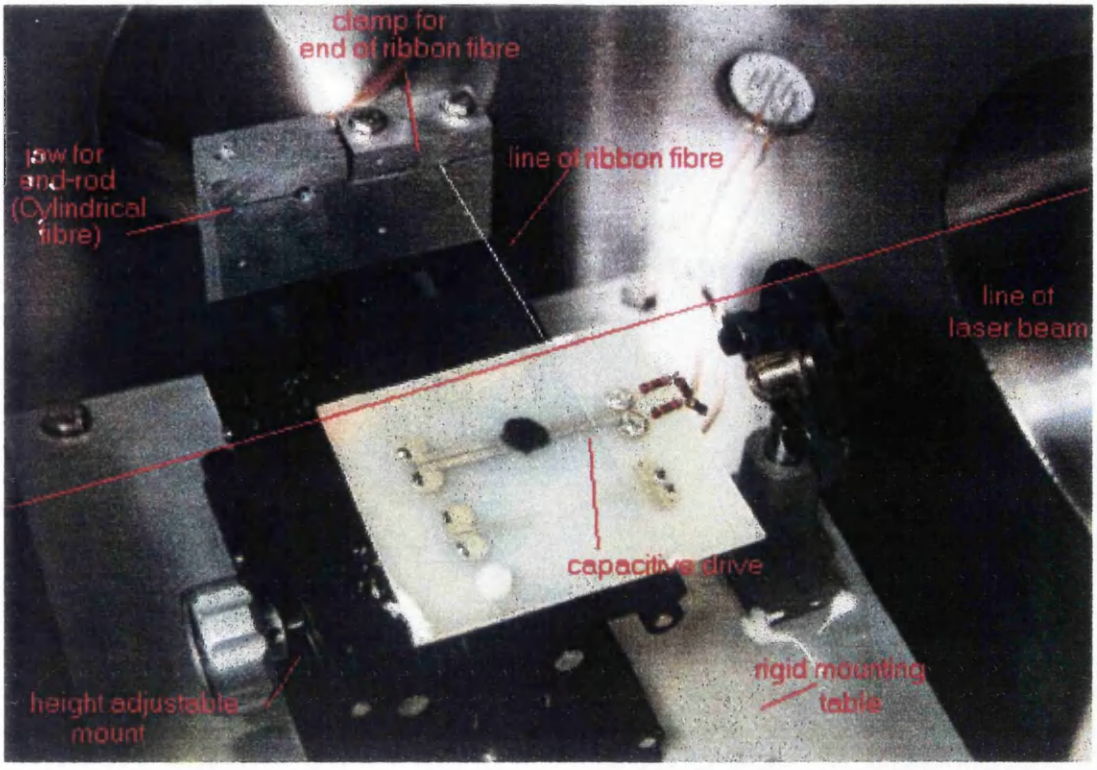

Fig(5.1): Photograph showing experimental arrangement inside vacuum tank for measurement of Q_{mat}.

signal generator. An ac signal was tuned to the fibre resonance and applied to the plates, generating an oscillating field across the gap which provided an increasing and decreasing attractive force on the fibre. Following excitation the high voltage supply was switched off, while the fibre amplitude decayed.

The optical arrangement used for ribbon fibre measurements is shown in Fig.(5.2). As the fibre was very fine, a 4 mW HeNe laser was used to illuminate the side of the fibre, with the resultant diffraction pattern sensed by a split photodiode. Vibration of the fibre gave rise to a movement of the diffraction fringes across the photodiode. The signals from each half were subtracted, with the corresponding sinusoidal photo-current giving a measure of the amplitude of the fibre motion. For the photodiode to provide a linear measurement of the signal it was necessary to ensure that the motion of the fringe was small compared to its dimensions on the photodiode.

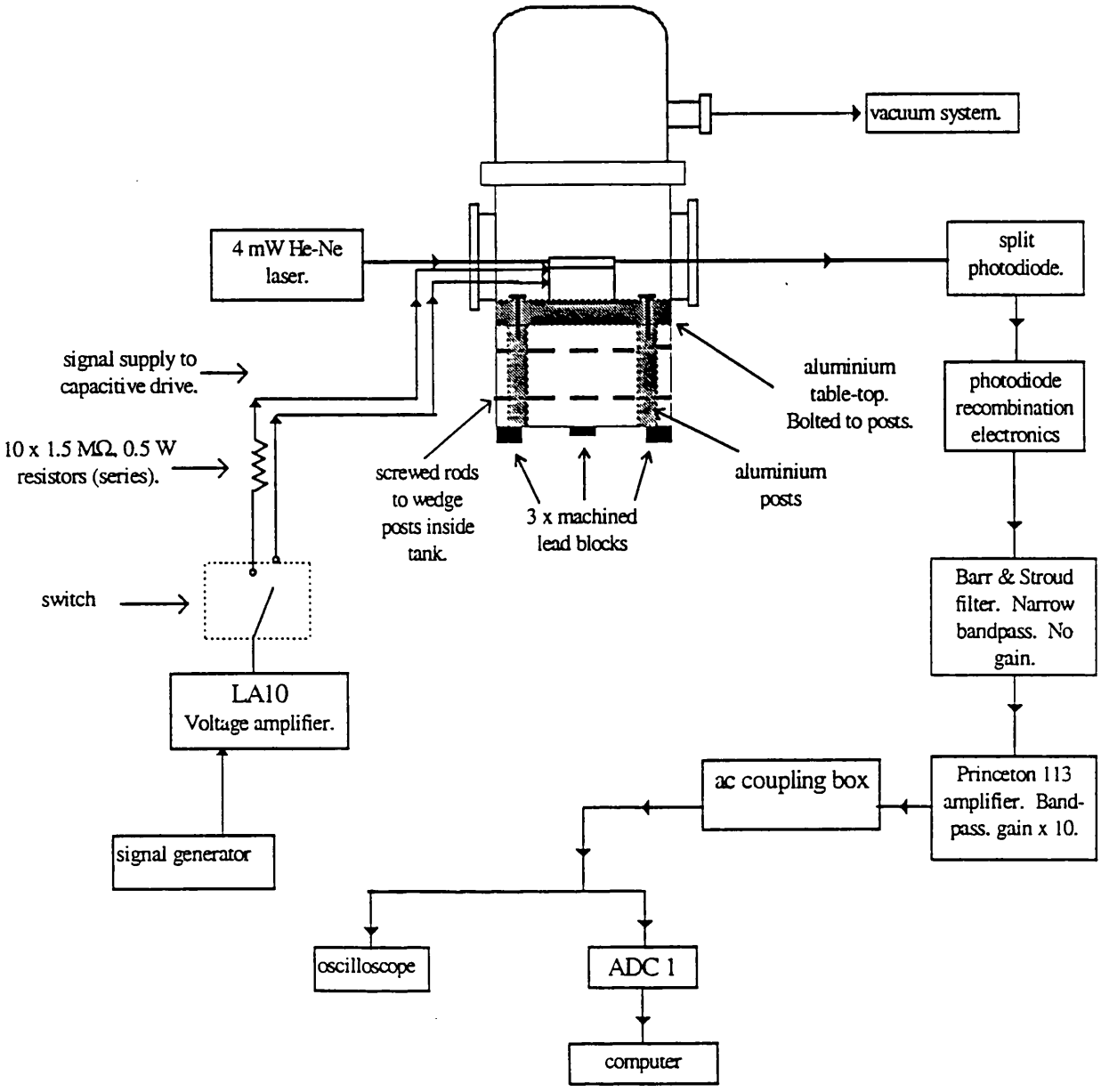

Fig(5.2): Overview of entire experimental arrangement.

A shadow sensing method was again employed to detect the decay in amplitude of the oscillating fibre, although certain changes were necessary to the basic technique, particularly for the case of future measurements on cylindrical fibres where motion is in more than one direction. Following initial excitation, the tip of cylindrical fibres typically follow an elliptical path where motion along one axis of vibration can apparently die away, while that in the perpendicular direction increases in amplitude. Thus future measurements involving cylindrical fibres may require a pair of split photodiodes, placed

* A ribbon fibre (rectangular cross-section).

perpendicularly to each other, allowing each direction of motion to be simultaneously monitored.

As a consequence of this arrangement, it was desirable to develop a computerised data acquisition system which could be tailored for use with fibres of both rectangular and cylindrical cross section. The subject of data acquisition in this experiment is discussed in more detail in section 5.3.

5.3
Data acquisition and analysis for material quality factor experiments.

5.3.1
Introduction

Ribbon fibres were chosen for initial tests as they tend to oscillate in one direction only, thus simplifying the measurement process. The single split photodiode used would result in a pair of signals requiring algebraic recombination. However, future measurements made using cylindrical fibres will require the use of a pair of photodiodes, thus requiring recombination of four signals.

Evaluation of the amplitude at a given time would be found by recombining the outputs of the two photodiodes recorded at that time. Suppose the split photodiode pair has outputs a, b, c and d, simultaneously measured at a time t (Fig.(5.3)).

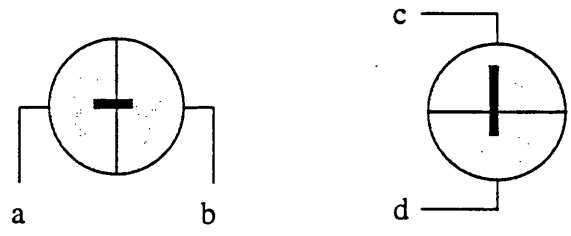

Fig.(5.3): Schematic diagram defining split photodiode outputs.

The recombined 'true' amplitude measurement for the fibre at time t will be given by equation (5.1).

$$A(t)=\sqrt{(a-b)^2+(c-d)^2} \qquad (5.1)$$

The need for a rather more sophisticated data acquisition system than used in pendulum quality factor measurements can be clearly seen. Handling the large amounts of data expected from such measurements in this way made the chart recording technique unsuitable for useful data recording, even for the ribbon fibres. Data collection and subsequent manipulation was made simpler and more efficient through the use of a computerised data acquisition system, providing automatic storage and recombination of data. Two programs were written for the purpose of data acquisition, designed for use with a [29]PC-30B interface card on a PC platform using Borland's Turbo C application. These were designed to be suitable for use with data for both cylindrical and ribbon fibres (listings are attached in Appendix B). A schematic diagram of the hardware system is shown in Fig.(5.4), where four photodiode signals are being input to the multiplexer.

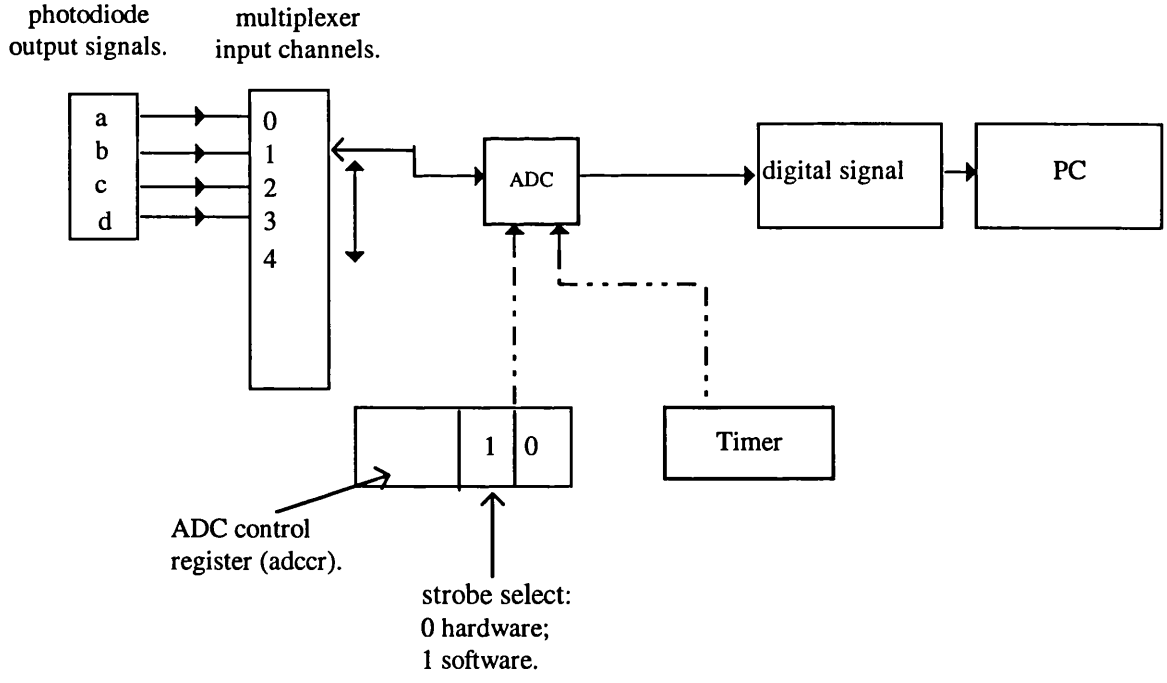

Fig.(5.4): Simplified schematic diagram of main components involved in data acquisition hardware for this system. *Note that adccr is set to binary number 2 ('10'), thus selecting software strobe operation. Four signals from photodiode in this case.*

[29] PC-30B interface card produced by *Flight Electronics Ltd.*

To understand the logistics of the data acquisition (DAQ) system design, we must first consider several important features of the hardware operation. Incoming analogue signals from the photodiode outputs are sent, via a multiplexer, to a 12 bit ADC. This converts analogue voltages in the range -10V to +10V. There is also a 12 bit DAC which accepts digital numbers in the range -2048 to +2047. The ADC works here by reading a sample from analogue voltage output of the multiplexer, then converting this to a digital number. However, this conversion process takes a certain length of time (around 25 - 30 μs) during which time no more data can be read. During sampling, the program must know to delay the ADC from reading the next set of data from the multiplexer until the ADC has finished converting the last set. This conversion only takes place when the ADC has been triggered by a 'strobe' pulse, so it is possible to set this up in such a way that the time between strobe pulses to the ADC is greater than 30 μs. This strobe pulse can either be generated in software (using a [30]library function, 'amreadsoftadc(int.channel)', written specifically for this purpose (not generally available)) or by a pulse from a timer chip in the interface card (in this case the library function 'amreadhardadc' must be used). For situations where timer accuracy is critical, the 'hard' strobes should be used.

For example, consider the single sinewave, sent via the multiplexer to ADC0 as shown below. Sampling of this single input is relatively straightforward, and requires the use of only one strobe source. Say 500 samples were to be taken at 1 kHz frequency; this would require the hard strobe to be set to trigger ADC0, with the strobe pulses set to 1 kHz. The 500 samples would then be read and converted at this frequency, and the results stored in some form of data array (perhaps also with the time of the sample run).

Once a strobe type has been chosen, there remains the question of how to select this in the program. This is done using the 8 bit ADC Control Register (ADCCR) shown in Fig.(5.4). Reading from right to left one can see that setting the second ('strobe select') bit to binary number 00 will enable 'hard' strobe operation. This is done through use of the command setting 'outportb(adccr,0)'. Alternately, one can enable software strobes using 'outportb(adccr,2)', which sets the ADCCR to binary number 10.

[30] Non-standard library functions developed in-house at Glasgow (McLeod, 1995).

As each of these strobes are controlled by different timer mechanisms, it is possible to configure the strobe rate of each independently - a feature which was extremely useful for our multi-channel sampling as we shall later see.

5.3.2
Data acquisition system requirements for measurement of Q_{mat}

There were four main system requirements for data acquisition in this experiment. Consider the multi channel input situation shown in figures (5.4) and (5.5)), where it is required that 500 samples be taken of each signal at 1 kHz say, with each sample being taken near-simultaneously across the multiplexer.

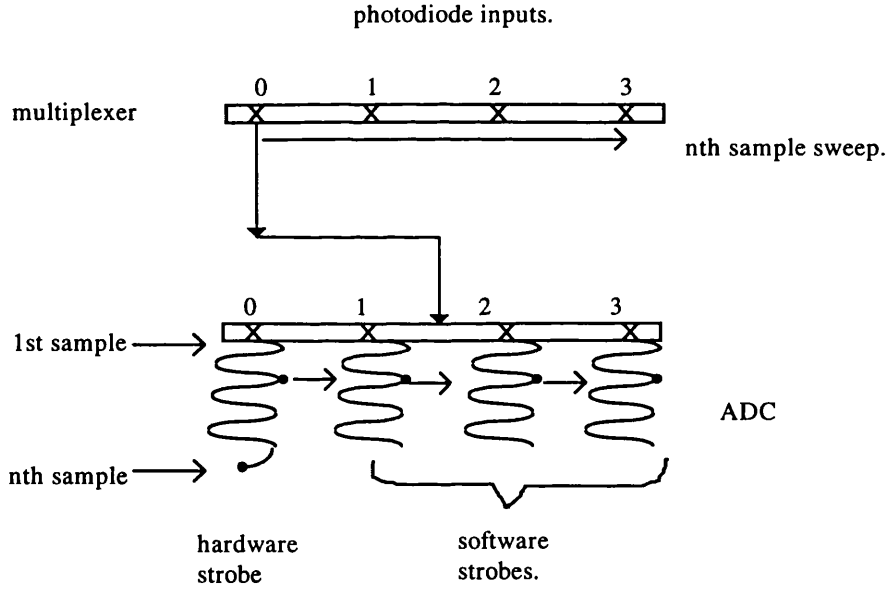

*Fig.(5.5): **Multi-channel operation of the ADC.** A sample is read from each photodiode input across the multiplexer during each sample run using software strobes. First sample (channel 0) in each run is read using the hardware strobe*

Multi channel operation requires that for each sample taken, the multiplexer outputs are read in a 'sweep' as quickly as possible, until all 500 samples have been taken for each photodiode signal (Fig (5.5)). If the hardware strobe is used to take the first sample

(using ADC0) in each sweep, and is then followed by the soft strobe for the remaining channels (ADC1, ADC2, ADC3) the sample frequency can be set at any value by the hard timer chip, while maintaining the fast 33 kHz 'sweep' frequency of the soft timer (which is fast enough to be considered near-simultaneous).

Once these analogue signals had been successfully read and converted into digital form, recombination of the four digital signals acquired and stored was performed (recall equation (5.1)). This would be done for each burst, producing a single resultant signal lasting the length of the burst. The rms amplitude of the resultant sine-wave for each burst then had to be found, with consideration also being given to the possibility of rms amplitude error. This error is likely to arise as it is unlikely that the final recombined sine-wave in each burst will consist of an integral number of half cycles. Finally, it was necessary to store the data in a useful form allowing easy access and the analysis of results. The solution to these requirements is now discussed.

5.3.3
Data Acquisition

Consider the program listing, attached in Appendix B. Note that a global variable, `nchan`, defining the number of ADC channels used (in this case 4) has been declared at the beginning of the code.

The function call '`setupsystem()`' sets up the software strobe (to default setting 33 kHz) using the function '`amsetupsoftadc()`'. The hardware strobe is also set up using the functions '`amsetuptimer()`' and '`amloadtime(2,1000)`', whose respective uses are to configure the internal timer chip to produce timed output pulses, and set the frequency of these pulses. It should be noted here that the hard strobe timer chip is controlled by a 2 MHz oscillator, where the desired frequency is set in this case to 1 kHz. Thus, by this stage we have configured both the soft and hard strobes for use, with the hard strobe setting the sample rate at frequency 1 kHz, and the soft strobes setting the sweep rate at 33 kHz. Both of these strobes will be used during the data sampling.

Here, the soft strobes are used to do most of the sampling, but will require the more reliable hard strobe timer chip to start off each sample run across the multiplexer.
On starting the program, the function call 'interval()' invites the user to specify the time interval desired between the data bursts. Typically this would be set to 1 minute, or less depending on the frequency. The value typed is then assigned to the global integer variable 'period'. A call to the function 'getnow()' then reads the start time of the experiment from an internal clock, assigning the value to the long integer variable t1.

As soon as t1 has been evaluated, the program will begin to sample the incoming data across the multiplexer in the call to function 'getdata()'. The hard strobe is initially switched on (reading the first ADC channel), using the command setting 'outportb(adccr,0)'. The hard strobe remains idle until the first zero crossing in ADC0 is detected, then immediately triggers ADC0 to read and convert the first sample of this first sine-wave. Software strobes are immediately switched on using 'outportb(adccr,2)' triggering ADC1, ADC2 and ADC3 to read and convert in turn the first sample from the remaining three sine-waves in a sweep.
After the sweep, the process begins again (as set by the 1 kHz sample rate) until 500 samples have been taken from each channel. The program then pauses while the time from the start of the experiment is counted. When the present time (t2) reaches the value t2= t1+ period, the sample run begins again for the next burst, and so on. After *n* bursts have been taken, there will be *n* sets of 4 sine-waves recorded.

5.3.4
Recombination of photodiode outputs

Recombination of data is performed during the call to function 'datareduce(volts,sig,time)'. Here, the four photodiode outputs are recalled from their storage array and the resultant recombined signal found using equation (5.1), written into the code. The recombined signal was then stored in a separate file (see section 5.3.6) with the corresponding burst time and represents the actual amplitude of the vibrating fibre.

5.3.5
Minimisation of rms amplitude error

Consider a sine-wave with amplitude A_0, described by the equation $A(t) = A_0 \sin\omega t$. When integrated with respect to time over an integer number of half cycles the rms amplitude will be expressed as shown in equation (5.2) below:

$$A_{rms} = \frac{A_0}{\sqrt{2}} \tag{5.2}$$

If, however, the integration time is extended by an amount ζ, corresponding to an additional part half cycle (i.e. $0 < \zeta < \pi/\omega$), we find that the rms amplitude as a function of ζ has the following form:

$$A(\zeta)_{rms} = \frac{A_0}{\sqrt{2}}\left\{\frac{\omega}{n\pi + \zeta\omega}\left(\frac{n\pi}{\omega} + \zeta - \frac{1}{2\omega}\sin 2\omega\left(\frac{n\pi}{\omega} + \zeta\right)\right)\right\}^{\frac{1}{2}} \tag{5.3}$$

The greatest deviation from the true rms amplitude given in equation (5.3), occurs where ζ is such that an extra ¼ cycle is included in the integration. For a given sample time, this error will be a maximum for the fundamental (lowest) frequency of the fibre, typically evaluated at around 1.5%.

There are two ways of reducing this error for a signal of given angular frequency. The first option is to increase the number of cycles included in the integration, *n*, which would reduce the effect of the error. A more desirable option for this experiment would be to include additional code which would conduct a search for the sample 'bin number' of the first and last minima of the rectified, sine-wave. Integration during the rms process would then only be carried out between these two bin numbers, ensuring the removal of the additional part cycle.

5.3.6
Data storage and analysis

Data was stored in a series of arrays identified by the user at the start of the program. A typical function call for the procedure is 'filename(fname)', which requests the file name, then sets up a pointer to this file and checks that it doesn't already exist. If it does happen to exist, the user is asked if data should be appended to this file, thus removing the possibility of data being overwritten each time a burst of data is stored. Three such files were set up to store the following data:

- 'filename(fname)': Sets up pointer, fptr, pointing to an array which stores the signals read in from the ADCs. Data is saved in the form [sample number (i), volts[nchan][i]]. This array is used during the call to function 'savedata()', with new data being appended after each burst.

- 'sigfilename(sigfname)': Sets up pointer, sigfptr, pointing to an array which stores the final recombined signal, created during the call to function 'datareduce()'. Data is saved in the form [burst time (t), sample number (i), recombined signal (sig(i)).

- 'rmsfilename(rmsfname)': Sets up pointer, rmsfptr, pointing to an array which stores the r.m.s. amplitude found from the final recombined signal taken in each burst, created during the call to function 'rms()'. Data is saved in the form:
  [burst time (t), rms, first minima bin no. (i1), last minima bin no. (i2)].

In all three arrays data was stored in a format that was compatible with that of the Excel spreadsheet. In doing so it was possible to transfer files directly from the hard disc to Excel, where the usual quality factor analysis procedures could be easily performed.

5.3.7
Data Analysis and removal of background noise using the Excel spreadsheet package.

Recall the analysis technique outlined in section 3.5. This method was again employed to find the amplitude ring-down time, hence Q_{mat}, for the ribbon fibres tested. This was done by transporting the data array containing the r.m.s. amplitude, $A(t)_{rms}$ of the vibration at different times, t, into an Excel spreadsheet, where a least squares fit could be performed for the best straight line corresponding to $ln\left(A(t)_{rms}\right)$ vs t.

The susceptibility of the fibre to background drive from spurious mechanical noise is more evident than during pendulum quality factor measurements. The presence of background noise results in an offset on the exponential decay curve of the fibre motion, which alters the gradient of the best fit straight line for the natural logarithm of total amplitude with time. An example of this is shown in Fig.(5.6) below, where some true amplitude data (series 1) has been offset by a constant, positive amount and re-plotted (series 2).

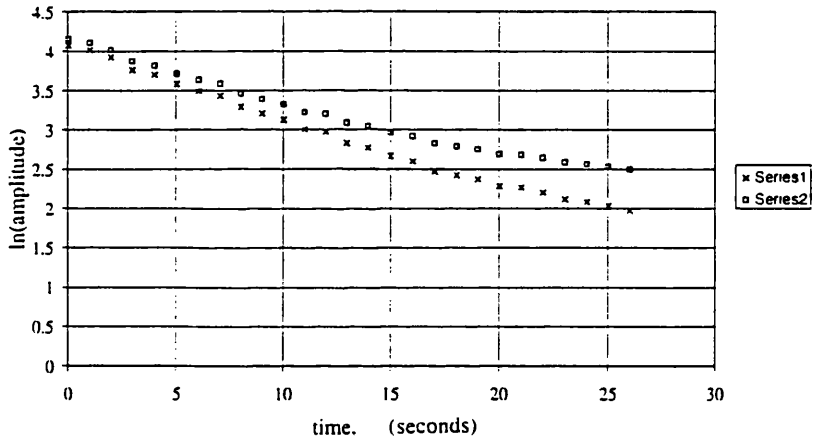

Fig(5.6): Plot illustrating the effect of a constant noise offset on the amplitude decay of a freely oscillating fibre.

For these experiments, where appropriate, the amplitude of the background drive, a, was found by allowing the fibre motion to decay completely to the level of the offset. This offset could then be removed in the following way:

Consider the energy associated with the oscillating fibre, with natural stored energy $E_s|_t$. If there is present a constant background drive, of amplitude a and uncorrelated with the fibre motion, it will contribute an additional energy:

$$\varepsilon = \beta \omega_0^2 a^2 \tag{5.4}$$

where β is a constant, thus giving the fibre a total apparent energy of:

$$E_{tot}\big|_t = E_s\big|_t + \varepsilon = \beta \omega_0^2 A_{tot}^2\big|_t \tag{5.5}$$

Where this $E_{tot}\big|_t$ has been written in terms of the amplitude, $A_{tot}\big|_t$, measured during the experiment. In order to evaluate the true ring-down time of the fibre, the background energy contribution must be removed allowing only the stored energy to be plotted. The stored energy can be expressed as:

$$\begin{aligned} E_s\big|_t &= E_{tot}\big|_t - \varepsilon \\ E_0 &= E_{tot}\big|_{t=0} - \varepsilon \end{aligned} \tag{5.6}$$

Now, the true decay in energy of the fibre can be expressed in the usual way as:

$$E(t) = E_0 e^{-\gamma t} \tag{5.7}$$

which, upon substitution of equation (5.6), becomes:

$$\left(A_{tot}^2\big|_t - a^2\right) = \left(A_{tot}^2\big|_{t=0} - a^2\right) e^{-\gamma t} \tag{5.8}$$

Taking the natural logarithm of each side of equation (5.8) gives:

$$ln\left[A_{tot}^2\big|_t - a^2\right] = ln\left[A_{tot}^2\big|_{t=0} - a^2\right] - \gamma t \tag{5.9}$$

which is the equation of a straight line, of gradient $(-\gamma)$ as required. Therefore we can see that for the correct evaluation of the gradient of the best fit straight line to be achieved, the background offset must be evaluated then subtracted in quadrature from the total amplitude values recorded before plotting. This procedure was carried out on the Excel spreadsheet where appropriate for the fibres tested during the course of these experiments.

5.4
Results

5.4.1
Results from first ribbon fibre (d=160 μm)

As an initial test of the system, the fundamental resonance (f_0) and first enharmonic resonance (f_1) of an oven-pulled fused silica ribbon of length 126 mm were excited using the capacitive drive tuned to 9.8 Hz and 54.4 Hz respectively. High material quality factors were not expected from this sample due to known exposure of the fibre to the atmosphere prior to the test. The measurement did, however, serve to highlight additional areas for attention, e.g. clamping technique and optical arrangement. The quality factors found were:

$$f_0 = 9.8\,\text{Hz} \qquad Q_0 = (2.22 \pm 0.05) \times 10^4$$
$$f_1 = 54.4\,\text{Hz} \qquad Q_1 = (4.09 \pm 0.04) \times 10^4$$

The thermoelastic limit placed on the measured quality factor of a fused silica ribbon fibre of thickness 0.16mm was calculated (section 3.2.2), and plotted in Fig.(5.7). Also plotted here are the two measured values of Q, which are clearly not being limited by the thermoelastic effect (thermoelastic limit predictions at these two frequencies are 1.61×10^6 and 6.24×10^5 for the fundamental and first enharmonic modes respectively).

The reason for the anticipated low values of Q_{mat} measured here was thought to be due to insufficiently good clamping of the fibre. Although a steel sleeve was used to hold the fibre in place (section 5.2), it was thought that the clamped end of the fibre itself didn't swell out enough to provide a reasonable clamping thickness.

The experimental set-up did, however, prove to operate satisfactorily for measurement of Q_{mat}, with results continuing to be taken on fused silica fibres (Rowan et al, 1996).

These measurements are providing very encouraging results, following correction of the problems noted during these initial tests.

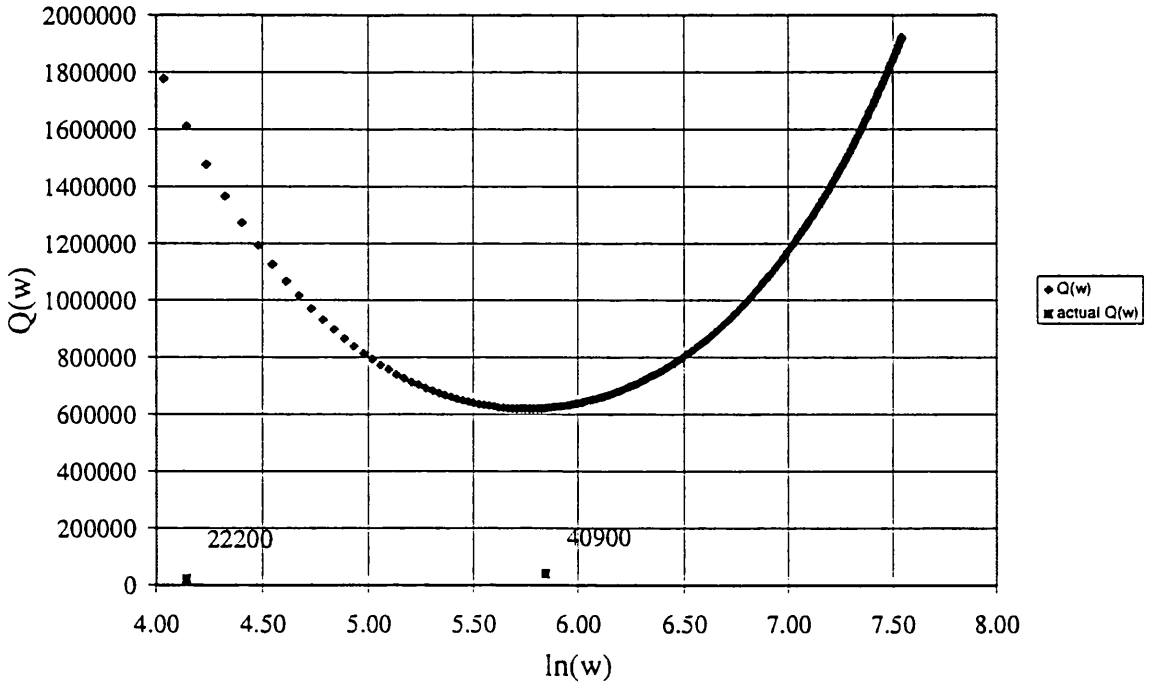

*Fig(5.7): **Comparison of measured and predicted quality factors of the fundamental mode and first overtone of a fused silica ribbon fibre (thickness 160 μm).** Curve above shows the upper limit set by thermoelastic damping to the quality factor.*

5.4.2
Results from second ribbon fibre (d=54 μm)

Recent results (Hough et al, 1996) have also been taking using this experimental arrangement and data acquisition system for a second oven-pulled fused silica fibre, of thickness 54μm , length 12.5 cm and width 0.3 cm. This ribbon was oven-pulled from a silica slide, with part of the slide being left attached at one end to provide a greater end-thickness on which to clamp down. It was hoped that by increasing the clamped area in this way there would be an improvement in the measured Q. The vacuum was maintained at a level of approximately 3×10^{-7} mbar . The Q_{mat} values obtained in this case, which were not limited by the thermoelastic effect, were measured at the fundamental resonance and first three enharmonic overtones. The values obtained were

very much better than those for the initial test fibre. A maximum value of Q_{mat}, thought to be very close to the real material Q of the oven-pulled fibres, was found for the first enharmonic Q_{mat}. A plot of these results, obtained by Hough et al (Hough et al, 1996), is shown in Fig.(5.8) below:

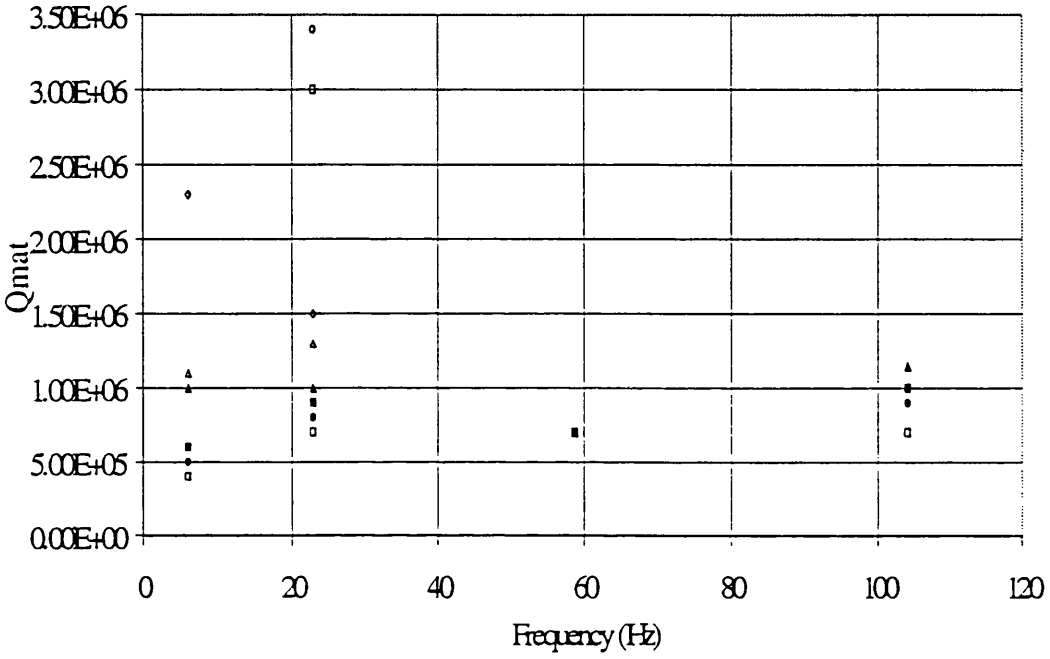

Fig(5.8): Plot of results obtained for measurement of material quality factor of a fused silica ribbon fibre, of thickness 54 μm.

The best results at each frequency are as follows:

$$f_0 = 6\ \text{Hz} \qquad Q_0 = (2.3)\times 10^6$$
$$f_1 = 22.8\ \text{Hz} \qquad Q_1 = (3.4)\times 10^6$$
$$f_2 = 58.6\ \text{Hz} \qquad Q_2 = (7)\times 10^5$$
$$f_3 = 104\ \text{Hz} \qquad Q_3 = (1.15)\times 10^6$$

The spread of results observed during these measurements was found to be due to coupling between modes of the fibre. This was most strongly observed between the 6

Hz and 22.8 Hz modes, where high values of Q_{mat} could not be observed simultaneously. There also seemed to be a strong temperature dependence on which mode was preferred; at higher room temperatures the Q_{mat} of the fundamental mode at 6 Hz was high and that of the 22.8 Hz mode was low, and vice versa. The reason for this behaviour is not yet fully understood, and is still being investigated.

It is clear from the best results listed above that it is possible to achieve material quality factors of order 10^6 for these oven-pulled fibres, which is very encouraging. These results indicate that in principle pendulum quality factors of order 10^8 should be possible for a four wire suspension, which is in fact an order of magnitude better than the value of 10^7 required by GEO 600.

Chapter 6
Wavefront distortion and attitude control of LISA.

6.1
Introduction

The design of spaceborne gravitational wave detectors has been under development over several years. During this time various design concepts have been discussed, culminating in the present system 'LISA' (Laser Interferometric Space Antenna), upon which the work presented in this chapter is based. 'LISA' is currently being proposed by an international collaboration as part of 'Horizon 2000 Plus', the European Space Agency's long term space science program.

Presented in this chapter will be the results of a short theoretical project carried out for the proposed spaceborne interferometric detector 'LISA', where phase measurement noise induced by the combined effects of laser phase front distortion and attitude stability of the space craft was investigated.

6.1.1
System description

The LISA system is fully described in a pre-phase A study report (Bender et al, 1996), but a brief summary of relevant parts will now be given.

The principle scientific objective of 'LISA' will be to provide a very low frequency detector for the observation of gravitational radiation in the frequency range 10^{-4} to 10^{-1} Hz , undetectable on Earth due to the local gravitational field gradient (Saulson, 1994). It is hoped that observation at these frequencies in the quiet space environment will allow the detection and investigation of gravitational waves from sources such as black hole and neutron star binary systems (Chapter 1).

'LISA' itself can be simply thought of as a space-borne interferometer system, based in principle on a Michelson interferometer. It will consist of 3 pairs of identical spacecraft in a heliocentric orbit, each pair of near craft forming one vertex of an equilateral triangle (Fig.(6.1)). Each of the six craft house their own local laser and transmit/receive telescope. The near craft lasers are phase locked together, thus providing a light source which can be considered to be common to both. Up to two craft can be lost (providing they are not at the same corner), with the interferometry continuing between a vertex (near) pair of craft and two end (far) craft.

The distance between each craft in the near pair at one vertex will be around 200 km, with the separation from each far pair being around $5\times10^{9}\,\mathrm{m}$. This armlength should allow 'LISA' to reach the required strain sensitivity of $h \approx 10^{-21}/\sqrt{\mathrm{Hz}}$. The science payload carried by each of the six LISA craft will be contained in a thermally shielded, carbon-epoxy cylindrical shell. The payload will comprise of four main assemblies, namely a transmit/receive telescope, the optical bench and components, a preamplifier disc and a radiator disc on which the lasers are mounted (Bender et al, 1996). Simply put, the central craft will each transmit a main beam, with power at source of around 1W and wavelength 1064 nm, to the corresponding far craft from an $f/1$ Cassegrain telescope system. The ideal transmission of such a beam will result in spherical wavefronts, centred on the transmitting mirror, reaching the far craft.

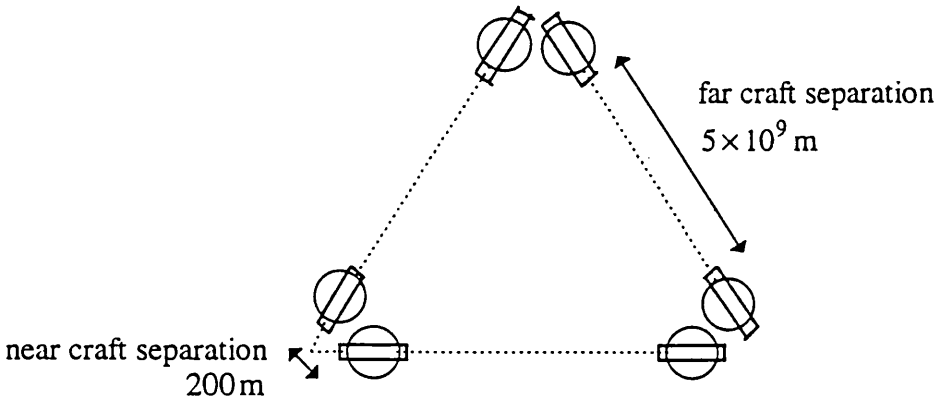

Fig.(6.1): Simple schematic diagram of the LISA spacecraft system.

At the far end, each of the receiving craft will sample over a small portion near the centre of the incoming spherical wavefronts, focus the collected light and direct it inside the

craft whereupon the beam will be reflected from the front face of the proof mass (Fig.(6.2)) and on to a photodiode. The phase of the collected light will then be compared with that of the receiving craft's own on-board laser, before being transponded back (Bender et al, 1996).

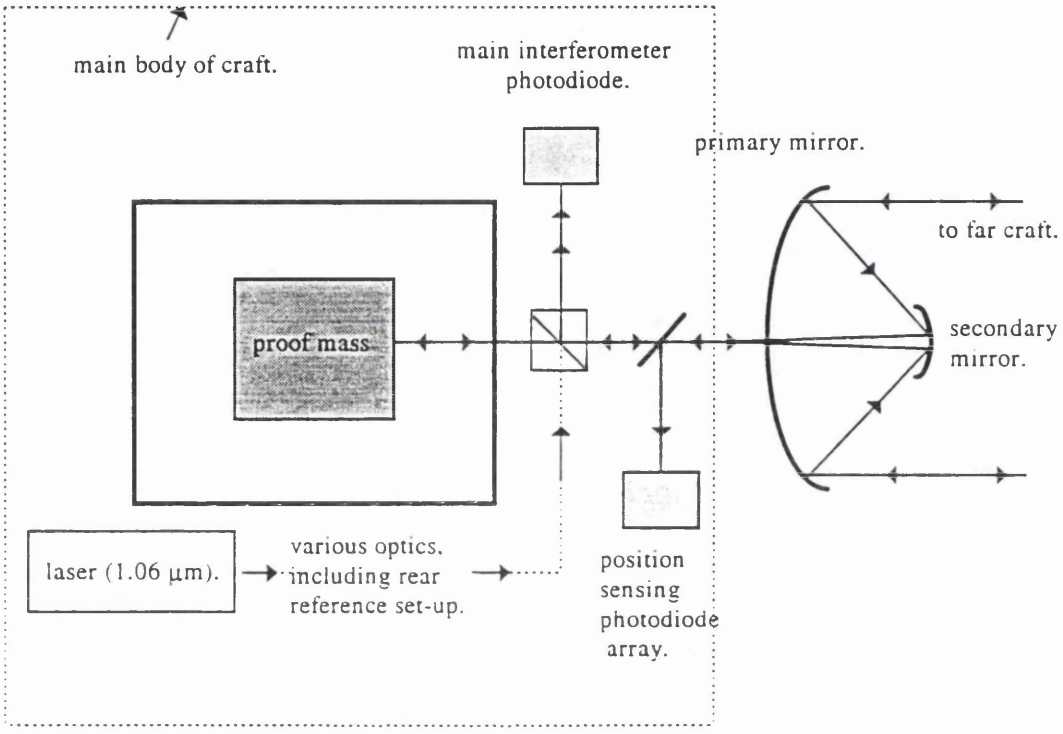

Fig.(6.2): Schematic diagram of spacecraft interior showing the position of the proof mass and transmit/receive optics.

Gravitational radiation would be detected by each spacecraft sensing a differential change in the phase of the laser beams being transmitted between each end/central craft pair. This phase change corresponds to a differential change in separation of the end and central craft. To ensure that the limit on the sensitivity set by noise is at a tolerable level, it will be necessary for the displacement noise associated with most noise sources in a single LISA craft to be restricted to $\delta x \leq 2 \times 10^{-12} \frac{\mathrm{m}}{\sqrt{\mathrm{Hz}}}$. Thus, the maximum value of phase error from the sources present in the system will be $\delta\phi \approx 1.2 \times 10^{-5}\ \mathrm{rads}/\sqrt{\mathrm{Hz}}$. It is unlikely in practice that either the transmitted wavefronts will be perfectly focused, or that the craft will maintain complete stability in the angular attitude obtained during the alignment phase. Failure to achieve both spacecraft attitude control and transmitted beam quality to a sufficient level of accuracy could have serious implications for the

accuracy of the phase measurement in the far-field; this situation forms the basis for much of the work reported in this chapter and will be covered in following sections.

6.1.2
Angular position noise and wavefront distortion in the transmit/receive telescope system.

Let us consider in more detail the Cassegrain f/1 telescope system used by each LISA craft for transmission and reception of the main interferometer laser beams (Fig.(6.3) below).

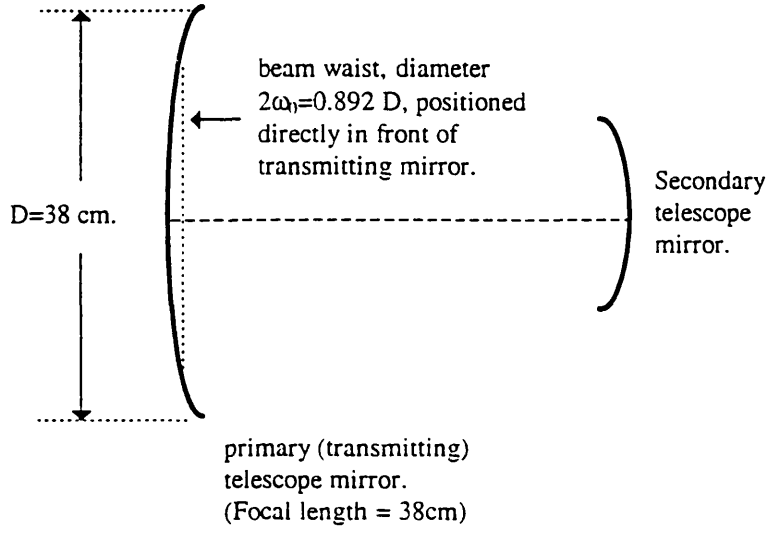

*Fig(6.3): **LISA transmit/receive Cassegrain telescope system.** Note ideal position of transmitted beam waist.*

The primary mirror diameter will be $D = 0.38$ m. It is intended that ideally the output beam for transmission to the far craft will form a waist of diameter $2\omega_0 = 0.892\,D$ immediately in front of the primary (transmitting) mirror; this value being chosen to give an optimal value of received power in the far field. Therefore one would expect the transmitted wavefronts to be plane at the mirror surface. However, it is more likely that the transmitted wavefront will have some degree of curvature imposed on it at the mirror, due either to displacement of the beam waist (by a distance 'y' from the mirror) or to the combination of surface quality defects throughout the optical system attached

to LISA occurring, e.g., in the optical fibres, and the large figure primary mirror. The net effect of these would result in curvature (i.e. a phase variation) across the transmitted wavefront, with the most serious form of near-field phase variation for our purposes being that of a single spatial cycle across the transmitted beam width.

Let us also consider the possibility of angular orientation noise in the LISA craft. Ideally, one would wish the transmitting and receiving craft to lie facing each other directly along the line of sight ('LOS') between the two telescopes. Due to position control limits imposed by the angular sensitivity of the alignment systems however they will most likely be subject to angular orientation noise, expressed in terms of two components; the static (or low frequency) offset from the LOS between the far and near craft, θ_{dc}, and the ac variation about this point, $\delta\theta$. The mechanism by which any angular orientation noise of the LISA craft can pick up the variation in phase across a portion of the incoming wavefront is now illustrated for the case of Gaussian beam defocus.

- Combined effect of angular orientation noise and wavefront distortion in the far-field.

As distances much greater than the [31]Rayleigh Range are involved the radius of curvature, $R(y)$, of the wavefront in the far-field is approximately equal to the distance between the measurement position and the waist position. If the beam forms a waist at the primary telescope mirror any angular change in position of the transmitting craft would merely cause the front to trace round its original position. No phase change would be detected in the far-field.

However, in the case of a defocused Gaussian beam (Fig.(6.4)) forming a waist at a distance 'y' in front of the primary mirror, we can see that the wavefront will no longer describe an arc whose centre of curvature lies at the pivot position. Thus the wavefront will change orientation with respect to receiving craft as the transmitting craft changes angular position, and an erroneous phase change will be detected. Similarly, in the case

---

[31] Rayleigh Range given by (Kogelnik & Li, 1966): $\frac{\pi \omega_o^2}{\lambda} \approx 9 \times 10^4$ m.

of optical surface imperfections, the centre of curvature of the transmitted wave will not lie at the transmitting mirror, also giving rise to an induced phase change in the far-field.

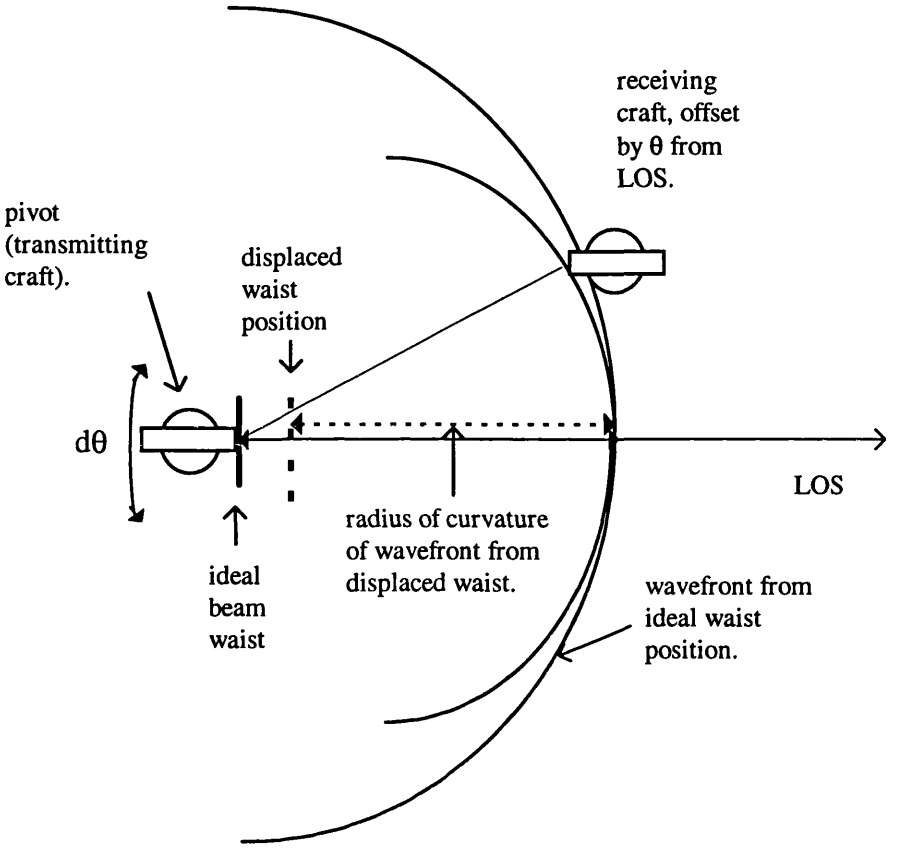

Fig(6.4): Diagram showing the difference in curvature of wavefronts emanating from a waist in the ideal position, and a displaced position.

The greater the spacecraft orientation noise level across the distorted phase front on the received beam, the higher the level of additional phase noise due to this source. Thus, from a reasonable estimate of pointing stability, one can define the likely requirements for the tolerable level of wavefront distortion in LISA. It would be useful at this stage to carry out an evaluation of the likely upper limit to the angular orientation noise of the system, defined by the shot-noise limited sensitivity of the alignment control system.

In the LISA system, light received from the far craft is used for angular orientation control in addition to the measurement of path length variations. A small fraction of the

light collected by the telescope is directed on to a multi-element diode (Fig.(6.2)), e.g. a quadrant photodiode, inside the body of the craft. Any change in the relative orientation of the transmitting and receiving craft will result in a shift in the beam across the photodiode, with a resulting change in the number of photons detected by individual quadrants. Provided the change in the number of photons detected is greater than the shot noise limited sensitivity, the photodiode will notice this shift in position and the spacecraft orientation will be correspondingly altered. We can use this information to calculate the limit to angular position sensitivity, $\delta\theta$, of the spacecraft. The value of static offset, θ_{dc}, will then be estimated to be a reasonable factor greater than this.

The incoming light power directed on to the LISA alignment photodiode is expected to be of the order $10^{-12}W$. As the frequency of the laser light is $\upsilon = 2.8\times10^{14}\,\mathrm{Hz}$, the number of photons arriving over 4 quadrants per second is given by:

$$N(s^{-1}) = \frac{10^{-12}}{h\nu} = 5.3\times10^{6}\,s^{-1} \qquad (6.1)$$

We can consider the effect of a change, $\delta\theta$, in attitude, along one axis of the photodiode array as follows. Let a beam of width 2σ, and originally illuminating each quadrant uniformly with n photons per quadrant in one second, move by an amount $\delta\sigma$, corresponding to a tilt of the spacecraft of $\delta\theta$. The number of photons now illuminating quadrant 1, say, is approximately $n+\frac{2n}{\sigma}\delta\sigma$ photons in one second, while the number illuminating the opposite quadrant (2) is given by $n-\frac{2n}{\sigma}\delta\sigma$ photons. Thus the total change in the number of photons detected across the two quadrants is $\frac{4n\delta\sigma}{\sigma}$.

This must be greater than the shot noise limit in order for the quadrant pair to detect the change. The total number of photons present in the beam in a 1s integration time is $4n\pm\sqrt{4n}$. Thus we can say that for detection of the shift in position of the beam to take place we must have:

$$\frac{\delta\sigma}{\sigma} \geq \frac{1}{2\sqrt{n}} \tag{6.2}$$

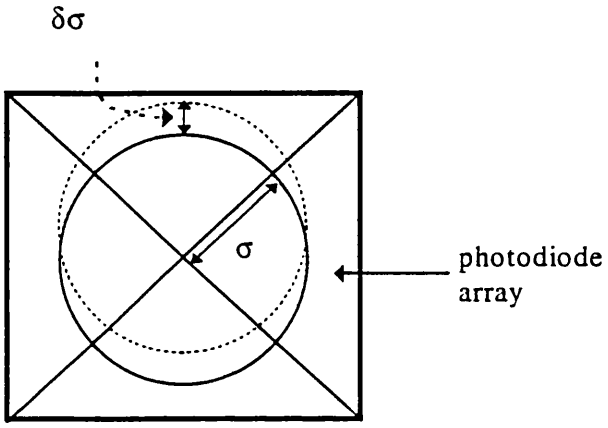

Fig(6.5): Shift of beam, radius σ, by an amount δσ, across one axis of the photodiode array.

As $\frac{\delta\sigma}{\sigma} = \frac{\delta\theta}{\theta}$, where θ is the angular resolution of the mirror in this case, we can say that the shot noise limited quadrant photodiode sensitivity isapproximately set by:

$$\delta\theta = \frac{1.22\lambda}{D2\sqrt{n}} \approx 1\text{nrad} \quad \text{in a 1s integration time.} \tag{6.3}$$

Based on these calculations, acceptable values of dc angular position offset from the nominal line of sight (LOS), θ_{dc}, and tilt noise, $\delta\theta$, of the receiving craft are generally taken to be $\theta_{dc} = 30$ nrads and $\delta\theta \approx 5$ nrads $/\sqrt{\text{Hz}}$, with an arbitrary safety factor built in for both cases, and combining to give a value of $|\theta_{dc}\delta\theta|_{LOS}$, of $1.5\times10^{-16}\ \text{rad}^2/\sqrt{\text{Hz}}$.

We must now find an expression for the variation in the phase of the beam received in the far-field as the transmitting craft is subjected to this angular position noise. This will also be related to the wavefront quality (i.e. the amount of phase variation imposed across the beam) on transmission. Thus, as we have already estimated $|\theta_{dc}\delta\theta|_{LOS}$, and

know that $\delta\phi \approx 1.2\times10^{-5}\,\text{rads}/\sqrt{\text{Hz}}$, we can set a reasonable limit on the level of distortion present on the transmitted beam. This will provide some indication of the accuracy required on the waist position, and also on the surface finish of the optics. We shall begin this process by describing a suitable method of finding the far-field phase variation from that in the near-field, which is based on standard Fraunhofer diffraction methods.

6.1.3
Phase variation in the far field - an introduction to the method used.

We can find the amplitude of the transmitted wave in the far field as an angular distribution about the transmitting mirror by considering the problem in terms of Fraunhofer diffraction of the transmitted wave. Here we must replace the transmitting telescope mirror with an equivalent diffraction aperture whose surface has a varying optical thickness along its length; this will provide a net phase shift on transmission which can be made equivalent to that imposed by the wavefront distortion. The diameter of the aperture will be the diameter of the primary telescope, while the net phase shift incurred will be represented by use of the appropriate aperture function, $a(z)$ (Braddick, 1965). A slit or other opening will have an aperture function $a(z)=1$. Where the aperture is covered with some form of attenuating material, $a(z)$ will be a real number, whilst if the material also changes the phase of the transmitted wave $a(z)$ will be represented by a complex number. By taking the Fourier Transform of the aperture function describing the system, an expression can be found for the amplitude of the diffracted wave, ψ, (Braddick, 1965) from which an expression for the phase, ϕ, can be extracted, i.e.:

$$\Psi = e^{-j2\pi\nu t}\int_{-\infty}^{+\infty} a(z)e^{\frac{j2\pi z\sin\theta}{\lambda}}dz$$

$$= \psi\, e^{-j2\pi\nu t} \tag{6.4}$$

where $\phi = \frac{\Im m(\psi)}{\Re e(\psi)}$. We must first find the form of aperture function which adequately describes the phase front variation across the transmitted beam. Let us consider the wavefront configuration on transmission in the case of Gaussian beam defocus, where the waist has been displaced by a distance y from the mirror surface. We can see (Fig.(6.6)) that the front lying at the mirror surface (shown here as the z-axis) will be curved rather than plane, with radius of curvature given by, e.g., Kogelnik & Li (Kogelnik & Li, 1966):

$$R(y) = y\left(1+\left(\frac{\pi\omega_0^2}{\lambda y}\right)^2\right) \tag{6.5}$$

As can be seen in Fig.(6.6) this curvature means that the centre of the transmitted front will lag the outermost portions by a maximum path length value of magnitude d. The magnitude of the phase shift at any point, z_t, measured from the centre of the wavefront, incurred due to this distortion, can be found from $\phi = 2\pi T/\lambda$. The direction of the y-axis denotes the direction of propagation of the beam. (It should be noted that this model may also be used when considering the effect of non-ideal optical surfaces in the LISA system. In fact, any limit to the value of d found in this way will represent the maximum phase shift allowed at one telescope from either optical surface imperfections or beam defocus).

From geometry (where $z_t << R(y)$), the optical path difference T across the curved Gaussian front can be expressed as:

$$T(z) = d - t(z) \approx d - \frac{z_t^2}{2R(y)} \tag{6.6}$$

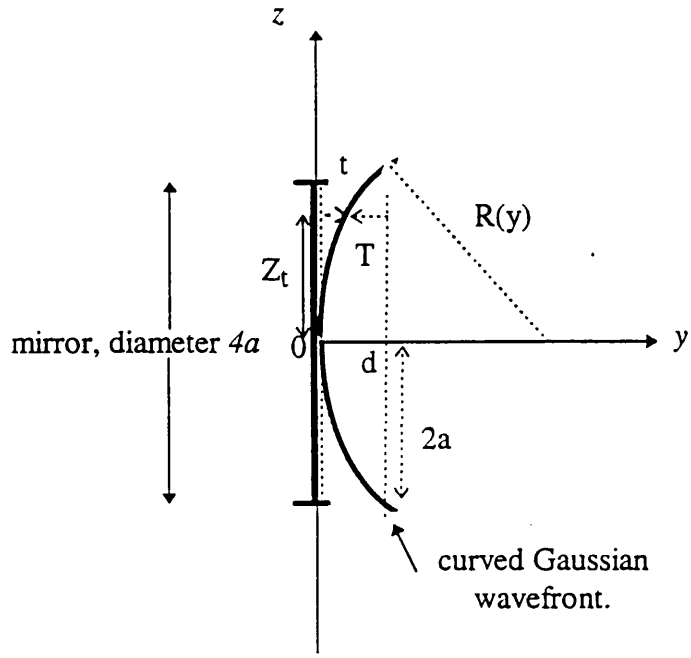

Fig.(6.6): Wavefront curvature of amplitude d at transmitting mirror due to Gaussian beam defocus.

Also from geometry we can redefine $R(y)$ in terms of a and d (assuming $a >> d$) as $R(y) \approx 2a^2/d$, thus:

$$T(z) \approx d - z_t^2 d\left(\frac{0.25}{a^2}\right) \tag{6.7}$$

The phase variation across the Gaussian wavefront can be reasonably represented by a single half cycle cosine function phase variation of amplitude d (Fig.(6.7)).
At any point across this cosine wavefront the imposed optical path difference can be expressed as $T = d\left(1 + \cos\theta\right)$, where θ has a range of $-\frac{\pi}{2} \rightarrow \frac{\pi}{2}$ across the aperture, whose diameter extends from $-2a \rightarrow 2a$ along the z axis as illustrated. Thus we can

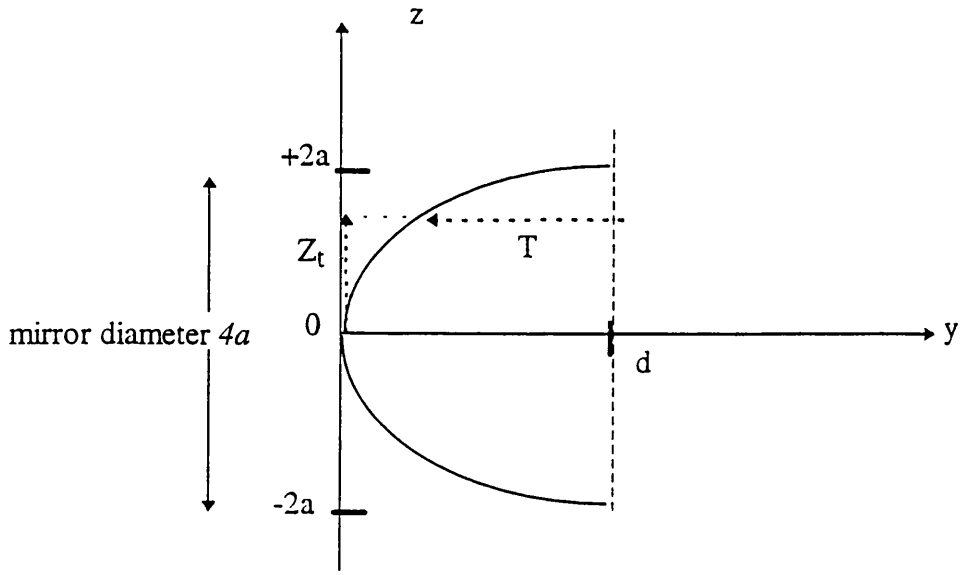

Fig(6.7): Wavefront curvature at the transmitting mirror for the case of a half spatial cycle cosine function distortion of amplitude d.

say that $\theta = \frac{\pi z}{4a}$ and, from the expansion for $cos\theta$ (where θ is small), we can also say:

$$T \approx d\cos\theta \approx d\left(1 - \left(\frac{\pi^2 z_t^2 d}{16a^2\, 2!}\right)\right) \approx d - z_t^2 d\left(\frac{0.31}{a^2}\right) \qquad (6.8)$$

Comparison of equation (6.8) with equation (6.7) indicates that the imposed optical path length (hence phase) variation of the defocused Gaussian beam and the cosine phase variation in the near field are of a similar form for the central region of the beam, with the cosine case in fact showing a slightly more pessimistic value. The equivalent aperture function would be described by $a(z) = exp\left[-j\left(kd\cos\frac{\pi z}{4a}\right)\right]$. It shall now be shown that, to a level of accuracy acceptable for this case, this aperture function can be further simplified by the use of a centrally-symmetric step-function phase delay across the aperture.

6.2
Fraunhofer diffraction method applied to the case of Gaussian beam defocus.

It has been seen already that the defocused Gaussian wavefront, with maximum path length variation of magnitude *d*, is well approximated by a cosine variation of amplitude *d*. However, it is generally much simpler to carry out the Fraunhofer diffraction analysis using a centrally-symmetric step function aperture, where the path length variation is incurred as a central 'step' of height *d*. It will be demonstrated here that this form of aperture is a good approximation to that of the cosine variation. The propagation of plane waves, normally incident on these apertures, will be assumed for these proofs. Investigation of the effect of the Gaussian amplitude profile on phase noise will be carried out in later sections.

6.2.1
Comparison of centrally symmetric cosine and step-function phase delay apertures.

- Cosine aperture result

We shall consider first the simple case of plane wave propagation through the cosine phase-delay aperture described above in section 6.1.3. Recalling equation (6.4), the amplitude in the far field of a plane wave diffracted through such an aperture can be written as:

$$\text{amplitude} = \psi_{cosine} = \int_{-2a}^{+2a} e^{i\left(kz\sin\theta - kd\cos\frac{\pi z}{4a}\right)} dz \qquad (6.9)$$

The exponential terms can be expanded using De Moivre's theorem for complex exponentials. From the resulting expression we find that the phase term associated with this waveform is given by:

$$\phi_{cos} = tan^{-1}\left\{\frac{\int_{-2a}^{+2a} sin\left(kz\sin\theta - kd\cos\frac{\pi z}{4a}\right)}{\int_{-2a}^{+2a} cos\left(kz\sin\theta - kd\cos\frac{\pi z}{4a}\right)}\right\}dz \qquad (6.10)$$

This can be simplified by substitution of the standard expansions for $sin\theta$, and $cos\theta$, taken to third order in θ, assuming θ is small. Thus, $sin\theta \approx \theta - \frac{\theta^3}{3!} + ...(terms)$ and $cos\theta \approx 1 - \frac{\theta^2}{2!} + ...(terms)$ can be substituted into equation (6.10).

After the resulting phase expression has been integrated we obtain the following expression for the phase at a point in the far-field:

$$\phi_{cosine} \approx \frac{3dk^3a^3\theta_{dc}^2}{\pi\left(4a - ak^2d^2 - \frac{8a^3k^2\theta_{dc}^2}{3}\right)} \qquad (6.11)$$

As can be seen from the θ_{dc}^2 terms, the phase of wavefronts arriving at the far craft is symmetric about the nominal line of sight, as one would expect. Differentiation with respect to θ gives us our final expression for $\left.\frac{d\phi}{d\theta}\right|_{\substack{plane \\ cosine}}$, namely the variation in phase in the far-field with position fluctuation of the craft transmitting the beam. Here the terms $a^3k^2\theta^2 \approx 10^{-14}$ and $\left(ak^2d^2\right)/4 \approx 2\times10^{-3}$ were assumed to be negligible:

$$\left.\frac{d\phi}{d\theta}\right|_{\substack{plane \\ cosine}} \approx -\frac{6}{4\pi}\left(k^3 d\, a^2\theta_{dc}\right) \qquad (6.12)$$

Now, recalling that that mirror diameter is defined to be $D = 4a$ we can rewrite equation (6.12) in the form:

$$\delta\phi\big|_{\substack{plane\\cosine}} \approx -\frac{1}{33}\left(k^3 d\, D^2 \big|\theta_{dc}\delta\theta\big|_{LOS}\right) \tag{6.13}$$

- Step-function phase delay aperture.

We shall compare the result in equation (6.13) with that for the simple case of the following single slit of height 4a in the z-direction. The aperture functions describe the introduction of a step-function phase shift of magnitude kd on light passing through the central section, where $k = 2\pi/\lambda$. In reality this would look, e.g., like a step of height $d/2$ on the centre of the transmitting mirror.

The amplitude of the transmitted wave in the far field can again be described by

$$\psi = \int_{-2a}^{+2a} a(z) e^{jkz\sin\theta}\, dz \tag{6.14}$$

Substitution of the appropriate aperture functions (Fig.(6.8)) followed by integration of the resulting expression yields:

$$\Psi = e^{j2\pi\nu t}\left[\frac{1}{jk\sin\theta} j\sin(2ka\sin\theta) - 2j\sin(ka\sin\theta)) + \frac{e^{-jkd}}{jk\sin\theta}\left(2j\sin(ka\sin\theta)\right)\right] \tag{6.15}$$

Now, $\sin(ka\sin\theta) \approx ka\sin\theta$, $\sin 2\theta = 2\sin\theta\cos\theta$ and $e^{-jkd} \approx (1 - jkd)$. Thus, our equation becomes:

$$\Psi = e^{j2\pi\nu t}\left(4a\cos(ka\theta) - j2akd\right) \tag{6.16}$$

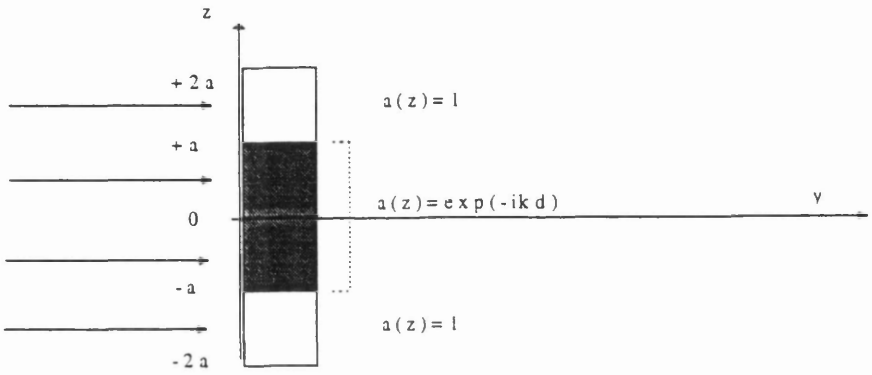

Fig(6.8): Centrally symmetric aperture, incurring a phase shift of magnitude kd on light passing through centre.

where small angle approximations have been taken for $ka\theta$ and θ. The resultant phase of this wave is found in the usual way, thus:

$$\phi = \frac{-kd}{2\cos(ka\theta)} \approx \frac{-kd}{2}\left[1 + \frac{k^2a^2\theta^2}{2}\right] \tag{6.17}$$

The rate of change of phase measured at a point in the far field with angular orientation of the transmitting craft is thus:

$$\delta\phi = -\frac{1}{32}\left(k^3 d D^2 \theta_{DC}\,\delta\theta\,|_{LOS}\right) \tag{6.18}$$

If we now compare equation (6.13), obtained using the cosine aperture, with equation (6.18) above we can see that they differ only by the numerical constants 1/33 and 1/32 respectively. This error of approximately 3 % is considered tolerable for our purposes as the use of the step-function phase delay aperture will provide the 'worst case' value. This form will be assumed for use in the final stage (section 6.2.2) where we shall introduce the variation in *amplitude* across the aperture due to the Gaussian nature of the beam intensity profile.

6.2.2
Effect of Gaussian amplitude profile on step-function result.

Recall the expression for diffracted amplitude in the far field due to plane wave illumination of the centrally symmetric step-function aperture previously described (equation.(6.14)).

As a first approximation to the Gaussian amplitude-weighted form of this expression, we shall introduce an amplitude weighting, $W(z)$, corresponding to the average amplitude of the part of the Gaussian profile each section encounters. It is firstly necessary to find the approximate form of our weighting term.

- Gaussian Amplitude weighting factor

From the theory of Gaussian optics given, e.g. by Kogelnik & Li (Kogelnik & Li, 1966), it is stated that the amplitude of the Gaussian (also known as the fundamental, or TEM_{00}) mode of propagation of a beam in the y direction is given by:

$$\psi = exp\left\{-j\left(P(y)+\frac{kr^2}{2q(y)}\right)\right\} \tag{6.19}$$

Here $P(y)$ represents a complex phase shift, r the distance from the optic axis, and $q(y)$ the complex beam parameter which contains information regarding the Gaussian intensity distribution of the beam. $q(y)$ is defined to be:

$$\frac{1}{q(y)} = \frac{1}{R(y)} - j\frac{\lambda}{\pi\omega_0^2} \tag{6.20}$$

As this is a one-dimensional treatment the radius vector $r = \sqrt{x^2 + z^2}$ has value z. In addition, if we assume for simplicity that we have a waist, of diameter 0.892 D, lying on the mirror surface we can set $\frac{1}{R(y)} = 0$ and equation (6.19) becomes:

$$\psi(r,y) = e^{\frac{-r^2}{\omega_0^2}} e^{-jP(y)} \tag{6.21}$$

From this we can isolate the weighting factor, expressed as :

$$W(z) = e^{\frac{-z^2}{\omega_0^2}} \tag{6.22}$$

which should be included in each of our original plane-wave integrals, equation (6.14), with the values of z depending on which part of the aperture is concerned. As the beam is arranged to form a waist of radius $\omega_0 = 0.446D$ at the primary mirror, we can express ω_0 in terms of a. For LISA, the primary mirror diameter is $D = 4a = 0.38\,\mathrm{m}$. Thus $\omega_0 = 1.78a$, and our Gaussian amplitude weighting expression is now of the form:

$$W(z) = exp\left(\frac{-z^2}{3.24a^2}\right) \tag{6.23}$$

To simplify the integration process, typical values of z will be inserted into each aperture section of equation (6.14), enabling a first approximation to the Gaussian weighted far-field amplitude expression to be found; e.g. for the central sections of the aperture let $z = \pm\frac{a}{2}$, thus $W(z)$ for the central section becomes:

$$exp\left(\frac{-z^2}{\omega^2(y)}\right) = exp\left(\frac{-a^2}{4(3.24)a^2}\right) = 0.92 \tag{6.24}$$

Similarly, for the outer sections, let $z = \pm\frac{3a}{2}$, whereupon:

$$exp\left(\frac{-9a^2}{4(3.24)a^2}\right)=0.5 \tag{6.25}$$

So our far-field amplitude expression for the whole diffracted Gaussian beam through a step-function aperture is now:

$$\psi = \int_{-2a}^{-a}(0.5)e^{ikz\sin\theta}dz + \int_{-a}^{+a} e^{-ikd}(0.92)e^{ikz\sin\theta}dz + \int_{a}^{2a}(0.5)e^{ikz\sin\theta}dz \tag{6.26}$$

which can again be integrated and put into complex form. Thus:

$$\frac{d\phi}{d\theta} = -0.9\left(\frac{k^3 d\, D^2\theta_{dc}}{32}\right) \tag{6.27}$$

i.e.

$$\left.\frac{d\phi}{d\theta}\right|_{\substack{Gaussian\\Step}} = 0.9\times\left(\left.\frac{d\phi}{d\theta}\right|_{\substack{Plane\\Step}}\right) \tag{6.28}$$

This expression (equation (6.28)) will remain true for any mirror diameter, provided the beam waist formed at the mirror has radius $\omega_0 = 0.446D$. It has been noted (Robertson, 1993), that a more pessimistic result of $\delta\phi \approx -\left(k^3 d\, D^2\, \theta_{dc}\delta\theta\right)/13$ can be obtained where truncation of the Gaussian beam is not built in to the calculation. However, this is not the situation in LISA, as truncation of the beam will occur upon reflection from the transmitting mirror. This clipping of the beam has been accounted for in the above aperture-based calculations.

Thus, although close in value to the Gaussian result, the case of a plane wave propagation through the cosine-function aperture shows a slightly worse case of beam distortion, and (for simplicity) is assumed for general use.

6.3
Summary of results and implications for the tolerable limit to wavefront distortion.

We wished to find a reasonable model for the effect of Gaussian beam defocus or poor optical surface quality on the error in phase measured in the far-field, where the imposed near field distortion was a half spatial cycle across the transmitted beam. Using a simple one-dimensional treatment it has been shown that the case of Gaussian beam defocus, where the maximum induced path difference across the wavefront has magnitude d, can be reasonably represented by a half spatial cycle of a centrally symmetric cosine variation of amplitude d. Plane wave propagation was assumed throughout, and it was noted that the use of a cosine function was only a good approximation to the defocused Gaussian beam case in the central region of the transmission aperture. It was also shown that this in turn could be further simplified to the form of a centrally symmetric step-function of step-height d. These approximations incurred errors of approximately 3 %, but showed the 'worst case' values of each. Thus it is to be expected that the use of the step function approximation would in fact show a more pessimistic result than would perhaps be the case. Similarly, when the approximate effects of Gaussian variation in laser beam intensity was included across the aperture, it could be seen that the plane wave propagation results were again a simplified 'worst case' measure of the situation. Thus the following expression for phase variation with spacecraft angular position noise and wavefront distortion was found:

$$\delta\phi = -\frac{1}{32}\left(k^3 d\, D^2 \left|\theta_{DC}\,\delta\theta\right|_{LOS}\right) \tag{6.18}$$

We can now use equation (6.18) to evaluate a reasonable working limit to d. For this we must recall that the angular position noise, $\left|\theta_{dc}\delta\theta\right|_{LOS}$, was estimated to be of order $1.5\times10^{-16}\ \mathrm{rad}^2/\sqrt{\mathrm{Hz}}$ (section 2.1.1), and that the limit to the measured phase due to

each noise source per craft is given by $\delta\phi \approx 1.2\times10^{-5}$ rads/$\sqrt{\text{Hz}}$. Thus, where $D = 0.38\,\text{m}$, and $k = \frac{2\pi}{\lambda} = \frac{2\pi}{10^{-6}}$, we can see that:

$$d \leq \frac{\lambda}{14}\,\text{m} \tag{6.29}$$

- Limits to optical surface distortion.

The implications of this limit to the required surface quality of the optical components are relatively straightforward. For many optical components, e.g. the primary mirror, the phase shift will be effectively doubled due to the double passage of light on reflection. Thus the surface quality specification for the LISA optical system, '*d/2*', has a value of $\frac{d}{2} \leq \frac{\lambda}{28} \approx 35$ nm which corresponds to the amplitude of the variation across the beam width.

- Limits to Gaussian beam waist displacement.

The maximum value of d allowed in the system will also have implications for the magnitude of the tolerable displacement of the beam waist from the transmitting mirror. We must first find the relationship between the maximum optical path variation across the transmitted beam, d, and the distance y between the displaced waist and the transmitting mirror. From the geometry of the situation (Fig.(6.9) below), we can see that d and the radius of curvature, $R(y)$, of the front lying on the mirror surface are related by:

$$R(y) \approx \frac{2a^2}{d} \tag{6.30}$$

where it has been assumed that $4a^2 >> d^2$.

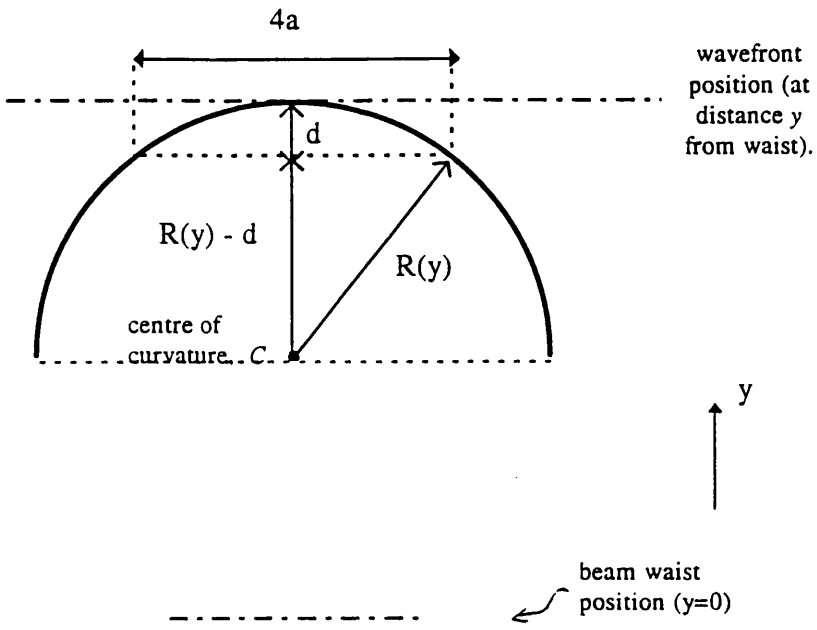

Fig.(6.9): Wavefront geometry relating radius of curvature, R(y), to wavefront distortion, d.

We can also relate $R(y)$ to y for the LISA system, where $\omega_0 = 0.446(4a)$, by:

$$R(y) = R(y) + \frac{10\pi^2 a^4}{\lambda^2 R(y)} \tag{6.31}$$

Substituting equation(6.30) into (6.31), and solving for y gives the result that

$$|y| \leq 3.7 \times 10^4 \text{ m} \quad or \quad |y| \leq 2.1 \times 10^4 \text{ m}. \tag{6.32}$$

Generally we shall take the former value as the limit to the distance between the mirror and the waist. The second solution arises due to the fact that the beam reaches maximum curvature at one Rayleigh Range, thereafter reducing in curvature again. This gives rise to another value of displacement where the radius of curvature at the mirror results in a maximum path variation of d.

It is expected that, with careful design, the requirements on both surface quality and waist displacement would be met, allowing the magnitude of the noise expected from this source to be maintained within the limit required by the system specifications.

Chapter 7
General Conclusions.

Much of the work outlined in this thesis has been directed towards developing the GEO 600 test mass pendulum suspension system, which is comprised of a seismic isolation stage followed by the suspension of the test mass from fused silica fibres. Reviews of the theoretical work underpinning these systems have been given in Chapters 1 and 3, and throughout Chapter 2.

The work reported in Chapter 2 has covered several areas relevant to the seismic isolation of the suspended test masses employed in laser interferometric gravitational wave detectors. In particular, the behaviour of RTV 615 silicone rubber has been investigated, where it was found that although RTV obeyed standard rules governing the behaviour of rubber in the horizontal (for strains of up to 30%), the vertical dynamic characteristics did not. It has been found that silicone rubber of this type displays a significantly higher compression modulus than predicted, which was found to be linear increasing for the range of mass values tested (where induced strain was less than 30% or so in all cases). Further investigations of RTV cylinders, with shape factor, S, ranging from 0.16 to 1.0, and under loads ranging from 0.7 kg - 4.3 kg, have shown that, in the unloaded state, the compression modulus of RTV was markedly higher for units with low shape factor than for those with a higher shape factor. In addition to this, the subsequent *rate* of stiffening with applied stress once load is applied is significantly *less* for low shape factor units than for high shape factors. The rate of stiffening for the rectangular unit tested was less than the cylindrical trend would have predicted for that shape factor, implying that perhaps this stiffening rate could be dependent also on the

surface configuration of the unit. Possible reasons for the observations made are discussed in the conclusions to section 2.3.4. These hypotheses will, of course, require further testing and possibly also additional information on, e.g., the physical chemistry of RTV, but the empirical formulae found as a result of this work have been seen to hold within tolerable limits of accuracy for units of the shape factors tested.

These results serve to illustrate the relative complexity of the behaviour of RTV compared to more standard rubbers. Certainly, the correct general use of RTV units, whose shape factor lies outwith the range of this test, will rely on further knowledge of the shape-dependent behaviour observed here.

Results following the identification of load-stiffening behaviour in RTV were then applied to the case of a replacement test-mass stack for the Glasgow 10 m prototype detector. This stack was constructed from separate identical legs separated by the RTV rectangles tested. Performance tests carried out (section 2.2) on the full stack provided extremely encouraging results, where good mechanical stability and adequate levels of isolation were predicted to be achieved. In particular, the use of small, stiff stack masses (rather that the horseshoe-shaped masses used prior to this redesign) prevented the problem of internal modes appearing in the frequency range of interest. Subsequent changes to the design of the double pendulum of this system have led to a less efficient overall performance of the system, however work is continuing (Killbourn, 1996) to reduce this problem as has been discussed in section 2.3.3.

Much of this stack design has formed the basis of a simple possible stack design for the GEO 600 detector. It was proposed that RTV units, of a shape factor already modelled empirically, be used in this stack, thus allowing the load-stiffening behaviour to be accounted for in any performance modelling carried out. In spite of this non-standard behaviour, RTV was chosen for use mainly due to its low out-gassing rates, although additional shielding would be required to comply with the stringent vacuum levels set for GEO 600. The use of stainless steel vacuum bellows as a possible capsule for these units was investigated in section 2.4.2, where the presence of high order modes was noted. These modes are extremely undesirable in any form of isolation system, but were successfully removed through the use of a grease lining in the bellows convolutions. As a result of the experiments carried out, it is thought likely that some form of bellows will be incorporated into the final GEO 600 isolation stack design.

The simple design proposal for the GEO 600 outlined in section 2.4 was intended for use where the working frequency range of the detector would lie above 100 Hz. Predictions of the vertical and horizontal transmissibility of this stack have shown that in principle a combination of soft metal bellows and load-stiffened RTV units may provide adequate isolation at 100 Hz, thus allowing the GEO 600 seismic isolation sensitivity goal of $h \approx 10^{-22}/\sqrt{\text{Hz}}$ to be met.

The work reported in Chapter 4 has highlighted the importance of effective reduction of recoil damping in the support structure used for the measurement of the pendulum quality factor of low-loss oscillators. In particular an expression was found defining the measurable limit of Q_{pend} in terms of the complex spring constant of the structure. Development of an effective technique for measurement of complex spring constant has allowed the evaluation of this limit of $(2.36 \pm 0.29) \times 10^7$ for a 210 g mass in the current system. It is expected that Q_{pend} measurements of order 10^7 should now be possible and free from the effects of recoil.

Preliminary Q_{pend} measurements, for hand and oven-pulled fused silica fibres supporting a 210 g glass mass yielded results of 1.9×10^6 and 3.07×10^6 respectively. Both results were lower than hoped but have served to highlight areas for future work if successful measurements of pendulum quality factors of 10^7 are to be achieved. Future work will include further tests of 210 g glass masses with both cylindrical and ribbon oven-pulled fibres. Eventually, it is also intended that the question of fibre attachment be addressed, again with light masses for initial tests. As contamination of the fibres during pendulum construction, albeit on a microscopic level, was observed to seriously affect results a more suitable method of construction will be adopted. This may involve optically contacting the fibres to the sides or top of a 500g silica mass, thus removing the need for Torr Seal near the fibres. This will also allow the pendulum, violin and internal modes of the pendulum to be investigated for this jointing method. As the final GEO 600 suspension will consist of a 16 kg mass it is intended that suitable fused silica fibres be used to suspend a mass such as this in dry Nitrogen. This will allow fatigue tests of fused silica to be carried out; to date there is no information on the long term behaviour

of our fibres under load; therefore this is an important area for our purposes which should not be overlooked.

Work will also continue on the RF oven operation. Preliminary tests have indicated that the oven method has produced fibres with a uniformity of diameter far exceeding their hand-pulled counterparts.

Fibres used for this experiment were part of an initial batch from the oven. Measurements have also been undertaken on the material quality factor of similar fibres, the results of which were outlined in Chapter 5. This has involved setting up a suitable test environment, and software system which has been successful in collecting and manipulating data. Although the initial tests were carried out on ribbon fibres, which mainly vibrate in only one dimension, the set-up was designed as far as possible to accommodate cylindrical fibres in future tests.

It could be seen from initial tests made on a ribbon fibre of thickness 160 μm that both the experimental equipment and the software system operated reliably, although low values of Q_{mat}, of around 2×10^{4} for the fundamental mode, were observed for this fibre. These low values were thought to be due to an inadequate thickness of the clamped end of the fibre, and possibly also due to uptake of water by the fibre from the atmosphere.

However, these experiments have been recently repeated using a fibre of thickness 54 μm where much better results have been obtained. Here measurement was made (Hough et al, 1996) of the ring-down times of the fibre amplitude for the fundamental mode and the first three harmonics. Clamping was improved by using the broadened, thicker end of the fibre where the slide from which the fibre was pulled was still joined, and atmospheric exposure was limited by the storage of fibres in an argon tube. The resulting values of Q_{mat} were noticeably higher than previously measured, with values at the various resonant frequencies lying in the range $7\times10^{5}-3.4\times10^{6}$, although some spreading of the results were observed at each frequency due to mode coupling.

The much higher values of material Q measured here have welcome implications for the value of pendulum Q achievable with such fibres. Recalling equation (3.29(a)) (footnote, section 3.3.2), where four wires are used for the suspension values of $Q_{mat}\approx7\times10^{5}$

should allow at least $Q_{pend} \geq 10^8$ to be achieved. This is well above the value of 10^7 required by GEO 600. However, to date pendulum quality factors of this order have not yet been measured experimentally at Glasgow, although work is continuing in this area (Rowan et al, 1996). Although most of the experimental and practical issues associated with measurement of pendulums of such high Q have been addressed, there remain areas where investigation is still underway.

Chapter 6 has dealt with the question of the required wavefront quality for the transmitted laser beams in the spaceborne gravitational wave detector, 'LISA'. Current estimates indicate that the phase measurement noise due to the combined effect of craft angular position noise and wavefront distortion must not exceed $\delta\phi \approx 1.2 \times 10^{-5}\ rads/\sqrt{Hz}$ for the required sensitivity to be reached (section 6.1.1). For a reasonable estimate of the angular position noise of the transmitting craft of $|\theta_{dc}\delta\theta|_{LOS} \sim 1.5 \times 10^{-16}\ rad^2/\sqrt{Hz}$ (section 6.1.2) this has led to a working specification on the combined surface quality of optical components in the LISA system, and also on the maximum tolerable beam waist displacement. Assuming the case of a cosine phase variation across the transmitted beam, a series of approximations were made which indicated that the case of Gaussian beam waist displacement could be represented by the much simpler case of plane wave propagation through a centrally-symmetric step-function aperture. The central 'step' gave rise to a phase delay, '*d*', on light passing through which was shown to give the following expression for phase variation in the far-field with angular position noise of the transmitting craft (equation (6.18)):

$$\delta\phi = -\frac{1}{32}\left(k^3 d D^2 |\theta_{DC}\,\delta\theta|_{LOS}\right)$$

It was also shown (section 6.2) that this step-function model result in fact gave a more stringent restriction than would actually be the case for a true displaced Gaussian beam, giving rise to an upper limit to the allowed beam waist displacement of $|y| \leq 3.7 \times 10^4$ m . As this step-function model provides a simplified way of dealing with the problem of Gaussian beam displacement, and gives the more pessimistic result, it is

generally used in calculations (Jafry, 1995), (Bender et al, 1996). In the case of optical surface defects, it was found that the maximum tolerable deviation arising from the entire optical system was of order 35 nm for a laser beam wavelength of 1.06 μm.

Finally, in Appendix A of this thesis, calculations and results for the theoretical investigation of the likely level of cross-coupling present in the second stage of the GEO 600 double pendulum were reported. At frequencies above ~ 100 Hz, this level was found to be constant, and has been denoted by the cross-coupling constant, *C*. By analysing the equations of motion of a mirror mass of moment of inertia, *I*, suspended by two wires (which differ in spring constant by δk) whose break-off positions on the mass are separated from the line through the centre of mass by a distance *2r*, the following equation for the cross-coupling transfer function at high frequencies (> 100 Hz) was found (equation (A.34)):

$$\frac{\delta x}{\delta y_c} \rightarrow \frac{r \delta k \chi}{I \omega_{pv2}^2} = C$$

This term is due to rocking of the mass about the centre of mass, with the cross-coupling arising as a result of a beam centring error, χ. An additional term, due to real horizontal translation of the centre of mass, becomes negligible in this frequency region. For [32]GEO 600 parameter values (equation (A.36)) this has been evaluated to be $C \approx 10^{-3}\%$.

Cross-coupling effects arising due to the effect of the radius of curvature of the Earth over the length of the interferometer arm have also been investigated. As reported in equation (A.3), the level of cross-coupling expected to arise in this case for GEO 600 is of order $C \approx 4.8 \times 10^{-3}\%$, giving rise to a combined cross coupling level at a single mass of $C_{TOTm} \approx 5 \times 10^{-3}\%$. As a rule, calculations for the GEO 600 system generally use the overestimated cross-coupling level of 0.1%.

[32] Equation (A.34) has also been applied to the case of the Glasgow 10 m prototype pendulum suspension, allowing the evaluation of the cross-coupling level of $C_{10m} \approx 0.1\%$ used in section 2.3.3

Appendix A
Cross-coupled transmission of vertical seismic noise in the GEO 600 test mass suspension system.

A1
Introduction

The importance of effective vertical isolation in passive anti-vibration systems, due to the presence of vertical to horizontal cross coupling mechanisms, has already been discussed in Chapter 2. There are various routes through which vertical to horizontal cross-coupling can occur, for instance through stiffness imbalance in the stack rubber units ((Cantley, 1991), (Giaime, 1994)). However, it is unlikely that cross-coupling in the stacks will be the only source, particularly where long or intermediate baseline detectors are concerned. Such will be the case for GEO 600 where it is expected that vertical to horizontal cross-coupling will arise, e.g., due to the angular offset of each test mass induced by the radius of curvature of the Earth's surface. In section A2, we shall evaluate this effect.

Additionally, the GEO 600 system is expected to consist of an upper stage on a single loop suspension attached to the centre of mass, followed by the test mass which is suspended by either four separate fibres, or a double loop, with the lower break-off points situated away from the centre of mass. It would therefore seem likely that most of the cross coupling would occur at the test mass stage due to the [33]geometry of the suspension arrangement - most likely through some inequality of the stiffness or the positions of the suspension wires. The preliminary study of this case is examined in section A3 for a 2-dimensional model, where it is assumed for simplicity that the mass is suspended on two identical pairs of wires or fibres.

---

[33] A study of the cross-coupling of an alternative system - a nested double pendulum - has been reported in (Stephens et al, 1991), where cross-coupling was seen to be most severe where there was misalignment of the suspension wire break-off points.

A2
Analysis of cross coupling due to the radius of curvature of the Earth.

First of all, let us consider a single arm, of length l, of a detector whose suspended test masses subtend an angle 2θ at the Earth's core (Fig.(A.1)). The radius of the Earth, R_E is $\sim 6.3 \times 10^6$ m.

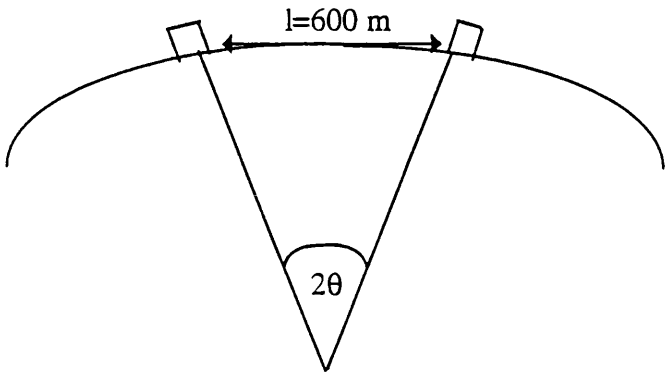

Fig(A.1): Single arm of interferometer subtending angle 2 θ at Earth's core.

The weight of each suspended mass, mg, will act downward along the direction of the Earth's radius. However, the test masses are also servoed to ensure that their reflective faces remain perpendicular to the incoming beam, which of course travels in a purely horizontal direction from each reflection and does not follow the Earth's surface curvature. Fig.(A.2) below shows schematically how this situation leads to the detection of horizontal movement of the mirror mass as a result of a purely vertical noise input.
A given disturbance, δy_0, will act in the true vertical direction (that is, along the direction of the Earth's radius and perpendicular to the tangent to the surface of the Earth at that point). This vertical noise input will 'bob' the test mass up and down along this line between the top of the suspension and the centre of the Earth (causing a vertical change in height of the centre of mass δy_c), while the mirror face is maintained at $90°$ to the incoming horizontal beam by the servos. Thus a change in path length, δx, induced by δy_0 will be detected.

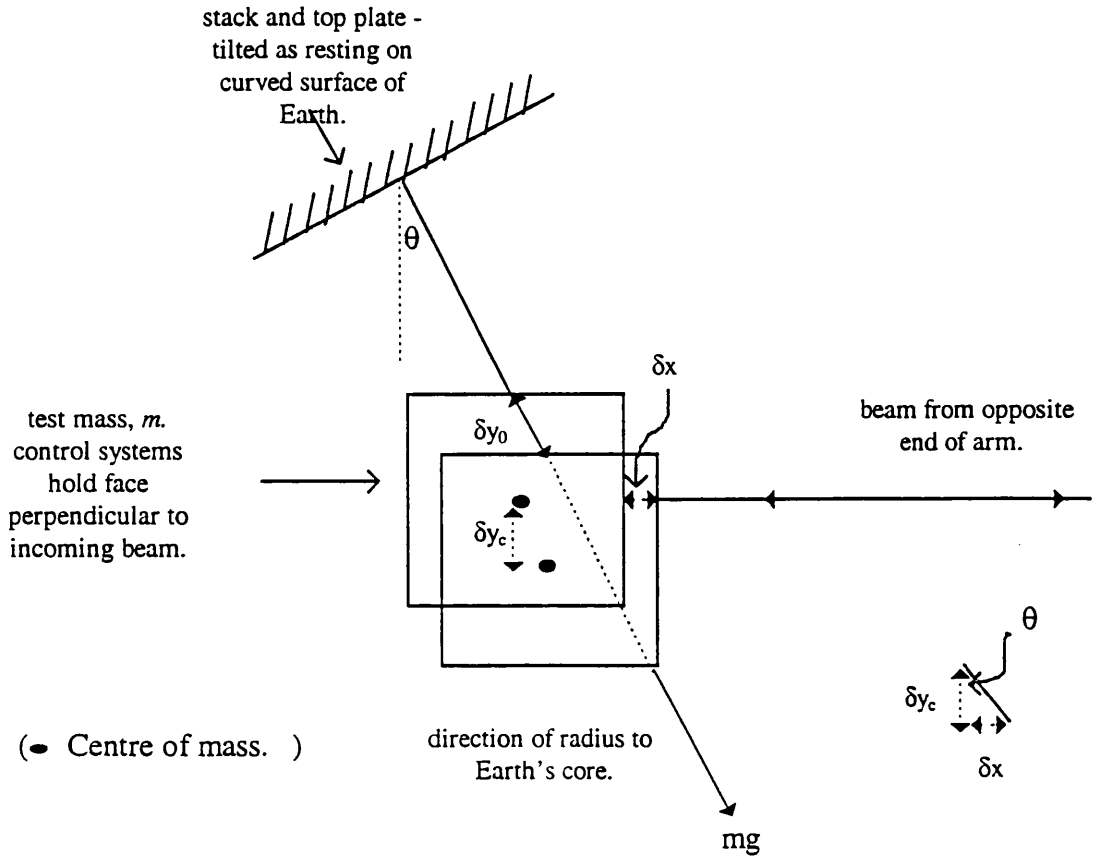

Fig(A.2): Closer view of cross-coupling mechanism due to radius of curvature of the Earth.

A reasonable evaluation of the level of cross-coupling to be expected here can be found simply from the geometry of the system (Fig.(A.2)). Here, the angle subtended by the horizontal path length change, δx, can be expressed as:

$$\frac{\delta x}{\delta y_c} \approx \theta \qquad \text{(A.1)}$$

where:

$$\theta \approx \frac{l/2}{R_E} = 4.8 \times 10^{-5} \text{ rads} \qquad \text{(A.2)}$$

for $l \approx 600\,\mathrm{m}$. Thus the level of cross-coupling arising from a single test mass suspension will be of the order:

$$\frac{\delta x}{\delta y_c} \approx 4.8 \times 10^{-3}\% \qquad \text{(A.3)}$$

Thus, the level of cross-coupling expected to arise as a result of the radius of curvature of the earth's surface is expected to be very small. However, it is also necessary to take into account any cross-coupling due to the next source examined here - that of the second pendulum stage.

A3
Analysis of cross coupling due to the inequality in stiffness of a double-loop test mass suspension.

We shall now examine the effect of cross-coupling through the second pendulum stage, arising due to the geometry of the suspension system. Consider first the test mass suspension, shown schematically in Fig.(A.3) below. Here the suspension wires have equal unloaded length, l, and vertical spring constants k_1 and k_2 as shown, where $k_1 \neq k_2$ and $(k_1 - k_2)$, is very small. Cross-coupling due to this difference in spring constants seemed worthy of investigation.

The level and form of any cross-coupling present can be found from the expression for the transfer function $\delta x/\delta y_c$, where δx is the total horizontal motion at the test mass due to cross-coupling and δy_c is the remnant vertical motion of the centre of mass of the test mass.

We can find $\delta x/\delta y_c$ through analysis of the equations of motion and static equilibrium of this system. We shall assume throughout that all angles of motion are small, and that each wire bends through an equal angle $\delta\theta$ with respect to the vertical. It will be shown that the total horizontal motion due to cross-coupled vertical noise can be defined by a combination of two terms; the first term arising due to rotational movement about the centre of mass, and the second term from translation of the centre of mass.

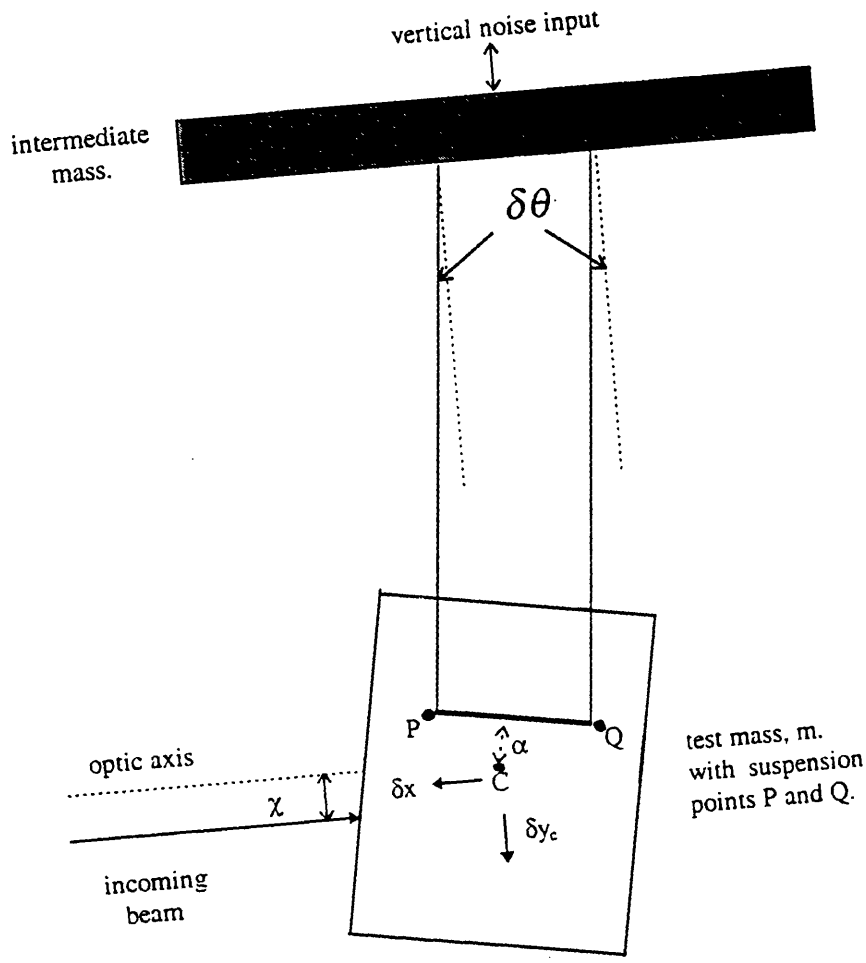

Fig(A.3): Suspended test mass with vertical to horizontal cross-coupling.

A3.1
Equations of static equilibrium

When loaded by the mass attached at suspension points P and Q, wires 1 and 2 will extend along the vertical axis by the amounts ε_1 and ε_2 respectively (Fig.(A.4)), until static equilibrium is reached.

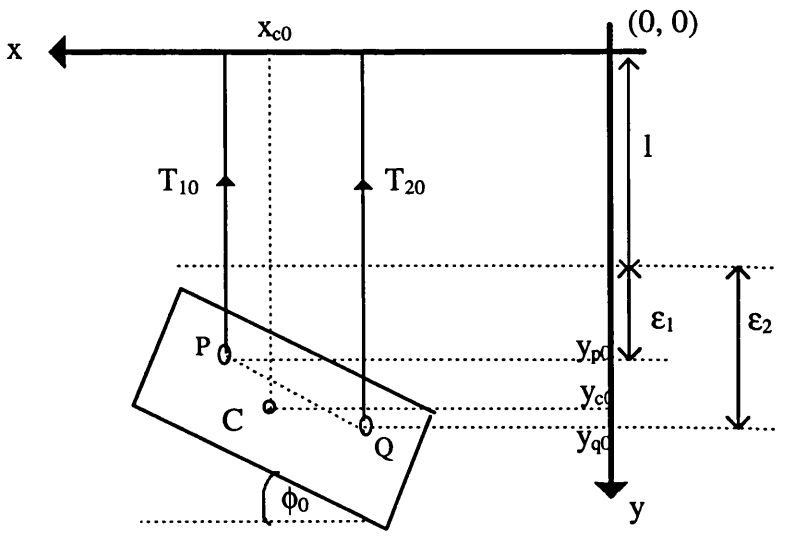

Fig(A.4): Suspended mass: Static equilibrium.

Although ε_1 and ε_2 will be constants of the system, the difference in spring constants ensures that $\varepsilon_1 \neq \varepsilon_2$. The stationary vertical and horizontal position co-ordinates of the centre of mass, *C*, at static equilibrium are given by (x_{co}, y_{co}). On reaching equilibrium the block makes a static angle ϕ_0 with the horizontal and the wires have tensions T_{10} and T_{20}, expressed by:

$$\begin{aligned} \text{P:} \quad & T_{10} = k_1 \varepsilon_1 \\ \text{Q:} \quad & T_{20} = k_2 \varepsilon_2 \end{aligned} \tag{A.4}$$

Resolution of the forces acting round the centre of mass, *C*, show that the following conditions of static equilibrium apply:

$$\begin{aligned} \ddot{y}_c = 0 &\Rightarrow (k_1 \varepsilon_1 + k_2 \varepsilon_2) = mg \\ \sum \tau_{Co} = 0 &\Rightarrow (\tau_{Qo} - \tau_{Po}) = 0 \end{aligned} \tag{A.5}$$

where the resultant torque about the centre of mass is denoted by τ_{Co}. From the geometry of the test mass system, this condition for rotational static equilibrium leads to the result below, where the angles η and ϕ_0 are shown in Fig.(A.4) above:

$$T_{20}\cos(\eta-\phi_0)-T_{10}\cos(\eta+\phi_0)=0 \tag{A.6}$$

A3.2
Equations of motion

We shall now consider the case where the mass has been disturbed from its equilibrium position by a periodic disturbance, $(0,\delta y_0)$ at the top suspension point of the wires (Fig.(A.5)).

This will in turn cause a periodic, linear disturbance of the position of the centre of mass, denoted by $(\delta x_c,\delta y_c)$, about the equilibrium position. Also resulting from this disturbance will be a swinging and/or bobbing of the mass, leading to periodic changes in the static extensions of the wires, the vertical components of which can be expressed as $\delta\varepsilon_1$ and $\delta\varepsilon_2$, assuming that $\delta\theta$ is small. These vertical components of extension can be defined by:

$$\begin{aligned}\delta\varepsilon_1 &= \delta y_0-\delta y_P\\ \delta\varepsilon_2 &= \delta y_0-\delta y_Q\end{aligned} \tag{A.7}$$

In total there are three equations of motion for the suspended mass, namely the horizontal and vertical equations of motion of C, and the rotational equation of motion of the mass about C. These shall now be considered in turn with a view to obtaining an expression for the total motion of the system.

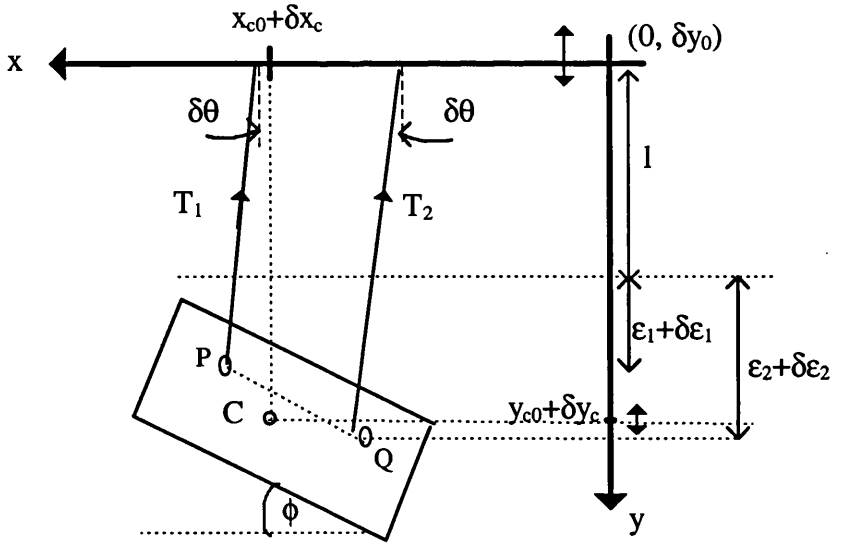

$|PC| = |QC| = r = \text{const.}$

$\hat{CPQ} = \hat{CQP} = \eta = \text{const.}$

Fig(A.5): Suspended mass: Dynamic case. *Mass now being driven by noise* $(0,\delta y_0)$ *at top of suspension. Wires changing length by* $\delta\varepsilon_1$ *and* $\delta\varepsilon_2$ *due to resulting oscillation. Centre of mass changing position by* $(\delta x_c, \delta y_c)$.

- Horizontal equation of motion of C

Assuming the angular change is small, and in the absence of damping, the horizontal restoring force (corresponding to a horizontal acceleration $\delta\ddot{x}_c$) acting on the centre of mass C during the motion is given by:

$$(T_1 + T_2)\delta\theta = m\delta\ddot{x}_c \qquad \text{(A.8)}$$

where:

$$T_1 = k_1(\varepsilon_1 + \delta\varepsilon_1) \text{ and } T_2 = k_2(\varepsilon_2 + \delta\varepsilon_2) \qquad \text{(A.9)}$$

Recalling equation (A.5), we can say that:

$$(k_1\varepsilon_1 + k_2\varepsilon_2) = mg >> (k_1\delta\varepsilon_1 + k_2\delta\varepsilon_2) \qquad \text{(A.10)}$$

Hence, following the substitution of these expressions into (A.8) above we can say that it becomes:

$$mg\delta\theta \approx m\delta\ddot{x}_c \qquad \text{(A.11)}$$

Thus, within the conditions assumed here, the horizontal equation of motion of the system is merely the usual expression for the horizontal restoring force of a pendulum of mass *m*, provided by the total tension in the suspension wires.

- Vertical equation of motion of C

The equation of motion in the vertical direction in the absence of damping is given in terms of the vertical acceleration of the centre of mass, $\delta\ddot{y}_c$, about the equilibrium position by (A.12) below:

$$(T_1 + T_2)cos\delta\theta = m\delta\ddot{y}_c + mg \qquad \text{(A.12)}$$

where the substitution of the expressions in equations (A.9) and (A.5) can again be made. This time however, the $\delta\varepsilon$ terms remain and equation(A.12) becomes:

$$k_1\delta\varepsilon_1 + k_2\delta\varepsilon_2 = m\ddot{y}_c \qquad \text{(A.13)}$$

In general, it is more likely that the magnitudes of the disturbances δy_0 and δy_c will be known, rather than those of the $\delta\varepsilon$ terms. Equation (A.13) would therefore be more useful when re-expressed in terms of δy_0 and δy_c, using equations (A.7) and the geometry of the system. Thus we can say that an equivalent form of (A.13) is:

$$k_1(\delta y_0 - \delta y_c - r\delta\phi) + k_2(\delta y_0 - \delta y_c + r\delta\phi) = m\delta\ddot{y}_c \qquad \text{(A.14)}$$

Hence, we can state that:

$$\left(\frac{\delta y_c - \delta y_0}{\delta y_0}\right) \approx \left(\frac{-s^2}{s^2 + 2\omega_v^2}\right) \qquad \text{(A.15)}$$

Note that the presence of the term $2\omega_v^2$ arises from $\omega_v^2 = k/m$ with the assumption that $k_1 \approx k_2 = k$. This equation shall be used later on in the derivation of the equation of rotational motion of the test mass, as is now discussed.

- Equation of rotational motion about C

The equation of rotational motion of the test mass about its centre of mass, *C*, is approached in a similar manner to the static equilibrium case which resulted in equation (A.6). The principal change to the system in this non-equilibrium case is of course that the mass is no longer hanging with respect to the horizontal at the equilibrium angle ϕ_0, but rather at some value $\phi = \phi_0 + \delta\phi$. The angular acceleration is therefore defined by $\delta\ddot{\phi}$.

Recalling equation (A.9) once again, the tension in the wires as the mass moves can be described by:

$$T_1 = k_1(\varepsilon_1 + \delta\varepsilon_1) \text{ and } T_2 = k_2(\varepsilon_2 + \delta\varepsilon_2) \qquad \text{(A.9)}$$

We can find a more suitable expression for $k_1\varepsilon_1$, shown in equation (A.16) below, in terms of the angular parameters involved in the system. This is done by using equations (A.4) and (A.6), with the assumption that standard small angle approximations can be made. Further, we can re-define $k_1\delta\varepsilon_1$ as in (A.17) below. Both of these processes assume that δk is very small.

$$k_1\varepsilon_1 \approx k_2\varepsilon_2(1+2\eta\phi_0) \approx k\varepsilon_2(1+2\eta\phi_0) \tag{A.16}$$

$$k_1 = k_2 + \delta k \approx k + \delta k \tag{A.17}$$

Similarly we can also relate $\delta\varepsilon_1$ and $\delta\varepsilon_2$ from the geometry of the system, with the result:

$$\left.\begin{aligned}\delta\varepsilon_1 &= -(\delta y_c - \delta y_0) - r\delta\phi \\ \delta\varepsilon_2 &= -(\delta y_c - \delta y_0) + r\delta\phi\end{aligned}\right\} \tag{A.18}$$

$$\Rightarrow \quad \delta\varepsilon_1 = \delta\varepsilon_2 - 2r\delta\phi$$

We are now in a position to consider the expression for the torque acting on the mass about C in terms of the system parameters involved (Fig.(A.6)).

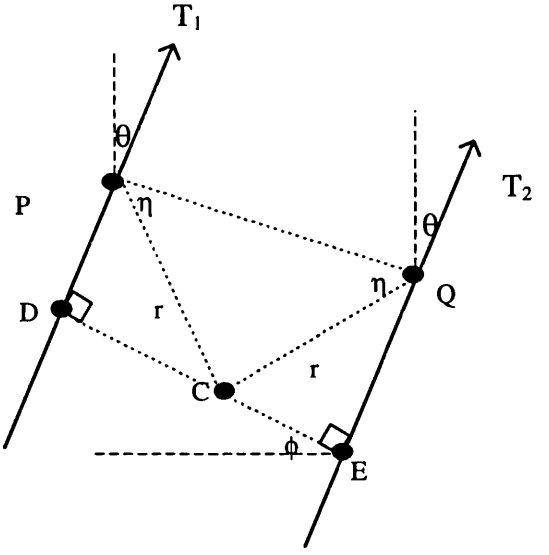

Fig(A.6): Parameters involved in the equations of motion for rotation of the mass about C.

The torque can be defined in the usual way as equation (A.19) below, where $\Delta = CD - CE$:

$$\begin{aligned} I\delta\ddot{\phi} &= \tau_P - \tau_Q \\ &= T_1.CD - T_2.CE \\ &= T_1(CE + \Delta) - T_2.CE \end{aligned} \tag{A.19}$$

(I being the moment of inertia of the suspended mass about an axis through C and perpendicular to the plane of the page).

We can now rewrite (A.19) by substituting the expressions outlined in equations (A.16), (A.17) and (A.18), which gives rise to the torque equation (A.20) below:

$$\begin{aligned} I\delta\ddot{\phi} \approx &\left[k\varepsilon_2(1+2\eta\phi_0)CE(1+\Delta/CE) - k\varepsilon_2.CE\right] + \\ &\left[(k+\delta k)(\delta\varepsilon_2 - 2r\delta\phi)CE(1+\Delta/CE) - k\delta\varepsilon_2.CE\right] \end{aligned} \tag{A.20}$$

The next stage of this process is to also determine CE and Δ in terms of r and the angular system parameters, which can be more easily evaluated. It is also useful at this point to further our definition of the extension terms ε_2 and $\delta\varepsilon_2$. We shall now outline the stages involved in doing so before using the result obtained to extend our form of equation (A.20).

By considering the geometry of the system (Fig.(A.6)), the distance terms CE and Δ involved in (A.20) can be expressed as:

$$\begin{aligned} CD &\approx r(1-\phi_0\eta) - r\eta(\delta\theta - \delta\phi) \\ CE &\approx r(1+\phi_0\eta) + r\eta(\delta\theta - \delta\phi) \end{aligned} \tag{A.21}$$

$$\frac{\Delta}{r} = -2\phi_0\eta - 2\eta(\delta\theta - \delta\phi) \tag{A.22}$$

We can start this substitution process by making the approximation that $\Delta/CE \approx \Delta/r$ in (A.20). Since $\dfrac{2\eta\phi_0\Delta}{r} << 1$, this gives us the following form of equation (A.20):

$$I\delta\ddot{\phi} = \left[k\varepsilon_2 r\left(2\eta\phi_0 + \frac{\Delta}{r}\right)\right] + \left[k\delta\varepsilon_2 r\left(\frac{\delta k}{k} - \frac{2r\delta\phi}{\delta\varepsilon_2} + \frac{\Delta}{r}\right)\right] \tag{A.23}$$

The next step in this process is to re-define the extension terms ε_2 and $\delta\varepsilon_2$. Let us consider first the condition for static equilibrium stated in (A.3). Recall that we have already assumed that the difference in wire spring constants is in fact very small (as will be the likely case in practice). This allowed us to use the approximation $k_1 \approx k_2 \approx k$, which implies that $\varepsilon_1 \approx \varepsilon_1 \approx \varepsilon$. Thus, from (A.3), we can say:

$$\varepsilon \approx \frac{mg}{2k} \tag{A.24}$$

Also, from equation (A.18), we can make the small angle approximation that:

$$\delta\varepsilon_2 \approx -(\delta y_C - \delta y_0) \tag{A.25}$$

Upon substitution of equations (A.22), (A.24) and (A.25), the form of (A.23) becomes:

$$\begin{aligned} I\delta\ddot{\phi} = &-mrg\eta(\delta\theta - \delta\phi) - r\delta k(\delta y_c - \delta y_0) - 2r^2 k\delta\phi \\ &+ 2rk\eta\phi_0(\delta y_c - \delta y_0) + 2rk\eta(\delta\theta - \delta\phi)(\delta y_c - \delta y_0) \end{aligned} \tag{A.26}$$

Now, recall the vertical equation of motion of the test mass defined in (A.15). We can incorporate this into our rotational equation by substituting it in place of the $(\delta y_c - \delta y_0)$ terms above. In doing so, and to lowest order in the angular terms (since very small), we find that:

$$I\delta\ddot{\phi} = -2r^2 k\delta\phi + r\delta k\left(\frac{s^2}{s^2 + 2\omega_v^2}\right)\delta y_0 \tag{A.27}$$

Equation (A.27) above represents the most useful form of the equation of motion of rotation about the centre of mass for the purpose in hand. This equation can now be used as the starting point for the derivation of the various terms involved in the cross-coupled horizontal motion of the mass. As already mentioned in the introduction to this appendix, this comprised of two term, both of which will now be derived.

- Component of cross-coupled motion arising from rotation of the mass.

We are now in a position to determine the transfer function of the horizontal component of motion of the front of the test mass due to rocking induced by the vertical drive. For this we can use the rotation equation of motion (A.27) directly to obtain:

$$\frac{\delta\phi}{\delta y_0} \approx \frac{r\delta k}{I\omega^2 + 2r^2 k} \tag{A.28}$$

where it is assumed that we are concerned mainly with frequencies well above those of the suspension wire resonances.

In terms of horizontal motion, this term is only important for our purpose if the incoming laser beam lies at an offset, χ , to the centre of the mirror face (Fig.(A.7)).

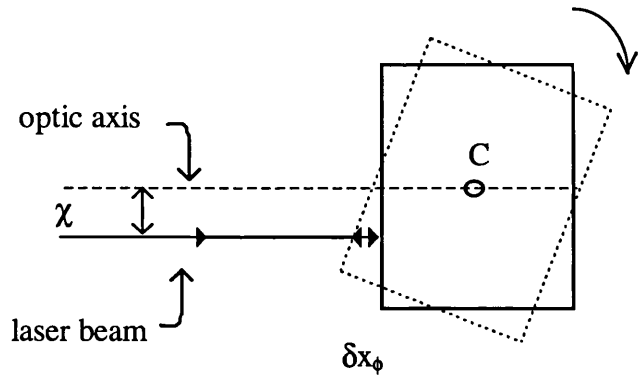

Fig.(A.7): Cross-coupling component arising due to the combination of rotation of the mass about C and the beam centering error χ.

We can see the reason for this from the simple geometrical relationship between δx_ϕ (the horizontal component of motion of the mirror face due to rocking about *C*) and $\delta\phi$:

$$\delta\phi = \frac{\delta x_\phi}{\chi} \tag{A.29}$$

Thus the form of our equation for $\delta x_\phi / \delta y_0$, which describes only part of the total cross-coupled motion, is given by (A.30) below:

$$\frac{\delta x_\phi}{\delta y_0} \approx \frac{r\delta k\,\chi}{I\omega^2 + 2r^2 k} \tag{A.30}$$

- Translation component of cross-coupled motion.

Fig.(A.8(a)) below illustrates this component.

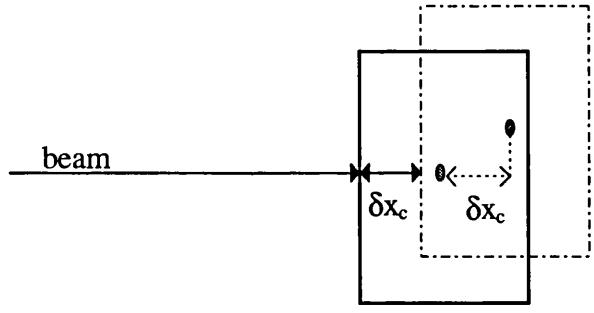

Fig(A.8(a)): Diagram showing the translation component of the cross-coupling.

Now, from the system geometry we can express the change in rotation angle, $\delta\phi$, in terms of the real horizontal *translation* of the centre of mass, δx_c (Fig.(A.8(b)). This

also involves the introduction of a new system parameter α - the perpendicular separation of the line of suspension to the line through C, as shown in Fig.(A.8(b)).

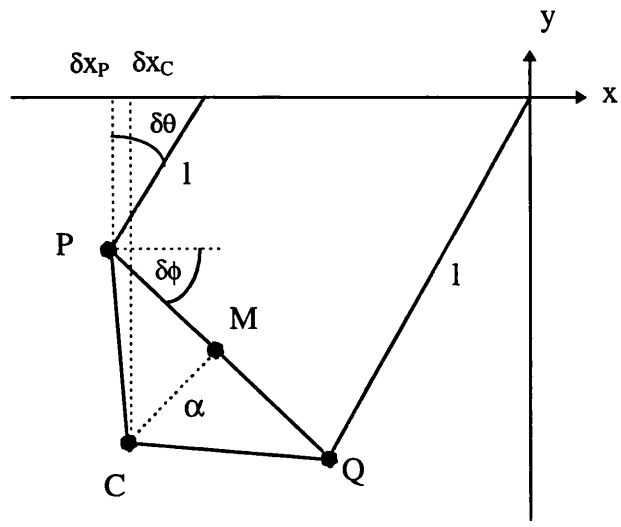

Fig.(A.8(a)): System geometry relevant to translation component of cross-coupling.

Now, from system geometry, one can say that $\delta\theta = -\frac{x_p}{l} = -\frac{x_c}{l} + \delta\phi\frac{\alpha}{l}$. In addition, it can be seen from equation (A.11) that $\delta\theta \approx \frac{s^2 x_c}{g}$ for small angular changes, where $s = j\omega$. Thus we can say that the relationship between $\delta\phi$ and δx_c is given by

$$\delta\phi = \delta x_c\left(\frac{ls^2 + g}{g\alpha}\right) \tag{A.31}$$

Now, by substituting equation (A.31) (and its second time derivative) into equation (A.27), we find that at high frequencies the transfer function δx_c to the purely vertical input, δy_0 can be expressed as

$$\frac{\delta x_c}{\delta y_0} \approx \frac{r\delta k\alpha g}{\omega^4 I l} \tag{A.32}$$

Thus we can combine results (A.30) and (A.32) to define the total horizontal motion of the mass due to cross-coupled vertical noise as:

$$\begin{aligned}\frac{\delta x}{\delta y_c} &= \left(\frac{\omega}{\omega_{pv2}}\right)^2 \left\{\frac{\delta x_\phi}{\delta y_0} + \frac{\delta x_c}{\delta y_0}\right\} \\ &= \left(\frac{\omega}{\omega_{pv2}}\right)^2 \left\{\frac{r\delta k}{I}\left(\frac{\chi}{\omega^2} + \frac{g\alpha}{\omega^4 l}\right)\right\}\end{aligned} \tag{A.33}$$

where the term $\left(\frac{\omega}{\omega_{pv2}}\right)^2$ is a conversion factor derived from the transfer function $\frac{\delta y_c}{\delta y_0}$, thus allowing the expression of our cross-coupling equation in terms of the more conventional δy_c rather than in terms of δy_0. It should be noted that this conversion assumes that we are looking at frequencies in the range above ω_{pv2}, the vertical resonance of the second pendulum stage.

A4
Discussion of cross-coupling expression derived in A3

In the real GEO 600 test mass suspension system, it is believed that the most likely source of cross-coupled noise at the test mass will be due to inequalities in the lower stage suspension wire spring constants. This may be possible due to, e.g., very slight variations in the cross-sectional area or length of the wires. Although likely to be extremely small, this difference in spring constant will undoubtedly have an effect on the motion of the mass. As a result of calculations carried out in section A3 the horizontal motion of the test mass due to cross-coupling from a purely vertical noise input has been found to be:

$$\frac{\delta x}{\delta y_c} = \left(\frac{\omega}{\omega_{pv2}}\right)^2 \left\{\frac{r\delta k}{I}\left(\frac{\chi}{\omega^2} + \frac{g\alpha}{\omega^4 l}\right)\right\}$$

There are several interesting points to note.

In the first instance, the cross-coupled motion due to $\delta x_\phi / \delta y_0$ is critically dependent on the amount by which the incoming laser beam is off-centre on the face of the mass. This is because the horizontal motion sensed by the beam due to this source is only *apparent* motion due to tilting of the mirror face, and not due to any real motion of the centre of mass (Fig(A.7)). Thus, if the beam is perfectly centred no path length change will be noticed due to δx_ϕ (to first order). In practice, however, the beam centring error is likely to be of order $\chi \approx 10^{-3}$ m.

Even if the beam did happen to be perfectly centred however, a path length change will still be detected due to the second term, δx_c, in the cross-coupling expression. This term corresponds to a *real* horizontal translation of the centre of mass (Fig.(A.9)). However, at high frequencies this term will become negligible due to its $1/\omega^4$ dependence.

Thus, at 100 Hz (our usual benchmark frequency for seismic noise considerations) the cross-coupling can be approximated by:

$$\frac{\delta x}{\delta y_c} \rightarrow \frac{r\delta k \chi}{I \omega_{pv2}^2} = C$$

(A.34)

where C is a constant known as the 'cross-coupling factor'. For typical values of the system parameters involved (and listed below in (A.36)), the cross-coupling factor expected for GEO 600 at a single test mass through this route can be evaluated to be:

$$C \approx 10^{-3}\%$$

(A.35)

$$
\begin{aligned}
&\delta k \approx 3.5\times 10^{3}\, Nm^{-1} \\
&2r \approx 5\times 10^{-3}\, m \\
&\chi \approx 10^{-3}\, m \\
&l \approx 0.25 m \\
&I \approx 0.0925\, kgm^{2} \\
&\omega_{v}^{2} \approx (2\pi\, 15) rads^{-1} \\
&\alpha \approx 10^{-3}\, m
\end{aligned}
\qquad \text{(A.36)}
$$

It should be noted that the values of cross-coupling factor reported in equations (A.35) and (A.3) are for a single test mass. A complete evaluation of this should consider the overall cross-coupling factor by taking into account the effect of the other test masses. If one wishes to look at the effect over the whole system, this value adds in quadrature according to the different contributions from the various masses present. For GEO 600 one must consider the effect over 4 suspended masses, where the subscript *1* denotes an end mirror and *2* a central mirror.

The total noise level, $\left.\frac{\delta x}{\delta y_c}\right|_{TOTm}$, due to both cross coupling sources at a single mirror mass is given by:

$$
\left.\frac{\delta x}{\delta y_c}\right|_{TOTm} = \sqrt{\left.\frac{\delta x}{\delta y_c}\right|_{wires}^{2} + \left.\frac{\delta x}{\delta y_c}\right|_{earth}^{2}}
\qquad \text{(A.37)}
$$

which can be evaluated from (A.35) and (A.3) as ~ 5×10^{-5}. In order to find the total noise over the four test masses and beamsplitter intended in the GEO 600 system, we must take into account the fact that only one mirror in each arm receives 2 bounces of light, whereas the remaining mirrors and beamsplitter receive only one. We shall therefore assume that the latter contribute only half the amount of noise to the system compared with the double-bounce mirrors. Also, noise from the beamsplitter is *correlated* in each arm. Thus the total noise in the system can be evaluated as follows:

$$\left.\frac{\delta x}{\delta y_c}\right|_{system} = \sqrt{\left.\frac{5}{2}\frac{\delta x}{\delta y_c}\right|^2_{TOTm} + \left.\frac{1}{2}\frac{\delta x}{\delta y_c}\right|^2_{TOTb}} \approx \sqrt{3}\left.\frac{\delta x}{\delta y_c}\right|_{TOT} \qquad \text{(A.38)}$$

i.e.

$$\left.\frac{\delta x}{\delta y_c}\right|_{system} \approx 9\times 10^{-5} \approx 0.01\% \qquad \text{(A.39)}$$

As the calculations performed in this appendix provide only a reasonable estimate of the cross coupling factor for the pendulum system, a more pessimistic value of 0.1% is usually used in calculations of the predicted seismic noise level at a single mirror mass. However, analysis of this sort is necessary to ensure that the value used will not underestimate this effect.

Appendix B
Sample Program Listing for Turbo C Data Acquisition System.

The attached program listing has been developed to handle data resulting from four simultaneous photodiode outputs. Various modified versions have also been used to collect and manipulate data arriving at a single input port of the multiplexer.

```
#include "funcs.h"
#include <string.h>
#include <sys\timeb.h>
#include <math.h>
int interval();
void setupsystem();
void filename(char[ ]);                    //function to get name for multi-channel data.
void sigfilename(char[ ]);                 //function to get name for single sine data.
void rmsfilename(char[ ]);                 // function to get name for r.m.s.[time] data.
void getdata(int [ ][500]);
void drawaxes();
void drawdata(int [ ][500]);
void savedata(int [ ][500], long);         //saves multi-channel data to file.
void datareduce(int [ ][500], int[ ], long); //does algebra and saves single sine.
void rms(int[ ], long);                          //gets r.m.s. per burst from single sine.
long getnow( );
int done();
#define nchan 4
FILE *fptr;
FILE *sigfptr;
FILE *rmsfptr;
void main( )
        {int volts[nchan][500], sig[500], i, j, fin;
```

```
        char fname[20], sigfname[20], rmsfname[20];
        long t1, t2, time;
        int period;
        setupsystem( );
        filename(fname);
        sigfilename(sigfname);
        rmsfilename(rmsfname);
        period=interval();
        t1=getnow();
        time=0;
        do
                {
                getdata(volts);
                drawaxes( );
                drawdata(volts);
                savedata(volts, time);
                while( ( t2=getnow( ) ) - t1 < period && !( fin=done( ) ) );
                t1=t2;
                datareduce(volts, sig, time);
                rms(sig, time);
                time=time+(period/1000);
                }
        while(!fin);
        fclose(fptr);
        fclose(sigfptr);
        fclose(rmsfptr);
        closegraph();
        }

int interval()
        {int period;
        printf ("type burst interval in milliseconds please\n");
        scanf ("%d", &period);
```

```
        return period;
        }

void setupsystem( )
        { amsetupsoftadc( );
        amsetuptimer( );
        amloadtimne(2, 1000);
        amsetgraphics( );
        setviewport(10, 10, 629, 469, 1);
        setfillstyle(1,9);
        }

void filename (char fname[20])
        {char ans;
        do{
                ans='y';
                printf ("Type name of file for storage of data from individual
                        input channels please.\n");
                fgets (fname, 20, stdin);
                if (fname[strlen (fname)-1]=='\n')  fname[strlen(fname)-1]=NULL;
                if (fptr=fopen(fname, "r"))  printf("File is opened for read\n");
                if (fptr!=NULL)
                        { fclose(fptr);
                        printf ("File already exists- OK to append?  (y/n)\n");
                        ans=getche();
                        }
                }
        while (ans!='y');
        if (fptr=fopen(fname, "a"))
                printf ("I've opened your file - please type <enter> to
                continue.\n");
        else printf ("Sorry -- you haven't got a file opened\n");
        getch();
```

```
}

void sigfilename (char sigfname[20])
    {char ans;
    do{
        ans='y';
        printf ("Type name of file for final storage of reduced data
            please.\n");
        fgets (sigfname, 20, stdin);
        if (sigfname[strlen (sigfname)-1]=='\n')
        sigfname[strlen(sigfname)-1]=NULL;
        if (sigfptr=fopen(sigfname, "r"))  printf ("File is opened for
        read\n");
        if (sigfptr!=NULL)
            { fclose(sigfptr);
            printf ("File already exists- OK to append?  (y/n)\n");
            ans=getche();
            }
        }
    while (ans!='y');
    if (sigfptr=fopen(sigfname, "a"))
        printf ("I've opened your file - please type <enter> to
        continue.\n");
    else printf ("Sorry -- you haven't got a file opened\n");
    getch();
    }

void rmsfilename (char rmsfname[20])
    {char ans;
    do{
        ans='y';
        printf ("Type name of file for final storage of r.m.s. data
        please.\n");
```

```
            fgets (rmsfname, 20, stdin);
            if (rmsfname[strlen (rmsfname)-1]=='\n')
            rmsfname[strlen(rmsfname)-1]=NULL;
            if (rmsfptr=fopen(rmsfname, "r"))  printf("File is opened for
            read\n");
            if (rmsfptr!=NULL)
                    { fclose(rmsfptr);
                    printf ("File already exists- OK to append?  (y/n)\n");
                    ans=getche();
                    }
            }
        while (ans!='y');
        if (rmsfptr=fopen(rmsfname, "a"))
                printf ("I've opened your file - please type <enter> to
                continue.\n");
        else printf ("Sorry -- you haven't got a file opened\n");
        getch();
        }

long getnow()
        { struct timeb t;
        ftime (&t);
        return (1000*t.time + t.millitm);
        }

int done()
        { if ( bioskey(1) )
                return(( bioskey(0) & 127)==27);
                return(0);
        }

void getdata (int volts[ ][500])
        { int i, j;
```

```
        outportb(adccr, 0);
        amreadadc();
        while(amreadhardadc()>=0);
        while( (volts[0][0]=amreadhardadc( ) )<0);
        for (j=1; j<nchan; j++)
                { volts [j][0] =amreadsoftadc(j);
                }
        outportb(adccr, 0);
        for (i=1; i<500; i++)
                { volts[0][i]=amreadhardadc( );
                for ( j=1; j<nchan; j++)
                        volts[j][i]=amreadsoftadc(j);
                        outportb(adccr, 0);
                }
        outportb(adccr, 2);
}

void drawaxes(void)
        { bar3d(0, 0, 619, 459, 0, 0);
        moveto(50, 230); linerel(520, 0);
        moveto(50, 420); linerel(0, -400);
        }

void drawdata(int v0[ ][500])
        { int i, j;
        moveto(50, 230-v0[0][0]);
        for (j=0; j<nchan; j++)
                { setcolor(15-j);
                moveto(50, 230-v0[j][0];
                for (i=1; i<500; i++)
                        lineto(50+i, 230-v0[j][i]);
                }
        }
```

```
void savedata (int volts[ ][500], long time)
        { int i, j;
        for (i=0; i<500; i++)
                { fprintf (fptr, "\n%ld", time);
                for (j=0; j<nchan; j++)
                        fprintf (fptr, "\t%5d\t%5d", i, volts[j][i] );
                }
        }

void datareduce (int volts[ ][500], int sig[500], long time)
        {
        int a, b, c, d, i;
        for (i=0; i<500; i++)
                { a=volts[0][i];
                b=volts[1][i];
                c=volts[2][i];
                d=volts[3][i];
                sig[i]=sqrt ( (a-b)*(a-b) + (c-d)*(c-d) );
                fprintf (sigfptr, "\n%ld\t%5d\t%5d", time, i, sig[i]);
                }
        }

void r.m.s. (int sig[500] long time)
        {
        int i, i1, i2;
        double sqr[500];
        double sumsqr;
        double rms;
        for (i=1; i<499; i++)
                { if (sig[i-1]>sig[i] && sig[i]<sig[i+1] && sig[i]<2)  //condition sig[i]<n
                                                                        // more accurate for small n.
                        { i1=i;                 // this should give the bin number of the first minima.
                        break; } }
```

```
for( i=499; i>0; i--)
        { if (sig [i+1] > sig[i] && sig [i] < sig [i-1] && sig [i] < 2)
                { i2=i;                 // this should be the bin number of the last minimum.
                break; } }
sumsqr = 0;
for (i=i1; i<i2; i++)                   // i.e. now only operating between 1st and last minima.
                                        //Thus r.m.s. error mostly eliminated since (i2-i1) should
                                        //correspond to an integral number of ½ cycles.

        {
        sqr[i]=(sig[i]*sig[i]);
        sumsqr=sumsqr + sqr[i];
        }

if (i2>i1)                      //Important 'if' statement to prevent program crash where i1=i2.
        { rms=sqrt (sumsqr/(i2-i1));
        }
else { outtext ("Negative square root!!!\n");
delay(5); }
fprintf(rmsfptr, "\n%ld\t%lf\t%d", time, r.m.s., i1, i2);
}
```

List of References.

(Abramovici et al, 1992) A. Abramovici et al, '*Science*'; **256** (1992) 325-333.

(Abramovici et al, 1995) A. Abramovici, P. Bender, R. Drever and colleagues, '*Gravitational Wave Astrophysics*', Proc. of 1994 Snowmass Summer Study, '*Particle and Nuclear Astrophysics and Cosmology in the next Millenium*'; Ed. E.W.Colb, R.D Peccei, (World Scientific Pub. Co.), 1995.

(Allen & Shellard, 1992) B. Allen, E. P. S. Shellard, Phys. Rev. D **45** (1992) 1898-1912.

(Bender et al, 1996) P. Bender, I. Ciufolini, K. Danzmann, W. Folkner, J. Hough, D. Robertson., A. Rüdiger , M. Sandford, R. Schilling, B. Schutz, R. Stebbins, T. Sumner, P. Touboul, S. Vitale, H. Ward, W. Winkler; '*LISA, Pre-Phase A Report*'; (MPQ 208), February 1996.

(Blair, 1991) *The Detection of Gravitational Waves*, Ed. D. G. Blair, Cambridge University Press, 1991.

(Bonazzola and Marck, 1994) S. Bonazzola and J. A. Marck, Annual Review of Nuclear and Particle Science, **45** (1994) 655-717.

(Bongs, 1993) K. Bongs, E. Morrison, Private communication, (1993).

(Braccini et al, 1995) S.Braccini et al, Phys. Lett. A, **199** (1995) 307-314.

(Braddick, 1965) H.J.J Braddick; '*Vibrations, waves and diffraction*', (McGraw-Hill), 1965.

(Braginsky et al,1992) V.B. Braginsky, V.P. Mitrofanov, and O.A. Okhrimenko, JETP Lett., **55** (1992) 432.

(Brustein et al, 1995) R. Brustein, M. Gasperini, M. Giovanni, and G. Veneziano, Proc. of '*International Euro-Physics Conference on High Energy Physics eps-hep-95*', Brussels, July 1995.

(Callan and Greene, 1952) H. B. Callan, R. F. Greene, Phys. Rev, **86** 5 (1952) 702-710.

(Cantley 1991) C. A. Cantley, Ph.D Thesis, University of Glasgow, 1991.

(Cantley 1992) C. A. Cantley, J. Hough, and N. A. Robertson; . Rev. Sci. Instrum., **63** 4 (1992) 2210-2219.

(Caves, 1982) C. M. Caves, Phys. Rev. D., **26** 8 (1982) 1817-1839.

(Curran & Lorimer, 1995) S. J. Curran and D. R. Lorimer, Mon. Not. R. Astron. Soc., April 1995.

(Drever et al, 1980) R. W. P. Drever, G. M. Ford, J. Hough, I. M. Kerr, A. J. Munley, J. R. Pugh, N. A. Robertson and H. Ward, *A gravity - wave detector using optical cavity sensing*, Proc. 9th Int. Conference on General Relativity and Gravitation, Jena, 1980.

(Einstein,1916) A. Einstein, '*Die Grundlage der Algemeinen Relativitätstheorie*', Annalen der Physik, **49** (1916) 769.

(Edelstein et al, 1978) W. A. Edelstein, J. Hough, J. R. Pugh, W. Martin, J. Phys. E: Sci. Instrum., **11** (1978) 710-712.

(Forward, 1978) R. L. Forward, Phys. Rev. D., **17** 2 (1978) 379.

(French, 1965) A. P. French, '*Vibrations and Waves*', M. I. T. Introductory Physics Series, (Van Nostrand International), 1965.

(Giaime et al, 1994) J. Giaime, P. Saha, D. Shoemaker, L. Sievers, Rev. Sci. Instrum. **67** 1 (1996), 208-214.

(Gillespie and Raab, 1993) A. Gillespie and F. Raab, Phys. Lett. A, **178**, (1993), 357-363.

(Gillespie, 1995) A. Gillespie, Ph.D. Thesis, Caltech, 1995.

(Gonzáles and Saulson, 1994) G.I González and P. R Saulson, J. Acoust. Soc. Am., **96** (1994) 207.

(Greenhalgh, 1993) J. Greenhalgh, Rutherford Appleton Laboratory, Private Communication, (1993).

(Hough et al, 1987) J. Hough, B. J. Meers, G. P. Newton, N. A. Robertson, H. ward, B. F. Schutz, I. F. Corbett and R. W. Drever, *Vistas in Astronomy*, **30** (1987) 109-134.

(Hough et al, 1989) J. Hough, B. F. Schutz, J. Ehlers, H. Welling, I. F. Corbett, V. Kose and colleagues, '*Proposal for a Joint German-British Interferometric Gravitational Wave Detector*', (MPQ 157), September 1989.

(Hough, Danzmann, Schutz et al, 1994) J. Hough, K. Danzmann, B.F. Schutz et al; '*GEO 600 - Proposal for a 600 m Laser-Interferometric Gravitational Wave Antenna*'; 20th September 1994.

(Hough et al, 1996) J. Hough, R. Hutchins, J. Logan, A. McLaren, M. Plissi, N. A. Robertson, S. Rowan, K. Strain, S. Twyford; Proc. Int. Conf. on Gravitational Waves: Sources and Detectors, Cascina, 1996. To be published.

(Hough, 1996) J. Hough, Private Communication (1996).

(Jafry, 1995) Y. Jafry, (Memo: LISA spacecraft roll control) Private communication (1995).

(Ju et al, 1993) L. Ju, D. G. Blair, and F. J. van Kann, '*Novel Isolation and Suspension Systems for Laser Interferometric Gravitational Wave Detectors*', Paper presented at Experimental Gravitation, Int. Symposium, Nathiagali, Pakistan,(IoP Publishing), 1993.

(Killbourn, 1996) S. Killbourn, University of Glasgow, Private communication (1996).

(Kimball &Lovell, 1927) A. L. Kimball and D. E. Lovell, Phys. Rev., **30** (1927) 948-959.

(Kogelnik & Li, 1966) H. Kogelnik & T. Li, Proc. I.E.E, **54** 10 (1966) 1312 - 1968.

(Kovalik & Saulson, 1993) J. Kovalik and P. R. Saulson, Rev. Sci. Instrum. **64** 10 (1993) 2942 - 2946.

Lake (in Mernagh, 1969) G. J. Lake; '*Silicone rubber*' in '*Rubbers Handbook*', Edited by L. R. Mernagh,(Morgan-Grampian Pub. Ltd.), 1969.

(Lindley, 1969) P. B. Lindley; '*The Basic Design of Springs*' in '*Rubbers Handbook*', Edited by L. R. Mernagh, (Morgan-Grampian Pub. Ltd.), 1969.

(Logan et al, 1991) J. E. Logan, N. A. Robertson, J. Hough, and P. J. Veitch, Phys. Lett. A, **161** (1991) 101-110.

(Logan et al, 1992) J.E. Logan, N.A. Robertson, J. Hough, Phys. Lett. A, **170** (1992) 352.

(Logan, 1993(a)) J. E. Logan, Ph.D. Thesis, University of Glasgow, 1993.

(Logan et al, 1993(b)) J. E. Logan, J. Hough, N. A. Robertson, Phys. Lett. A, **183** (1993) 145-152.

(Logan et al, 1994(a)) J. E. Logan, N. A. Robertson, J. Hough, Optics Communications **107** (1994) 342-346.

(Logan et al, 1994(b)) J. E. Logan, J. Hough, N. A. Robertson, K. Danzmann, and R. Hutchins, Proc. of MG7, Stanford, 1994 (in press).

(Logan et al, 1995) J. E. Logan, J. Hough and N. A. Robertson, Private Communication (1995).

(Logan et al, 1996) J. E. Logan, J. Hough, R. Thomson, Phys. Lett. A, 1996, in press.

(Martin, 1978) W. Martin, Ph.D Thesis, University of Glasgow, 1978.

(McLeod, 1995) A. McLeod, University of Glasgow, Private communication (1995).

(Meers, 1988) B. J. Meers, Phys. Rev. D., **38** 8 (1988) 2317-2326.

(Mernagh, 1969) '*Rubbers Handbook*', Edited by L. R. Mernagh, (Morgan-Grampian Publishers Ltd.), 1969.

(Morrison, 1993) E. Morrison; Ph.D. Thesis, University of Glasgow, 1993.

(Painter, 1954) G. W. Painter, in '*Rubber Age*', **74** (1954) 701.

(Plissi, 1996) M. V. Plissi, K. A. Strain, and J Hough, University of Glasgow, Private communication (1996).

(Press and Thorne, 1972) W. H. Press and K. S. Thorne, Annual Review of Astronomy and Astrophysics, **10** (1972) 335.

(Quinn et al, 1992) T. J. Quinn, C. C. Speake , L. M. Brown, Phil. Mag. **65** (1992) 261-276.

(Quinn et al, 1994) T. J. Quinn, C. C. Speake , W. Tew, R. S. Davis, L. M. Brown, Report presented at Workshop on Thermal Noise in Laser Interferometers, Caltech, January 1994.

(Nowick & Berry, 1972) A.S Nowick and B.S Berry, '*Anelastic Relaxation in Crystalline Solids*', (Academic, New York), 1972.

(Robertson et al, 1982) N. A. Robertson, R. W. Drever, I. Kerr, and J. Hough, J. Phys. E: Sci. Instrum., **15** (1982) 1101-1104.

(Robertson, 1993) D.I Robertson, University of Glasgow, Private communication (June, 1993).

(Robertson & Killbourn, 1993) D.I Robertson & S. Killbourn, Private communication (June 1993).

(Robertson et al, 1995) D.I. Robertson, E. Morrison, J. Hough, B.J. Meers, G. P. Newton, N.A Robertson, K.A Strain, and H. Ward, Rev. Sci. Instrum. **66** 9 (1995).

(Rowan, 1995) S. Rowan, Ph.D. Thesis, University of Glasgow, 1995.

(Rowan et al, 1996) S. Rowan et al, Talk presented at the *'LISA'* workshop, Rutherford Appleton Laboratory, July 1996, To be submitted to Classical & Quantum Gravity.

(Saulson, 1990) P. R. Saulson, Phys. Rev. D, **42** 8 (1990) 2437-2445.

(Saulson, 1994) P. R. Saulson, *'Fundamentals of Interferometric Gravitational Wave Detectors'*, (World Scientific Pub. Co.), 1994.

(Schutz, 1986) B. F. Schutz, Nature, **323** (1986) 310-311.

(Schutz 1996). B. F. Schutz, *The detection of gravitational waves*, To be published in *Proceedings of 1995 Les Houches School on Astrophysical Sources of Gravitational Radiation*, Ed. J. A. Marck and J. P. Lasota, (Springer Berlin), 1996.

(Shoemaker et al, 1988) D Shoemaker, R. Schilling, L. Schnupp, W. Winkler, K. Maischberger, and A. Rüdiger, Phys. Rev. D., **38** 2 (1988) 423-432.

(Snowdon, 1979) J. C. Snowdon, *'Vibration Isolation: Use and Characterisation'*, NBS Handbook 128, (U.S. Dept. of Commerce / NBS Washington DC), 1979.

(Stebbins et al, 1994) R. Stebbins, D. Newell, S. Richman, P. Bender, J. Faller, J.Mason, SPIE Vol. 2264 *'Vibration Monitoring and Control'* (1994) / 27.

(Stephens et al, 1991) M. Stephens, P. Saulson, and J. Kovalik; Rev. Sci. Instrum. **62** 4 (1991).

(Strain and Meers, 1991) K. A. Strain and B. J. Meers, Phys. Rev. Lett., **66** 11 (1991) 1391-1394.

(Taylor & Weisberg, 1982) J. H. Taylor and J. M. Weisberg, The Astrophysical Journal, **253** (1982) 908-920.

(Tutukov & Yungelson, 1993) A. V. Tutukov and L. R. Yungelson, Mon. Not. R. Astron. Soc., **260** (1993) 675-678.

(Twyford, 1994) S. M. Twyford, Proc. 4th GEO 600 Workshop, Hanover, Dec. 2-4, 1994.

(Wagoner, 1984) R. V. Wagoner, Phys. Journ., **278** (1984) 345-348.

(Weber, 1960) J. Weber, Phys. Rev., **117** 1 (1960) 306-313.

(Weiss, 1972) R. Weiss, M. I. T. Quarterly Progress Report No. 105, 1972.

(Wilson & Mathews, 1995) J. R. Wilson and G. J. Mathews, Am. Phys. Soc., **75** 23 (1995) 4161-4164.

(Winkler, 1993) W. Winkler, Private Communication, 1993.

(Winkler et al, 1994) W. Winkler, R. Schilling, K. Danzmann, J. Mizuno, A. Rudiger, and K. A. Strain; App. Opt. **33** (1994) 7547.

(Winterflood, 1994) J. Winterflood, in '*Minutes of the Thermal Noise Workshop*', Pisa, Nov. 30 1994.

(Zener, 1937) C. Zener, Phys. Rev., **52** (1937) 230.